2018

Numerical Modeling Of Collision And Agglomeration Of Adhesive Particles In Turbulent Flows

Farzad Farajidizaji
University of Vermont

NUMERICAL MODELING OF COLLISION AND AGGLOMERATION OF ADHESIVE PARTICLES IN TURBULENT FLOWS

A Dissertation Presented

by

Farzad Farajidizaji

to

The Faculty of the Graduate College
of

The University of Vermont

In Partial Fulfillment of the Requirements
for the Degree of Doctor of Philosophy
Specializing in Mechanical Engineering

October, 2018

Defense Date: May 21, 2018
Dissertation Examination Committee:

Jeffrey S. Marshall, Advisor
George Pinder, Ph.D., Chairperson
Yves Dubief, Ph.D.
William Louisos, Ph.D.
Cynthia J. Forehand, Ph.D., Dean of the Graduate College

ABSTRACT

Particle motion, clustering and agglomeration play an important role in natural phenomena and industrial processes. In classical computational fluid dynamics (CFD), there are three major methods which can be used to predict the flow field and consequently the behavior of particles in flow-fields: 1) direct numerical simulation (DNS) which is very expensive and time consuming, 2) large eddy simulation (LES) which resolves the large scale but not the small scale fluctuations, and 3) Reynolds-Averaged Navier-Stokes (RANS) which can only predict the mean flow. In order to make LES and RANS usable for studying the behavior of small suspended particles, we need to introduce small scale fluctuations to these models, since these small scales have a huge impact on the particle behavior.

The first part of this dissertation both extends and critically examines a new method for the generation of small scale fluctuations for use with RANS simulations. This method, called the stochastic vortex structure (SVS) method, uses a series of randomly positioned and oriented vortex tubes to induce the small-scale fluctuating flow. We first use SVS in isotropic homogenous turbulence and validate the predicted flow characteristics and collision and agglomeration of particles from the SVS model with full DNS computations. The calculation speed for the induced velocity from the vortex structures is improved by about two orders of magnitude using a combination of the fast multiple method and a local Taylor series expansion. Next we turn to the problem of extension of the SVS method to more general turbulent flows. We propose an inverse method by which the initial vortex orientation can be specified to generate a specific anisotropic Reynolds stress field. The proposed method is validated for turbulence measures and colliding particle transport in comparison to DNS for turbulent jet flow.

The second part of the dissertation uses DNS to examine in more detail two issues raised during developing the SVS model. The first issue concerns the effect of two-way coupling on the agglomeration of adhesive particles. The SVS model as developed to date does not account for the effect of particles on the flow-field (one-way coupling). We focused on examination of the local flow around agglomerates and the effect of agglomeration on modulation of the turbulence. The second issue examines the microphysics of turbulent agglomeration by examining breakup and collision of agglomerates in a shear flow. DNS results are reported both for one agglomerate in shear and for collision of two agglomerates, with a focus on the physics and role of the particle-induced flow field on the particle dynamics.

CITATIONS

Material from this dissertation has been published in the following form:

Dizaji, F. F., & Marshall, J. S.. (2016). An accelerated stochastic vortex structure method for particle collision and agglomeration in homogeneous turbulence. *Physics of Fluids*, *28*(11), 113301.

Dizaji, F. F., & Marshall, J. S.. (2017). On the significance of two-way coupling in simulation of turbulent particle agglomeration. *Powder Technology*, *318*, 83-94.

Dizaji, F. F., Marshall, J. S., & Grant, J. R.. (2018). A stochastic vortex structure method for interacting particles in turbulent shear flows. *Physics of Fluids*, *30*(1), 013301.

Material from this dissertation has been submitted for publication to Journal of Fluid Mechanics on 5/9/2018 in the following form:

Dizaji, F. F., Marshall, J. S., & Grant, J. R.. Collision and breakup of fractal particle agglomerates in a shear flow. Journal of Fluid Mechanics.

DEDICATION

To my lovely Azerbaijan

ACKNOWLEDGEMENTS

Firstly, I would like to express my sincere gratitude to my advisor Prof. Jeffrey Scott Marshall for the continuous support of my Ph.D study and related research, for his patience, motivation, and immense knowledge. His guidance helped me in all the time of research and writing of this thesis. I could not have imagined having a better advisor and mentor for my Ph.D study. Also, I would like to thank Dr. John R. Grant for his guidance and helps during my project.

Besides my advisor, I would like to thank the rest of my thesis committee: Prof. George Pinder, Dr. Yves Dubief, and Dr. William Louisos, for their insightful comments and encouragement, but also for the hard question which incented me to widen my research from various perspectives.

Last but not the least, I would like to thank my family for supporting me spiritually throughout writing this thesis and my life in general. Also, I want to thank myself for doing this research in the best way I can and without seeing my family for four years.

TABLE OF CONTENTS

Page

LIST OF TABLES

LIST OF FIGURES

Figure Page

CHAPTER 1: Motivation and Objective

1.1 Motivation

Particle collision and agglomeration play an important role in a wide range of turbulent flows applications involving small particles or droplets. Droplet collision and merger is a key element to cloud formation and precipitation development (Devenish et al., 2012). Indeed, ice particle collision and subsequent contact electrification in clouds is believed to be responsible for cloud electrical charging, leading to lightning discharge (Helsdon et al., 2001; Saunders, 1994). Particle agglomeration is particularly important in aerosol flow problems, such as fly ash collection from combustion processes (Xu et al., 2010), flame-synthesis of nanoparticles (Zhang et al., 2012), electrostatic precipitator operation (Dong et al., 2018), cyclone particle separators (Paiva et al., 2010), and snow crystal formation (Kajikawa et al., 2000).

One challenge in simulating turbulent particle agglomeration is the difficulty in simulating the turbulent flow itself. The most accurate way approach to turbulence simulation is direct numerical simulation (DNS), in which all scales of the turbulent motion are directly solved using the Navier-Stokes equation. However, DNS is so computationally demanding that it is not possible in all but very simple flow domains at relatively low Reynolds numbers. It is therefore necessary to sacrifice some of accuracy to get a less expensive method for turbulence simulation. Large-eddy simulation (LES) achieves this simplification by directly computing only the large-scale motions and modeling the effect of smaller scale motions on the larger scales. LES has been found to provide accurate simulations for many flows, but it also is too computationally demanding for many practical flow fields, as well as for applications such as design and

flow control that require rapid flow-through times. The Reynolds-averaged Navier-Stokes (RANS) method is a traditional approach to turbulence simulation which solves the Reynolds-averaged Navier-Stokes equations only for the mean velocity field, and then also solves for certain additional variables that characterize the turbulent motion. When using RANS method to evolve particle flows, it is necessary to also implement some method to generate the subgrid-scale turbulent fluctuations that is consistent with the computed turbulence measures, since these subgrid-scale fluctuations have an important effect on the particle motion.

A common approach to dealing with this problem is the stochastic Lagrangian method (SLM) (Thomson, 1987; Sawford, 1991; Pope and Chen, 1990), in which a set of stochastic differential equations are solved to generate a synthetic turbulence fluctuation field with the correct time scales of turbulent motion. Example simulations show that for non-interacting particles, SLM works well for prediction of dispersion of non-interacting particles (see Figure 1.1). For interacting particles in turbulent flows, however, SLM experiences difficulties. As shown in Figure 1.2(a), when two particles lie near each other, they must experience similar induced forces, so that these forces on the nearby particles will be correlated. By contrast, stochastic Lagrangian methods employ uncorrelated stochastic forcing at each particle. This lack of correlation isn't particularly a problem for non-interacting particles since it doesn't have a large impact on the overall dispersion of the particles, but it has a very significant impact on the relative motion of two nearby particles. As a consequence, the standard SLM approach cannot be used for particles that interact with each other.

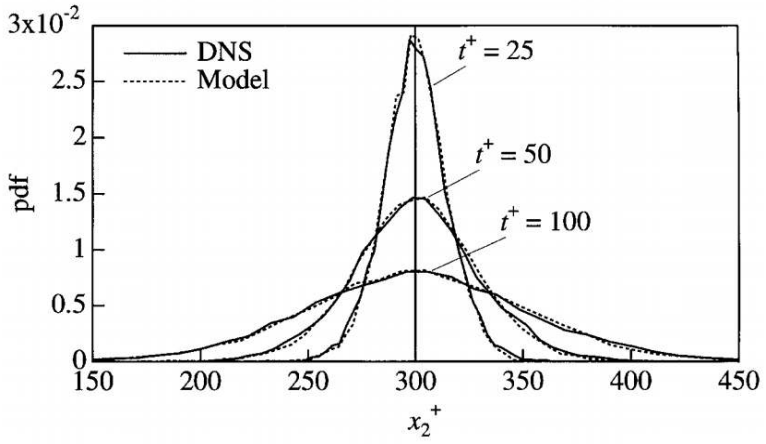

Figure 1.1. Dispersion of fluid elements in a channel flow originating at a distance, $x_2^+ = 300$ in the wall-normal direction, as predicted from DNS (solid line) and SLM (dotted line). (Reproduced from Mito and Hanratty, 2002).

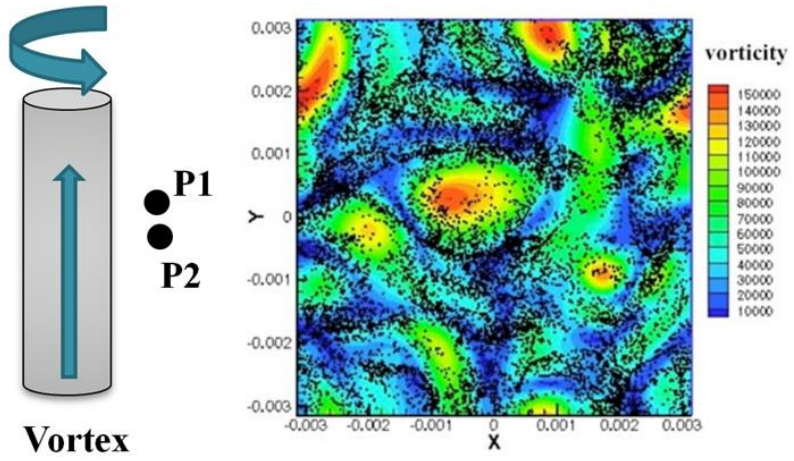

Figure 1.2. (a) Schematic showing two particles near each other close to a vortex tube. (b) Cross-section of a turbulent flow showing the normal vorticity component with particles superimposed. (Reproduced from Garcia, 2009)

In searching for a new method to generate subgrid-scale turbulence, two considerations should be kept in mind. The first consideration is that the presence of coherent eddies within turbulent flows has a major impact on the local concentration field of particles, particularly if the particles are heavier than the surrounding fluid and are therefore thrown out of the eddy core by the eddy centrifugal force. Eddy-induced

particle clustering leads to formation of regions of high particle concentration surrounding the turbulent eddies, which dramatically increases particle collision rate and (for adhesive particles) agglomerate sizes, as shown in Figure 1.2(b). This observation suggests use of a method for generating synthetic turbulence that either generates or is based on vortex tubes. The second consideration is that particle collision and adhesion processes occur on very small time scales, which makes the numerical simulation of colliding and adhesive particles numerically stiff. This is especially true in simulations using the soft-sphere discrete element method (DEM), which requires that the time scale during particle collision be resolved by the numerical method. As a result, the method for synthetic turbulence generation needs to be fast.

A first step toward the use of a vortex structure model for turbulent particle transport was made by Ayyalasomayajula et al. (2008), who proposed a model in which the turbulent eddies were represented by a two-dimensional vortex array and a stochastic algorithm was used to vary the strength of each vortex in time. A schematic of the 2D vortex model is illustrated in Figure 1.3, where the black dots represent the vortex centers, L is the separation distance between the vortices, and the arrows represent the directions of the circulations. While this approach is extremely simplistic, it nevertheless accurately reproduced the probability density function of the acceleration field in the turbulent flow.

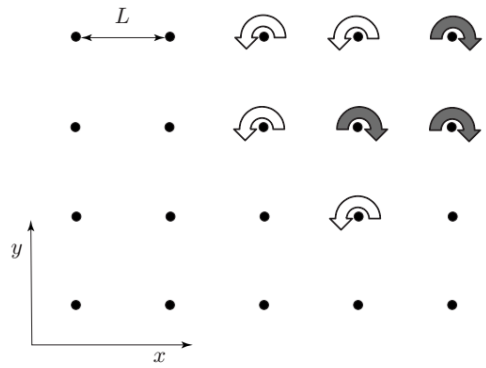

Figure 1.3 Schematic of the 2D vortex model of Ayyalasomayajula et al. (2008). The black dots represent the vortex centers. (Reproduced from Ayyalasomayajula et al., 2008)

Sala and Marshall (2013) proposed a 3D vortex-based model which they called the stochastic vortex structure (SVS) method. In the SVS method, the turbulent vorticity field is approximated by a set of finite-length vortex structures which are randomly positioned and oriented in the flow field, as shown in Figure 1.4. In this early version of the SVS method, the vortices were fixed in space and it was only used for isotropic homogenous turbulence. The original SVS method was also fairly slow, since it needed to predict the induced velocity from each vortex onto the nodal points of a grid covering the flow field at each time step of the computation. There is therefore a need to improve the speed of the SVS method and to expand the types of flow fields to which the method can be applied.

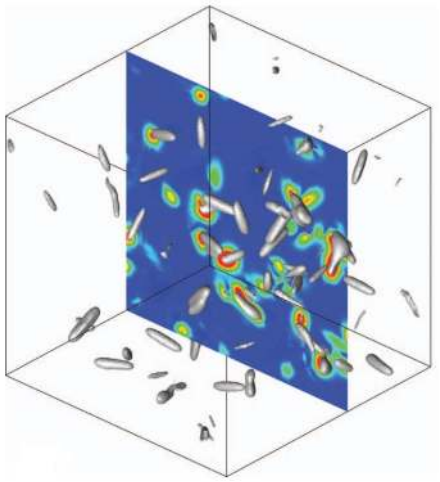

Figure 1.4. Illustration of the coherent vortex structures in an isotropic homogeneous turbulence. (Reproduced from Sala and Marshall, 2013)

Aside from these issues, the SVS method has the inherent limitation that it does not account for the effect of particles on the turbulent flow. While flows with a high particle concentration can induce large-scale changes in turbulence, even flow fields with smaller concentration of adhesive particles can exhibit high local concentration near agglomerates, with associated important role of particle-induced flow. A number of researchers have studied the effect of individual particles on turbulence (Crowe, 2000; Eaton, 2009; Saber et al., 2015; Poelma and Ooms, 2006; Rao et al., 2012; Balachandar and Eaton, 2010); however, there is almost no research to date on the effect of particle agglomeration on turbulence modulation.

The process of turbulent agglomeration is dominated by collision and adhesion of particles to each other, which occurs first with individual particles, then small agglomerates, followed by progressively larger agglomerates. If the turbulence conditions are held constant, the agglomerates will eventually grow large enough to start breaking up and an equilibrium state will be achieved. This process of agglomerate growth

approaching equilibrium is illustrated in Figure 1.5, which plots the average number of particles in an agglomerate versus time in a turbulent flow. Sonntag and Russell (1986) report that the agglomerate radius of gyration in this equilibrium state decreases as the shear rate increases. Lian et al. (1998), Kun et al. (1999), Schäfer et al. (2007), and Tong et al. (2016) have numerically studied the collision of two equal-sized agglomerates; however, in this work the agglomerates are assumed to be highly packed whereas the agglomerates formed in turbulent flows are loosely-structured fractal agglomerates. Very little research has been done to date on the collision of two loosely packed agglomerates, typical of turbulent agglomeration processes. Additional DNS research is required both for understanding the turbulent agglomeration process and the role of the particle-fluid two-way interaction on this process.

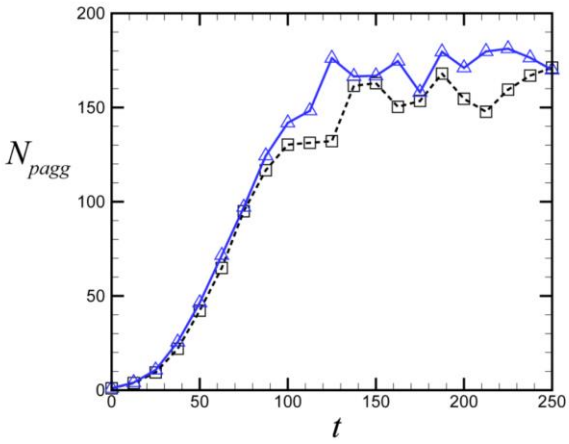

Figure 1.5. Plot showing time variation of the average number of particles per agglomerate(N_{pagg}) over a long run time leading to a statistical equilibrium condition, for SVS with NV = 2048 (blue curve) and DNS (dashed curve). (Reproduced from Dizaji and Marshall, 2016).

1.2. Objective and Scope

The main objective of this dissertation is to advance the so-called stochastic vortex structure (SVS) method for generating synthetic turbulence using randomly positioned

vortex structures. The generated flow-field can be coupled to Reynolds-averaged Navier-Stokes (RANS) models to compensate for the lack of small-scale fluctuations when computing particulate turbulent flows, which has an important impact on the collision and agglomeration of particles. Potential future application of the method for reconstructing the small scales in large eddy simulation (LES) is also possible, but was not examined specifically in the dissertation. In addition, two related studies were performed using the DNS approach to investigate specific physical problems related to particle agglomerates in turbulent flow that arose in the course of the research.

In the early version of the SVS method (Sala and Marshall, 2013), the vortex tubes were randomly positioned and oriented and their strength was varied in time. However, the position of the vortex structures in this early version was fixed and the SVS computations were quite slow. Additionally, while the method was effective for prediction of particle collision rate, it was not found to be successful for simulation of particle agglomeration. The only application of the early SVS method was to isotropic homogeneous turbulence, and it was not clear how it might be extended to more general flows. In the current work, the SVS method was extended in numerous ways. In the first study, vortices are no longer fixed and are instead allowed to move freely according to the surrounding flow field. In the early version of SVS, the effect of each vortex was calculated on each target grid point in order to calculate the fluctuating velocity. This slow algorithm is replaced in the current work by the fast multipole method, which calculates the effect of an entire group (box) of neighboring source vortices on a course grid and then uses a local Taylor series expansion to interpolate onto a fine grid covering the flow field. The synthetic turbulent field generated by SVS was validated in the

current work to accurately predict both particle collision as well as a variety of measures of agglomerate formation for adhesive particles. In a second study, a new inverse method was developed and validated by which vortex orientation can be adjusted in the SVS method to produce a desired Reynolds stress field for general anisotropic, inhomogeneous turbulent flows. The effectiveness of this new SVS method for particle transport in anisotropic turbulence was validated versus DNS for turbulent jet flow.

During development of the SVS method, a number of issues arose involving the physics of the turbulent agglomeration process, specifically concerning the role of the particle-induced flow field on agglomerate formation. These issues are relevant to the topic of the dissertation in order to understand the limitations of the SVS method, where we note that the SVS method developed to date inherently lacks the ability to account for the effect of particles on the fluid flow. A third study was conducted using DNS to understand the effect of two-way coupling on the agglomeration of particles and vice versa. A fourth study was conducted, again using DNS, to examine the microphysics of agglomerate breakup and collision in turbulent agglomerate formation, with specific focus on the structure and role of the particle-induced fluid flow. During these two DNS studies, it was observed that the size of the agglomerates approaches a steady state which is controlled by both the turbulent shear rate and the collision of agglomerates with other agglomerates. This observation led to the more detailed investigation in the fourth study, which conducted numerical experiments with both one single agglomerate in a shear flow and with collision of two agglomerates in a shear flow.

CHAPTER 2: LITERATURE REVIEW

2.1. Turbulent Vortex Systems

2.1.1. Vortex models

Turbulence is one of the most challenging unsolved chapters of fluid mechanics. There are lots of attempts to study turbulence from different points of view and approaches, encompassing a wide range of experimental, analytical and computational methods. In turbulence studies, it is common to divide the turbulence into three different scales - energy-containing scale, inertial range and dissipation range. Kolmogorov (1941) derived a formula for the energy spectrum of turbulence in the inertial subrange as

$$E(k) = C\varepsilon^{2/3}k^{-5/3} \tag{2-1}$$

This spectrum gives the distribution of energy E among turbulent vortices as a function of wavenumber k (which scales inversely with eddy size) and shows that energy density is lower for the smaller vortices and energy is more concentrated in the larger scale vortices. A schematic representation of power spectrum and energy cascade is shown in Figure 2.1.

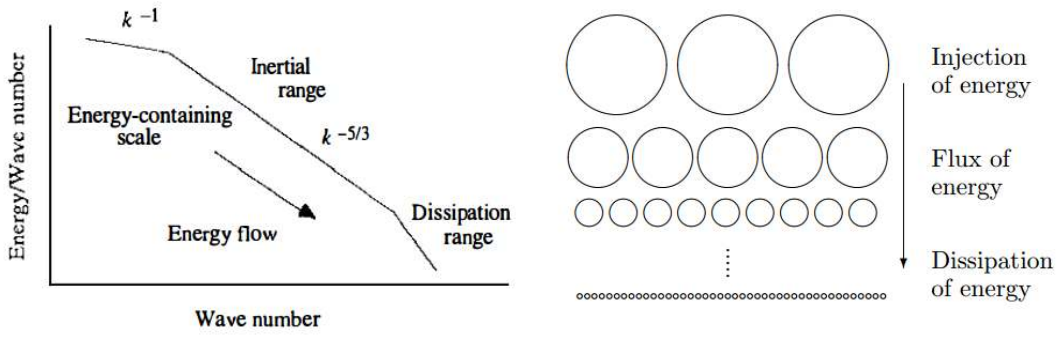

Figure 2.1. (a) A schematic representation of a power spectrum of fluctuations of the total energy of solar wind fields (Reproduced from Goldstein (1995), (b) energy cascade which goes from larger to smaller eddies (Reproduced from Tryggeson, 2007)

Turbulence is known to be induced by a set of coherent vortex structures, which result from instability modes of the basic flow (Fiedler, 1988). Figure 2.2 shows examples of intense vortical structures with tube- or worm-like shape in turbulent flows.

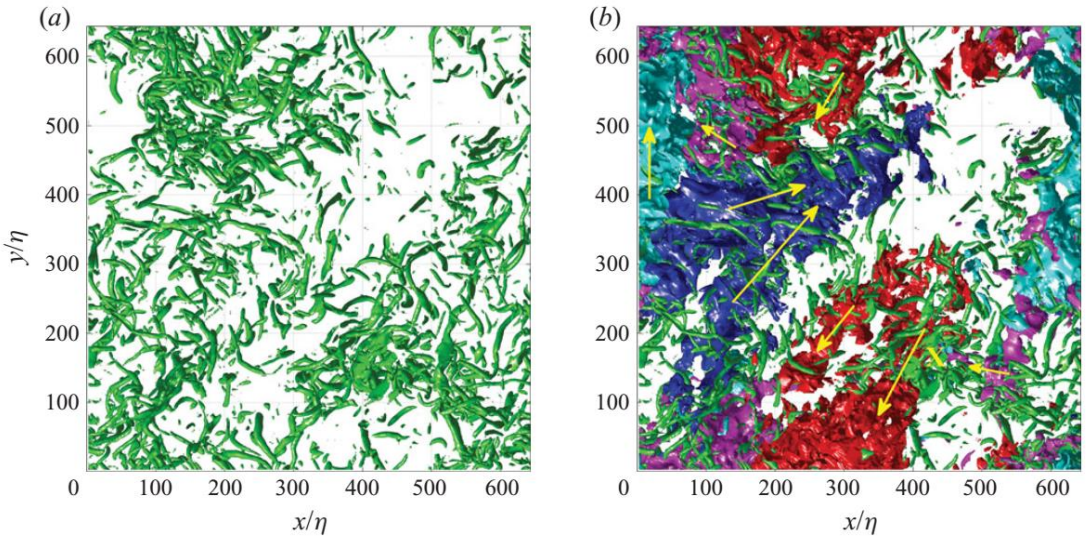

Figure 2.2. Visualization of the intense vortical structures in a subvolume of isotropic turbulence (green) without (a) and with (b) a number of uniform velocity zones (blue, red, cyan and magenta depending of the flow direction as indicated by the arrows) (Reproduced from Elsinga 2010)

Taylor (1938) argued that intensification of vorticity through vortex stretching and vorticity decay through viscous diffusion are the two important dynamical mechanisms which control the dissipation of energy in turbulence. By assuming that these two mechanisms are in balance, Burgers (1948) found an exact solution to the Navier-Stokes equations for a constant-density fluid. The exact solution of a 3-D vortex satisfying the Navier-Stokes equation given by Burgers is given in cylindrical polar coordinates (r,θ,z) as

$$u_r = -\frac{\alpha r}{2}, \qquad u_\theta = -\frac{\Gamma}{2\pi r}\left[1-\exp\left(-\frac{\alpha r^2}{4\nu}\right)\right], \qquad u_z = \alpha z \tag{2-2}$$

where $\alpha > 0$ is the constant stretching rate and Γ is the vortex circulation. The vorticity is given by

$$\omega = \frac{\alpha\Gamma}{4\pi\nu}\exp\left(-\frac{\alpha r^2}{4\nu}\right)e_z \tag{2-3}$$

A schematic diagram of the Burgers vortex and a plot of the circumferential velocity u_θ is given in Figure 2.3.

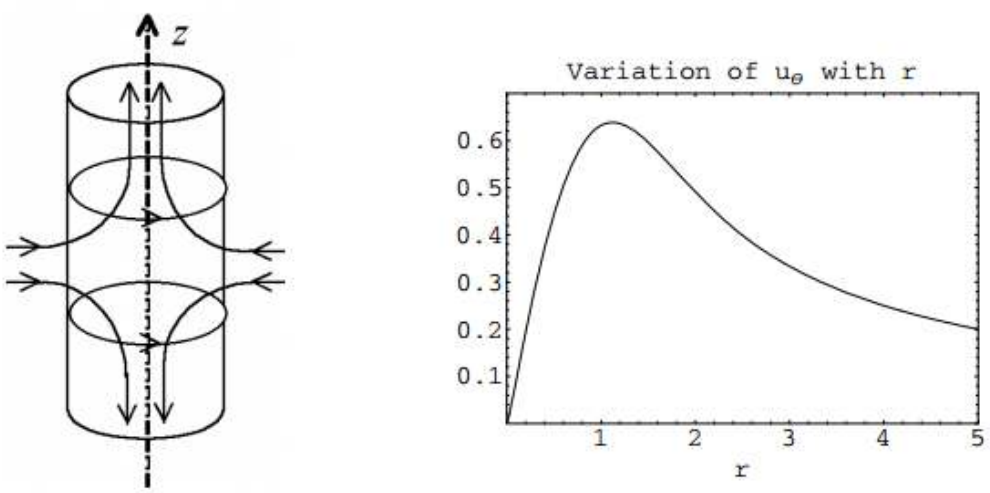

Figure 2.3: (left) Picture of Burgers' vortex. (right) The variation of u_θ with r (Reproduced from Tryggeson, 2007).

2.1.2. Analytical methods for vortex modeling

One of the early theories for modeling the small-scale structures of turbulence was proposed by Townsend (1951), who used a random distribution of either vortex sheets or vortex tubes (Burger's vortices) to simulate anomaly and spatial inhomogeneity of turbulent motion and to generate a power spectrum. Townsend (1951) used an expression for vorticity field of the form

$$\omega = \frac{\Gamma}{\pi\delta^2}\exp(-r^2/\delta^2) \tag{2-4}$$

in which the vortex core length scale is $\delta = 2\sqrt{\upsilon/c}$ and c is the axial stretching rate. For a system of N_V Burgers vortices of length l and strength Γ, the enstrophy is given by

$$\Omega = \frac{N_V \Gamma^2 l}{4\pi\delta^2 V} \tag{2-5}$$

The general expression (Lundgren, 1982; Pullin and Saffman, 1993) for power spectrum for a random superposition of straight, infinitely long, non-axisymmetric vortex tubes in polar coordinates (r,θ) is

$$E(k) = \frac{N}{k}\sum_{-\infty}^{\infty}\left|\int_0^{\infty} J_n(kr)\omega_n(r)rdr\right|^2 \tag{2-6}$$

in which J_n is the Bessel function of the first kind of order n. By substituting the Burgers vorticity distribution (2-4) into the filter (2.6), the shell-summed energy spectrum (Saffman, 1997) is obtained as

$$e(k) = \frac{N_V \Gamma^2 l}{4\pi V k}\exp(-\delta^2 k^2/4) \tag{2-7}$$

This expression is derived based on the assumption that the energy generated by each vortex is additive, i.e., that each vortex induces velocity in a finite volume which is only influenced by that single vortex. While this assumption is common in vortex-based turbulence models, it is nevertheless rather suspect as nearby vortices in fact do interact with each other. Integrating over the wavenumber interval $(k_{\min}, k_{\max})$ gives the turbulent kinetic energy as

$$E = \int_{k_{\min}}^{k_{\max}} e(k)dk = \frac{N_V \Gamma^2 l}{4\pi V}\left[E_1(\delta^2 k_{\min}^2/4) - E_1(\delta^2 k_{\max}^2/4)\right] \tag{2-8}$$

where $E_1(.)$ is the exponential integral function.

Lundgren (1982) furthered development of vortex-based turbulence modeling by proposing a spiral vortex representation for turbulent vortices (unsteady stretched spiral vortices) as a replacement for the Burgers vortices used in Townsend's model. Each vortex in the Lundgren model has the form of a slender, axially strained spiral vortex solution of the Navier-Stokes equation. The tightening of the spiral turns by the differential rotation of the induced swirling velocity produces a cascade of velocity fluctuations to smaller scale. The spectrum of each vortex in this model satisfies the Kolmogorov energy spectrum, given by

$$E(k) = Ak^{-5/3} \exp[-\frac{2}{3}(\nu k^2/a)] \tag{2-9}$$

Pullin and Saffman(1993), inspired by Lundgren's work on spiral vortices, used their model to calculate vorticity and velocity-derivative moments for homogeneous isotropic turbulence. They also proposed a specific form of the relaxing spiral vortex which is modeled by a rolling-up vortex layer embedded in a background containing opposite signed vorticity and with zero total circulation at infinity. Using their model, they have derived expressions for moment of vorticity ($\Omega_{2p} = \hat{\Omega}_{2p} R_\lambda^{p/2-3/4}$), hyper-flatness ($F_{2p} = \hat{F}_{2p} R_\lambda^{p/2-3/4}$) and hyper-skewness ($S_{2p+1} = \hat{S}_{2p+1} R_\lambda^{p/2-3/4}$).

Hatakayema and Kambe (1997) analytically studied the statistical properties and scaling of a set of randomly distributed Burgers' vortices. In homogeneous isotropic turbulence, the structure function S_p was shown to follow a power law in the inertial range as a function of distance *s* between the velocity measurement points as

$$S_p = \left\langle [\Delta v_l(x,s)]^p \right\rangle \approx s^{\zeta_p} \tag{2-10}$$

where ζ_p is the scaling exponent of the *p*th order structure function. They found that in the inertial range, the third-order structure function is negative and the scaling exponent is nearly unity in accordance with Kolmogorov's four-fifths law. They also estimated scaling exponents up to $25th$ order and predicted the probability density function (p.d.f.) of vorticity strength.

Wilczek and Friedrich (2009) studied dynamical aspects of turbulence and the non-Gaussian nature of the vorticity probability density functions both analytically and numerically. They derived an equation for p.d.f. of the vorticity field and showed that it compared well to their direct numerical simulation data (Figure 2.4).

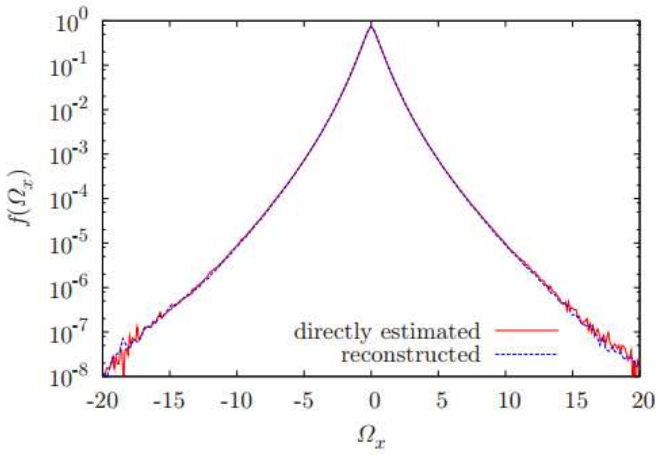

Figure 2.4 Logarithmic plot of the vorticity p.d.f estimated directly from direct numerical simulation data and the reconstructed p.d.f. according to algebraic equation. (Reproduced from Wilczek and Friedrich, 2009)

They find two regions in the vorticity p.d.f. which reveals the non-Gaussian nature of the vorticity p.d.f. in a nonstationary flow field: 1) the inner region of the p.d.f. is quenched due to the dominant vorticity diffusion and 2) the outer region of the p.d.f. develops fat

tails due to stretching of the strong vortices. The temporal evolution of the vorticity field is visualized in Figure 2.5.

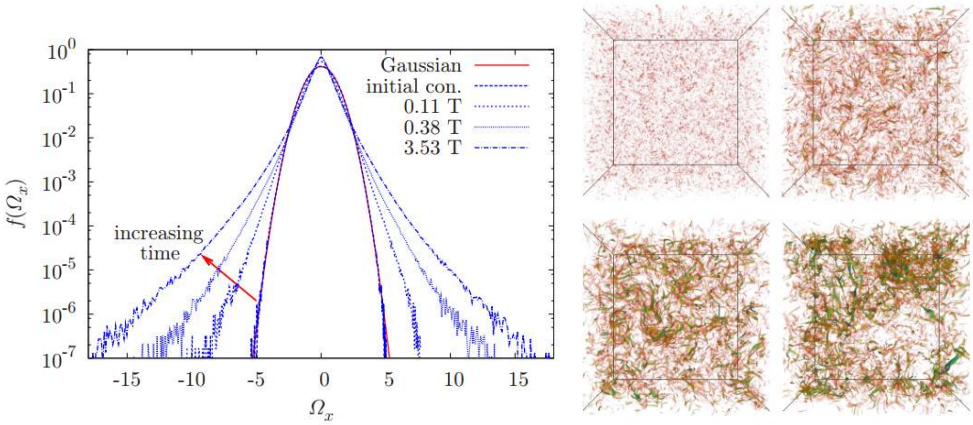

Figure 2.5. (a) Temporal evolution of the vorticity p.d.f.s from a Gaussian initial condition. (b)Volume rendering of the absolute value of vorticity above a fixed threshold for different stages of the nonstationary simulation from top left to bottom right: initial condition, 0.11T, 0.38T, and 3.53T. (Reproduced from Wilczek and Friedrich, 2009)

Min et al . (1996) used both two-dimensional singular vortex and vortex blob methods and a three-dimensional vortex blob method to numerically calculate the velocity field in homogeneous turbulence. Probability density functions (p.d.f.s) of the velocity and the velocity difference fields were calculated. The p.d.f for velocity differences of a system of singular vortex elements was shown to be of Cauchy form in the case of small separation δr, both in 2 and 3 dimensions. For non-singular vortex blobs using an intermediate $\delta r = 0.05$ value, tails deviate from the Cauchy distribution and approach an exponential distribution at large distances (Figure 2.6).

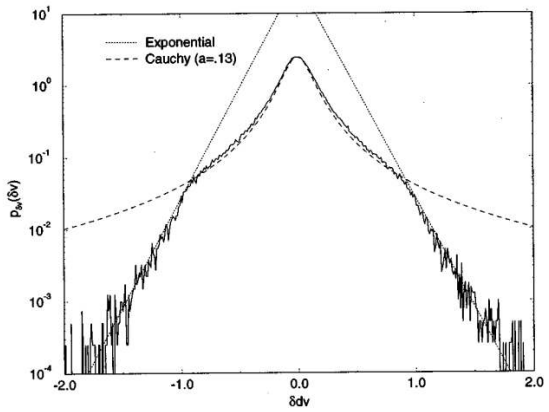

Figure 2.6. (a). Probability density functions. of the normalized velocity difference for 150 vortices and $\delta r = 0.05$. (Reproduced from Min et al., 1996)

Kivotides and Leonard (2003) performed numerical computations where homogeneous turbulence was generated by a set of finite-length vortex structures, and showed empirically this system generates an energy spectrum that satisfies the Kolmogorov $k^{-5/3}$ scaling in the turbulence inertial range. Figure 2.7 presents the energy spectra at two different times $t = 0.09$ and $t = 0.14$, comparing the compute spectrum with the Kolmogorov spectrum.

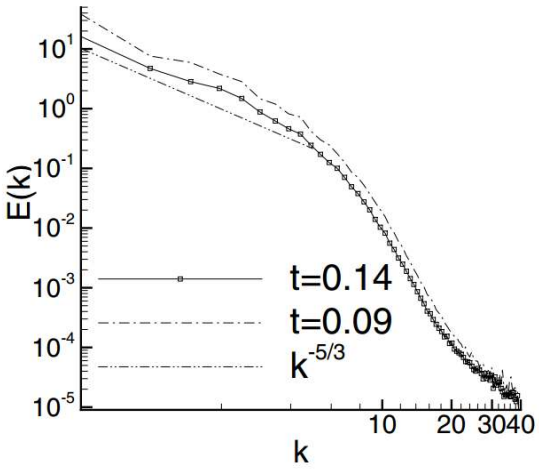

Figure 2.7 Energy spectra at two different time $t = 0.09$ and $t = 0.14$ (Reproduced from Kivotides and Leonard, 2003)

2.1.3. Numerical simulation and experimental results for vortex modeling

While the notion that turbulence can be generated by a set of vortex structures has been discussed for a long time, completion of such a model requires certain scaling information to address issues such as:

1) how vortices are distributed in the turbulent field

2) sizes of vortices (length and core lengths)

3) lifetime of the vortices

Some of these issues were addressed using direct numerical simulation as well as experimental approaches.

Vincent and Meneguzzi (1991) used direct numerical simulation (DNS) to show that velocity derivatives are strongly non-Gaussian both in the inertial and the viscous subranges and that the flow is organized in very elongated vorticity tubes. Their visualizations of the vorticity flow-field (Figure 2.8(a)) show vortex tubes that are of the same order as the integral scale, with core radius on the order of a few dissipation scales. Figure 2.8(b) shows a cut through a typical vorticity tube and thickness of vortex is completely measurable from below Figure.

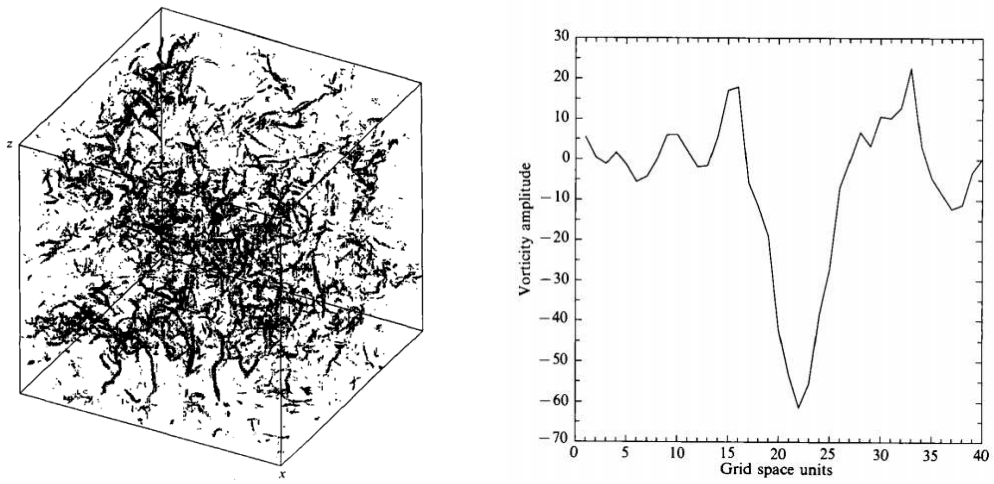

Figure 2.8(a) View of the vorticity field, represented by a vector of length proportional to the vorticity amplitude at each grid point. (b) Cut through a typical vorticity tube along a direction perpendicular to its axis (Reproduced from Vincent and Meneguzzi 1991)

Vincent and Meneguzzi (1994) investigated the characteristics of homogeneous turbulence more deeply to find dynamics of vorticity tubes in a continuation of their previous study. They identified shear instability of thin vorticity sheets as the primary mechanism for vortex tube generation in three-dimensional turbulent flow. In order to estimate the lifetime of the vortex structures, they followed the motion in time of five vortices, identified as A, B, C, D and E in Figure 2.9 at two different times separated by one eddy turnover time (~ L/v_0 where L is the integral scale and v_0 is the root-mean-square velocity). From analyzing A, B, C, D and E vortices in both Figures, they estimated the vortex structure lifetime as 5-10 times the turnover time.

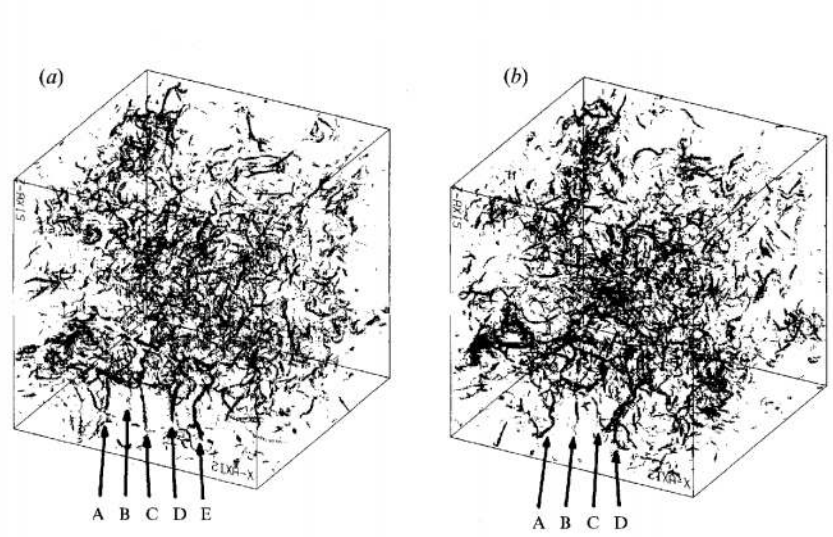

Figure 2.9 (a) View of the vorticity field: vorticity vectors are reprcsented by arrows, here too small to be seen individually. Only vectors with modulus above a certain threshold are displayed. The tubes marked A, B, C, D, E are approximately parallel. (b) The same as (a) a little more than one turnover time later. Note the parallel motion of tubes A, B, C, D and the merging of the tubes D and E. (Reproduced from Vincent and Meneguzzi, 1994)

Jimenez et al. (1993) numerically simulated homogeneous, isotropic turbulent flow fields at high resolution, giving insight into the coherent vortex filaments and their associated scales. They have plotted the histogram of vorticity as shown in Figure 2.10. Small-scale turbulence $\omega' = (\varepsilon / \nu)^{0.5}$ is used to normalize the vorticity.

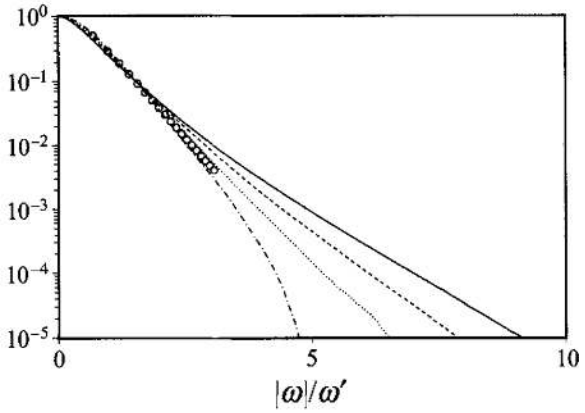

Figure 2.10. One-dimensional histogram vorticity for $\mathrm{Re}_\lambda = 35 - 170$. Open circles are from Ruetsch and Maxey (1991) at $\mathrm{Re}_\lambda = 62$ (Reproduced from Jimenez et al., 1993)

From visualization of the flow field, Jimenez et al. (1993) found that most of the volume in the flow is occupied by relatively 'weak' non-coherent vorticity, with strong coherent vortices filling only a small fraction of the space. Based on his finding, Jimenez et al. (1993) divided flow field into two parts:

1) weak vortices $0.2\omega' < |\omega| < \omega'$, referred to as background vortices
2) intense vortices $|\omega| > \omega'$, referred to as 'worms' .

Jimenez et al. (1993) found that the structure of the weak and strong vortices are very different. Regions of weak vorticity do not have an apparent structure, whereas the strong vorticity tends to be organized in tubes or ribbons (or 'worms') as shown in Figure 2.11.

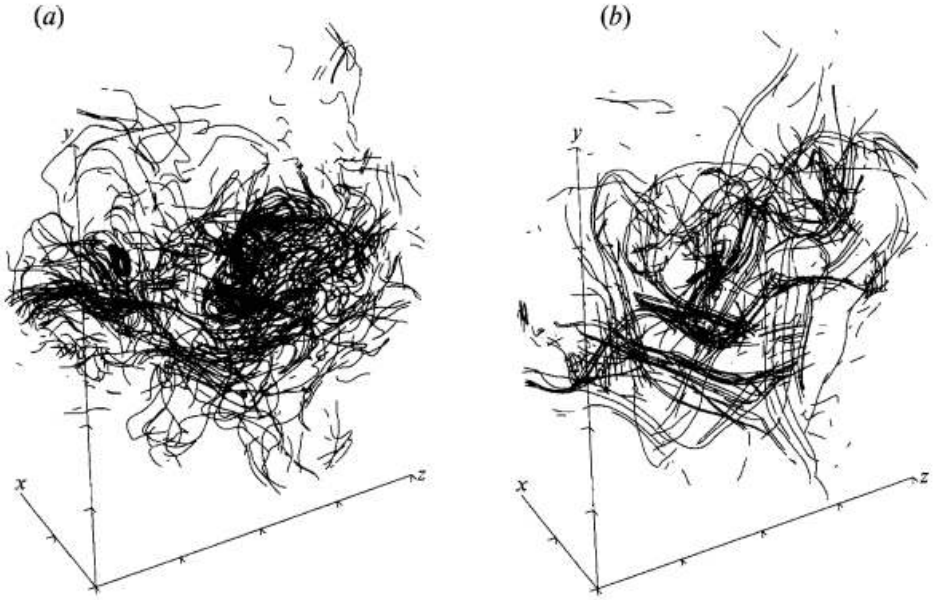

Figure 2.11. Vortex lines for homogeneous isotropic turbulence, $\mathrm{Re}_\lambda = 168$.(a) weak vortices, (b) strong vortices (Reproduced from Jimenez et al., 1993)

By means of an automatic tracking algorithm, Jimenez et al. (1993) determined scaling laws for the kinematic properties of the vortex 'worms'.

Belin et al (1996) experimentally studied intense vortex filaments in fully-developed turbulent shear flow between two counter-rotating disks. Helium gas at low temperature was used as the fluid between the disks. They found that at low Reynolds number, $\mathrm{Re}_\lambda \le 700$, turbulence is dominated by a set of strong, coherent vortex structures of finite length and with tubular shape, surrounded by a sea of weak random (non-coherent) vortices.

The typical radius δ of the vortex worms scale with the Kolmogorov length scale η according to $\delta \cong 3.9\eta$, the vortex length is proportional to the Lagrangian integral scale, and the vortex strength γ is characterized by the vortex Reynolds number $\mathrm{Re}_\gamma = \gamma / \upsilon$, which varies in proportional to the square root of the Taylor microscale Reynolds number $\mathrm{Re}_\lambda = v_0 \lambda / \nu$, or $\mathrm{Re}_\gamma \approx \mathrm{Re}_\lambda^{0.5}$. These scaling relationships where derived theoretically by Jimenez et al. (1993) and Kambe and Hatakeyama (2000), and validated via direct numerical simulation and via experiments by Jimenez et al. (1993) and Belin et al. (1996), respectively. The probability density distributions (p.d.f.) of radius and strength for the strong vortices were found to have a log-normal form, as given in Figure 2.12 from Jimenez et al. (1993).

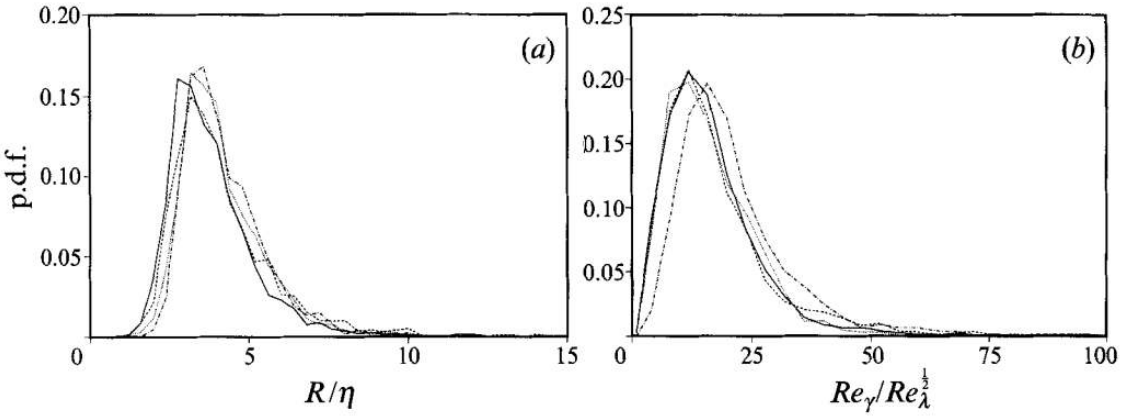

Figure 2.12. Probability density of (a) worm radius and (b) circulation at four different Reynolds numbers $\mathrm{Re}_\lambda = 35-170$. (Reproduced from Jimenez et al., 1993)

A similar log-normal probability distribution is observed in the p.d.f. of vortex size obtained in the experimental study of Belin et al. (1996) plotted in Figure 2.13, where we again find that the vortex core radius scales with the Kolomogrov length scale. Belin et al.'s experimental results demonstrate coherent vortex scaling that compares well with the direct numerical simulations of Jimenez et al. (1993).

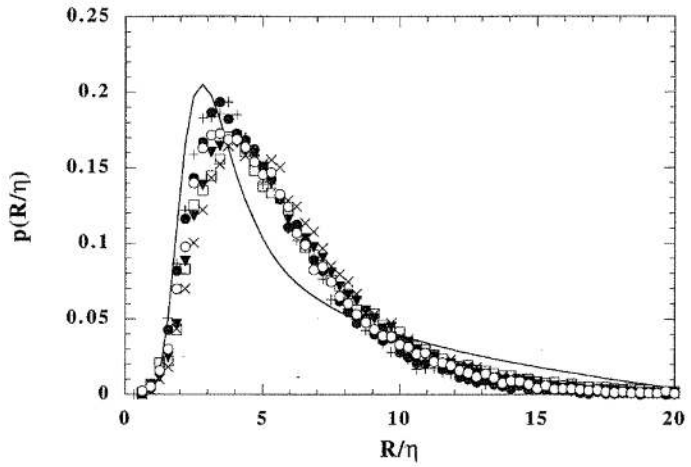

Figure 2.13. Size distribution of the worms, for different Reynolds number for $\mathrm{Re}_\lambda = 151$ to $\mathrm{Re}_\lambda = 718$ shown as symbols (Belin et al., (1996)). full line is obtained from Jimenez et al.(1993). (Reproduced from Belin et al., 1996)

Previous studies discussed above have provided information about turbulent coherent vortices such as shape, length, core radius and life time. This information can be used in a vortex-based model to generate synthetic turbulence to model subgrid-scale particle motion in a turbulent particulate flow. A first step toward the use of a vortex structure model for turbulent particle transport was made by Ayyalasomayajula et al. (2008), who proposed a model in which the turbulent eddies are represented by a two-dimensional vortex array and a stochastic algorithm is used to vary the strength of each vortex in time. A schematic of the 2D vortex model is illustrated in Figure 2.14(a), where the black dots represent the vortex centers, L is the separation distance between the vortices, and the arrows represent the directions of the circulations. While this approach is extremely simplistic, it nevertheless accurately reproduced the probability density function of the acceleration field in the turbulent flow. Sala and Marshall (2013) proposed a 3D vortex-based model which they called the stochastic vortex structure (SVS) method. In the SVS method, the turbulent vorticity field is approximated by a set of finite-length vortex structures which are randomly positioned and oriented in the flow field, as shown in Figure 2.14(b). SVS gives good results for particle clustering and collision (Sala and Marshall, 2013); however, this early version of the SVS method requires improvement in a number of aspects. Specifically, in the original version of the SVS method the vortices were fixed in space and it is only used for isotropic homogenous turbulence. The original SVS method was fairly slow, since it needed to predict the induced velocity from each vortex onto the nodal points of a grid covering the flow field at each time step of the computation. There is therefore a need to improve the

speed of the SVS method and to expand the types of flow fields to which the method can be applied.

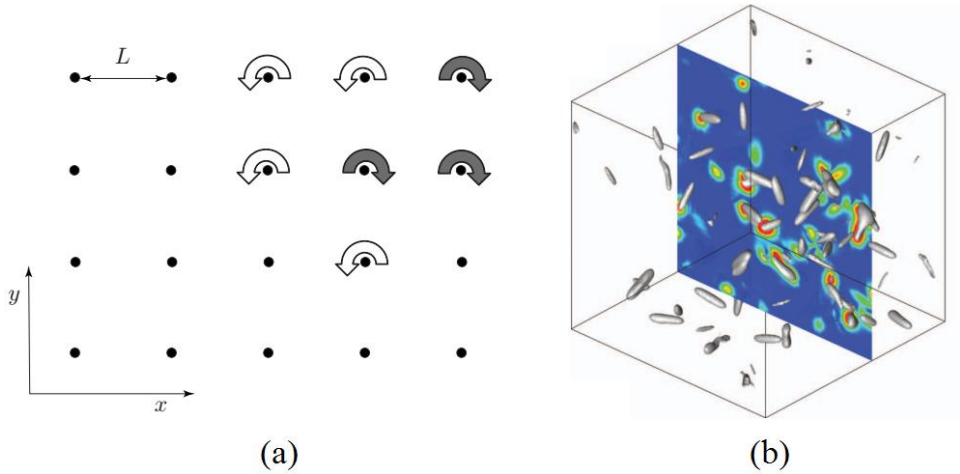

Figure 2.14 (a) Schematic of the 2D vortex model of Ayyalasomayajula et al. (2008). The black dots represent the vortex centers. (Reproduced from Ayyalasomayajula et al., 2008), (b) Illustration of the coherent vortex structures in an isotropic homogeneous turbulence. (Reproduced from Sala and Marshall, 2013)

2-2 Particle motion in turbulence

2-2-1 Particle transport mechanisms

Particle transport in turbulent flows is a ubiquitous process in fluid dynamics, occurring in an immense number of applications, including droplet and particulate transport in the atmosphere, river and coastal sediment transport, dust transport in clean rooms and manufacturing processes, particulate coal and biofuel combustion, diesel exhaust transport, and a wide range of manufacturing processes. The particle response to the fluid is governed primarily by the Stokes number St, which is defined as the ratio of the time scale of the fluid motion (τ_F) to the intrinsic response time scale of the particles (τ_P), such that $St = \frac{\tau_P}{\tau_F} = \frac{\rho_P d_P^2 U}{18 \mu L}$. Stokes number can be used as a measure of the type

of response of particles to changes in a fluid flow, and it is of particular importance in discussing the two mechanisms of particle response to turbulence discussed below.

1) **Particle dispersion** occurs at all Stokes numbers, but it is the dominant mechanism when $St \approx 0$, for which case particles are transported nearly as passive tracers in the flow field. Particle dispersion tends to make the particle concentration field homogeneous, as shown in Figure 2.15.

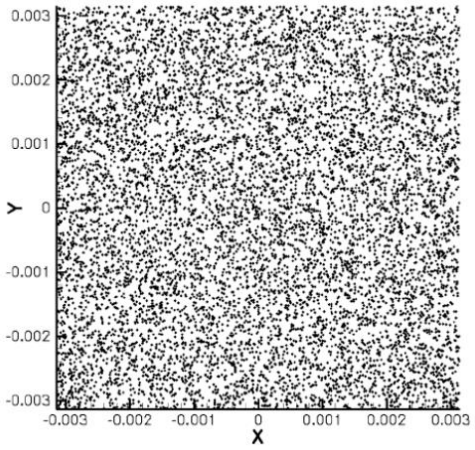

Figure 2.15. 2D slice showing concentration field at $St_\eta = 0$ (stokes based on Stokes number based on the Kolmogorov time scale). (Reproduced from Garcia, 2009)

2) **Particle clustering** occurs for intermediate values of the Stokes number ($St \approx 1$) when the particles are more dense than the fluid. In this case, centrifugal force acts to throw the particles out of the vortex cores, such that they accumulate in the region between the eddies. Figure 2.16 shows an example of a concentration field exhibiting particle clustering for a turbulent particulate flow with $St \approx 1$.

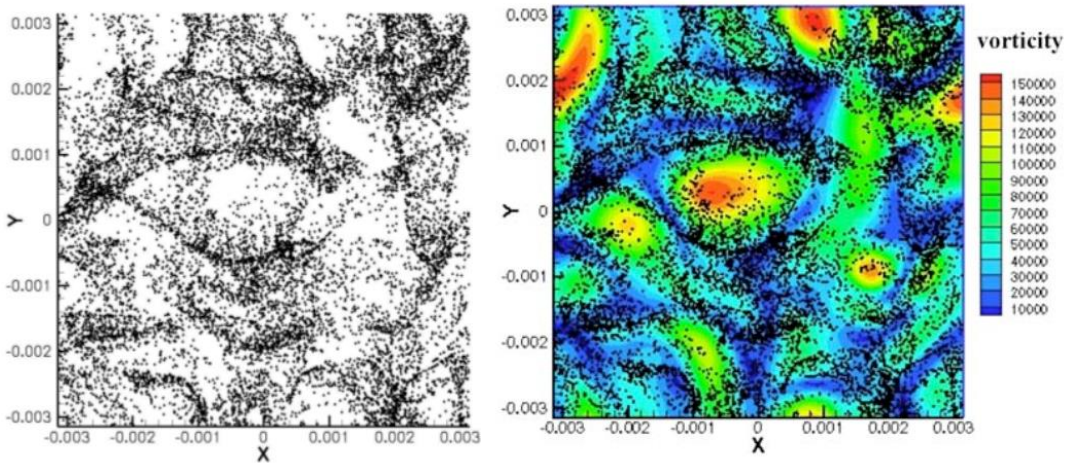

Figure 2.16. (a) 2D slice showing concentrated particle fields at $St_\eta = 1$, (b) Vorticity snapshot with particles superimposed (Reproduced from Garcia, 2009)

Tang et. al (1992) has studied self-organization of particle dispersion in a plane wake. Besides Stokes number, this study examined the role of stretching and folding of particle streaklines, which are associated with vortex development and merging interactions, for characterizing particle dispersion mechanisms. The competition between the effects of Stokes number and the stretching and folding mechanism of the vortices led to particle distributions shown in Figure 2.17. As might be expected, these figures demonstrate that the particles remain in the vortex cores for very small Stokes numbers, collect in high-concentration sheets surrounding the vortex cores for intermediate values of the Stokes number, and are minimally effected by the flow field at large Stokes number values.

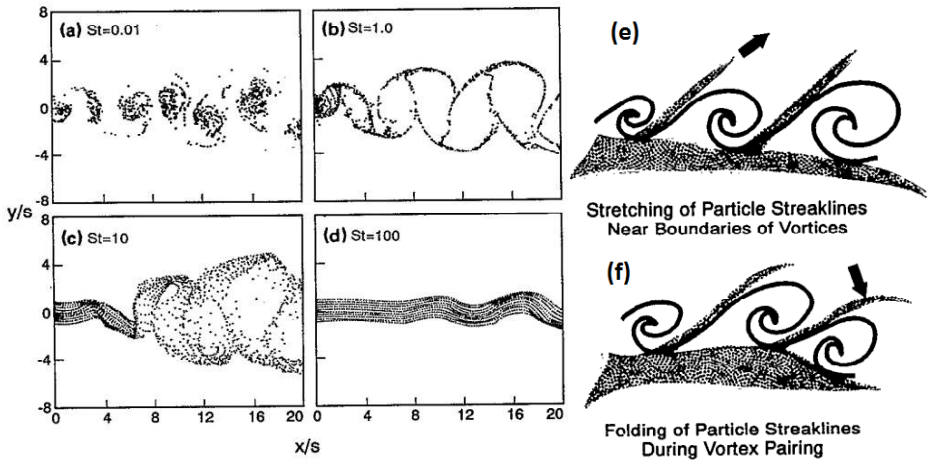

Figure 2.17. Instantaneous particle dispersion patterns from numerical simulation of the plane wake. (a) $St = 0.01$ (b) $St = 1.0$ (c) $St = 10$ (d) $St = 100$ (e) Schematic stretching of particle streaklines near boundaries of vortices(f) Schematic folding of particle streaklines during vortex pairing. (Reproduced from Tang et al., 1992)

Reeks (2014) has studied the transport, mixing and agglomeration of particles in turbulent flow. He similarly found that turbulent flow can demix (segregate) the particles at intermediate values of the Stokes number when particles have a higher density than the surrounding fluid. Segregation reaches a maximum when $St = 1$, at which particles segregate into regions of high strain rate in-between the regions of high vorticity. Segregation was observed for all of the Stokes number values examined by Reeks (2014), but for cases with higher Stokes numbers it takes longer to reach to the same level of segregation as observed for intermediate Stokes number values. Figure 2.18 shows the segregation pattern at $t = 20$ (nondimensionalized by the integral time scale) for 3 values of the particle Stokes number - $St = 0.05, 0.5, 5$.

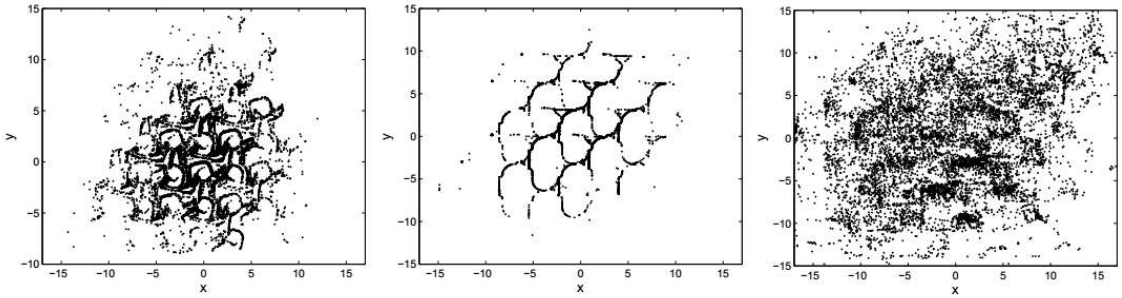

a) $St = 0.05$ b) $St = 0.5$ c) $St = 5$

Figure 2.18. Segregations as a function of particle Stokes number St (a)-(c) based on positions of 10^4 particles after time $t = 20$ in a non-isotropic random straining flow. (Reproduced from Reeks, 2014)

The tendency of particles to cluster can be characterized by the radial distribution function (RDF), $g(r)$, defined by

$$g(r) = \frac{1}{4\pi\rho_0 r^2}\frac{dN}{dr} \tag{2-11}$$

where the average number of particles per unit volume ρ_0 is related to the particle volume fraction C_p by $\rho_0 = 6C_p/\pi$, and $N(r)$ is the average number of neighboring particles whose centroids are located within a radial distance r from a given particle centroid. Direct numerical simulations of heavy particles suspended in a turbulent fluid performed by Sundaram and Collins (1997) report both the RDF and value of RDF at initial particle contact, which is plotted as a function of Stokes number in Figure 2.19(a). Figure 2.19(b) shows a clear peak in the RDF value for intermediate values of the Stokes number ($St \approx 1$), indicating a greater tendency of the particles to form clusters at intermediate Stokes numbers.

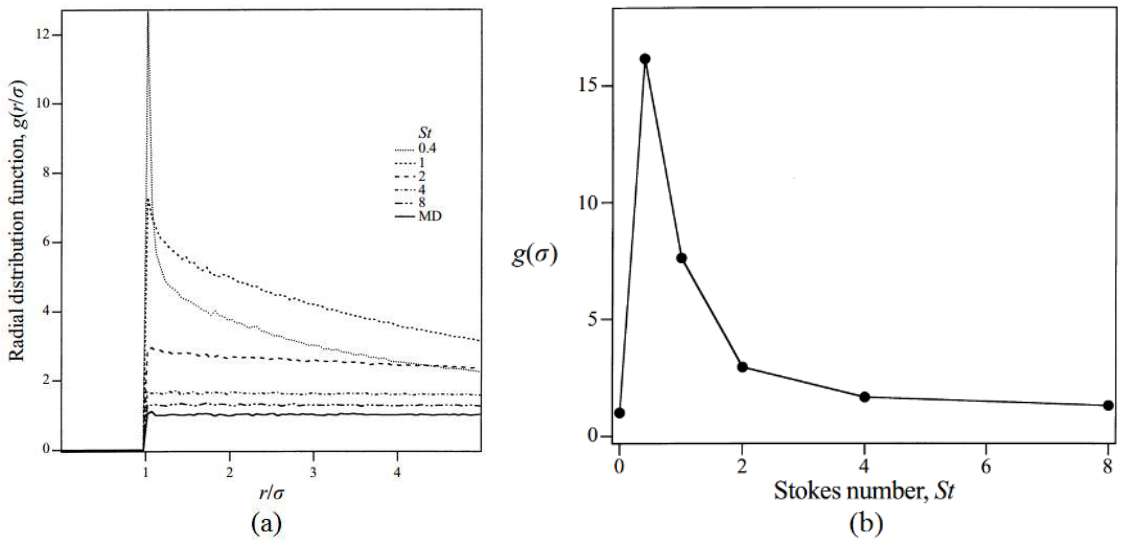

Figure 2.19. Radial distribution functions (RDF) upto 5σ for various Stokes numbers. The RDF for a randomly distributed particle system is plotted for comparison (Reproduced from Sundaram and Collins, 1997).

Fayed and Ragab (2013) studied particle collisions with suspended bubbles in homogeneous isotropic turbulence, which is of interest because the particles were heavier than the fluid and the bubbles were lighter than the fluid. The turbulent vortices thus drew the bubbles inward toward the vortex centers and expelled the particles from the vortices. Figure 2.20 shows the regions of high vorticity (red) and regions of high strain rate (blue). Particles accumulate in the high strain rate region between the vortex cores, while bubbles tend to concentrate in regions of high vorticity within the vortex cores.

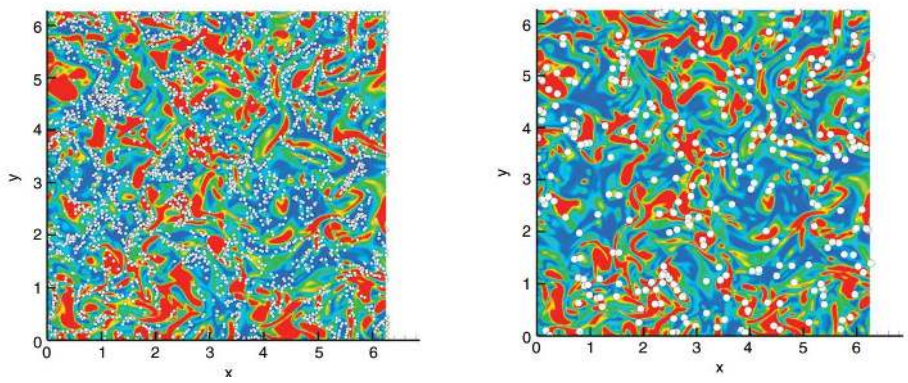

Figure 2.20. A snapshot of particles-bubbles segregation, $St_p = 0.924$, $St_\lambda = 96$, $N = 256$. (a) Particles accumulation in high strain regions (b) Bubbles accumulation near high vorticity regions. (Reproduced from Fayed and Ragab, 2013)

2-2-2 Collision models

Collision models for particles that are heavier than the fluid are typically divided into two limiting types depending on Stokes number:

1) The zero-inertia collision model developed by Saffman and Turner (1956) in which particles follow the carrier flow path (shear (orthokinetic) collision mechanism), which is valid for low Stokes numbers;

2) The high-inertia collision model developed by Abrahamson (1975) in which particle velocities that are completely decorrelated from the carrier fluid velocities (accelerated-independent collision mechanism), which is valid for high Stokes numbers.

A more detailed classification of five different collision mechanisms is given in Table 1.1., along with illustrations of typical collision events for each mechanism in Figure 2.21.

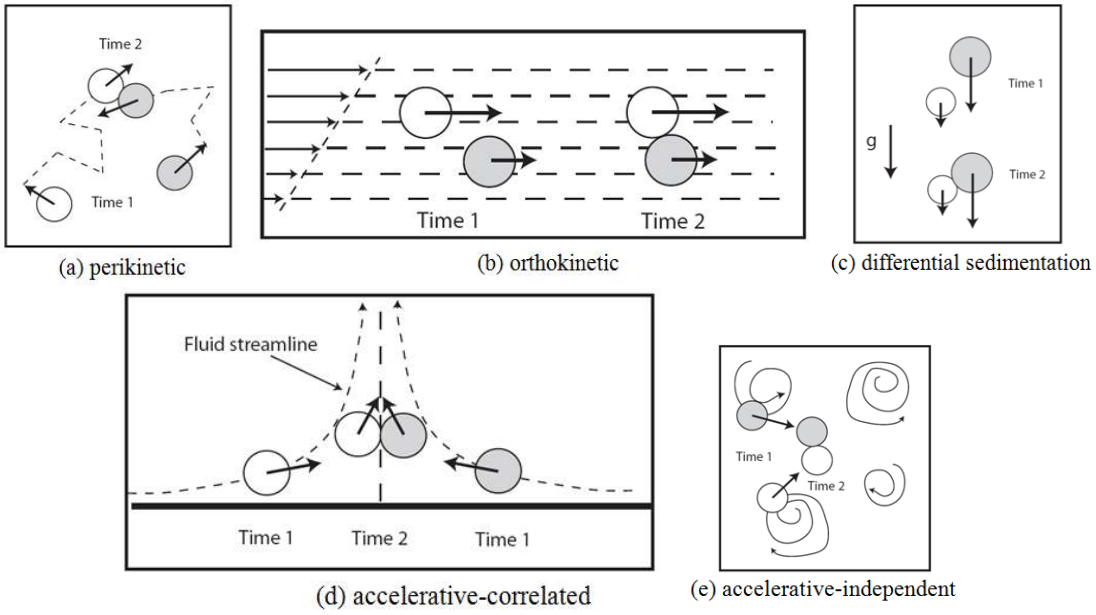

Figure 2.21: Illustrations of different collision mechanisms (Reproduced from Marshall and Li, 2014)

Table 1.1. Collision mechanisms's description and limitations Meyer and Deglon (2011)

Mechanism	**Description**	**Continues phase flow regime**	**Scale and flow regime of dispersed phase**
Brownian motion (perikinetic)	Particle collision due to random Brownian motion of particles	Laminar	Particles are small, less than 1 μm
Shear (orthkinetic)	Particles follow streamlines and collide due to different positions within shear flow field	Laminar and turbulent	Various length scales; $St \leq 1$
Differential sedimentation	Particles of different sizes exhibit different settling velocities leading to collisions	Laminar	Various length scales; Various particle relaxation times
Accelerative-correlated	Particles deviate from streamlines and collide. Particle and carrier fluid velocities are correlated or partly correlated	Turbulent	Intermediate particle sizes; Various particle relaxation times
Accelerative-independent	Particles are thrown randomly from eddy to eddy and collide. Particle and carrier fluid velocities are uncorrelated	Highly turbulent	Particles are larger than viscous dissipation eddies; $St \geq 10$

In order to quantify the collision and make it more comparable, the collision kernel (Γ) is defined. For a monodisperse system consisting of N_p particles in a volume

Ω, the collision rate per unit volume, $\dot{N}_c$, can be written in terms of the collision kernel as

$$\dot{N}_c = \Gamma \frac{n_0^2}{2} \tag{2-12}$$

provided that $N_p >> 1$, where $n_0 \equiv N_p / \Omega$ is the average particle number concentration in the volume. Saffman and Turner (1956) developed two formulations of the geometric collision kernel for zero-inertia particles based on the collision sphere and collision cylinder concepts:

$$\Gamma^{spherical} = 2\pi R^2 \left\langle |w_r| \right\rangle \tag{2-13}$$

$$\Gamma^{cylindrical} = \pi R^2 \left\langle |w_r| \right\rangle g(R) \tag{2-14}$$

In these equations, w_r is the radial component of the relative velocity $\mathbf{w}$, namely, $w_r = \mathbf{w}.\mathbf{R}/R$, in which $\mathbf{R}$ is the separation vector and $R = |\mathbf{R}|$. Schematic diagrams illustrating the collision sphere and collision cylinder paradigms are presented in Figure 2.22. It was argued by Wang et al. (1998) that the collision sphere formulation provides more accurate results for zero-inertia particles.

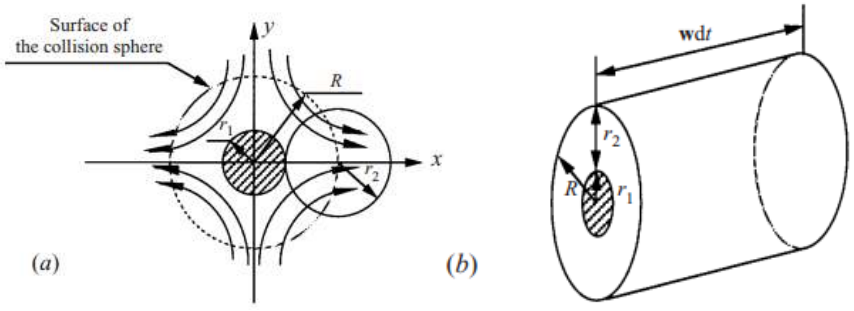

Figure 2.22. Geometrical description of the two statistical formulations for particle collusions: (a) Projection of the collision sphere on the (x, y)-plane. (b) The concept of the collision cylinder. (Reproduced from Wang et al., 2000)

Other researchers have derived their own expressions for the collision kernel. Meyer and Deglon (2011) gave a full description of these models for various ranges of Stokes number. Choi et al. (2011) studied the collision of heavy particles in homogeneous turbulence using DNS in different Stokes number regimes (zero inertia and high inertia), obtaining the results for collision rates presented in Figure 2.23. The various models for finite Stokes number approach the Saffman-Turner model at very low Stokes number and the Abrahamson model for very large Stokes number, with a peak value of collision rate at some intermediate value of the Stokes number.

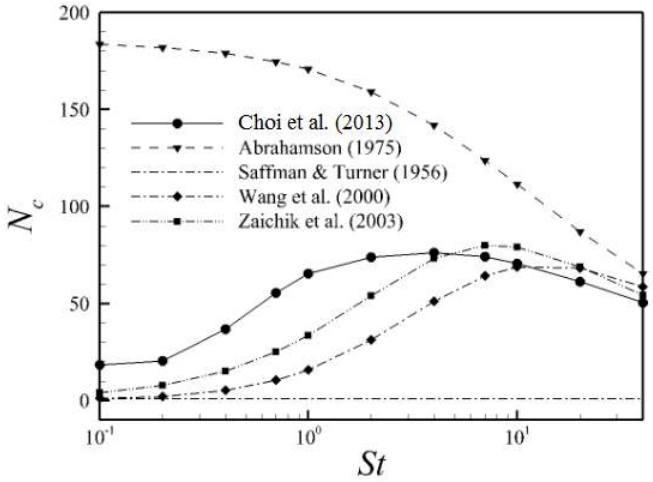

Figure 2.23. Particle collision rate as a function of Stokes number in homogeneous turbulence, as given by various models. (Reproduced from Choi et al., 2011)

2-3 Agglomeration

Particle agglomeration by fluid turbulence occurs in a large range of natural flow problems and industrial processes. Examples of natural processes include dispersion of atmospheric particulates, sediment transport and deposition in estuaries, removal of pollutants by sediment deposition in aquatic systems, particle transport from volcanic plumes, and agglomeration of ice crystals in the atmosphere during formation of snow

flakes. The number of industrial processes involving turbulent agglomeration is immense, a few examples being fine particle separation in gas cyclones, wastewater treatment, additive manufacturing processes, flame synthesis of nanoparticles, and ash capture from combustion furnaces. Many industrial products are produced from powders or by precipitation from reactive solutions, examples including 3D printing, ceramic materials, catalysts, and many pharmaceutical products.

2-3-1 Fractal dimension

As particles collide with each other, there are two possibilities; 1) they will bounce off, or 2) they will stick together. There exists a large literature on how attraction and repulsion forces of different types act during particle collision to determine whether two colliding particles will stick together or separate. A complete discussion of different types of adhesion forces and related models combining these forces with elastic rebound and frictional forces during particle collisions is given by Marshall and Li (2014), and will not be repeated here. Rather, the current section focuses on the characterization and dynamics of the agglomerates themselves - various measures that can be used to characterize agglomerates, how agglomerates interact with the surrounding fluid flow, and how they break up.

Each agglomerate is characterized by the number of particles N contained in the agglomerate and the radius of gyration R_g, which is defined by

$$R_g = \left[\frac{1}{N} \sum_{i=1}^{N} \left| \mathbf{x}_i - \bar{\mathbf{x}} \right|^2 \right]^{1/2} \tag{2-15}$$

In this equation, $\bar{\mathbf{x}}$ denotes the position vector of the agglomerate centroid and $\mathbf{x}_i$ is the centroid of the *i*th particle within the agglomerate. The fractal dimension D_f is defined as the exponent in the power law relationship

$$N = K_f (R_g / d)^{D_f}, \tag{2-16}$$

where K_f is a coefficient (called the fractal pre-factor). The value of D_f varies over the interval $1 \le D_f \le 3$ depending on the agglomerate formation mechanism. Figure 2.24 shows typical images of agglomerates formed with monodisperse primary particles for different agglomerate formation processes. Diffusion-limited (DLCA) and ballistic cluster–cluster (BCCA) agglomerate formation have relatively loose structures with $D_f \le 2$, whereas diffusion-limited (DLA) and ballistic particle–cluster (BPCA) agglomerate formation exhibits more packed structure with $D_f \ge 2$.

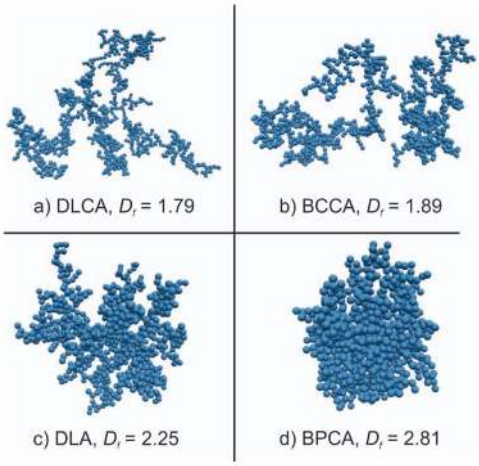

Figure 2.24 Agglomerates consisting of 1024 monodisperse primary particles made by (a) diffusion-limited (DLCA) and (b) ballistic cluster–cluster (BCCA) agglomeration as well as by (c) diffusion-limited (DLA) and (d) ballistic particle–cluster (BPCA) agglomeration. (Reproduced from Eggersdorfer, 2012)

Derksen (2013) studied agglomeration in turbulent flow by means of particle-resolved, direct numerical simulations. The simulations show the continuous formation and breakage of agglomerates as a result of the turbulence and the attractive potential. The average size of the agglomerates is a pronounced function of the strengths of turbulence and interaction potential. They found values of fractal dimension (D_f) in the range of 1.4 to 1.8. For turbulent agglomeration of latex particles in stirred tanks, Selomulya et al. (2001) report values of D_f between 1.7 and 2.1 and Waldner et al. (2005) report values of D_f between 1.8 and 2.6. Figure 2.25 shows an example of how to fit a line in order to find the fractal dimension.

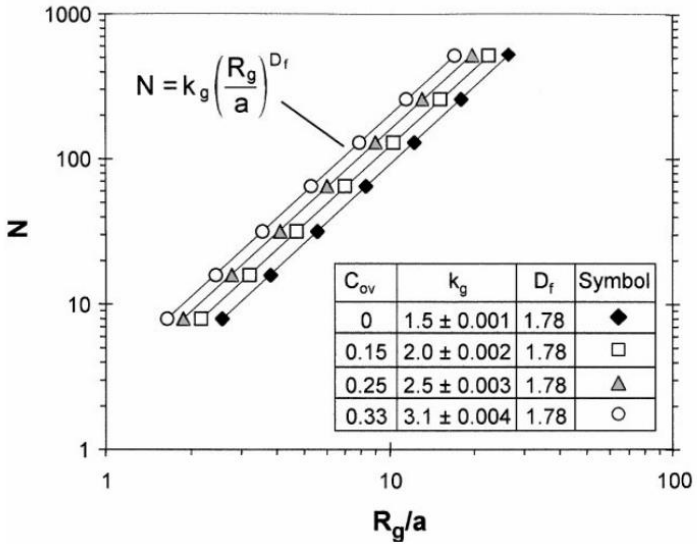

Figure 2.25. Number of particles in aggregates as a function of radius of gyration normalized by particle radius, yielding the fractal dimension and fractal pre-factor of simulated aggregates with different overlap parameter, C_{ov}. (Reproduced from Brasil et al. ,1999)

Jiang and Logan(1991) and Kusters et al. (1997) found that the particle volume fraction of the agglomerate can be related to the fractal dimension by

$$\varphi_i = \varphi_0 \left(R_{gyr,i} / r_p \right)^{D_f - 3} \tag{2-17}$$

where φ_0 is a constant. If $D_f < 3$, an increase in agglomerate size results in a decrease in average particle volume fraction.

2-3-2 Stress on agglomerates and erosion mechanisms

Gastaldi and Vanni (2011) studied the distribution of stresses in rigid fractal-like agglomerates in a uniform flow field. The particles within an agglomerate interact with the surrounding fluid flow, modifying the drag force on the agglomerate and the permeability of the agglomerate to the fluid. As shown in the example in Figure 2.26(a), the central part of an aggregate is screened from the permeation of the external fluid and consequently the drag forces on the inner monomers are small in comparison to those on the outermost particles. Figure 2.26(b) shows the intensities of the forces acting on the primary particles of a cluster-cluster (CC) aggregate with D = 1.9 and of two particle-cluster (PC) aggregates with D_f = 1.9 and 2.3. External forces (i.e., the sum of drag and body force) increase from the center of the cluster to the outer regions and the most intense values are always found on some of the most external monomers.

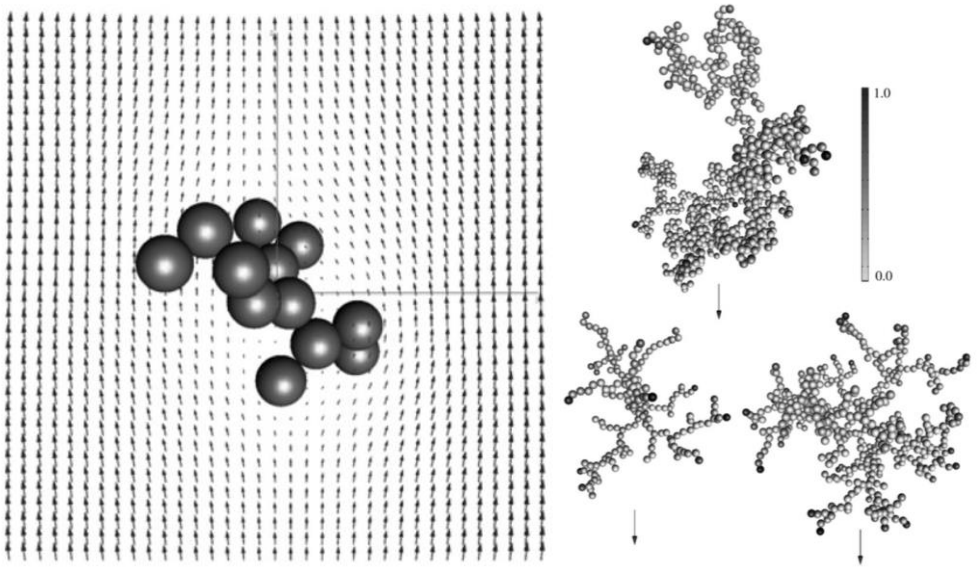

Figure 2.26 (a) Velocity vectors near a small aggregate of 13 monomers in a reference frame moving with the aggregate. (b) Relative intensity of the external forces acting on the primary particles of settling aggregates: above: CC aggregate with D = 1.9; below: PC aggregates with D = 1.9 (left) and 2.3 (right). (Reproduced from Gastaldi and Vanni, 2011)

Stress on agglomerates due to hydrodynamic forces can eventually cause agglomerates to break up. Rwei et al. (1990, 1991) proposed the fragmentation number Fa to characterize the agglomerate breakup mechanism. Fragmentation number is defined as the ratio of the viscous shear stress to the strength of the agglomerate, or

$$Fa = \frac{\mu\dot{\gamma}}{T} \tag{2-18}$$

where $\dot{\gamma} = \sqrt{2\mathbf{D}:\mathbf{D}}$ is the magnitude of the rate of deformation tensor, $\mathbf{D} = [\nabla\mathbf{v} + (\nabla\mathbf{v})^{\mathrm{T}}]/2$, with $\mathbf{v}$ being the flow velocity. The term T in (2-18) denotes the characteristic cohesive strength of the agglomerate. Rumpf (1962) considered the agglomerate as a collection of spherical particles of radius a occupying a volume fraction φ bonded to each other via cohesive forces, and obtained an expression for the agglomerate tensile strength as

$$T = \frac{9}{32}\frac{\varphi}{\pi a^2} n_b F \tag{2-19}$$

where F represents the average binding force of a single bond and n_b is the average number of bonds per particle. Three main agglomerate breakup mechanisms are listed below (Babick 2016):

1) **Fragmentation** (or rupture) of the agglomerate, which yields several fragments, the size of which being in the same order of magnitude. Fragmentation occurs at high stress.

2) **Erosion** of the agglomerate surface, which results in a steady size reduction of the agglomerate size mode and the appearance of a fine size mode, which is related to the eroded primary particles or aggregates. Erosion is dominant for small stresses ($1 < Fa < 100$) (Bałdyga et al., 2008).

3) **Shattering** of the agglomerate, which means breakup into a large number of fragments considerably smaller than the original agglomerate. Shattering is the expected breakup mode at extremely high stresses ($Fa > 10^4$) (Bałdyga et al., 2009).

These mechanisms are illustrated in Figure 2.27, and experimental pictures of each mechanism are given in Figure 2.28.

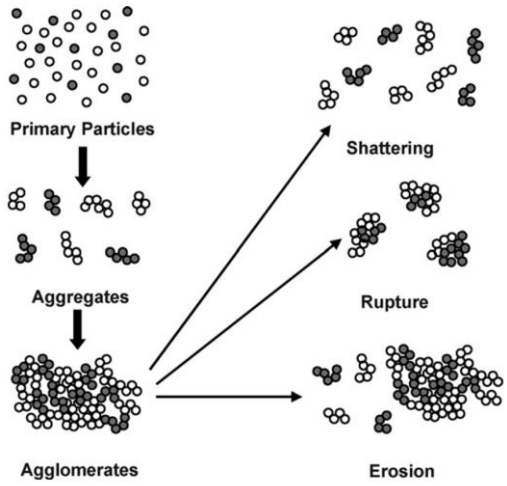

Figure 2.27. Schematic representation of agglomerate formation and break up. (Reproduced from Özcan-Taşkin et al., 2009)

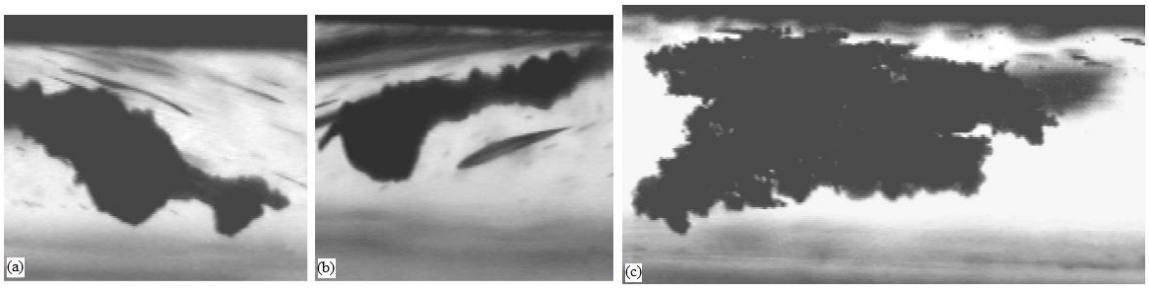

Figure. 2.28. Experimental pictures illustrating different agglomerate breakup mechanisms: (a) fragmentation (or rupture), (b) erosion, and (c) shattering. (Reproduced from Scurati et al., 2005)

2-3-3 Permeability

The dynamic behavior of agglomerates significantly differs from spherical solid particles (Matsoukas and Friedlander, 1991; Friedlander, 2000). To analyze the motion of agglomerates, permeability (k_a) is introduced which shows the impregnability ($k_a \to 0$) or pregnability ($k_a \to 1$) of the agglomerate, indicating to what extent the agglomerate acts like a solid sphere. A schematic diagram of a porous agglomerate is

illustrated in Figure 2.29, where d is the agglomerate's characteristic size, d_p is the size of the pore, d_s is the size of the primary particles, and η is the fluid collection efficiency.

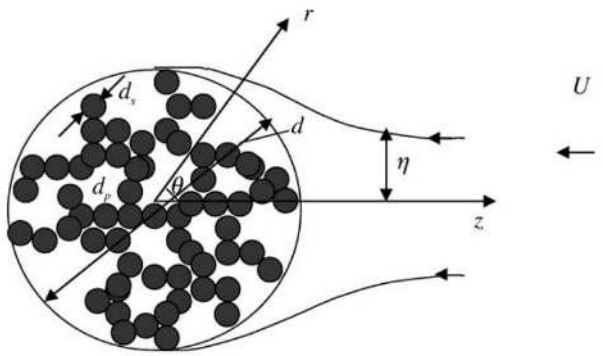

Figure. 2.29. Schematic of porous agglomerate (Reproduced from Vainshtein and Shapiro, 2005)

The average agglomerate porosity φ can be expressed via the volume of the primary particles as $\varphi = 1 - \left(\frac{d}{d_s}\right)^{D_f - 3}$. The average size of a single pore for an agglomerate formed of uniform spheres is $d_p = d_s \frac{\varphi}{1.5(1-\varphi)}$. The viscous permeability (k) is defined as $k \approx d_s^2[f(\varphi)]$ (Happel, 1958) and the molecular permeability (K) as $K \approx d_s^2\left[g(\varphi, Kn_p)\right]$. The effective agglomerates permeability k_a is then given by

$$k_a = k + K \approx d_s^2\left[f(\varphi) + g(\varphi, Kn_p)\right] \tag{2-20}$$

The Brinkman parameter is defined as $\beta = d/2\sqrt{k_a}$ (Shapiro et al., 2012) and the drag of an agglomerate moving with velocity U relative to the surrounding gas can be estimated by (Sutherland and Tan, 1970)

$$F_{drag}^{cont} = 3\pi\mu dU(1+1.5\beta^{-2})^{-1} \tag{2-21}$$

The mobility diameter in the continuum regime is defined as

$$d_m^{cont} = \frac{d}{1+(N/K_f)^{(1-D_f)/D_f}/3} \tag{2-22}$$

in which k_f is the prefactor in the equation defining the fractal dimension ($N = K_f(R_g/d)^{D_f}$).

Another way to model the porous floc was suggested by Torres et al. (1991) and Kusters et al. (1997). In their model it was assumed that the agglomerate consists of an impermeable core and a completely permeable shell, as shown in Figure 2.30. The outer collision radius, R, of the floc, which represents the distance within which another floc must approach for coagulation to occur, is given by

$$\mathrm{R}^2 = \frac{D_f+2}{D_f}\frac{d^2}{4} \tag{2-23}$$

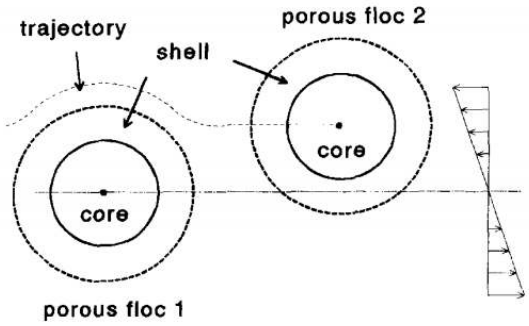

Figure. 2.30. Shell-core model for a particle agglomerate. (Reproduced from Kusters et al., 1997)

Debye's shielding ratio (ξ) is defined as

$$\xi = \frac{R}{\sqrt{k_a}} \tag{2-24}$$

For $\xi > 20$, the ratio of hydrodynamic radius and outer collision radius can be approximated by (Jones, 1978)

$$\frac{R_H}{R} = \frac{1 - \xi^{-1}\tanh(\xi)}{1 + \frac{3}{2}\xi^{-2} - \frac{3}{2}\xi^{-3}\tanh(\xi)} \tag{2-25}$$

and for values $\xi \le 20$, values of R_H / R are given in table 1.2.

Table 1.2. Ratio of hydrodynamic radius to outer collision radius as a function of the Debye's shielding ratio. (Kusters et al. 1997)

ξ_i	∞	70	40	15	10.89	10	8	6	5	4	3	2	1
R_H / R	1	0.984	0.971	0.909	0.865	0.850	0.802	0.722	0.662	0.581	0.474	0.336	0.175

2-3-3 Force chains

Flow-fields induce forces on agglomerates, and since agglomerates are "fragile", they are unable to support certain types of incremental loading without plastic rearrangement of the particles (Cates et al., 1999). The force distributed in an agglomerate in such a way that some particles bear most of the induced force compared to other particles. A force chain consists of a set of particles within a "compressed" granular material that are held together and jammed into place by a network of mutual compressive forces (Peters et al., 2005). By plotting these force chains, one can identify how these compression forces are transmitted across an agglomerate.

One way to identify a force chain is to find the particles which are compressed more than the average compression of the agglomerate (Peters et al. (2005). Figure 2.31 shows the pathway of force transmission in a small set of particles, and the force chain is

indicated by a gray line. The double-sided arrow through the particle center represents the direction of the most compressive principal stress.

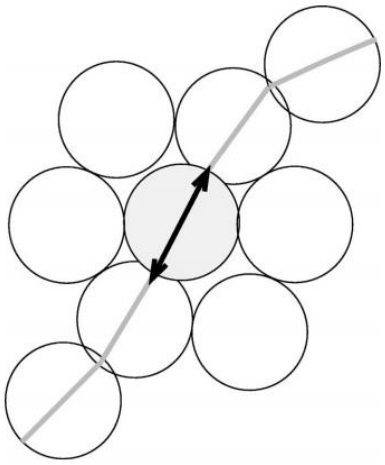

Figure. 2.31. Particles in an idealized portion of a force chain. (Reproduced from Peters et al., 2005).

Between the force chains are regions of low stress, whose particles are shielded from the high-compression effects of the particles above by vaulting and arching. A set of interconnected force chains is known as a force network (Kondic et al., 2012). Figure 2.32 shows the force chain network in a two-dimensional layer of granular materials under isotropic compression.

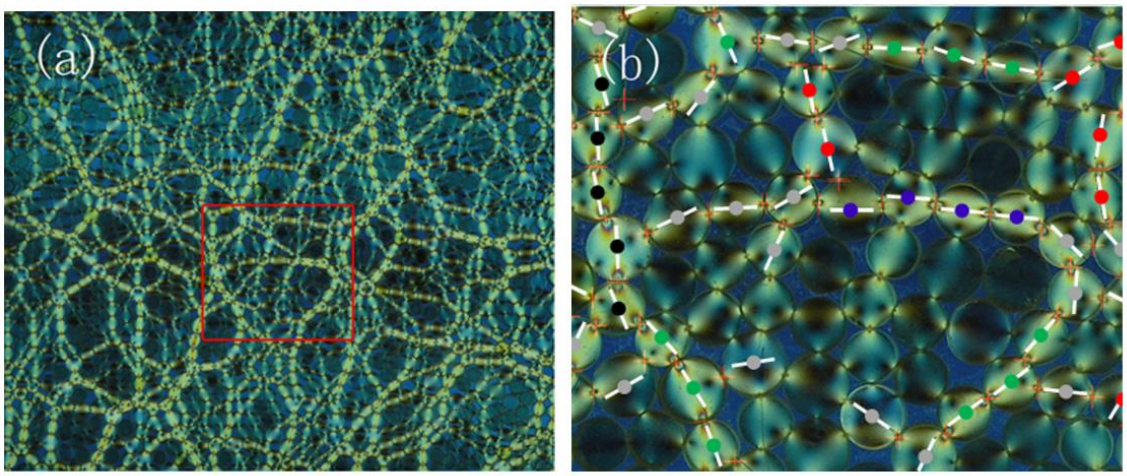

Figure. 2.32 (a) An example of a force-chain network in a 2D layer of granular materials under isotropic compression. Here bidisperse photoelastic disks are used. (b) The portion of panel (a) indicated by the red rectangle, showing several force chains of different lengths using different colors. (Reproduced from Zhang et al., 2014)

2-4 Collision of agglomerates

Collision of agglomerates is a ubiquitous phenomenon which happens over a large range of scales. Collision of asteroids (Farinella et al., 1982, Ormel et al., 2007, 2009) or collision of atomic nuclei (Keeley et al., 2007) are qualitatively similar phenomenon at two ends of the size spectrum. Agglomerate collision is a common occurrence in different operations in the food and drug manufacturing industry (Tong et al., 2016). Turbulent agglomeration can be divided into three different stages (Dizaji and Marshall 2016); 1) collision and agglomeration happens between two single particles which creates small agglomerates; 2) collision and agglomeration happens between small agglomerates to form larger agglomerates; and 3) large agglomerates collide with each other causing them to break into smaller agglomerates. Over sufficient time and under quasi-steady turbulent flow conditions, the adhesive particles will develop a state of statistical equilibrium in which the rate of agglomerate formation by collision will be

balanced by the rate of agglomerate breakup, such that the mean agglomerate size will achieve a critical value. Sonntag and Russell (1986) report that the agglomerate radius of gyration in this equilibrium state decreases as the shear rate increases ($R \propto S^{-m}$). Seyvet and Navard (2000) used silica agglomerates to show that detachment of fragments due to agglomerate collision can lead to agglomerate breakup at a much lower overall stress than the well-known erosion and rupture mechanisms that control breakup of a single agglomerate in a shear flow. Collision between two silica agglomerates flowing in opposite directions (shear rate is $5s^{-1}$) and detachment of a fragment is shown in Figure 2.33.

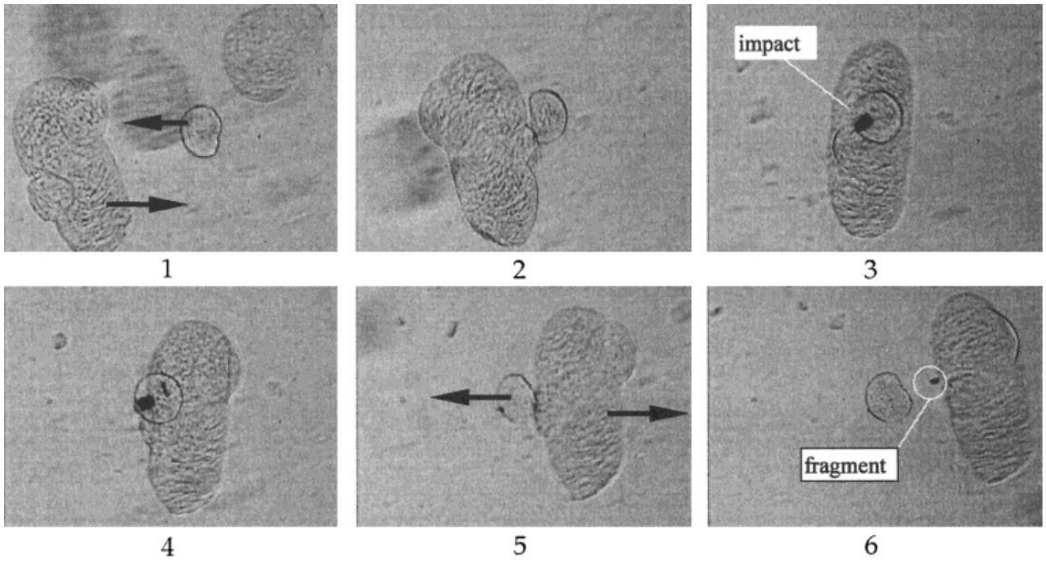

Figure 2.33. Collision between two silica agglomerates (Reproduced from Seyvet and Navard, 2000)

2-4-1 Equivalent agglomerate models

In order to reduce the complexity of modeling agglomerates, an equivalent sphere model has often been used in the literature (Breuer and Almohammed, 2015). Three different ways that this equivalent sphere is sometimes defined are outlined below:

a) Volume-equivalent sphere model (VSM) - In this classical model, it is assumed that an agglomerate can be replaced by a single spherical particles of diameter d_{ag}, whose volume is equal to the sum of the volume of all of the individual particles in the agglomerate. An illustration for a two-particle agglomerate is shown in Figure 2.34(a), where the equivalent particle diameter is $d_{ag} = \sqrt[3]{d_1^3 + d_2^3}$.

b) Inertia-equivalent sphere model (ISM) - The radius of gyration is used to describe the size of an agglomerate and to show how the mass is distributed around the center of agglomerate (Figure 2.34(b)). For two agglomerating particles, the radius of gyration is given by $R_g = \sqrt{\frac{I_{cm}}{m_1 + m_2}}$ in which I_{cm} is the moment of inertia about the center of mass and m_1 and m_2 are the mass of each particle, so that the equivalent diameter is $d_{ag} = \sqrt{20/3} R_g$.

c) Closely packed sphere model (CSM) - This model assumed that an agglomerate is built up from spherical particles including an interstitial space between its primary particles as shown in Figure 2.34(c). The equivalent particle diameter is chosen as the smallest value that encloses the primary particles.

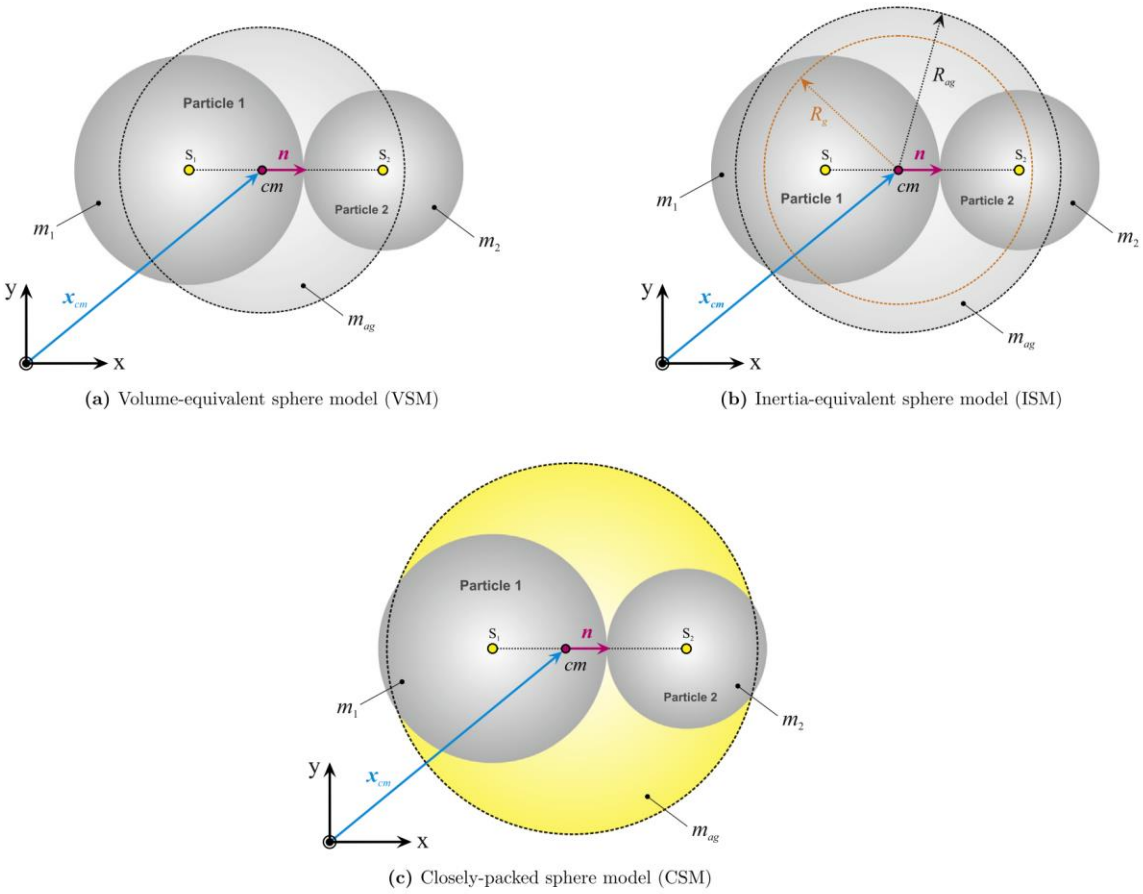

(a) Volume-equivalent sphere model (VSM)

(b) Inertia-equivalent sphere model (ISM)

(c) Closely-packed sphere model (CSM)

Figure 2.34. Procedures to model the structure of the agglomerate. (Reproduced from Breuer and Almohammed, 2015)

These equivalent sphere models are the basis of the population balance approach for modeling agglomerate formation. It is also used in the 'extended' hard sphere model, developed by Kosinski and Hoffmann (2010), which extended the hard-sphere model for binary particle collisions to formation of agglomerates of an arbitrary number of particles. Using this equivalent sphere implies a loss of some physics associated with the agglomerate collisions, since it admits only two possible scenarios following a collision of two agglomerates - the agglomerates can stick together or they can bounce. However, in reality the physics of agglomerate collision is much more complex than indicated by

these two scenarios. For example, one or both of the agglomerates can completely shatter, or the agglomerates can exchange particles with each other.

2-4-2 Agglomerate behavior in different regimes

In order to better understand the physics of agglomerate collision, it is necessary to track the behavior of each particle within the agglomerate individually (e.g., using the discrete element method). The literature on this topic is divided into three categories below, based on a combination of numerical studies and a few experiment investigations.

2-4-2-1 Behavior of a single agglomerate in shear flow

Using numerical simulation, Potanin (1993), Higashitani et al. (2001) and Zeidan et al. (2007) studied the deformation and breakup of a single agglomerate in a simple shear flow. Snapshots of the deformation and breakup of the particle-cluster aggregate composed of mono-dispersed particles are shown in Figure 2.35 for a case exhibiting breakup in the shear flow.

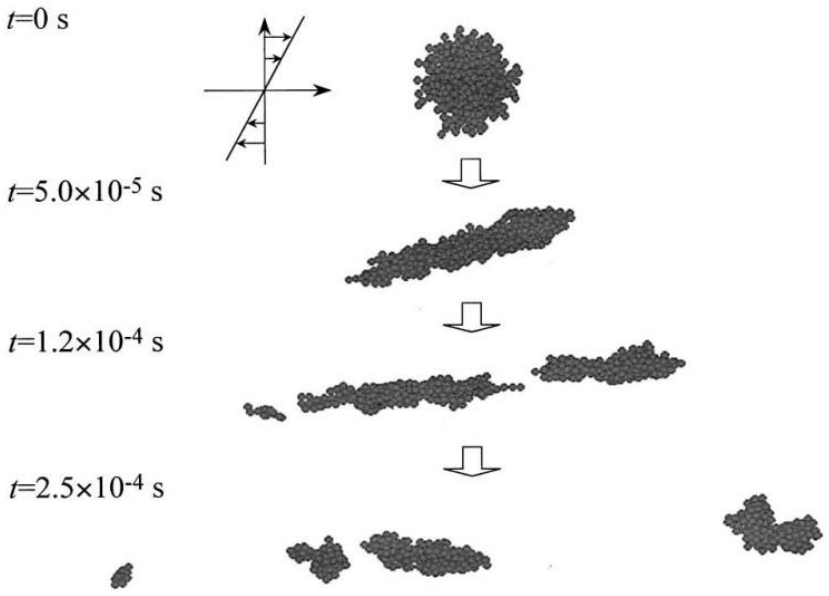

Figure 2.35. Fragmentation of an agglomerate in simple shear flow. (Reproduced from Higashitani et al., 2001)

Higashitani et al.(2001) found using DEM simulations that the average number of particles in broken fragments $< i >$ can be written as a power law of the ratio of the fluid drag force on the particles to the adhesive force acting between particles, or

$$< i >= 2.79 \times \left(\frac{F_{Drag}}{F_{adhesive}} \right)^{-0.872} \tag{2-26}$$

This power-law dependence matches well with a similar expression obtained experimentally by Sonntag and Russel (1986).

Serra et al. (1997) experimentally showed that based on particle concentration and shear stress, different regimes have been observed for the behavior of a single aggregate in shear flow. a) For concentrations less than a critical value, the final diameter of the aggregate is independent of concentration and depends only on shear. b) For high concentration, the final diameter of aggregate depends on both shear stress and particle concentration.

2-4-2-2 Collision of an agglomerate with a wall

Ning et al. (1997), Thornton et al. (1999), Thornton and Liu (2004), Kafui and Thornton (2000), Moreno et al. (2003), Moreno-Atanasio and Ghadiri (2006), Iimura et al. (2009a and 2009b), Tong et al.(2009), and Nguyen et al.(2014) have numerically studied the collision of an agglomerate with a wall (obstacle). In these studies, impact velocity, angle of impact and surface energy were identified as the most important factors influencing breakage of agglomerates. We note that many of these studies either had no surrounding fluid, or else the surrounding fluid exerted only a minor force on the particles, so that the collision process was controlled by particle inertia. A measure of breakup called the 'damage ratio' is defined as the proportion of the initial bonds that are

broken during an impact. As impact velocity and impact angle increases, the damage ratio increases and the agglomerates shatter into more pieces, as shown in Figure 2.36(a). However, Figure 2.36(b) shows that increase in adhesive surface energy causes a decrease in damage ratio, which means that the agglomerates tend to remain as a single agglomerate (or adhesive to each other).

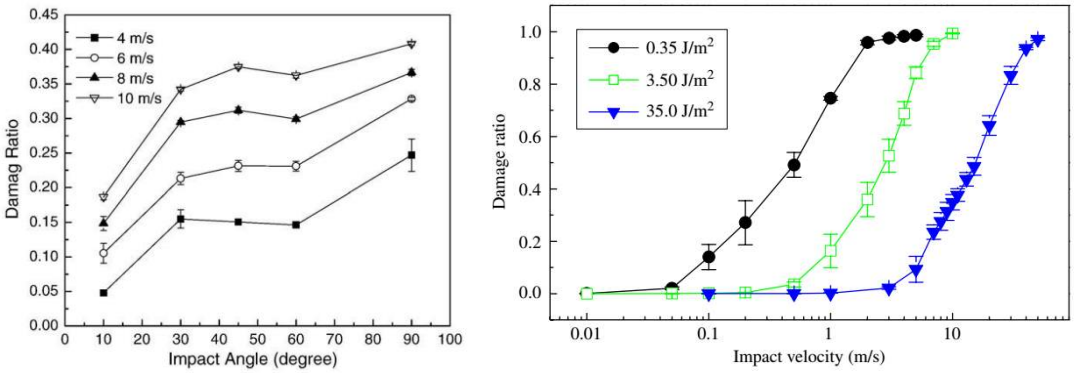

Figure 2.36. Damage ratio as a function of (a) impact angle for different impact velocities (Reproduced from Tong et al. 2009) (b) surface energy (Reproduced from Moreno-Atanasio and Ghadiri, 2006)

2-4-2-3 Collision of two agglomerates

Lian et al. (1998), Schäfer et al. (2007), Seizinger and Kley (2013), Gunkelmann et al. (2016), Ihalainen et al. (2012), and Kun and Herrmann(1999) have numerically studied the collision of two agglomerates, focusing specifically on inertia-dominated impact of tightly-packed agglomerates, as is typical in applications in particulate drug delivery via dry particle inhalers and similar devices. Collision of two agglomerates has a different nature than the collision of an agglomerate and a wall. In agglomerate-wall collision, the wall is treated as a solid material and all impact energy transfers to the agglomerate. However, in agglomerate-agglomerate collision both the agglomerates can

deform and the impact energy is distributed between them. Fracture and fragmentation processes of agglomerates due to impact at low energies are illustrated in Figure 2.37.

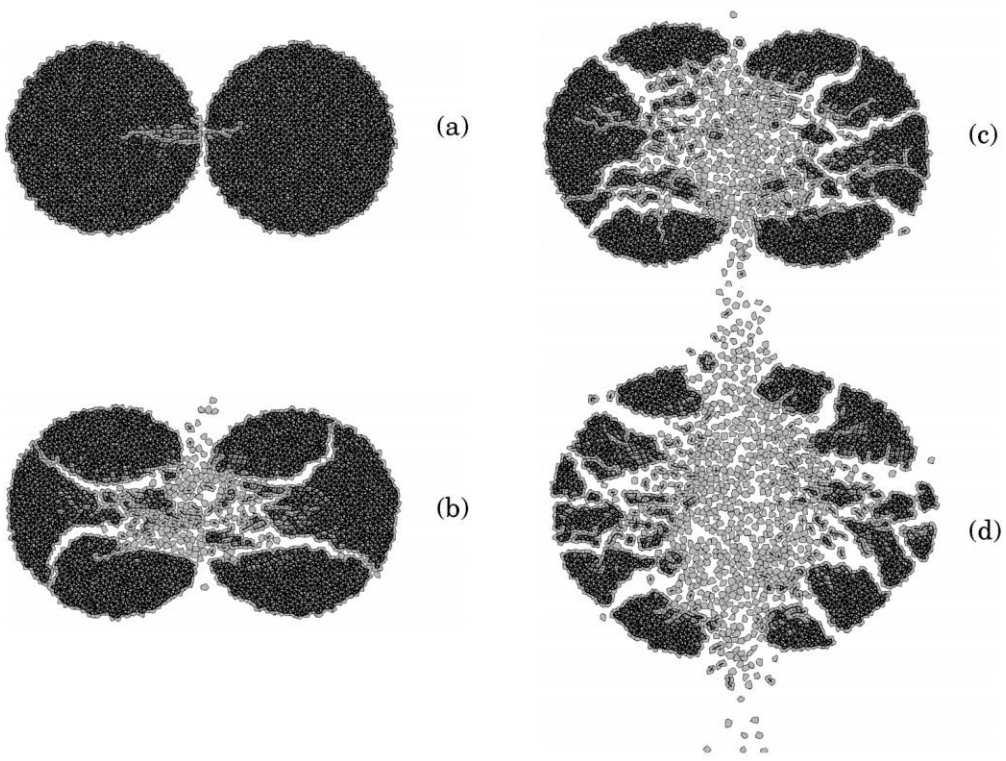

Figure 2.37. The final breaking scenarios of collisions of disks at different impact energies E_0. The values of the parameter η are 0.09, 0.2, 0.3, and 0.5 for (a), (b), (c), and (d), respectively. (Reproduced from Kun and Herrmann, 1999)

To characterize the collision events, a dimensionless parameter $\eta = \sqrt{\frac{E_0}{E_b}}$ is introduced by Kun and Herrmann (1999) in which E_b is the particle binding energy and E_0 is the total initial kinetic energy of the colliding bodies. Alternatively, one can define $\eta \approx v_0 / \sqrt{E_s}$ in which E_s is the surface energy and v_0 denotes the impact velocity of the particles. Using the ratio $\varepsilon_R = E_R / E_0$ (the energy released by breaking E_R to the total

kinetic energy E_0), two distinct final states of the impact process are identified: 1) damaged and 2) fragmented states, with a sharp transition in-between which is shown in Figure 2.38.

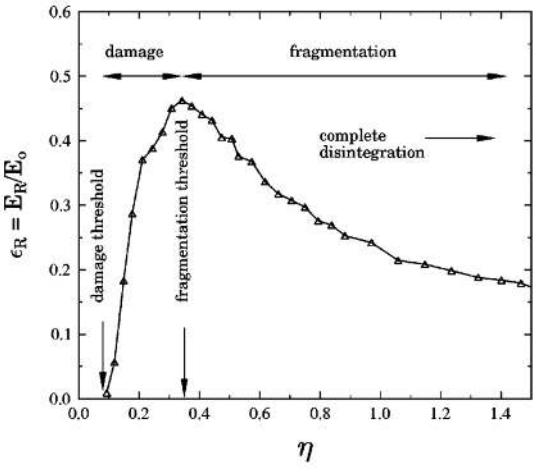

Figure 2.38. The transition point (fragmentation threshold) between the damaged and fragmented states is identified with the position of the maximum of ε_R . (Reproduced from Kun and Herrmann, 1999)

Beitz et al. (2011) have experimentally studied the low-velocity collisions of centimeter-sized aggregates of compressed dust particles. They observed several mechanisms at different impact velocities *v*, including: a) bouncing ($v < 40 cms^{-1}$), b) partial fragmentation ($v > 20 cms^{-1}$), c) particle exchange ($v < 190 cms^{-1}$) and d) disruptive fragmentation ($v > 190 cms^{-1}$). Figure 2.39 shows these four mechanisms in collision of dust aggregates as a function of impact velocity.

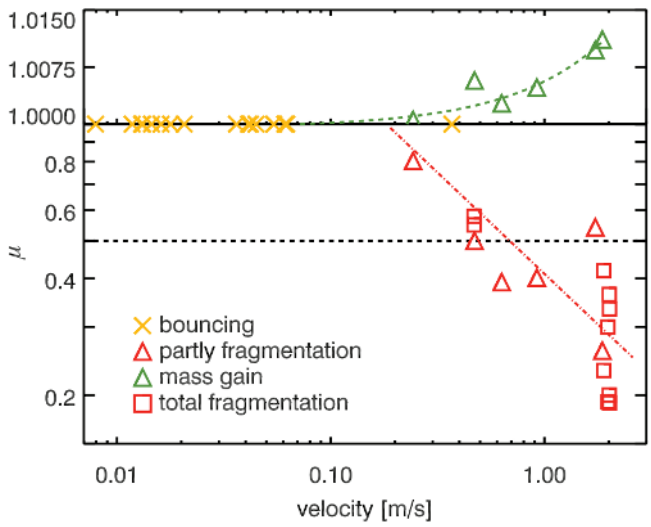

Figure. 2.39. Strength of fragmentation μ as a function of impact velocity. (Reproduced from Beitz et al., 2011)

It is noted that nearly all of the previous research on agglomerate collisions has been performed for inertia-dominated collisions of tightly-packed agglomerates. By contrast, turbulent agglomeration processes typically involve shear-dominated collisions of loosely-packed agglomerates (i.e., agglomerates typified by fractal dimensions D_f significantly less than 3). Repeating the same experiments or computations with loose aggregates adds lots of more complexity both to design and conduct of the experiments or computations and to the results. Also, for shear-dominated collision processes, the fluid flow plays an important role in the collision process and it therefore cannot be neglected or consigned a minor role as has been done for inertia-dominated collision studies. In the literature to date, there is a lack of detailed studies of the behavior of two loose agglomerates during collisions, particularly under conditions of shear-dominated collisions. This is a much harder problem to deal with since both high agglomerate void fraction and strong shear forces change the physics of the problem entirely. Extracting

loosely-structured agglomerates typical of turbulent formation processes and making them to collide under controlled shearing conditions in a physical experiment is almost impossible, so detailed study in this problem will likely need to be pursued numerically.

Final Conclusion and Recommendations

Small-scale turbulent flow fluctuations have very important influence on the motion, collision and agglomeration of suspended particles. While these small-scale fluctuations can be modeled using direct numerical simulation (DNS), this method is limited to problems with relatively low Reynolds numbers and simple geometrical configurations. Other turbulence simulation methods for more practical problems, such as large eddy simulation (LES) or Reynolds-averaged Navier Stokes (RANS) simulations, do not predict the small-scale fluctuations. The stochastic vortex structure (SVS) method is an approach for generating synthetic turbulence which can be used directly as an independent research tool, or it can be coupled to RANS or LES computational results to compensate for the lack of small-scale fluctuations in modeling the turbulent motion of particulate fluids. Since SVS uses vortex tubes to generate turbulence, we are able to change the core radius, length, strength, orientation and number of vortices to adjust the results for given turbulent flows (as expressed, for instance, by the Reynolds stress tensor given by a RANS calculation). The early version of SVS (Sala and Marshall, 2013) was designed for isotropic, homogeneous turbulence, so that the vortex orientations were random and vortices were fixed in space. The SVS computations were also fairly slow, in some cases taking longer than the DNS computations used for validation. In the current research, the SVS method was extended and validated in a series of different steps listed as below:

1) The algorithm was modified to allow the vortices the ability to move freely in the flow field, which is more realistic and allows prediction of time-varying fluctuations even at fixed points.

2) The velocity calculation algorithm is replaced by the fast multipole method, which calculates the effect of an entire group (box) of neighboring source vortices on a coarse grid and then uses a local Taylor series expansion to interpolate onto a fine grid covering the flow field. The new method has improved the velocity calculation speed by approximately two orders of magnitude.

3) Flow field parameters, collision kernel and size and fractal dimension of agglomerates generated by SVS are successfully compared with DNS results.

4) An inverse method is developed by which vortex initial orientation can be set to reproduce a prescribed Reynolds stress fields. With use of this inverse method, SVS was successfully used to generate predict turbulence measures and particle transport and collision measures for anisotropic turbulence in a turbulent free jet flow.

5) For both isotropic turbulence and turbulent shear flows, SVS has been successfully validated versus DNS predictions and available data to accurately and effectively calculate the dispersion and collision of suspended particles.

The SVS method has proven to be accurate and effective for simulating the effect of subgrid-scale turbulent fluctuations on interacting particles (i.e., particles that undergo collision or thermal/chemical interactions). While the current research has significantly advanced the SVS method, there remain a number of limitations and obstacles to its general usage. For instance, as pointed out in Paper #3 of this dissertation, the inverse procedure that was developed for the vortex orientation in anisotropic turbulence is subject to a limitation on the Reynolds stress tensor which is violated in some turbulent shear flows. Secondly, the fluctuations generated by the SVS method do not in general obey the no-slip condition on a surface, and the method therefore has

limited applicability for turbulent boundary layer flows. Thirdly, the SVS method developed to date includes only one-way coupling, and as such it does not account for the effect of the particles on the fluid flow. This is particularly important in development of particle agglomerates and clusters, where the particle concentration becomes locally large. Finally, our work with SVS to date has been in conjunction with a RANS computation that provides knowledge of the Reynolds stress tensor. As noted above, the LES technique experiences similar problems with lack of small scales for particle transport, but we have not examined how SVS might be extended to work in conjunction with LES.

In part motivated by trying to understand the restrictions imposed by the limitations of the SVS method, two areas of independent research were conducted using the DNS method to study the role of turbulent agglomeration on the surrounding fluid flow. One of these studies examined the effect of two-way coupling on turbulent agglomeration of particles (in comparison to one-way coupling) and the attenuation of turbulence in the presence of agglomerates. We observed that the particles cause enhanced attenuation of the turbulent kinetic energy compared to computations with no particles. The rate of attenuation increased with increase in the particle size and mass loading. In a series of computations repeated both with adhesion and without adhesion, we observed little difference in the rate of particle attenuation, except for the largest size particles. Examination of the agglomeration process indicated that significant agglomeration occurred during the computations, but that this agglomeration did not appear to have a significant influence on the turbulence modulation.

Both DNS and SVS results show that average agglomerates sizes increase during turbulent agglomeration until an equilibrium condition is reached. This happens since shear and collision of agglomerates with each other act like erosion mechanisms, which resist the unconditional growth of agglomerates. A second DNS study was performed to explore the microphysics of turbulent agglomeration processes. In this study, the effect of fluid shear and of collision of agglomerates was investigated using DNS by placing loosely-packed agglomerates from a turbulent agglomeration process in a simple shear flow, and then using DNS with two-way coupling to compute the agglomerate evolution under shear. Of particular interest in these computations was the discovery of the flow field induced by a particle agglomerate in a shear flow, which was found to have the form of two tilted horseshoe vortices with opposite sign. Agglomerate collision was observed to work either to promote merger of two agglomerates or to enhance erosion and breakup of the agglomerates depending on the extent of collision and adhesion of the particles.

These DNS studies improved our understanding of basic processes involving turbulent agglomeration and its two-way interaction with the surrounding fluid. We were particularly interested in these studies in the local fluid flow that forms as a response to the particle forces induced on the fluid by the agglomerate particles, and in how this local flow impacts the agglomerate dynamics. To what extent the SVS method can be further extended to deal with these type of two-way fluid-particle interactions on the scale of the agglomerates must wait for future research.

REFERENCES

Abrahamson, J. (1975). Collision rates of small particles in a vigorously turbulent fluid. *Chemical Engineering Science*, *30*(11), 1371-1379.

Ayyalasomayajula, S., Warhaft, Z., & Collins, L. R. (2008). Modeling inertial particle acceleration statistics in isotropic turbulence. *Physics of Fluids*, *20*(9), 095104.

Babick, F. (2016). *Suspensions of colloidal particles and aggregates* (Vol. 20). Heidelberg: Springer.

Balachandar, S., & Eaton, J. K. (2010). Turbulent dispersed multiphase flow. *Annual Review of Fluid Mechanics*, *42*, 111-133.

Bałdyga, J., Makowski, Ł., Orciuch, W., Sauter, C., & Schuchmann, H. P. (2008). Deagglomeration processes in high-shear devices. *Chemical Engineering Research and Design*, *86*(12), 1369-1381.

Bałdyga, J., Makowski, Ł., Orciuch, W., Sauter, C., & Schuchmann, H. P. (2009). Agglomerate dispersion in cavitating flows. *Chemical engineering research and design*, *87*(4), 474-484.

Beitz, E., Güttler, C., Blum, J., Meisner, T., Teiser, J., & Wurm, G. (2011). Low-velocity collisions of centimeter-sized dust aggregates. *The Astrophysical Journal*, *736*(1), 34.

Belin, F., Maurer, J., Tabeling, P., & Willaime, H. (1996). Observation of intense filaments in fully developed turbulence. *Journal de Physique II*, *6*(4), 573-583.

Brasil, A. M., Farias, T. L., & Carvalho, M. G. (1999). A recipe for image characterization of fractal-like aggregates. *Journal of Aerosol Science*, *30*(10), 1379-1389.

Breuer, M., & Almohammed, N. (2015). Modeling and simulation of particle agglomeration in turbulent flows using a hard-sphere model with deterministic collision detection and enhanced structure models. *International Journal of Multiphase Flow*, *73*, 171-206.

Burgers, J. M. (1948). A mathematical model illustrating the theory of turbulence. In *Advances in applied mechanics* (Vol. 1, pp. 171-199). Elsevier.

Cates, M. E., Wittmer, J. P., Bouchaud, J. P., & Claudin, P. (1999). Jamming and static stress transmission in granular materials. *Chaos: An Interdisciplinary Journal of Nonlinear Science*, *9*(3), 511-522.

Choi, J. I., Kwon, O., & Lee, C. (2011). Inter-particle collision in particle-laden isotropic turbulence. In *Journal of Physics: Conference Series* (Vol. 318, No. 5, p. 052012). IOP Publishing.

Crowe, C. T. (2000). On models for turbulence modulation in fluid–particle flows. *International Journal of Multiphase Flow*, *26*(5), 719-727.

Derksen, J. J. (2013). Direct simulations of aggregates in homogeneous isotropic turbulence. *Acta Mechanica*, *224*(10), 2415-2424.

Devenish, B. J., Bartello, P., Brenguier, J. L., Collins, L. R., Grabowski, W. W., IJzermans, R. H. A., ... & Warhaft, Z. (2012). Droplet growth in warm turbulent clouds. *Quarterly Journal of the Royal Meteorological Society*, *138*(667), 1401-1429.

Dizaji, F. F., & Marshall, J. S. (2016). An accelerated stochastic vortex structure method for particle collision and agglomeration in homogeneous turbulence. *Physics of Fluids*, *28*(11), 113301.

Dong, M., Zhou, F., Zhang, Y., Shang, Y., & Li, S. (2018). Numerical study on fine-particle charging and transport behaviour in electrostatic precipitators. *Powder Technology*, *330*, 210-218.

Eaton, J. K. (2009). Two-way coupled turbulence simulations of gas-particle flows using point-particle tracking. *International Journal of Multiphase Flow*, *35*(9), 792-800.

Eggersdorfer, M. L., Kadau, D., Herrmann, H. J., & Pratsinis, S. E. (2011). Multiparticle sintering dynamics: from fractal-like aggregates to compact structures. *Langmuir*, *27*(10), 6358-6367.

Elsinga, G. E., & Marusic, I. (2010). Universal aspects of small-scale motions in turbulence. *Journal of Fluid Mechanics*, *662*, 514-539.

Farinella, P., Paolicchi, P., & Zappalà, V. (1982). The asteroids as outcomes of catastrophic collisions. *Icarus*, *52*(3), 409-433.

Fayed, H. E., & Ragab, S. A. (2013). Direct numerical simulation of particles-bubbles collisions kernel in homogeneous isotropic turbulence. *The Journal of Computational Multiphase Flows*, *5*(3), 167-188.

Fiedler, H. E. (1988). Coherent structures in turbulent flows. *Progress in Aerospace Sciences*, *25*(3), 231-269.

Friedlander, S. K. (2000). Smoke, Dust, and Haze: Fundamentals of Aerosol Dynamics.

Garcia, M. (2009). Développement et validation du formalisme euler-lagrange dans un solveur parallele et non-structuré pour la simulation aux grandes échelles. *France Thèse*.

Gastaldi, A., & Vanni, M. (2011). The distribution of stresses in rigid fractal-like aggregates in a uniform flow field. *Journal of colloid and interface science*, *357*(1), 18-30.

Goldstein, M. L., Roberts, D. A., & Matthaeus, W. H. (1995). Magnetohydrodynamic turbulence in the solar wind. *Annual review of astronomy and astrophysics*, *33*(1), 283-325.

Happel, J. (1958). Viscous flow in multiparticle systems: slow motion of fluids relative to beds of spherical particles. *AIChE Journal*, *4*(2), 197-201.

Hatakeyama, N., & Kambe, T. (1997). Statistical laws of random strained vortices in turbulence. *Physical Review Letters*, *79*(7), 1257.

Helsdon, J. H., Wojcik, W. A., & Farley, R. D. (2001). An examination of thunderstorm-charging mechanisms using a two-dimensional storm electrification model. *Journal of Geophysical Research: Atmospheres*, *106*(D1), 1165-1192.

Higashitani, K., Iimura, K., & Sanda, H. (2001). Simulation of deformation and breakup of large aggregates in flows of viscous fluids. *Chemical Engineering Science*, *56*(9), 2927-2938.

Iimura, K., Suzuki, M., Hirota, M., & Higashitani, K. (2009a). Simulation of dispersion of agglomerates in gas phase–acceleration field and impact on cylindrical obstacle. *Advanced Powder Technology*, *20*(2), 210-215.

Iimura, K., Yanagiuchi, M., Suzuki, M., Hirota, M., & Higashitani, K. (2009b). Simulation of dispersion and collection process of agglomerated particles in collision with fibers using discrete element method. *Advanced Powder Technology*, *20*(6), 582-587.

Jiang, Q., & Logan, B. E. (1991). Fractal dimensions of aggregates determined from steady-state size distributions. *Environmental Science & Technology*, *25*(12), 2031-2038.

Jiménez, J., Wray, A. A., Saffman, P. G., & Rogallo, R. S. (1993). The structure of intense vorticity in isotropic turbulence. *Journal of Fluid Mechanics*, *255*, 65-90.

Jones, R. B. (1978). Hydrodynamic interaction of two permeable spheres III: Mobility tensors. *Physica A: Statistical Mechanics and its Applications*, *92*(3-4), 571-583.

Kajikawa, M., Kikuchi, K., Asuma, Y., Inoue, Y., & Sato, N. (2000). Aggregation of needle snow crystals. *Atmospheric research*, *55*(2), 131-138.

Kafui, K. D., & Thornton, C. (2000). Numerical simulations of impact breakage of a spherical crystalline agglomerate. *Powder Technology*, *109*(1-3), 113-132.

Kambe, T., & Hatakeyama, N. (2000). Statistical laws and vortex structures in fully developed turbulence. *Fluid Dynamics Research*, *27*(4), 247-267.

Keeley, N., Raabe, R., Alamanos, N., & Sida, J. L. (2007). Fusion and direct reactions of halo nuclei at energies around the Coulomb barrier. *Progress in Particle and Nuclear Physics*, *59*(2), 579-630.

Kivotides, D., & Leonard, A. (2003). Quantized turbulence physics. *Physical review letters*, *90*(23), 234503.

Kolmogorov, A. N. (1941, February). The local structure of turbulence in incompressible viscous fluid for very large Reynolds numbers. In *Dokl. Akad. Nauk SSSR* (Vol. 30, No. 4, pp. 299-303).

Kondic, L., Goullet, A., O'Hern, C. S., Kramar, M., Mischaikow, K., & Behringer, R. P. (2012). Topology of force networks in compressed granular media. *EPL (Europhysics Letters)*, *97*(5), 54001.

Kosinski, P., & Hoffmann, A. C. (2010). An extension of the hard-sphere particle–particle collision model to study agglomeration. *Chemical Engineering Science*, *65*(10), 3231-3239.

Kun, F., & Herrmann, H. J. (1999). Transition from damage to fragmentation in collision of solids. *Physical Review E*, *59*(3), 2623.

Kusters, K. A., Wijers, J. G., & Thoenes, D. (1997). Aggregation kinetics of small particles in agitated vessels. *Chemical Engineering Science*, *52*(1), 107-121.

Lian, G., Thornton, C., & Adams, M. J. (1998). Discrete particle simulation of agglomerate impact coalescence. *Chemical Engineering Science*, *53*(19), 3381-3391.

Lundgren, T. S. (1982). Strained spiral vortex model for turbulent fine structure. *The Physics of Fluids*, *25*(12), 2193-2203.

Marshall, J. S., & Li, S. (2014). *Adhesive particle flow*. Cambridge University Press.

Matsoukas, T., & Friedlander, S. K. (1991). Dynamics of aerosol agglomerate formation. *Journal of Colloid and Interface Science*, *146*(2), 495-506.

Meyer, C. J., & Deglon, D. A. (2011). Particle collision modeling–a review. *Minerals Engineering*, *24*(8), 719-730.

Min, I. A., Mezić, I., & Leonard, A. (1996). Levy stable distributions for velocity and velocity difference in systems of vortex elements. *Physics of fluids*, *8*(5), 1169-1180.

Mito, Y., & Hanratty, T. J. (2002). Use of a modified Langevin equation to describe turbulent dispersion of fluid particles in a channel flow. *Flow, turbulence and combustion*, *68*(1), 1-26.

Moreno, R., Ghadiri, M., & Antony, S. J. (2003). Effect of the impact angle on the breakage of agglomerates: a numerical study using DEM. *Powder Technology*, *130*(1-3), 132-137.

Moreno-Atanasio, R., & Ghadiri, M. (2006). Mechanistic analysis and computer simulation of impact breakage of agglomerates: Effect of surface energy. *Chemical engineering science*, *61*(8), 2476-2481.

Ning, Z., Boerefijn, R., Ghadiri, M., & Thornton, C. (1997). Distinct element simulation of impact breakage of lactose agglomerates. *Advanced Powder Technology*, *8*(1), 15-37.

Özcan-Taşkin, N. G., Padron, G., & Voelkel, A. (2009). Effect of particle type on the mechanisms of break up of nanoscale particle clusters. *Chemical Engineering Research and Design*, *87*(4), 468-473.

Paiva, J., Salcedo, R., & Araujo, P. (2010). Impact of particle agglomeration in cyclones. *Chemical Engineering Journal*, *162*(3), 861-876.

Peters, J. F., Muthuswamy, M., Wibowo, J., & Tordesillas, A. (2005). Characterization of force chains in granular material. *Physical review E*, *72*(4), 041307.

Poelma, C., & Ooms, G. (2006). Particle-turbulence interaction in a homogeneous, isotropic turbulent suspension. *Applied Mechanics Reviews*, *59*(2), 78-90.

Pope, S. B., & Chen, Y. L. (1990). The velocity-dissipation probability density function model for turbulent flows. *Physics of Fluids A: Fluid Dynamics*, *2*(8), 1437-1449.

Potanin, A. A. (1993). On the computer simulation of the deformation and breakup of colloidal aggregates in shear flow. *Journal of colloid and interface science*, *157*(2), 399-410.

Pullin, D. I., & Saffman, P. G. (1993). On the Lundgren–Townsend model of turbulent fine scales. *Physics of Fluids A: Fluid Dynamics*, *5*(1), 126-145.

Rao, A., Curtis, J. S., Hancock, B. C., & Wassgren, C. (2012). Numerical simulation of dilute turbulent gas-particle flow with turbulence modulation. *AIChE Journal*, *58*(5), 1381-1396.

Reeks, M. W. (2014). Transport, mixing and agglomeration of particles in turbulent flows. In *Journal of Physics: Conference Series* (Vol. 530, No. 1, p. 012003). IOP Publishing.

Rumpf, H. (1962). The Strength of Granules and Agglomeration. *Agglomeration*, John Wiley, 379-418.

Rwei, S. P., Manas-Zloczower, I., & Feke, D. L. (1990). Observation of carbon black agglomerate dispersion in simple shear flows. *Polymer Engineering & Science*, *30*(12), 701-706.

Rwei, S. P., Manas-Zloczower, I., & Feke, D. L. (1991). Characterization of agglomerate dispersion by erosion in simple shear flows. *Polymer Engineering & Science*, *31*(8), 558-562.

Saber, A., Lundström, T. S., & Hellström, J. G. I. (2015). Turbulent modulation in particulate flow: A review of critical variables. *Engineering*, *7*(10), 597.

Saffman, P., & Turner, J. S. (1956). On the collision of drops in turbulent clouds. *Journal of Fluid Mechanics*, *1*(1), 16-30.

Saffman, P. G. (1997). Vortex models of isotropic turbulence. *Philosophical Transactions of the Royal Society of London A: Mathematical, Physical and Engineering Sciences*, *355*(1731), 1949-1956.

Sala, K., & Marshall, J. S. (2013). Stochastic vortex structure method for modeling particle clustering and collisions in homogeneous turbulence. *Physics of Fluids*, *25*(10), 103301.

Saunders, C. P. R. (1994). Thunderstorm electrification laboratory experiments and charging mechanisms. *Journal of Geophysical Research: Atmospheres*, *99*(D5), 10773-10779.

Sawford, B. L. (1991). Reynolds number effects in Lagrangian stochastic models of turbulent dispersion. *Physics of Fluids A: Fluid Dynamics*, *3*(6), 1577-1586.

Schäfer, C., Speith, R., & Kley, W. (2007). Collisions between equal-sized ice grain agglomerates. *Astronomy & Astrophysics*, *470*(2), 733-739.

Scurati, A., Feke, D. L., & Manas-Zloczower, I. (2005). Analysis of the kinetics of agglomerate erosion in simple shear flows. *Chemical Engineering Science*, *60*(23), 6564-6573.

Selomulya, C., Amal, R., Bushell, G., & Waite, T. D. (2001). Evidence of shear rate dependence on restructuring and breakup of latex aggregates. *Journal of colloid and interface science*, *236*(1), 67-77.

Seyvet, O., & Navard, P. (2000). Collision-induced dispersion of agglomerate suspensions in a shear flow. *Journal of applied polymer science*, *78*(5), 1130-1133.

Shapiro, M., Vainshtein, P., Dutcher, D., Emery, M., Stolzenburg, M., Kittelson, D. B., & McMurry, P. H. (2012). Characterization of agglomerates by simultaneous measurement of mobility, vacuum aerodynamic diameter and mass. *Journal of Aerosol Science*, *44*, 24-45.

Sundaram, S., & Collins, L. R. (1997). Collision statistics in an isotropic particle-laden turbulent suspension. Part 1. Direct numerical simulations. *Journal of Fluid Mechanics*, *335*, 75-109.

Sutherland, D. N., & Tan, C. T. (1970). Sedimentation of a porous sphere. *Chemical Engineering Science*, *25*(12), 1948-1950.

Tang, L., Wen, F., Yang, Y., Crowe, C. T., Chung J. N., & Troutt, T. R. (1992). Self-organizing particle dispersion mechanism in a plane wake. *Physics of Fluids A: Fluid Dynamics*, *4*(10), 2244-2251.

Taylor, G. I. (1938). Production and dissipation of vorticity in a turbulent fluid. *Proceedings of the Royal Society of London. Series A, Mathematical and Physical Sciences*, 15-23.

Thomson, D. J. (1987). Criteria for the selection of stochastic models of particle trajectories in turbulent flows. *Journal of Fluid Mechanics*, *180*, 529-556.

Thornton, C., Ciomocos, M. T., & Adams, M. J. (1999). Numerical simulations of agglomerate impact breakage. *Powder Technology*, *105*(1-3), 74-82.

Thornton, C., & Liu, L. (2004). How do agglomerates break?. *Powder Technology*, *143*, 110-116.

Tong, Z., Zhong, W., Yu, A., Chan, H. K., & Yang, R. (2016). CFD–DEM investigation of the effect of agglomerate–agglomerate collision on dry powder aerosolisation. *Journal of Aerosol Science*, *92*, 109-121.

Torres, F. E., Russel, W. B., & Schowalter, W. R. (1991). Floc structure and growth kinetics for rapid shear coagulation of polystyrene colloids. *Journal of colloid and interface science*, *142*(2), 554-574.

Townsend, A. A. (1951). On the fine-scale structure of turbulence. *Proc. R. Soc. Lond. A*, *208*(1095), 534-542.

Tryggeson, H. (2007). Analytical Vortex Solutions to the Navier-Stokes Equation (doktorsavhandling).

Vainshtein, P., & Shapiro, M. (2005). Mobility of permeable fractal agglomerates in slip regime. *Journal of colloid and interface science*, *284*(2), 501-509.

Vincent, A., & Meneguzzi, M. (1991). The spatial structure and statistical properties of homogeneous turbulence. *Journal of Fluid Mechanics*, *225*, 1-20.

Vincent, A., & Meneguzzi, M. (1994). The dynamics of vorticity tubes in homogeneous turbulence. *Journal of Fluid Mechanics*, *258*, 245-254.

Waldner, M. H., Sefcik, J., Soos, M., & Morbidelli, M. (2005). Initial growth kinetics and structure of colloidal aggregates in a turbulent coagulator. *Powder technology*, *156*(2-3), 226-234.

Wang, L. P., Wexler, A. S., & Zhou, Y. (2000). Statistical mechanical description and modelling of turbulent collision of inertial particles. *Journal of Fluid Mechanics*, *415*, 117-153.

Wilczek, M., & Friedrich, R. (2009). Dynamical origins for non-Gaussian vorticity distributions in turbulent flows. *Physical Review E*, *80*(1), 016316.

Xu, X. G., Li, S. Q., Li, G. D., & Yao, Q. (2009). Effect of co-firing straw with two coals on the ash deposition behavior in a down-fired pulverized coal combustor. *Energy & Fuels*, *24*(1), 241-249.

Zeidan, M., Xu, B. H., Jia, X., & Williams, R. A. (2007). Simulation of aggregate deformation and breakup in simple shear flows using a combined continuum and discrete model. *Chemical Engineering Research and Design*, *85*(12), 1645-1654.

Zhang, Y., Shuiqing, L., Deng, S., Yao, Q., & Stephen, D. T. (2012). Direct synthesis of nanostructured TiO2 films with controlled morphologies by stagnation swirl flames. *Journal of Aerosol Science*, *44*, 71-82.

Zhang, L., Wang, Y., & Zhang, J. (2014). Force-chain distributions in granular systems. *Physical Review E*, *89*(1), 012203.

Chapter 3: An Accelerated Stochastic Vortex Structure Method for Particle Collision and Agglomeration in Homogeneous Turbulence

Farzad F. Dizaji and Jeffrey S. Marshall
School of Engineering, The University of Vermont

Corresponding Author: Jeffrey S. Marshall, School of Engineering, The University of Vermont, Burlington, VT 05405, U.S.A. PHONE: 1 (802) 656-3826, EMAIL: jmarsha1@uvm.edu.

Keywords: stochastic vortex structures; fast multipole method; particle collision; turbulent agglomeration

Abstract

Modeling the response of interacting particles, droplets or bubbles to subgrid-scale fluctuations in turbulent flows is a long-standing challenge in multiphase flow simulations using the Reynolds-Averaged Navier-Stokes (RANS) approach. The problem also arises for large-eddy simulation (LES) for sufficiently small values of the Kolmogorov-scale particle Stokes number. This paper expands on a recently proposed stochastic vortex structure (SVS) method for modeling of turbulence fluctuations for colliding or otherwise interacting particles. An accelerated version of the SVS method was developed using the fast multipole expansion and local Taylor expansion approach, which reduces computation speed by two orders of magnitude compared to the original SVS method. Detailed comparisons are presented showing close agreement of the energy spectrum and probability density functions of various fields between the SVS computational model, direct numerical simulation (DNS) results, and various theoretical and experimental results found in the literature. Results of the SVS method for particle collision rate and related measures of particle interaction exhibit excellent agreement with DNS predictions for homogeneous turbulent flows. The SVS method was also used with adhesive particles to simulate formation of particle agglomerates with different values of the particle Stokes and adhesion numbers, and various measures of the agglomerate structure are compared to DNS results.

3.1. Introduction

Particle collision and agglomeration play an important role in a wide range of turbulent flow applications involving small particles or droplets. Droplet collision is a key element to cloud formation and precipitation development (Devenish et al., 2012).

Particle agglomeration is particularly important in aerosol flow problems, such as fly ash collection from combustion processes (Xu et al., 2010), flame-synthesis of nanoparticles (Zhang et al., 2012), cyclone particle separators (Paiva et al., 2010), and snow crystal formation (Kajikawa et al., 2000), for which adhesive particles have Stokes numbers sufficiently close to unity that they display significant drift relative to the fluid trajectories. Agglomerate formation is preceded by particle collision, where the particle collision rate is controlled either by the fluctuating turbulent shear flow (for smaller size particles) or by particle inertia (for larger particles). The fluctuating turbulent shear stress also controls agglomerate breakup (Serra et al., 1997; Higashitani et al., 2001). Over long time, the distribution of particle agglomerate sizes is determined by a balance between influences increasing collision rate and influences enhancing agglomerate breakup.

A wide variety of turbulence models have been developed using the Reynolds-averaged Navier-Stokes (RANS) approach, ranging from the popular two-equation models, such as $k-\varepsilon$ and $k-\omega$, to full Reynolds stress models. RANS models yield numerical predictions for the mean turbulent velocity field as well as for certain averaged quantities associated with the Reynolds stress tensor. However, additional modeling is required for RANS simulations to account for the role of turbulent fluctuations on particle transport. A similar need for subgrid-scale modeling of turbulent fluctuations arises for large eddy simulations (LES) when the Kolmogorov-scale Stokes number is less than a critical value of about three (Jin et al., 2010).

While numerous effective methods are available to simulate the effect of subgrid-scale fluctuations for transport of non-interacting particles (e.g., Wilson and Sawford, 1996; Loth, 2007; Minier et al., 2014; Pope, 2011), turbulent subgrid-scale simulation for

interacting particles remains an unresolved modeling challenge. There are a number of reasons why subgrid-scale modeling for interacting particles poses difficulties. Firstly, the mechanics of interacting particles depends sensitively on the distance between the particles at small values of separation. Particles that are sufficiently close to each other experience highly correlated fluid velocities induced by the nearby turbulent eddies. Models which employ independent (uncorrelated) stochastic forcing at each particle consequently cannot be used for interacting particles. Secondly, particle collision and adhesion processes occur on very small times scales, which makes the numerical simulation of colliding and adhesive particles numerically stiff. This is particularly a problem for simulations using the soft-sphere discrete element method (DEM), which is usually necessary for dealing with particle agglomerates that form upon collision of adhesive particles. Consequently, small time steps must be taken for the particle transport and the subgrid-scale turbulent fluctuation modeling must be sufficiently fast for the computation to be manageable. Thirdly, the eddy structures of the turbulent flow play an important role both in dispersing particles and in inducing clustering in the region in-between the eddies (Squires and Eaton, 1991; Bec et al., 2007; Grits et al., 2006; Falkovich and Pumir, 2004). Eddy-induced particle clustering leads to formation of regions of high particle concentration within the turbulence, which dramatically increases particle collision rate and agglomerate sizes (Sundaram and Collins, 1997; Zaichik et al., 2006; Reade and Collins, 2000). Particle preferential concentration has particularly interesting consequences in bidisperse flows involving particles that are both heavier and lighter than the fluid, such as heavy particles and bubbles in a liquid (Fayed, 2013; Fayed and Ragab, 2013), for which case the heavy particles cluster in the high shear regions in-

between the eddies and the light particles (bubbles) cluster within the turbulent eddies. As a consequence of the issues of computation time and preferential concentration, many of the synthetic turbulence approaches that have been developed for reconstruction of initial or inlet conditions in large-eddy simulations (Kraichnan, 1970; Smirnov et al., 2000; Tabor and Baba-Ahmadi, 2010; Lund et al., 1998) are not useful for subgrid-scale modeling of flows with interacting particles.

Clustering of non-adhesive particles in turbulent flows is largely due to inertial particle drift across curved fluid streamlines associated with the presence of turbulent eddies (Squires and Eaton, 1991). A vortex structure representation of the turbulent flow consequently presents a natural approach for capturing this effect in the turbulence model. Of course, vortex-based structural models have long been discussed in the turbulence flow literature. Notable among these are Townsend's (1951) model of homogeneous turbulence as a collection of Burger's vortices and Lundgren's (1982) spiral vortex model of turbulence. The scaling and structure of coherent vortices was examined by Jiménez et al. (1993) in homogeneous turbulence based on results of high-resolution direct numerical simulations (DNS) and by Belin et al. (1996) in a turbulent shear flow using experiments with low-temperature helium gas. Both studies found that the vorticity field for low Reynolds number turbulence is dominated by a set of strong, coherent vortex structures of finite length and with tubular shape, surrounded by a sea of weak random (non-coherent) vorticity. The length and core radius of the coherent vortices were found to scale with the integral length scale and the Kolmogorov length scale, respectively, and the vortex strength was found to scale with the square root of the microscale Reynolds number. Analysis of the Townsend and Lundgren models was given

by Pullin and Saffman (1993) and Saffman (1997), who derive an expression for the energy spectrum and other measures for isotropic turbulence. Kivotides and Leonard (2003) report results of a computation in which homogeneous turbulence is represented by a set of finite-length vortex structures, and show that this system generates an energy spectrum that satisfies the Kolmogorov $k^{-5/3}$ scaling in the turbulence inertial range. The effect of vortex straining on the energy spectrum of a group of randomly advected vortices is discussed by Malik and Vassilicos (1996). Hatakeyama and Kambe (1997) demonstrate good agreement for structure functions of homogeneous turbulence between those generated by a group of random strained Burgers vortices and the classical Kolmogorov theory. Use of vortex models to generate accurate PDF curves for velocity increment, acceleration and vorticity is discussed by Min et al. (1996), Wilczek et al. (2008), and Wilczek and Friedrich (2009).

A first step toward use of a vortex structure model for turbulent particle transport was made by Ayyalasomayajula et al. (2008), who proposed a model in which the turbulent eddies are represented by a two-dimensional vortex array and a stochastic algorithm is used to vary the strength of each vortex in time. Although extremely simple, this model was shown to yield reasonable results for particle acceleration statistics and clustering. A three-dimensional stochastic vortex structure (SVS) model was proposed by Sala and Marshall (2013), in which the turbulent vorticity field is approximated by a set of finite-length, fixed vortex structures which are randomly positioned and oriented in the flow field. Predictions of the SVS model for turbulence energy spectrum and particle collision rate were found to be in close agreement with DNS predictions. However, the

original SVS method was rather slow and only considered transport and collision of non-adhesive particles.

The current paper extends the SVS model proposed by Sala and Marshall (2013) in two respects: (1) a variation of the fast multipole method FMM and local Taylor expansions are used to dramatically accelerate the SVS computations and (2) the performance of the SVS method is examined for prediction of turbulent agglomeration of adhesive particles. Successful simulation of turbulent agglomeration requires both that the particle collision model is accurately simulated by SVS, but also that the fluctuating turbulent shear stress responsible for agglomerate breakup and erosion is accurately predicted We also report more extensive comparisons with DNS data, as well as detailed sensitivity testing of the SVS model results to various input parameters. The basic SVS model is described in Section 3.2. In Section 3.3, a fast multipole method is developed for computing the velocity field induced by the vortex structures, which is found to yield nearly two orders of magnitude increase in computational speed compared to direct velocity computation. Sections 3.4-3.6 present different types of validation and sensitivity tests for the SVS model. Section 3.4 examines measures of the turbulent flow field. Section 3.5 examines prediction of collision rate for non-adhesive particles, and Section 3.6 examines use of SVS for prediction of turbulent agglomeration with adhesive particles. Conclusions are given in Section 3.7.

3.2. Stochastic Vortex Structure Method

Particle collisions in turbulent flows depend primarily on the eddy Stokes number, which can be written as a function of eddy size ℓ as

$$\mathrm{St}_\ell \equiv m u_\ell / 3\pi\mu d\ell, \tag{3-1}$$

where d and m are the particle diameter and mass, respectively, and μ is the fluid viscosity. In the inertial range, the characteristic velocity u_ℓ of eddies of size ℓ varies with turbulence dissipation rate per unit mass ε as $u_\ell \sim (\varepsilon\ell)^{1/3}$ (Frisch, 1995). Since the dissipation rate is approximately independent of scale in the inertial range, the Stokes number varies with ℓ approximately as $\mathrm{St}_\ell \sim \ell^{-2/3}$. Particles are largely transported by the fluid flow for eddies where $St_\ell << 1$ and the particle inertia filters out the turbulence fluctuations for eddies where $St_\ell >> 1$ (Ayyalasomayajula et al., 2008; Marshall and Li, 2014). In-between these extremes, there exists an eddy size ℓ for which $St_\ell = O(1)$, in which the particles are thrown out of the turbulent eddies and collect in high-concentration sheets in the interstitial region between the eddies.

The stochastic vortex structure (SVS) model approximates the turbulent vorticity field by a collection of vortex structures placed and oriented randomly in the flow field. In the simplest version of the SVS model, the vortex structures all have the same finite length *L*, core radius δ, and strength Γ, although a multiscale version of the SVS model has also been developed. The vortex length *L* is assumed in the current paper to be of the order of magnitude of the turbulence integral length scale $\ell_0 = 0.5\, u_0^{\,3} / \varepsilon$, where u_0 is the turbulence root-mean-square velocity. Based on the well-established observation that strain rate in the inertial range scales as u_0 / λ (Frisch, 1995), Kambe and Hatakeyama (2000) used a scaling analysis to derive an approximation for vortex core radius as $\delta \cong 3.9\eta$, where $\lambda = u_0 (15\nu / \varepsilon)^{1/2}$ is the Taylor microscale, $\eta = (\nu^3 / \varepsilon)^{1/4}$ is the

Kolmogorov length scale, and ν is the kinematic viscosity. This estimate is in good agreement with experimental and numerical results (Jimenez et al., 1993; Belin et al., 1996). The current paper uses a somewhat larger assumption $\delta = 8\eta$ for vortex core radius in order to ensure sufficient number of grid points to adequately resolve the velocity gradient across the vortex cores. Each vortex structure has a lifetime T_V which is assumed to be proportional to the integral time scale, $T_\ell = q/3\varepsilon$, where $q = 1.5u_0^2$ is the turbulent kinetic energy per unit mass. While the coherent vortices in a turbulent flow may in practice last significantly longer than T_ℓ, the results of the model are not sensitive to value of T_V. The initial age of the n^{th} vortex structure, τ_{0n}, is specified as a random variable, where the ratio τ_{0n}/T_V has a uniform distribution between 0 and 1. If t_{0n} denotes the time at which the vortex structure is initiated, then the current age of the vortex structure $\tau_n(t)$ is given by

$$\tau_n = \tau_{0n} + t - t_{0n}. \tag{3-2}$$

When $\tau_n(t)$ exceeds the specified lifespan T_V, the vortex structure is removed and a new vortex structure is introduced with random position and orientation in the flow.

The vortex structures induce a velocity field **u** which is computed using the accelerated method described in Section 3.3. Each of the N_V vortex structures are advected in time by moving the two endpoints of the vortex structure by solving

$$\frac{d\mathbf{x}_{n,i}}{dt} = \mathbf{u}(\mathbf{x}_{n,i}, t), \tag{3-3}$$

where the index *n* identifies the vortex structure and *i* (=1,2) identifies the endpoint of the structure under consideration. After moving the end points, the vortex length is reset to *L*.

The centroid position $\mathbf{x}_n$ and unit tangent vector $\boldsymbol{\lambda}_n$ for each structure are then recomputed from the positions of the new endpoint locations.

3.3. Accelerated Method for Velocity Calculation

The stochastic vortex structures constitute a *kinematic* representation of the turbulent flow, which is intended to generate a synthetic fluctuating velocity field that exhibits similar statistical properties to the actual turbulent flow. The *dynamics* of the turbulent flow is simulated by whatever RANS model is used to compute parameters such as turbulent kinetic energy and dissipation rate, and not via the SVS model. With this point in mind, it is recalled that a divergence-free vorticity field $\boldsymbol{\omega}$ can be generated from the vorticity $\boldsymbol{\omega}^*$ associated with a set of finite-length vortex tubes as

$$\boldsymbol{\omega} = \boldsymbol{\omega}^* + \nabla\zeta\,, \tag{3-4}$$

where

$$\nabla^2\zeta = -\nabla\cdot\boldsymbol{\omega}^*. \tag{3-5}$$

Substituting (4) into the Biot-Savart equation

$$\mathbf{u}(\mathbf{x},t) = -\frac{1}{4\pi}\int_V \frac{\mathbf{s}\times\boldsymbol{\omega}(\mathbf{x}',t)}{s^3}\,dv'\,, \tag{3-6}$$

where $s \equiv |\mathbf{s}| \equiv |\mathbf{x}-\mathbf{x}'|$, and using Green's theorem, one can readily show that the $\nabla\zeta$ term in (3.4) makes no contribution to the induced velocity field (see Appendix).

For computation of particle transport, it is more efficient to compute the fluid velocity on a Cartesian grid covering the computational domain, and then interpolate the velocity from the grid nodes onto the Lagrangian particles that move through the grid. This is particularly true when using a multiple time-scale algorithm for particle transfer

(Marshall, 2009), in which the fluid velocity is computed on a larger time step than that used for transport of either free or colliding particles. The computations in the current paper are performed using a 128^3 Cartesian grid to cover a cubic, triply-periodic domain with side length 2π.

To accelerate the velocity computation, we utilize the combination of an optimized fast multipole method (FMM) for computing the velocity field induced by sufficiently distant vortex structures and a local Taylor expansion to reduce the number of points at which the Biot-Savart integral must be solved. The accelerated method is based on a partitioning of the computational domain into a tree family of boxes consisting of some number M levels, each of which covers all grid points in the domain. The first level ($m = 1$) consists of the entire grid, and has only one box. The second level ($m = 2$) consists of 8 boxes, which are obtained by dividing the side length of each box in level 1 by a factor of two, as illustrated in Figure 3.1. This division process is repeated for subsequent levels, with the number of boxes in each level m increasing as 8^{m-1}. The boxes associated with the highest level are called the *small boxes* of the box family.

The velocity is evaluated at each point of the Cartesian grid by solving for the contribution to the Biot-Savart integral (3.6) from all vortex structures in the computational domain, as well as from neighboring domains necessary to enforce the periodic boundary condition. In order to perform the computation efficiently, we first associate with each grid point a specific smallest box of the tree family in which the grid point is contained, which is called the *target box* of the grid point. The velocity within each target box is determined by integrating the Biot-Savart integral over the vortex structures contained within some set of boxes (called *source boxes*) that can be at any

level of the box tree family, but where the set of source boxes is required to cover each vortex structure within the computational domain exactly once (i.e., the source boxes cannot overlap). Each target box interacts with each source box either *directly* or *indirectly*. In a direct interaction, the velocity induced by each vortex structure in the source box is evaluated individually on each grid point within the target box. In an indirect interaction, the induced velocity from all vortex structures within the source box is computed at the center of the target box at one time using a multipole expansion, and then the induced velocity is extrapolated onto the grid points within the target box by a local Taylor series expansion. Lists are compiled for each target box of source boxes with which the target box interacts directly and indirectly. The selection of source boxes and the box interaction lists were constructed using the optimized approach proposed by Marshall et al. (2000), which is based on an analytical error estimate for the multipole expansion derived by Salmon and Warren (1994).

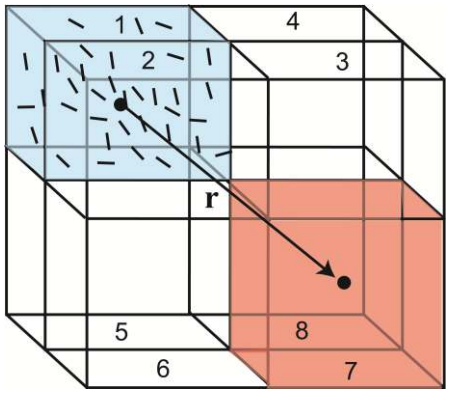

Figure 3.1. Image representing two levels of the box family used to cover the computational grid. The first level consists of the entire grid, and the second level consists of the eight individual boxes numbered 1-8 in the image. An example is shown where box 1 is a source box (blue online) and box 7 is a target box (red online), where the vector pointing from the centroid of box 1 to that of box 7 is indicated by an arrow and denoted by **r**. The individual vortex structures contained within box 1 are represented by short line segments within the box.

3.3.1. Direct Velocity Computation – Interpolation from the Data Plane

For a source box that interacts directly with a given target box, the velocity induced by each vortex structure in the source box is computed at each grid point in the target box. The velocity computation is done by first pre-computing the velocity induced by a vortex structure of unit strength on the *data plane*, which is defined as the positive r-z plane relative to the axis of the vortex structure (Figure 3.2). This computation is performed once at the beginning of the computation and the results are stored.

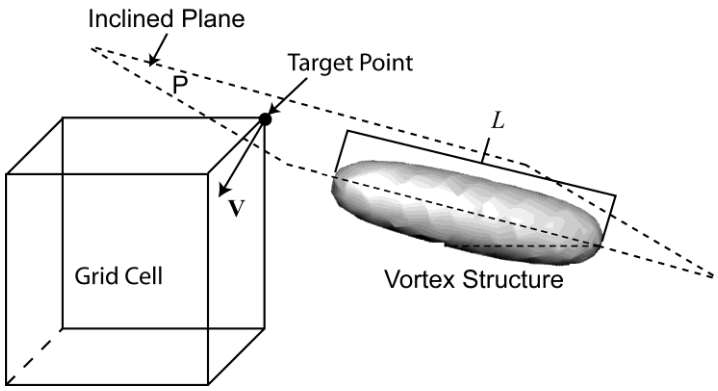

Figure 3.2. Schematic diagram showing the interpolation procedure used for direct computation of the velocity induced by a vortex structure on a node of the grid cell. Here L is the length of the vortex structure, and P identifies the inclined plane from which the induced azimuthal velocity **v** induced by the vortex is interpolated.

The induced velocity on the data plane is determined by computing the induced velocity normal to the *r-z* plane of a coordinate system that is local to a vortex structure of unit strength, where the vortex center is located at the origin of the local coordinate system. The velocity at each point of the grid used to cover the data plane is determined using a Gaussian vortex blob method (Marshall and Grant, 1996), where the number of vortex blobs, N_b, used to discretize the vortex structure is set equal to $N_b = \text{int}(\beta L/\delta)$, and where the Gaussian radius of the blob is set equal to the vortex structure radius δ and β is a blob overlap coefficient. If the centroid of the i^{th} vortex blob is denoted by $\mathbf{b}_i$, $i = 1,\ldots,N_b$, the associated vorticity field is given by

$$\boldsymbol{\omega}_i(\mathbf{x},t) = \frac{\boldsymbol{\Omega}_i}{\pi^{3/2}\delta^3}\exp\left(-\frac{|\mathbf{x}-\mathbf{b}_i|^2}{\delta^2}\right) \tag{3-7}$$

Here, the blob amplitude $\boldsymbol{\Omega}_i$ is given by

$$\boldsymbol{\Omega}_i = (\Gamma L/N_b)\,\boldsymbol{\lambda}_b \tag{3-8}$$

and $\boldsymbol{\lambda}_b$ is a unit vector tangent to the vortex structure axis. Substituting (3.7) into the Biot-Savart integral (3.6) yields the velocity field induced by the i^{th} vortex blob at a target point **x** as

$$\mathbf{u}_i(\mathbf{x},t) = \frac{P\left(\frac{3}{2}, \frac{|\mathbf{x}-\mathbf{b}_i|^2}{\delta^2}\right)}{4\pi|\mathbf{x}-\mathbf{b}_i|^3}\ \boldsymbol{\Omega}_i \times (\mathbf{x}-\mathbf{b}_i), \tag{3-9}$$

where $P(a,z)$ is the incomplete gamma function with limits $P(a,0)=0$ and $P(a,\infty)=1$. When $a=3/2$ and $z=x^2$ for some real variable *x*, a convenient expression for the incomplete gamma function in terms of the error function erf(*x*) can be written as (Abramowitz and Stegun, 1965)

$$P(\tfrac{3}{2}, x^2) = \text{erf}(x) - \frac{2xe^{-x^2}}{\sqrt{\pi}}. \tag{3-10}$$

The velocity at any point **x** on the data plane is obtained by summing the velocity induced by all N_b vortex blobs, as given by (3.9).

At subsequent times, the induced velocity from a vortex structure *m* at grid point **x** is obtained by interpolation from the data plane. This interpolation is performed by centering the data plane at the vortex structure centroid $\mathbf{x}_m$, and orienting the plane so that it passes through the target point **x** and is tangent to the vortex axis unit vector $\boldsymbol{\lambda}_m$, as illustrated in Figure 3.2. The grid cell in which lies the point **x** is obtained in the data plane by integer division and the velocity induced by the vortex structure is interpolated onto the target point and reoriented to lie in the global coordinate system, yielding a velocity contribution $\mathbf{u}'_m$ on point **x** from vortex structure *m*. The periodic boundary condition is enforced by including velocity induced by vortex structures in one period on

each side of the computational domain, resulting in $27N_V$ total vortex structures if the entire computation is performed directly. The total direct velocity at a point **x** from the N_{dir} vortex structures for all source boxes on the direct interaction list (including vortex structures in the side domains used to enforce periodic boundary conditions) is then given by

$$\mathbf{u}_{dir}(\mathbf{x},t) = \sum_{m=1}^{N_{dir}} \mathbf{u}'_m \Gamma_m \tag{3-11}$$

Since the sum (3.11) must be computed for every grid point within the Cartesian grid, it is very time consuming if the summation is performed over all vortex structures in the computational domain and the neighboring periods of the computational domain. For this reason, the direct interaction list is restricted to only a small number of source boxes with centroids located sufficiently close to the centroid of the target box.

3.3.2. Indirect Velocity Computation – Multipole Expansion

For a source box ℓ that interacts *indirectly* with the target box, the contribution of all vortex structures in box ℓ are evaluated at any point **x** in the target box using the multipole expansion (Greengard and Rokhlin, 1987)

$$\Delta\mathbf{u}_\ell(\mathbf{x},t) = \frac{1}{4\pi}\sum_{m=0}^{\infty}\sum_{n=0}^{\infty}\sum_{k=0}^{\infty}\frac{(-1)^{m+n+k}}{m!\,n!\,k!}\mathbf{I}_{\ell,mnk}\times\frac{\partial^{m+n+k}}{\partial x^m\partial y^n\partial z^k}\left(\frac{\mathbf{r}}{r^3}\right), \tag{3-12}$$

where $\mathbf{r} = \mathbf{x} - \boldsymbol{\xi}_\ell$ is the vector from the centroid $\boldsymbol{\xi}_\ell = \xi_{1,\ell}\mathbf{e}_x + \xi_{2,\ell}\mathbf{e}_y + \xi_{3,\ell}\mathbf{e}_z$ of box ℓ to the point **x**. The box moment $\mathbf{I}_{\ell,mnk}$ of box ℓ is defined by

$$\mathbf{I}_{\ell,mnk} = \int_{V_\ell} (x-\xi_{1,\ell})^m (y-\xi_{2,\ell})^n (z-\xi_{3,\ell})^k\,\boldsymbol{\omega}(\mathbf{x},t)\,dv. \tag{3-13}$$

The box moments are evaluated by first computing the moment J_{mnk} of a single vortex structure of unit strength aligned in the $\hat{x}$-direction about the vortex centroid in a local coordinate system ($\hat{x}, \hat{y}, \hat{z}$), which is given by

$$J_{mnk} = \int_V \hat{x}^m \hat{y}^n \hat{z}^k \hat{\omega}(\hat{\mathbf{x}} - \hat{\mathbf{x}}')\, dv', \tag{3-14}$$

where $\hat{\omega}(\mathbf{x})\boldsymbol{\lambda}$ is the vorticity field associated with the vortex structure and $\boldsymbol{\lambda}$ is a unit vector along the vortex axis. For a vortex structure of length L and core radius δ, we find

$$J_{000} = L, \qquad J_{100} = J_{010} = J_{001} = 0, \qquad J_{200} = J_{020} = J_{002} = L\delta^2/2. \tag{3-15}$$

Since the values of J_{mnk} are isotropic (the same for all directions), it is not necessary to translate between the local coordinate system used to compute (3.14) and the global Cartesian coordinate system. The moment $\mathbf{I}_{\ell,mnk}$ of a box ℓ is obtained by summing over the moments J_{mnk} of all of the N_ℓ vortex structures in box ℓ, which have vortex strengths Γ_i and centroid locations $\mathbf{c}_i$, giving

$$\mathbf{I}_{\ell,mnk} = \sum_{i=1}^{N_\ell} \sum_{q=0}^{m} \sum_{s=0}^{n} \sum_{t=0}^{k} \binom{m}{q}\binom{n}{s}\binom{k}{t} (c_{i1} - \xi_{\ell 1})^q (c_{i2} - \xi_{\ell 2})^s (c_{i3} - \xi_{\ell 3})^t$$

$$\times \Gamma_i \, J_{(m-q)(n-s)(k-t)} \boldsymbol{\lambda}_\ell. \tag{3-16}$$

Once the moments of all of the smallest size boxes are obtained using (3.16), the moments of higher-generation boxes are obtained from the translation formula

$$\mathbf{I}_{\ell,mnk} = \sum_{i=1}^{8} \sum_{q=0}^{m} \sum_{s=0}^{n} \sum_{t=0}^{k} \binom{m}{q}\binom{n}{s}\binom{k}{t} (\xi_{i1} - \xi_{\ell 1})^q (\xi_{i2} - \xi_{\ell 2})^s (\xi_{i3} - \xi_{\ell 3})^t$$

$$\times \mathbf{I}_{i,(m-q)(n-s)(k-t)}, \tag{3-17}$$

where *i* denotes one of the eight offspring boxes of parent box ℓ.

3.3.3. Indirect Velocity Computation – Local Taylor Series Expansion

The derivative term in (3.12) depends on the location of the target point **x**. Since we compute the velocity at each point of a N^3 Cartesian grid, there are typically a large number of target points within a given box. The local expansion method accelerates the process of computing the indirect component of the velocity field by evaluating the velocity induced by a source box ℓ with centroid $\boldsymbol{\xi}_\ell$ at the centroid $\hat{\boldsymbol{\xi}}_b$ of the target box *b* (defined as the smallest box containing the target point **x**), and then determining the velocity at each individual grid point **x** using a local Taylor series expansion of $\mathbf{K}(\mathbf{x}-\boldsymbol{\xi}_\ell)=\mathbf{r}/r^3$ about the target box center $\hat{\boldsymbol{\xi}}_b$, given by

$$\mathbf{K}(\mathbf{x}-\boldsymbol{\xi}_\ell)=\sum_{m=0}^{\infty}\sum_{n=0}^{\infty}\sum_{k=0}^{\infty}\frac{(x-\hat{\xi}_{b1})^m(y-\hat{\xi}_{b2})^n(z-\hat{\xi}_{b3})^k}{m!\,n!\,k!}\frac{\partial^{m+n+k}}{\partial x^m\partial y^n\partial z^k}\mathbf{K}(\hat{\boldsymbol{\xi}}_b-\boldsymbol{\xi}_\ell). \quad (3\text{-}18)$$

Substituting (3.18) into (3.12) and truncating the summation after *P* terms gives the contribution of source box ℓ to the velocity at grid point **x** as

$$\Delta\mathbf{u}_\ell(\mathbf{x},t)=\sum_{m=0}^{P}\sum_{n=0}^{P}\sum_{k=0}^{P}\mathbf{D}_{\ell,mnk}(x-\hat{\xi}_{b1})^m(y-\hat{\xi}_{b2})^n(z-\hat{\xi}_{b3})^k, \quad (3\text{-}19)$$

where

$$\mathbf{D}_{\ell,mnk}=\sum_{q=0}^{P-m}\sum_{s=0}^{P-n}\sum_{t=0}^{P-k}\frac{\mathbf{B}_{\ell,qst}}{m!n!k!}\times\frac{\partial^{m+q}}{\partial x^{m+q}}\frac{\partial^{n+s}}{\partial y^{n+s}}\frac{\partial^{k+t}}{\partial z^{k+t}}\mathbf{K}(\mathbf{x}-\boldsymbol{\xi}_\ell),$$

$$\mathbf{B}_{\ell,qst}=\frac{1}{4\pi}\frac{(-1)^{q+s+t}}{q!s!t!}\mathbf{I}_{\ell,qst}. \quad (3\text{-}20)$$

3.4. Example Computations

A series of example computations were performed with 512 vortex structures on a 128^3 grid with *B* different levels of box division. The order *p* of terms in the multipole

and local expansions was allowed to vary from $p = 0$ to a maximum of $p = 2$ for all of the remaining computations. The order of the interaction is set for each source-target box combination as a function of the distance d between the box centers. The critical separation distance for each order is specified as a function of the box size b at the highest level B, such that we use order

$$p = \begin{cases} 0 & \text{if } d_0 \le d < d_1 \\ 1 & \text{if } d_1 \le d < d_2 \\ 2 & \text{if } d_2 \le d \end{cases}, \tag{3-21}$$

where $d_0 = \alpha_0 b$, $d_1 = \alpha_1 b$, and $d_2 = \alpha_2 b$. If $d < d_0$, the source box is placed on the direct interaction list of the target box.

Results for computations with different values of B are shown in Table 3.1 for a case with critical distance coefficients $\alpha_0 = 4$, $\alpha_1 = 3$, and $\alpha_2 = 2$. The table lists the computed value of turbulent kinetic energy (TKE) (a measure of accuracy), the CPU time, and the percentage of the total possible boxes placed on the direct list (averaged over all target points). The CPU time results are for single-processor calculations for ease of comparison. It is noted that some source boxes do not enclose any vortex structures, in which case the box is ignored and not placed on either the direct or indirect list. At the top of the table is data for a computation in which the velocity is computed using only the direct interaction. For $B \le 4$, the TKE error for computations using the accelerated method is less than 1.5% of the direct computation, while the CPU time is reduced to less than 3% of that for the direct computation.

The CPU time is reduced further for the case with $B = 5$ to about 1.5% of the direct computation time, but at the same time the TKE error increases to about 16%. The

reason for this sudden increase in TKE error is that the box size *b* grows progressively smaller as *B* is increased, so that an increasingly large percentage of the computation is performed using the indirect approach. As discussed by Salmon and Warren (1994), the multipole expansion error increases in a nonlinear manner as the critical distance decreases. Based on the results in Table 3.1, we selected to perform the remainder of the computations in the paper with $B = 4$ and $\alpha_0, \alpha_1, \alpha_2 = 4, 3, 2$.

Table 3.1. Comparison of CPU time, percentage of the computation performed directly (in terms of number of boxes of the smallest size), and flow measures such as turbulent kinetic energy and enstrophy for the direct computation and for indirect computations with four different levels of the boxing scheme used for the velocity acceleration method. The computations were performed with $N_v = 512$ vortex structures, with critical distance coefficients $\alpha_0 = 4$, $\alpha_1 = 3$, and $\alpha_2 = 2$.

Smallest Box Level	% direct boxes	TKE	Enstrophy	CPU time (s)
direct	**100**	**1.528**	**51.449**	**1065.5**
2	100	1.528	51.449	1107.9
3	36.6	1.522	51.434	460.7
4	0.816	1.507	51.611	23.7
5	0.0183	1.497	52.153	12.8

3.4. Analysis of the SVS Synthetic Turbulence Field

The key parameters associated with the SVS method are the number of vortex structures N_V in the computational domain, the strength of each vortex structure Γ, the vortex length *L*, and the vortex core radius δ. These parameters can be related to various measures of the turbulent flow field, such as the turbulent kinetic energy per unit mass *E*, the dissipation rate per unit mass ε, and the enstrophy per unit volume Ω, defined by

$$E = \frac{1}{2V}\int_V \mathbf{u}\cdot\mathbf{u}\, dv, \qquad \varepsilon = \frac{2\nu}{V}\int_V D_{ij}D_{ij}\, dv, \qquad \Omega = \frac{1}{2V}\int_V \boldsymbol{\omega}\cdot\boldsymbol{\omega}\, dv, \tag{3-22}$$

where D_{ij} are the components of the rate of deformation tensor, $\mathbf{u}$ and $\boldsymbol{\omega}$ are the velocity and vorticity vectors, respectively, and V is the computational domain volume. For homogeneous, isotropic turbulence, the dissipation rate and the enstrophy are related by $\varepsilon = 2\nu\Omega$.

The enstrophy can be estimated using the expression for a Burgers vortex (Burgers, 1948) in a field with axial stretching rate c, in which the vorticity field has the form of a Gaussian

$$\omega = \frac{\Gamma}{\pi\delta^2}\exp(-r^2/\delta^2) \tag{3-23}$$

and the Gaussian radius is $\delta = 2\sqrt{\nu/c}$. For a system of N_V Burgers vortices of length ℓ and strength Γ, the enstrophy is given by

$$\Omega = \frac{N_V\Gamma^2\ell}{4\pi\delta^2 V}. \tag{3-24}$$

A theoretical expression for the energy spectral density $e(k)$ in a system of N_V Burgers vortices of length ℓ and strength Γ is given by Saffman (1997) as

$$e(k) = \frac{N_V\Gamma^2\ell}{4\pi V k}\exp(-\delta^2 k^2/4), \tag{3-25}$$

where k is the wavenumber magnitude. This expression is derived based on the assumption that the vortices do not interact with each other, so that the energy induced by

each vortex can be added together to obtain the total system energy. Integrating over the wavenumber interval ($k_{\min}, k_{\max}$) gives the turbulent kinetic energy as

$$E = \int_{k_{\min}}^{k_{\max}} e(k)\, dk = \frac{N_V \Gamma^2 \ell}{4\pi V} [E_1(\delta^2 k_{\min}^2 / 4) - E_1(\delta^2 k_{\max}^2 / 4)], \tag{3-26}$$

where $E_1(\cdot)$ is the exponential integral function.

A series of computations was performed in which the number of vortex structures in the computational domain was varied from 32 to 512, and the product $N_V \Gamma^2$ varies from 0-4000. The velocity field is computed using the accelerated method described in Section 3. The mean computed values of enstrophy Ω and turbulent kinetic energy E obtained from the definitions (3.22) are plotted as a function of $N_V \Gamma^2$ in Figure 3.3a. In both cases, the computational results collapse onto a single line, as predicted by (3.24) and (3.26). Since both enstrophy (and hence dissipation rate) and turbulent kinetic energy are proportional to the combination $N_V \Gamma^2 \ell / V$, the modeler is free to select N_V based on an alternative criterion and then to set Γ to obtain the desired turbulent kinetic energy.

There is a slight variation in the computational values of turbulent kinetic energy and enstrophy depending on the randomly-selected positions and orientations of the vortex structures. In order to characterize the amount of variation caused by the random character of the SVS algorithm, the turbulent kinetic energy and enstrophy calculations were repeated 10 times and the root-mean-square value was calculated for different values of the number of vortex structures, N_v, in the computational domain, with fixed value of $N_V \Gamma^2 = 2000$. The standard deviation and mean values of these results were obtained, the ratio of which yields the relative standard deviation σ_E / E and σ_Ω / Ω. A

plot of the relative standard deviations is shown in Figure 3.3b as functions of N_V. The standard deviations exhibit some variation with number of vortices for small values of N_V, but for $N_V \geq 64$ they are nearly independent of number of vortices. The standard deviation for turbulent kinetic energy is about 4-5% of the mean value, whereas that for enstrophy is only about 1% of the mean value. We note that this deviation is not a resolution error; since enstrophy is computed from the velocity gradients it is significantly more sensitive to resolution errors than is the kinetic energy field. Rather, the observed fluctuations arise from the variation in position and orientation of the vortices between the different configurations examined. Since the vorticity field is largely confined to the region within and immediately surrounding the vortex structures, it is reasonable that the relative standard deviation for enstrophy should be small, provided that the vortex structures do not overlap. The higher value of the relative standard deviation for turbulent kinetic energy arises from the fact that the velocity field at any point in the flow is dependent not only on its position relative to the nearest vortex structure, but rather on all vortex structures in the flow field.

The power spectrum $e(k)$ was examined for a series of computations with $N_V\Gamma^2 = 200$ and numbers of vortices of $N_V = 512$, 256, 128, 64, and 32, with values of Γ adjusted to give the specified product value. The spectrum lines fall on top of each other and cannot be distinguished, which confirms the prediction from (3.25) that the spectrum depends on N_V and Γ through the combination $N_V\Gamma^2\ell/V$. In Figure 3.4, we compare the SVS computational spectrum for the case with $N_V = 512$ to Saffman's approximate prediction (3.25). The theoretical expression is found to be significantly

higher than the SVS computational values, particularly for higher values of *k*. This result is likely due to the fact that Saffman assumed all vortices to be non-interacting, and so he simply added the kinetic energy of each vortex (associated with its own self-induced velocity) to obtain the total kinetic energy. In the computations, the vortex structure orientation is random, so the induced velocity from one structure will counter that from other structures at sufficiently large distances, thus reducing the total kinetic energy. Also shown in Figure 3.4 is a line indicating $k^{-5/3}$ dependence, which fits the computational plot reasonably well within the low-wavenumber inertial range, similar to the observations of Kivotides and Leonard (2003).

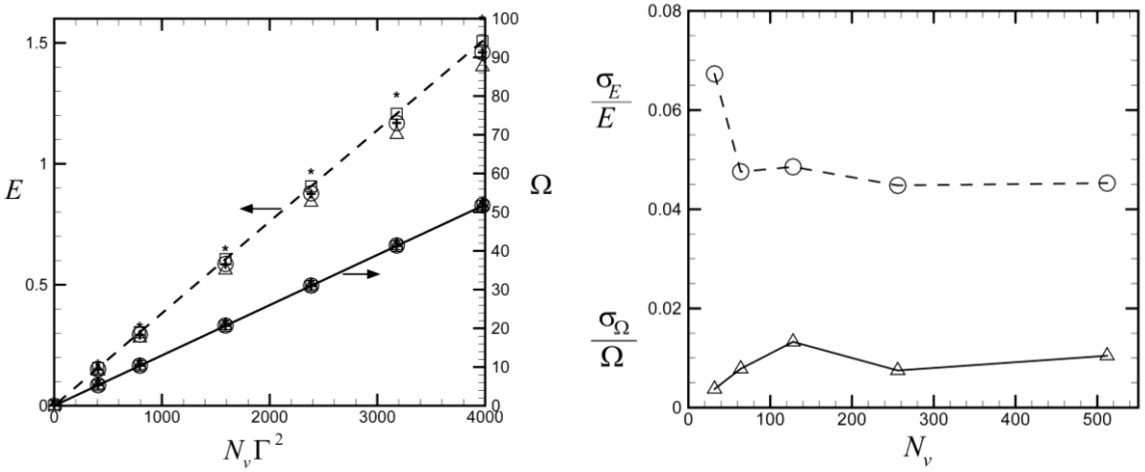

Figure 3.3. Plots showing (a) the mean enstrophy Ω (solid line, on the right-hand axis) and the turbulent kinetic energy *E* (dashed line, on the left-hand axis) as functions of the product $N_v\Gamma^2$ and (b) the relative root-mean-square enstrophy σ_Ω/Ω (solid line) and turbulent kinetic energy σ_E/E (dashed line) variation as functions of number of vortex structures (with $N_v\Gamma^2 = 2000$). Computations are for a case with $L = \ell_0 = 0.885$ and $\delta = 0.126$. The data in (a) are for $N_v = 512$ (squares), 256 (circles), 128 (triangles), 64 (plus signs), and 32 (asterisks), with Γ adjusted accordingly. The lines are best fits to the data.

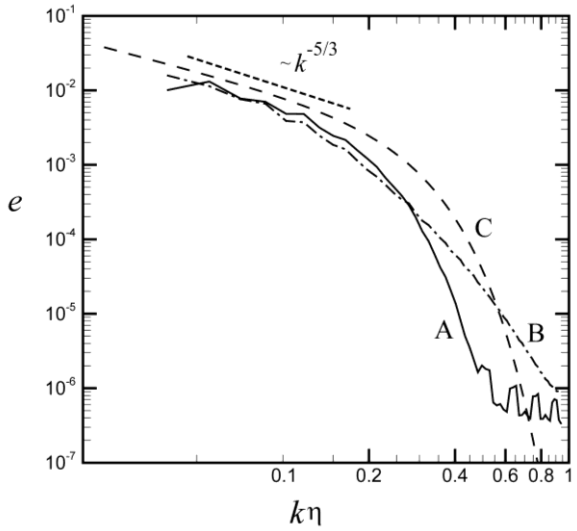

Figure 3.4. Power spectrum from an SVS computation with $N_V\Gamma^2 = 200$ and $N_V = 512$ (solid line, A), compared to a computational result from DNS (dashed-dotted line, B) and the theoretical result Eq. (3-25) from Saffman (1997) (dashed line, C). Also shown is a straight line indicating $k^{-5/3}$ dependence in the inertial range (short dashed line).

The SVS predictions are compared in Figure 3.4 to the results of a pseudo-spectral direct numerical simulation (DNS) computed on a 128^3 grid, similar to that presented by Vincent and Meneguzzi (1991). The flow is initiated by a randomly perturbed velocity field with uniform probability distribution for wavenumbers spanning the interval $1 \le k \le 64$. Dealiasing is performed by setting the coefficients of the highest 1/3 wavenumber coefficients to zero using a spherical filter. A preliminary computation is run without forcing until time $t = 10$ in order to allow the turbulence to develop a range of length scales characteristic of statistically stationary homogeneous isotropic turbulence. The computation is then restarted with non-zero forcing, where the transform of the forcing vector is assumed to be proportional to the fluid velocity transform, such that (Lundgren, 2003; Rosales & Meneveau, 2005)

$$\hat{\mathbf{f}} = \begin{cases} C\hat{\mathbf{u}} & \text{for } k < k_{crit} \\ 0 & \text{for } k > k_{crit} \end{cases}, \tag{3-27}$$

where the coefficient C is adjusted at each time step so as to maintain approximately constant turbulent kinetic energy. The current computations are performed with $k_{crit} = 5$, so that the forcing acts only on the large-scale eddies. Various parameter values characterizing the DNS computations are given in Table 3.2. The spectrum predicted by the DNS computations compares well with the SVS predictions for low values of wavenumber ($k < 20$), but for high wavenumber the SVS spectrum decays much more quickly than does the DNS results. This rapid decay at high wavenumber is consistent with the fact that the vortex radius for these computations was specified to be eight times larger than the Kolmogorov length scale, so the SVS flow field has little energy at very small length scales.

Table 3.2. Scaling variables charaterizing the fluid turbulence.

Turbulent kinetic energy, q	0.14	Taylor microscale, λ	0.27
Mean dissipation rate, $\langle\varepsilon\rangle$	0.016	Microscale Reynolds number, Re_λ	81
Kinematic viscosity, ν	0.001	Integral length, ℓ_0	0.89
Kolmogorov length, η	0.016	Integral time, T_ℓ	2.9

The velocity probability density function (PDF) in one coordinate direction (x-direction), normalized by the root-mean-square value, was computed for a series of SVS computations with $N_V\Gamma^2 = 3975$ and different number of vortex structures. Unlike the power spectrum, the velocity PDF exhibits significant variation with value of N_V. This observation indicates that the velocity PDF varies with N_V and Γ independently, and not

only through the product $N_V \Gamma^2$. The PDF has a fat tail for low values of N_V, typical of a superstatistical system (Beck, 2008), but the PDF functions for large values of N_V (greater than about 500) approach an asymptotic curve that is nearly Gaussian. In Figure 3.5a, a comparison is shown of the velocity PDF for the case with $N_V = 512$, a DNS simulation (symbols), and a best-fit Gaussian curve $p(v) = 0.8\exp(-0.5v^2)$, where $v \equiv v_x / v_{x,rms}$. The DNS results are in close agreement with the Gaussian function, as expected (Voth et al., 1998). The SVS predictions fit well to the Gaussian function for $v_x / v_{x,rms} < 3$, but for higher values of v_x they exhibit higher values. This difference indicates that while still very rare, high velocity occurrences are more common for the SVS computations than for the DNS simulations.

The PDF of the *x*-component of the fluctuating fluid acceleration field is plotted in Figure 3.5b. Fluid acceleration is computed from the SVS or DNS velocity field for post-processing purposes using a centered difference approximation in space and a forward difference in time. We again find that the PDF plot is sensitive to the value of N_V, but that it approaches an asymptotic curve for values of N_V greater than about 500. The SVS prediction for the case with $N_V = 512$ is compared to the DNS results in Figure 3.5b. Also shown in this figure is the empirical expression for the PDF

$$p(a) = 1.8\exp\left[-a^2 / \{(1+|ac_1 / c_2|^{c_3})c_2^2\}\right], \tag{3-28}$$

obtained experimentally by La Porta et al. (2001). In this expression, $a \equiv a_x / a_{x,rms}$, and the coefficients are given by a best fit to La Porta et al.'s experimental data as $c_1 = 0.539$, $c_2 = 1.588$, and $c_3 = 0.508$. The SVS prediction for acceleration PDF with $N_V = 512$ is

found to agree closely with both the DNS prediction and with the experimental correlation (3.28), and in all cases the acceleration PDF exhibits non-Gaussian statistics characterized by fat tails, typical of a highly intermittent signal. Mordant et al. (2004) associates the acceleration intermittency in turbulent flows with the presence of coherent vortex structures, so agreement between the SVS and DNS simulations for the acceleration PDF is another indication that the coherent vortices are correctly modeled in the SVS representation.

The PDF of the vorticity component ω_x is plotted in Figure 3.6 from SVS results with $N_v = 2048$ vortex structures in the computational domain. The vorticity is determined by first computing the synthetic turbulence velocity field, as discussed in Section 3.3, and then numerically differentiating using a centered finite-difference method to obtain vorticity from $\boldsymbol{\omega} = \nabla \times \mathbf{u}$. The PDF for vorticity is sensitive to the number of vortex structures used for the SVS computations, and because the vorticity is evaluated using a velocity gradient it required a somewhat larger number of vortices to reach the asymptotic state for large vortex numbers than did the velocity or acceleration PDFs. The SVS vorticity PDF is shown in Figure 3.6 to be in excellent agreement with the vorticity PDF obtained from the DNS predictions.

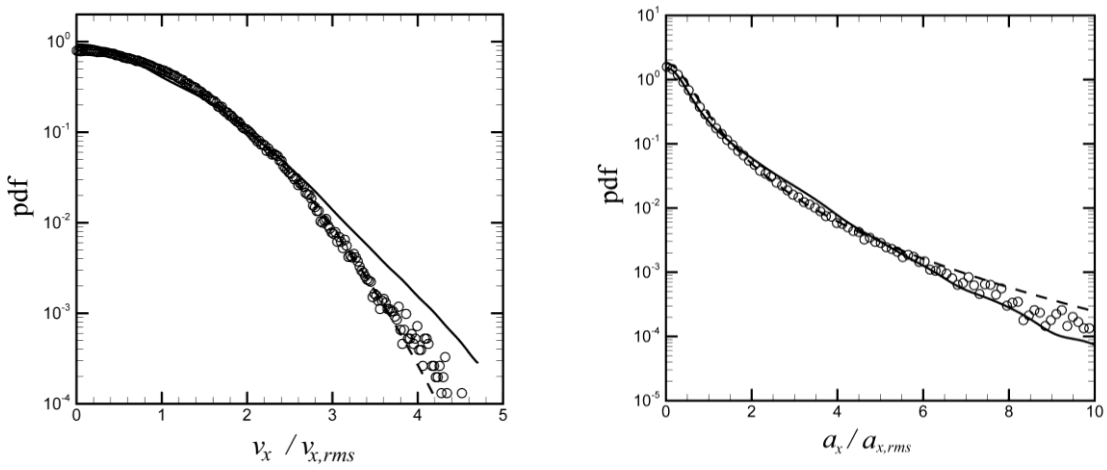

Figure 3.5. Plots showing the PDF of the *x*-component of (a) velocity and (b) acceleration. (a) Comparison of PDF for SVS computation with $N_v = 512$ (solid line), DNS (symbols), and a best-fit Gaussian curve (dashed line). (b) Comparison of PDF for SVS computation with $N_v = 512$ (solid line), DNS (symbols), and the experimental correlation (3-28) of La Porta et al. (2001) (dashed line).

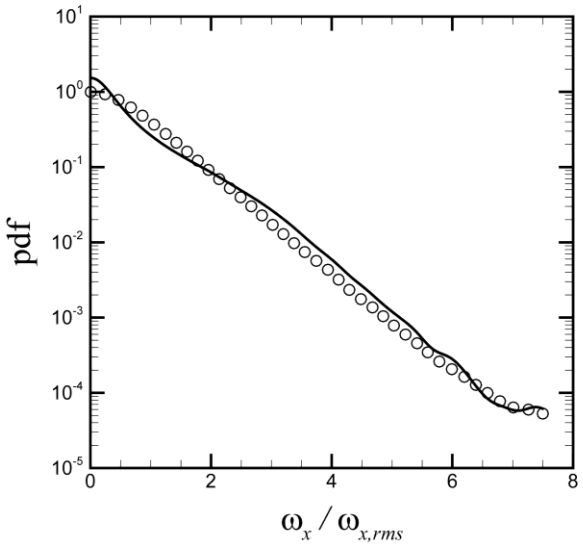

Figure 3.6. Plot comparing the PDF of the *x*-component of vorticity from SVS simulations (solid line), with $N_V \Gamma^2 = 350$ and $N_v = 2048$, and DNS results (symbols).

3.5. Validation of SVS Predictions for Particle Collision Rate

The SVS predictions for particle interactions were validated by comparison to DNS results with use of a soft-sphere discrete-element method (DEM) simulation for a set of N_p colliding non-adhesive particles of diameter *d* and mass *m*. The computations solve the momentum and angular momentum equations for the particle velocity and rotation rate, given by

$$m\frac{d\mathbf{v}}{dt} = \mathbf{F}_F + \mathbf{F}_A, \qquad I\frac{d\boldsymbol{\Omega}}{dt} = \mathbf{M}_F + \mathbf{M}_A, \tag{3-29}$$

subject to forces and torques induced by the fluid flow ($\mathbf{F}_F$ and $\mathbf{M}_F$) and by the particle collision and adhesion ($\mathbf{F}_A$ and $\mathbf{M}_A$). Here, *I* is the moment of inertia, and **v** and **Ω** are the particle velocity and rotation rate, respectively. The dominant fluid force is the particle drag force, but we also accounted for secondary forces including the Saffman and Magnus lift forces and the added mass and pressure gradient force on the particles. Particle Reynolds numbers were small, allowing use of the Stokes drag law and low Reynolds number lift laws (Saffman, 1965, 1968; Rubinow and Keller, 1961). Collisions were detected when the distance between two particles is less than the particle diameter. Collision forces between the particles include the normal elastic and dissipative forces, sliding resistance, and twisting resistance. Particle normal collision was computed for non-adhesive particles using the nonlinear Hertz (1882) theory for normal elastic force, the Tsuji et al. (1992) model for normal dissipative force, and the Cundall and Strack (1979) model for sliding resistance. The fluid velocity was interpolated from a 128^3 fluid grid onto the Lagrangian particle locations with cubic accuracy using the M4' variation of the B-spline interpolation method, which was originally developed by Monaghan

(1985a) and is commonly used in spherical particle hydrodynamics (Monaghan, 1985b) and for regridding in vortex methods (Cottet and Koumoutsakos, 2000). The multiple-time step algorithm of Marshall (2009) was used with three different time step levels, corresponding to the fluid, particle and collision time scales, arranged from largest to smallest. The reported computations used a fluid time step of $\Delta t = 0.01$ for a duration of 10,000 time steps. The DNS runs were initiated using a preliminary computation without particles with 5000 time steps to establish a statistically-steady turbulent flow. Simulations were performed on a cubic grid with 2π side length and 46,656 particles.

A listing of integral flow measures for the different cases examined in this comparison is given in Table 3.3. The number of vortices was varied from $N_V = 32$ to 2048 in the SVS runs SVS-1a through SVS-1g in order to examine the effect of number of vortices on the collision results, and in each case the value of vortex circulation was adjusted to maintain nearly constant turbulent kinetic energy. The computations were performed for values of the integral-scale Stokes number St_0 of 0.07, 0.34, and 1.7, where St_0 is defined by (3.1) with $u_\ell = u_0$ and $\ell = \ell_0$. The corresponding values of the Kolmogorov-scale Stokes number St_K for these three cases are 0.81, 3.94, and 19.9, respectively. A filtered DNS computation (DNS-F) was also performed in which the coefficients of the highest 67% of the wavenumbers ($k > 21.3$) was set to zero, which yields an energy spectrum very close to the SVS spectrum. The filtered DNS run is used as a method to determine the influence of small-scale fluctuations on the particle collisions. Beside kinetic energy, integral measures listed in Table 3.3 include enstrophy Ω, a vorticity magnitude measure ω_{95}, and a stretching rate measure *S*. The vorticity

magnitude measure ω_{95} is defined as the value of vorticity magnitude for which 95% of the grid points have a lower vorticity magnitude. The stretching measure *S* is defined as the average over the flow field of the maximum value of the logarithmic stretching rate $\lambda_1 = \dot{\Lambda} / \Lambda$. Here, Λ is the stretch of a material line segment along the principal direction of the rate of deformation tensor **D** associated with the largest eigenvalue λ_1 of **D**. Since **D** is symmetric, the eigenvalues of **D** can be efficiently computed using the Smith algorithm (Smith, 1961). The enstrophy for the filtered DNS run (DNS-F1) is about twice the value for the associated SVS run (SVS-1), and the enstrophy for the unfiltered DNS run (DNS-1) is about 20% higher than that for the filtered DNS run due to the contribution of the small vortices filtered out in the DNS-F1 run. In accordance with the result (3.24), the enstrophy remains nearly constant in the SVS runs (SVS-1a through SVS-1g) as the number of vortices is changed with $N_V \Gamma^2$ held constant. The vorticity magnitude parameter ω_{95} is about 40% larger and the stretching measure *S* is about 15% larger for the DNS run compared to the SVS-1a run.

Table 3.3. List of parameter values and resulting particle collision kernel α_{11} for runs validating SVS prediction of turbulent particle collision rate. The runs indicated by DNS-F are a filtered version of the DNS runs with the Fourier coefficients set to zero for the highest 67% of the wavenumbers.

Run	Number of Vortices, N_V	Stokes Number, St_0	Turbulent Kinetic Energy, E	Enstrophy, Ω	Vorticity Strength Parameter, ω_{95}	Stretching Measure, S	Collision Kernel, $\alpha_{11}\,(\times 10^{-4})$
DNS-1	**NA**	**0.34**	**0.122**	**9.80**	**5.29**	**1.49**	**3.92**
DNS-F1	NA	0.34	0.122	8.13	4.83	1.47	3.82
SVS-1a	2048	0.34	0.111	4.06	3.66	1.29	3.27
SVS-1b	1024	0.34	0.113	4.09	3.89	1.27	3.40
SVS-1c	512	0.34	0.117	4.04	3.63	1.20	3.40
SVS-1d	256	0.34	0.113	4.05	2.89	1.09	3.39
SVS-1e	128	0.34	0.108	4.04	1.94	0.97	3.37
SVS-1f	64	0.34	0.112	4.03	1.37	0.82	3.21
SVS-1g	32	0.34	0.122	4.04	1.12	0.69	2.90
DNS-2	**NA**	**0.07**	**0.122**	**9.80**	**5.29**	**1.49**	**0.709**
DNS-F2	NA	0.07	0.122	8.13	4.83	1.47	0.680
SVS-2a	2048	0.07	0.115	4.06	3.66	1.29	0.714
SVS-2b	1024	0.07	0.113	4.10	3.89	1.27	0.705
SVS-2c	512	0.07	0.117	4.04	3.63	1.20	0.670
DNS-3	**NA**	**1.7**	**0.122**	**9.80**	**5.29**	**1.49**	**61.5**
DNS-F3	NA	1.7	0.122	8.13	4.83	1.47	61.0
SVS-3a	2048	1.7	0.115	4.06	3.66	1.29	60.5
SVS-3b	1024	1.7	0.113	4.10	3.89	1.27	60.5
SVS-3c	512	1.7	0.117	4.04	3.63	1.20	60.5

The total number of collisions was found to increase almost linearly with time, and the slope of this line was used to compute the collision rate per unit volume $\dot{n}_C$. From this value, the collision kernel α_{11} was computed using the definition

$$\dot{n}_C = \frac{1}{2}\alpha_{11} n^2, \tag{3-30}$$

where $n = N_p / V$ is the number of particles per unit volume. The predicted value of α_{11} for each case was computed from (3.30) using the specified value of n and the computed value of $\dot{n}_C$ based on a linear fit to the total number of collisions, and the resulting values

of collision kernel are listed in Table 3.3. A comparison of the collision kernels between the full DNS, the filtered DNS, and the SVS method was conducted for integral-scale Stokes numbers of St_0 = 0.07, 0.34, and 1.7, where the Stokes number is changed by modification of the particle diameter. As predicted by collision theory (Saffman and Turner, 1956; Abrahamson, 1975), the collision kernel increases with particle diameter (indicated by increasing Stokes number), with DNS predictions of $\alpha_{11} = 5.8 \times 10^{-5}$, 3.26×10^{-4} and 6.45×10^{-3} for St_0 = 0.07, 0.34, and 1.7, respectively. The filtered DNS predictions for collision kernel are within about 4% of the full DNS predictions for each case, indicating that the small scales of the turbulent motion have little effect on the collision coefficient. The collision kernel for the SVS model with 2048 vortices was about 16% lower than the full DNS prediction for the St_0 = 0.34 case, and the SVS model predictions for α_{11} were within 0.8% and 5.7% of the full DNS predictions for the St_0 = 0.07 and 1.7 cases, respectively. The effect of number of vortex structures on the SVS predictions was examined by repeating the run for St_0 = 0.34 with 32, 64, 128, 256, 512, 1024 and 2048 vortices, while at the same time adjusting the vortex strength to keep the kinetic energy approximately constant.

The tendency of particles to cluster can be characterized by the radial distribution function (RDF), $g(r)$, defined by

$$g(r) = \frac{1}{4\pi\rho_0 r^2}\frac{dN}{dr}, \tag{3-31}$$

where the average number of particles per unit volume ρ_0 is related to the particle volume fraction C_p by $\rho_0 = 6C_p/\pi$, and $N(r)$ is the average number of neighboring

particles whose centroids are located within a radial distance r from a given particle centroid. The value of $g(r)$ is estimated by counting for each particle the number of neighboring particles that fall into a set 400 spherical bins, each of width $\Delta r = 0.00015$, surrounding the given particle. The number of particles in each bin is averaged over all particles in the computational domain and over 1000 time steps near the end of the computations in order to smooth the distribution. Figure 3.7 shows a comparison of the RDF for both a DNS computation (DNS-1) and SVS with $N_V = 2048$ vortex structures (SVS-1a) at an integral Stokes number $St_0 = 0.34$, which are observed to exhibit close agreement.

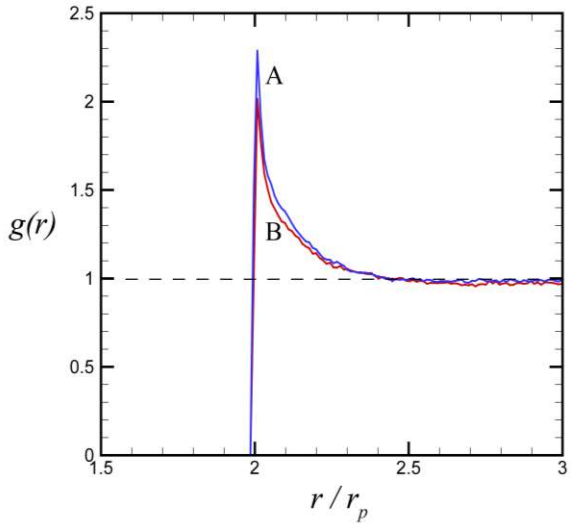

Figure 3.7. Comparison of the radial distribution function as a function of radius at $St_0 = 0.34$ for a SVS computation (SVS-1a) with $N_v = 2048$ vortex structures (A, blue line) and a DNS computation (DNS-1) (B, red line).

As noted by Zaichik et al. (2006), the collision kernel is proportional to the product of the radial distribution function $g(r)$ (RDF) and the relative radial velocity $\langle w_r \rangle$ (RRV) evaluated at collision ($r = 2r_p$). Each of these quantities was separately

computed for cases with different Stokes number to examine the individual quantities that make up the collision kernel. A set of plots is given in Figure 3.8 showing RDF and RRV at collision as a function of the Kolmogorov-scale Stokes number St_K for both DNS results and SVS results with $N_V = 2048$ vortices. Our predictions are compared to the DNS results for RDF and RRV of Fayed and Ragab (2013) for $\mathrm{Re}_\lambda = 77$ and of Wang et al. (2000) for $\mathrm{Re}_\lambda = 75$, and to the DNS results for RDF of Sundaram and Collins (1997) for $\mathrm{Re}_\lambda = 54$. The RDF value for $St_K = 19.9$ is nearly the same in the SVS and DNS predictions, and so the two symbols for DNS and SVS results are almost coincident in Figure 3.8a. The RDF exhibits a very thin peak near the collision point for small Stokes number, which contributes to the high data variability in Figure 3.8a. Both the DNS and SVS predictions in Figure 3.8 are in reasonable agreement with each other and with literature values.

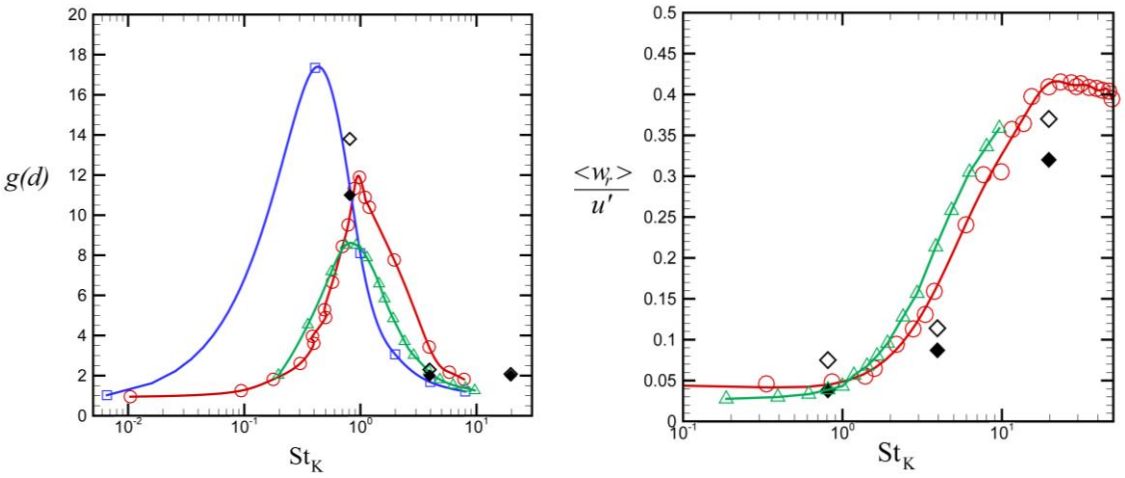

Figure 3.8. Plot showing (a) radial distribution function (RDF) and (b) relative radial velocity (RRV) at collision as functions of the Kolmogorov Stokes number St_K. Plots show DNS data of Wang et al. (2000) at $\mathrm{Re}_\lambda = 75$ (circles, red line), DNS data of Sundaram and Collins (1997) for $\mathrm{Re}_\lambda = 54$ (squares, blue

line), DNS data of Fayed and Ragab (2013) for $\mathrm{Re}_\lambda = 77$ (deltas, green line), and our DNS predictions (filled diamonds) and SVS predictions (open diamonds) for $\mathrm{Re}_\lambda = 81$.

3.6. Validation of SVS Predictions for Turbulent Particle Agglomeration

Computations to examine turbulent agglomeration were conducted with a similar DEM algorithm as described in the previous section, but with modification of the collision force and torque models to account for adhesion effects. In particular, the normal elastic and adhesive van der Waals force was computed using the model of Johnson, Kendall and Roberts (1971) (i.e., the JKR model). Adhesion introduces a strong rolling resistance torque, for which we used the model of Dominik and Tielens (1995), along with experimental results of Ding et al. (2008) to set the critical angle for onset of particle rolling. The effect of adhesion on the sliding resistance was modeled using an expression derived by Thornton (1991). We also included a crowding correction term for the particle drag force developed by Di Felice (1994). A comprehensive summary of the computational method for both adhesive and non-adhesive particles is given by Marshall (2009). The reported computations used a fluid time step of $\Delta t = 0.005$ for a duration of 20,000 time steps, with a total of 46,656 particles. As discussed in the previous section, the DNS runs were initiated using a preliminary computation without particles with 5000 time steps to establish a statistically-steady turbulent flow.

A particle agglomerate constitutes a set of particles which are bonded to each other, either directly or via other intermediate particles of the agglomerate, via soft (e.g., van der Waals) bonds. A set of particles bonded via hard bonds (e.g., sintered particles) is referred to as an aggregate, and is outside the scope of this paper. Agglomerate development in the turbulent flow field is characterized in the current paper using two

dimensionless parameters – the Stokes number St and the adhesion parameter Ad. The adhesion parameter Ad is a ratio of adhesive force to particle inertia, defined by the ratio

$$\mathrm{Ad}_\ell = \frac{\gamma}{\rho_p u_\ell^2 r_p}, \tag{3-32}$$

where the adhesive surface energy density γ is equal to half the work required to separate two surfaces that are adhesively bound per unit surface area. Both the Stokes number in (3.1) and adhesion parameter were defined using the characteristic length scale ℓ_0 and velocity scale u_0 of the turbulence integral scale for the fluid length and velocity scales ℓ and u_ℓ, which is indicated by a subscript '0'.

Plots showing SVS predictions for the total number of particles contained in an agglomerate, N_{tot}, and the average number of particles per agglomerate, N_{pagg}, as functions of time are given for a case with $\mathrm{St}_0 = 0.34$ and $\mathrm{Ad}_0 = 11$ in Figure 3.9 for different values of the number of vortex structures, N_V, ranging from 128 to 2048. The vortex strength is adjusted to maintain a constant turbulent kinetic energy in each case. While the collision kernel listed in Table 3.3 approaches a nearly constant value for N_V of about 128 and greater, the agglomeration measures shown in Figure 3.9 continue to exhibit significant dependence on vortex number up to about $N_V = 512$. The DNS predictions, indicated by the heavy dashed line in Figures 3.9a and b, are found to be in excellent agreement with the limiting value of the SVS predictions for large N_V.

The run shown in Figure 3.9 was extended to a time of $t = 250$ to examine the continued agreement between SVS and DNS as the equilibrium condition is reached. The average number of particles per agglomerate is plotted versus time for this extended run

in Figure 3.10, showing that the SVS run (with $N_V = 2048$) and DNS continue to exhibit reasonable agreement at long time. The value of the average number of particles per agglomerate fluctuates in time when this statistical equilibrium state is reached due to breakup and recollision of large agglomerates.

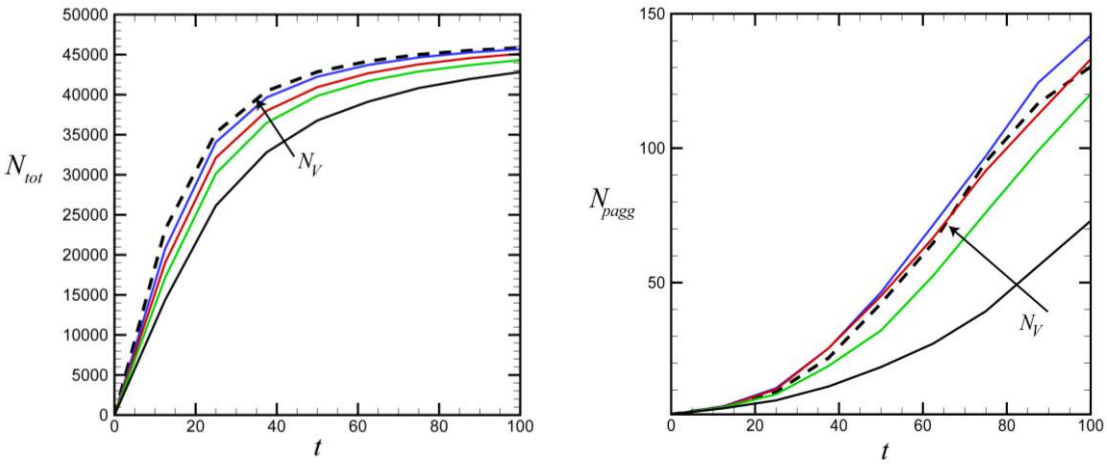

(a) (b)

Figure 3.9. Effect of number of vortex structures on turbulent agglomeration for SVS runs with St_0 = 0.34 and Ad_0 = 11, where all runs have the same value of turbulent kinetic energy. The plots show (a) the total number of particles contained in agglomerates N_{tot} and (b) the average number of particles per agglomerate N_{pagg} as functions of time. Plots are given for different numbers of vortex structures, with $N_v = 128$ (black line), 256 (green line), 512 (red line), and 2048 (blue line). The DNS results are indicated using a dashed line.

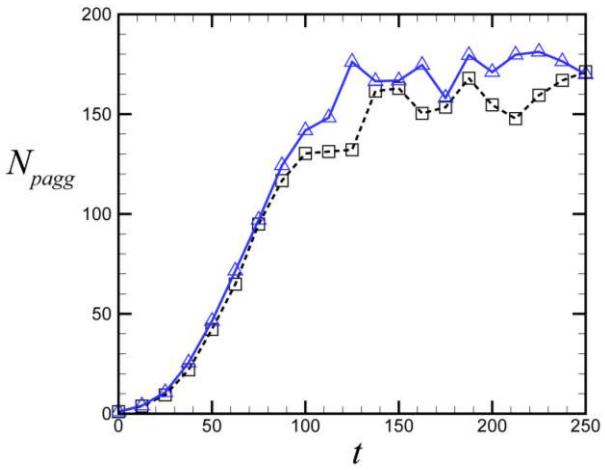

Figure 3.10. Plot showing average number of particles per agglomerate over a long run time leading to a statistical equilibrium condition, for SVS with $N_V = 2048$ (blue curve) and DNS (dashed curve).

The effect of Stokes number is shown in Figure 3.11, which compares SVS predictions with $N_V = 2048$ vortex structures and DNS predictions for values of the Stokes number of $St_0 = 0.1$, 0.2 and 0.34, in all cases with $Ad_0 = 11$. The different Stokes numbers are produced by changing the particle diameter, with all other parameters held constant. Plots are given both for the average number of particles per agglomerate, N_{pagg}, and for the total number of agglomerates, N_{agg}, as functions of time. The value of N_{pagg} decreases rapidly with decrease in St_0, going from $N_{pagg} = 130$ at $t = 100$ for $St_0 = 0.34$ to $N_{pagg} = 10$ for $St_0 = 0.1$. The peak value of the number of agglomerates is shown in Figure 3.11b to be nearly the same for the three cases, but the peak occurs at a later time as the Stokes number decreases. The observed differences in agglomeration measures with change in St_0 are primarily due to decreasing collision rate as the Stokes number decreases, which is consistent with theoretical predictions for collision rate at both small and large Stokes numbers (Saffman and Turner, 1956; Abrahamson, 1975). Good agreement is observed between the SVS and DNS predictions.

The effect of adhesion parameter is examined in Figure 3.12, which compares SVS predictions with $N_V = 2048$ vortex structures and DNS predictions for values of the adhesion parameter of Ad_0 = 5.5, 11, 28 and 110, in all cases with St_0 = 0.34. The different adhesion parameter values are produced by changing the adhesion surface energy density γ, with all other parameters held constant. As expected, the average number of particles per agglomerate decreases in Figure 3.12a with decrease in Ad_0. The total number of agglomerates in Figure 3.12b is found to peak at nearly the same time for the different values of Ad_0, but to then decrease rapidly after the peak value for high values of Ad_0, indicating that agglomerates are colliding to form larger agglomerates. For Ad_0 = 5.5, the number of agglomerates decreases slowly after the peak since colliding agglomerates might not adhere to each other or might breakup again into smaller agglomerates. Again, good agreement is observed between the SVS and DNS predictions.

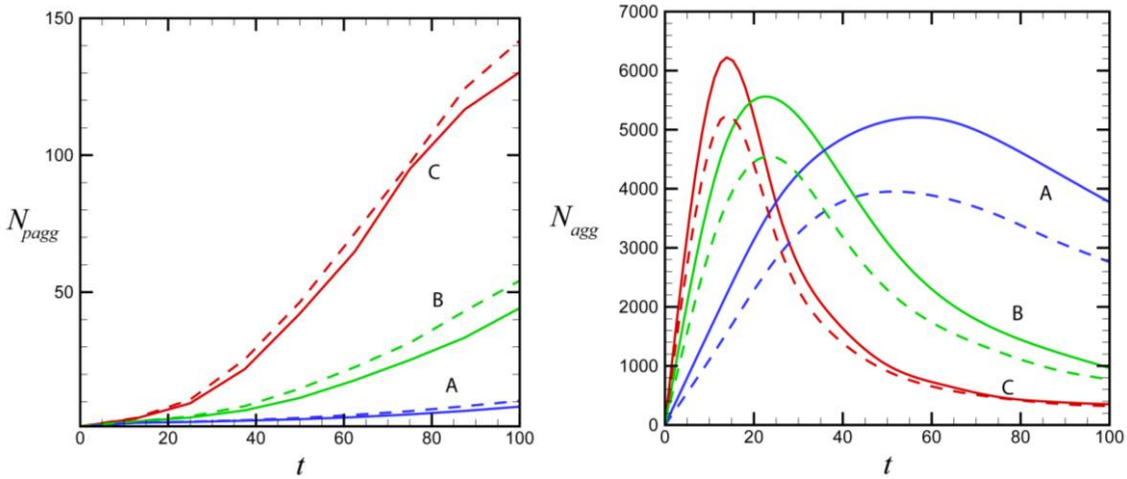

Figure 3.11. Effect of Stokes number on (a) number of particles per agglomerate (N_{pagg}) and (b) number of agglomerates (N_{agg}) for DNS computations (solid lines) and SVS computations (dashed lines) with $N_V = 2048$ vortex structures. Computations are for St_0 = 0.1 (A, blue), 0.2 (B, green) and 0.34 (C, red), with Ad_0 = 11.

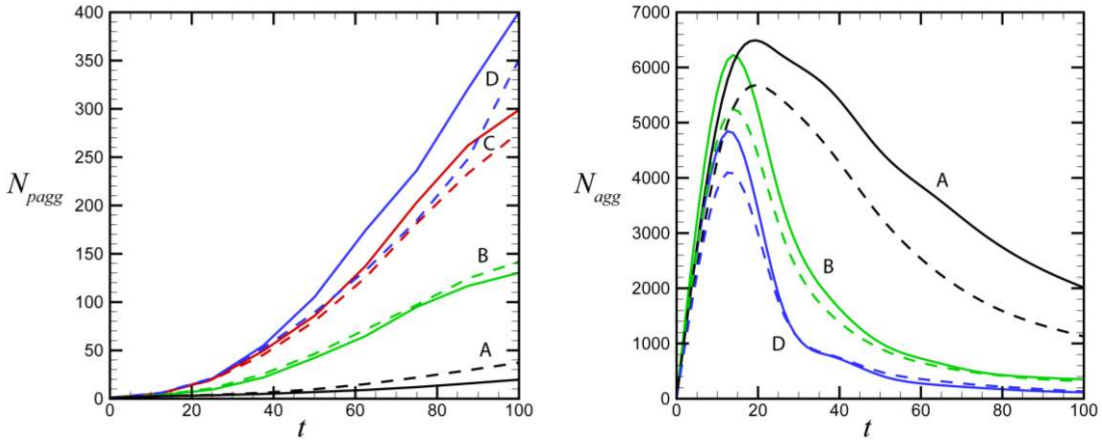

Figure 3.12. Effect of adhesion parameter on (a) number of particles per agglomerate (N_{pagg}) and (b) number of agglomerates (N_{agg}) for DNS (solid lines) and SVS computations (dashed lines) with $N_V = 2048$ vortex structures. Computations are for Ad_0 = 5.5 (A, black), 11 (B, green), 28 (C, red), and 110 (D, blue), with St_0 = 0.34. The C and D lines in (b) are nearly coincident, so only the D line is shown.

The *agglomerate number distribution* indicates the percentage of agglomerating particles contained in agglomerates consisting of *n* particles. The agglomerate number distribution is sorted into logarithmic bins of base 2, where the value of bin size indicates the nominal number of particles in agglomerates within the bin. A plot showing the agglomerate number distribution for a case with St_0 = 0.34 and Ad_0 = 11 is shown in Figure 3.13. SVS predictions with $N_V = 2048$ vortex structures are observed to yield a number distribution that is reasonably close to that obtained using DNS.

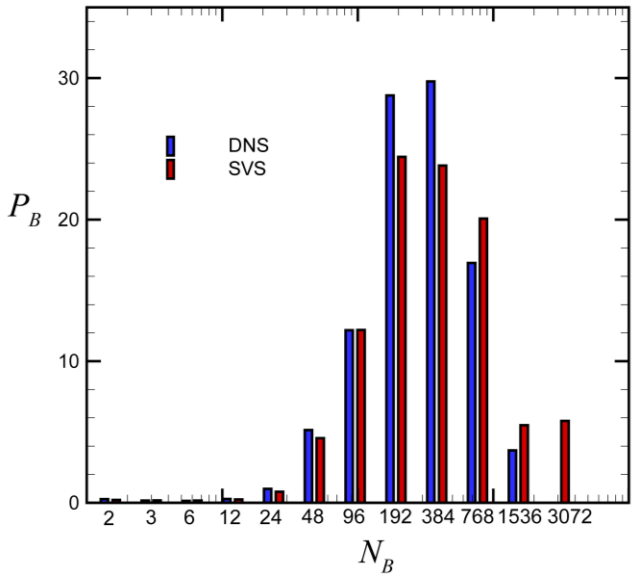

Figure 3.13. Plot showing the percentage of particles, P_B, contained in agglomerates with different numbers of particles. The number of particles in the agglomerate are grouped logarithmically into bins, with average number of particles for the given bin indicated by N_B. The plot compares DNS results (blue bars) with SVS results (red bars) for a case with $N_V = 2048$ vortex structures.

Each agglomerate is characterized by the number of particles N contained in the agglomerate and the radius of gyration R_g, which is defined by

$$R_g = \left[\frac{1}{N} \sum_{i=1}^{N} \left| \mathbf{x}_i - \bar{\mathbf{x}} \right|^2 \right]^{1/2}. \tag{3-33}$$

In this equation, $\bar{\mathbf{x}}$ denotes the position vector of the agglomerate centroid and $\mathbf{x}_i$ is the centroid of the i^{th} particle within the agglomerate. It is well known that particle agglomerates admit a power law relating N and R_g given by (Adachi and Ooi, 1990; Liu et al., 1990; Jiang and Logan, 1991)

$$N = K\left(R_g / d\right)^D, \tag{3-34}$$

where K is a coefficient (called the fractal pre-factor) and the exponent D is called the fractal dimension of the agglomerate. The value of D varies over the interval $1 \le D \le 3$

depending on the agglomeration formation mechanism (Brasil et al., 2001). For instance, Eggersdorfer et al. (2011) cites typical values of $D = 2.5$ for diffusion-limited agglomeration, $D = 3.0$ for ballistic particle-cluster agglomeration, and $D = 1.8$ for diffusion-limited cluster-cluster agglomeration. For turbulent agglomeration of latex particles in stirred tanks, Selomulya et al. (2001) report values of D between 1.7 and 2.1 and Waldner et al. (2005) report values of D between 1.8 and 2.6. A log-log plot of N versus R_g / d for both DNS results and SVS predictions with $N_V = 2048$ is shown in Figure 3.14. The DNS and SVS predictions are in excellent agreement, and both are found to exhibit a best-fit line with slope $D = 2.3$. As discussed above, this value of fractal dimension of the particle agglomerates is in good agreement with values noted in previous experimental literature for turbulent agglomeration.

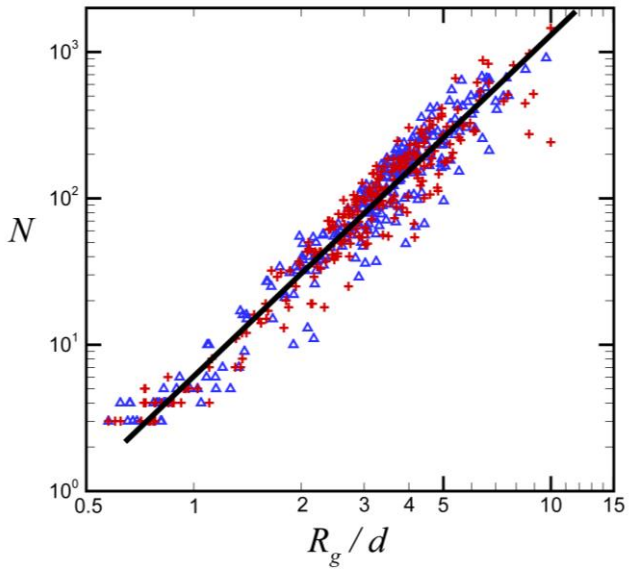

Figure 3.14. Plot showing the number of particles in an agglomerate N versus the ratio of the gyration radius to the primitive particle diameter, R_g / d, with both DNS data (triangles, blue) and SVS data with $N_V = 2048$ (crosses, red). The solid line is a best-fit to the data with a slope of $D = 2.3$.

3.7. Conclusions

An accelerated form of the stochastic vortex structure (SVS) method for subgrid-scale turbulence modeling for interacting particles was developed using the method of multipole expansions. It was shown that with only five box levels, the accelerated method can reduce the velocity computation time by two orders of magnitude, with error in the total turbulent kinetic energy (TKE) prediction of less than 2%. The effect of the stochastic nature of the SVS algorithm on prediction of mean quantities was examined, and it was found that the ratio of the standard deviation to the mean value obtained from repeated runs with different vortex positions and orientations was about 5% for TKE and 1% for enstrophy. Characteristics of the SVS synthetic turbulence predictions were examined against results of direct numerical simulation (DNS) and various theoretical and experimental results from the literature. The predicted energy spectrum was compared against both DNS results and approximate theoretical results from Saffman (1997), and shown to be in reasonable agreement with both for moderate and small values of wavenumber (less than about 20), but (as expected) to give too low values for higher wavenumbers. The predicted velocity, acceleration and vorticity probability density functions (PDFs) were found to be sensitive to the number of vortex structures used, but to approach the DNS predictions for large number of vortex structures. SVS predictions for other integral measures, such as the ω_{95} measure of the maximum vorticity magnitude and the average stretching rate measure, also exhibit good agreement with DNS.

Though the validation of the statistical properties of SVS-generated fields is encouraging, the ultimate arbiter of the robustness of this model is whether or not it

achieves the ultimate modeling objectives. To this end, simulations with colliding, non-adhesive particles were performed comparing the SVS predictions for radial distribution function, relative radial velocity, and collision kernel to DNS results. Computations were performed for an integral scale Stokes number range of 0.07 – 1.7, yielding good agreement between SVS and DNS predictions. The simulations indicate that the SVS results for collision rate are not very sensitive to the number of vortex structures as long as this number is sufficiently large. DNS and SVS simulations were also performed for collision and agglomeration of adhesive particles over a range of Stokes number and adhesion parameter values. Agglomeration measures examined include total number of particles captured in agglomerates, number of agglomerates, average number of particles per agglomerate, number distribution of agglomerates, and agglomerate fractal dimension. Values of these agglomeration measures were found to approach values close to those of the DNS predictions for sufficiently high numbers of vortex structures.

The paper suggests that the stochastic vortex structure method provides a rapid, reliable approach for modeling subgrid-scale turbulence fluctuations for flows with interacting particles. The SVS method is consistent with the large-scale energy spectrum and the various probability density function curves that describe homogeneous turbulence, as well as with a wide range of integral measures of the turbulent flow. The speed-up in velocity field computation introduced in the current version of the SVS method makes this approach highly efficient compared to other synthetic turbulence approaches. Because the SVS method deals directly with the vortical structures that dominate the large-scale motion of the turbulence, it allows accurate prediction of

phenomena, such as particle clustering, that are dependent on the structural form of the turbulent eddies.

We note that the current validation study was conducted for a relatively low Reynolds number flow for which the integral-scale Stokes number was close to unity. For high Reynolds number turbulence, there exists a large range of scales between the integral scale and Kolmogorov scale. A study using the wavelet-based coherent vortex simulation approach by Nejadmalayeri et al. (2013) found that the number of energy-containing structures at a fixed kinetic energy level increases linearly with Reynolds number in homogeneous turbulence. While the SVS method has not yet been tested for high Reynolds numbers for purposes such as prediction of particle collision rate, we speculate that it may not be necessary to cover the entire range of these length scales with the synthetic turbulent flow. Rather, it might be sufficient to introduce SVS structures only for a length scale ℓ for which the eddy Stokes number St_ℓ is closest to unity. Eddy structures much larger than this scale ℓ will simply advect the particles with minimal relative motion between the particles, and the fluctuations associated with eddies much smaller than ℓ will be filtered out by the particle inertia. However, we also recall that several experimental and computational studies have observed that intense vortex structures are less prominent for high Reynolds number turbulence (with $\mathrm{Re}_\lambda \geq O(1000)$) than is the case at low Reynolds numbers (Belin et al., 1996; Ishihara et al., 2009). The potential effectiveness of vortex-based methods such as SVS at high turbulent Reynolds numbers will therefore need to be carefully assessed in future work.

Acknowledgement

This research was supported by the U.S. National Science Foundation under grant CBET-1332472.

Appendix

Substituting (3.4) into the Biot-Savart equation (3.6) gives the induced velocity at a point **x** as

$$\mathbf{u}(\mathbf{x},t) = -\frac{1}{4\pi}\int_V \frac{\mathbf{s}\times\boldsymbol{\omega}^*(\mathbf{x}',t)}{s^3}\,dv' - \frac{1}{4\pi}\int_V \frac{\mathbf{s}\times\nabla'\zeta(\mathbf{x}',t)}{s^3}\,dv'. \qquad (3.A.1)$$

Making use of the identity $\mathbf{s}/s^3 = -\nabla(1/s) = \nabla'(1/s)$ and the vector identity $\nabla\times\nabla\zeta = 0$, Green's theorem can be used to write the integral in the second term on the right-hand side of (3.A.1) as

$$\frac{1}{4\pi}\int_V \frac{\mathbf{s}\times\nabla'\zeta(\mathbf{x}',t)}{s^3}\,dv' = \frac{1}{4\pi}\int_V \nabla'\times(\frac{1}{s}\nabla'\zeta')\,dv' = \frac{1}{4\pi}\int_S \mathbf{n}'\times(\frac{1}{s}\nabla'\zeta')\,da, \qquad (3.A.2)$$

where *S* is the bounding surface of *V*. At large distances $|\mathbf{x}| >> L$, the gradient field $\nabla\zeta$ has the form of a dipole that decays with distance *r* as $O(1/r^3)$. Consequently, the surface integral in (3.A.2) approaches zero as $S\to\infty$, leading to the conclusion that the velocity field is entirely induced by the non-gradient part $\boldsymbol{\omega}^*$ of the vorticity field.

References

Abrahamson, J., Collision rates of small particles in a vigorously turbulent fluid. *Chemical Engineering Science* **30**, 1371-1379 (1975).

Abramowitz, M., and Stegun, I.A., *Handbook of Mathematical Functions*. Dover Publ., New York (1965).

Adachi, Y., and Ooi, S., Geometrical structure of a floc. *Journal of Colloid and Interface Science* **135**(2), 374-384 (1990).

Ayyalasomayajula, S., Warhaft, Z., and Collins, L.R., Modeling inertial particle acceleration statistics in isotropic turbulence. *Physics of Fluids* **20**, 095104 (2008).

Bec, J., Biferale, L., Cencini, M., Lanotte, A., Musacchio, S., and Toschi, F., Heavy particle concentration in turbulence at dissipative and inertial scales. *Physical Review Letters* **98**, 084502 (2007).

Beck, C., Superstatistics: Theoretical concepts and physical applications. In: *Anomalous Transport: Foundations and Applications*, Klages, R., Radons, G., Sokolov, I.M. (eds.), Wiley-VCH Verlag GmbH & Co. KGaA, Weinheim, Germany (2008).

Belin, F., Maurer, J., Tabeling, P., and Willaime, H., Observation of intense filaments in fully developed turbulence. *Journal de Physique II France* **6**, 73-585 (1996).

Brasil, A.M., Farias, T.L., Carvalho, M.G., and Koylu, U.O., Numerical characterization of the morphology of aggregated particles. *Journal of Aerosol Science* **32**, 489-508 (2001).

Burgers, J.M., A mathematical model illustrating the theory of turbulence. *Advances in Applied Mechanics* **1**, 171-199 (1948).

Cottet, G.-H., and Koumoutsakos, P.D., *Vortex Methods: Theory and Practice*. Cambridge University Press, Cambridge, UK, p. 229 (2000).

Cundall, P.A., and Strack, O.D.L., A discrete numerical model for granular assembles. *Geotechnique* **29**(1), 47-65 (1979).

Devenish, B.J., Bartello, P., Brenguier, J.L., Collins, L.R., Grabowski, W.W., IJzermans, R.H.A., Malinowski, S.P., Reeks, M.W., Vassilicos, J.C., Wang, L.P., and Warhaft, Z., Droplet growth in warm turbulent clouds. *Quarterly Journal of the Royal Meteorological Society* **138**, 1401-1429 (2012).

Di Felice, R., The voidage function for fluid-particle interaction systems. *International Journal of Multiphase Flow* **20**, 153-159 (1994).

Ding, W., Zhang, H. and Cetinkaya, C., Rolling resistance moment-based adhesion characterization of microspheres. *The Journal of Adhesion* **84**, 996-1006 (2008).

Dominik, C., and Tielens, A.G.G.M., Resistance to rolling in the adhesive contact of two elastic spheres. *Philosophical Magazine A* **92**(3), 783-803 (1995).

Eggersdorfer, M.L., Kadau, D., Hermann, H.J., and Pratsinis, S.E., Multiparticle sintering dynamics: From fractal-like aggregates to compact structures. *Langmuir* **27**, 6358-6367 (2011).

Falkovich, G., and Pumir, A., Intermittent distribution of heavy particles in a turbulent flow. *Physics of Fluids* **16**(7), L47-L50 (2004).

Fayed, H.E., Particles and bubbles collisions frequency in homogeneous isotropic turbulence and applications to minerals flotation machines. Ph.D. dissertation, Virginia Polytechnic Institute and State University, Blacksburg, Virginia (2013).

Fayed, H.E., and Ragab, S.A., Direct numerical simulation of particles-bubbles collisions kernel in homogeneous isotropic turbulence. *Journal of Computational Multiphase Flows* **5**(3), 167-188 (2013).

Frisch, U., *Turbulence – The Legacy of A.N. Kolmogorov*. Cambridge University Press, Cambridge, U.K. (1995).

Greengard, L., and Rokhlin, V., A fast algorithm for particle simulations. *Journal of Computational Physics* **73**, 325-348 (1987).

Grits, B., Pinsky, M., and Khain, A., Investigation of small-scale droplet concentration inhomogeneities in a turbulent flow. *Meteorol Atmos Phys* **92**, 91-204 (2006).

Hatakeyama, N., and Kambe, T., Statistical laws of random strained vortices in turbulence. *Physical Review Letters* **79**(7), 1257-1260 (1997).

Hertz, H., Über die Berührung fester elastischer Körper. *J. reine und angewandte Mathematik* **92**, 156-171 (1882).

Higashitani, K., Iimura, K. and Sanda, H., Simulation of deformation and breakup of large aggregates in flows of viscous fluids. *Chemical Engineering Science* **56**, 2927-2938 (2001).

Ishihara, T., Gotoh, T., and Kaneda, Y., Study of high–Reynolds number isotropic turbulence by direct numerical simulation. *Annual Review of Fluid Mechanics* **41**, 165-180 (2009).

Jiang, Q., and Logan, B.E., Fractal dimensions of aggregates determined from steady-state size distributions. *Environmental Science and Technology* **25**, 2031-2038 (1991)

Jiménez, J., Wray, A.A., Saffman, P.G., and Rogallo, R.S., The structure of intense vorticity in isotropic turbulence. *Journal of Fluid Mechanics* **255**, 65-90 (1993).

Jin, G., He, G.W., and Wang, L.P., Large-eddy simulation of turbulent collision of heavy particles in isotropic turbulence. *Physics of Fluids* **22**, 055106 (2010).

Johnson, K.L., Kendall, K., and Roberts, A.D., Surface energy and the contact of elastic solids. *Proceedings of the Royal Society of London A* **324**, 301-313 (1971).

Kajikawa, M., Kikuchi, K., Asuma, Y., Inoue, Y., and Sato, N., Aggregation of needle snow crystals. *Atmospheric Research* **55**, 131-138 (2000).

Kambe, T., and Hatakeyama, N., Statistical laws and vortex structures in fully developed turbulence. *Fluid Dynamics Research* **27**, 247-267 (2000).

Kivotides, D., and Leonard, A., Quantized turbulence physics. *Physical Review Letters* **90**(23), 234503 (2003).

Kraichnan, R.H., Diffusion by a random velocity field. *Physics of Fluids* **13**, 22-31 (1970).

La Porta, A., Voth, G.A., Crawford, A.M., Alexander, J., and Bodenschatz, E., Fluid particle acceleration in fully developed turbulence. *Nature* **409**, 1017-1019 (2001).

Liu, J., Shih, W.Y., Sarikaya, M., and Aksay, I.A., Fractal colloidal aggregates with finite interparticle interactions: energy dependence of the fractal dimension. *Physical Review A* **41**(6), 3206-3213 (1990).

Loth, E., Numerical approaches for motion of dispersed particles, droplets and bubbles. *Progress in Energy and Combustion Science* **26**, 161-223 (2000).

Lund, T.S., Wu, X., and Squires, K.D., Generation of turbulent inflow data for spatially-developing boundary layer simulations. *Journal of Computational Physics* **140**, 233-258 (1998).

Lundgren, T.S., Strained spiral vortex for turbulent fine structure. *Physics of Fluids* **25**, 2193-2203 (1982).

Lundgren, T.S., Linearly forced isotropic turbulence. *Annual Research Briefs*, pp. 461-473, CTR, Stanford (2003).

Malik, N.A., and Vassilicos, J.C., Eulerian and Lagrangian scaling properties of randomly advected vortex tubes. *Journal of Fluid Mechanics* **326**, 417-436 (1996).

Marshall, J.S., Discrete-element modeling of particulate aerosol flows. *Journal of Computational Physics* **228**, 1541-1561 (2009).

Marshall, J.S., and Grant, J.R., Penetration of a blade into a vortex core: vorticity response and unsteady blade forces. *Journal of Fluid Mechanics* **306**, 83-109 (1996).

Marshall, J.S., Grant, J.R., Gossler, A.A. and Huyer, S.A., Vorticity transport on a Lagrangian tetrahedral mesh. *Journal of Computational Physics* **161**, 85-113 (2000).

Marshall, J.S. and Li, S., *Adhesive Particle Flow: A Discrete Element Approach*, Cambridge University Press, New York (2014).

Min, I.A., Mezić, I., and Leonard, A., Lévy stable distributions for velocity and vorticity difference in systems of vortex elements. *Physics of Fluids* **8**, 1169-1180 (1996).

Minier, J.-P., Chibbaro, S., and Pope, S.B., Guidelines for the formation of Lagrangian stochastic models for particle simulations of single-phase and dispersed two-phase turbulent flows. *Physics of Fluids* **26**, 113303 (2014).

Monaghan, J.J., Extrapolating B splines for interpolation. *Journal of Computational Physics* **60**, 253-262 (1985a).

Monaghan, J.J., Particle methods for hydrodynamics. *Computer Physics Reports* **3**, 71-124 (1985b).

Mordant, N., Lévêque, E., and Pinton, J.F., Experimental and numerical study of the Lagrangian dynamics of high Reynolds turbulence. *New Journal of Physics* **6**, 116 (2004).

Nejadmalayeri, A., Vezolainen, A., and Vasilyev, O.V., Reynolds number scaling of coherent vortex simulation and stochastic coherent adaptive large eddy simulation. *Physics of Fluids* **25**, 110823 (2013).

Paiva, J., Salcedo, R., and Araujo, P., Impact of particle agglomeration in cyclones. *Chemical Engineering Journal* **162**, 861-876 (2010).

Pope, S.B., Simple models of turbulent flows. *Physics of Fluids* **23**, 011301 (2011).

Pullin, D.I., and Saffman, P.G., On the Lundgren-Townsend model of turbulent fine scales. *Physics of Fluids* **5**(1), 126-145 (1993).

Reade, W.C. and Collins, L.R., A numerical study of the particle size distribution of an aerosol undergoing turbulent coagulation. *Journal of Fluid Mechanics* **415**, 45-64 (2000).

Rosales, C., and Meneveau, C., Linear forcing in numerical simulations of isotropic turbulence: physical space implementations and convergence properties. *Physics of Fluids* **17**(9), 095106 (2005).

Rubinow, S.I., and Keller, J.B., The transverse force on a spinning sphere moving in a viscous fluid. *Journal of Fluid Mechanics* **11**, 447-459 (1961).

Saffman, P.G., The lift on a small sphere in a slow shear flow. *Journal of Fluid Mechanics* 22, 385-400 (1965).

Saffman, P.G., Corrigendum to 'The lift force on a small sphere in a slow shear flow'. *Journal of Fluid Mechanics* 31, 624 (1968).

Saffman, P.G., Vortex models of isotropic turbulence. *Philosophical Transactions of the Royal Society of London A* **355**, 1949-1956 (1997).

Saffman, P.G. and Turner, J.S., On the collision of drops in turbulent clouds. *Journal of Fluid Mechanics* **1**(1), 16-30 (1956).

Sala, K., and Marshall, J.S., Stochastic vortex structure method for modeling particle clustering and collisions in homogeneous turbulence. *Physics of Fluids* **25**(10), 103301 (2013).

Salmon, J.K., and Warren, M.S., Skeletons from the treecode closet. *Journal of Computational Physics* **111**, 136-155 (1994).

Selomulya, C., Amal, R., Bushell, G., and Waite, T.D., Evidence of shear rate dependence on restructuring and breakup of latex aggregates. *Journal of Colloid and Interface Science* **236**, 67-77 (2001).

Serra, T., Colomer, J., and Casamitjana, X., Aggregation and breakup of particles in a shear flow. *Journal of Colloid and Interface Science* **187**, 466-473 (1997).

Smirnov, A., Shi, S., and Celik, I., Random flow generation technique for large eddy simulations and particle-dynamics modeling. *Journal of Fluids Engineering* **123**, 359-371 (2001).

Smith, O.K., Eigenvalues of a symmetric 3×3 matrix. *Communications of the ACM* **4**(4), 168 (1961).

Squires, K.D., and Eaton, J.K., Preferential concentration of particles by turbulence. *Physics of Fluids A* **3**, 1169-1178 (1991).

Sundaram, S. and Collins, L.R., Collision statistics in an isotropic particle-laden turbulent suspension. I. Direct numerical simulations. *Journal of Fluid Mechanics* **335**, 75-109 (1997).

Tabor, G.R., and Baba-Ahmadi, M.H., Inlet conditions for large eddy simulation: A review. *Computers & Fluids* **39**, 553-567 (2010).

Thornton, C., Interparticle sliding in the presence of adhesion. Jo*urnal Physics D: Applied Physics* **24**, 1942-1946 (1991).

Townsend, A.A., On the fine scale of turbulence. *Proceedings of the Royal Society of London A* **208**, 534-542 (1951).

Tsuji, Y., Tanaka, T., and Ishida, T., Lagrangian numerical simulation of plug flow of cohesionless particles in a horizontal pipe. *Powder Technology* **71**, 239-250 (1992).

Vincent, A., and Meneguzzi, M., The spatial structure and statistical properties of homogeneous turbulence. *Journal of Fluid Mechanics* **225**, 1-20 (1991).

Voth, G.A., Satyanarayan, K., and Bodenschatz, E., Lagrangian acceleration measurements at large Reynolds numbers. *Physics of Fluids* **10**(9), 2268-2280 (1998).

Waldner, M.H., Sefcik, J., Soos, M. and Morbidelli, M., Initial growth kinetics of aggregates in turbulent coagulator. *Powder Technology* **156**, 226-234 (2005).

Wang, L.-P., Wexler, A.S., and Zhou, Y., Statistical mechanical description and modeling of turbulent collision of inertial particles. *Journal of Fluid Mechanics* **415**, 117–153 (2000).

Wilczek, M., and Friedrich, R., Dynamical origins for non-Gaussian vorticity distributions in turbulent flows. *Physical Review E* **80**, 016316 (2009).

Wilczek, M., Jenko, F., and Friedrich, R., Lagrangian particle statistics in turbulent flows from a simple vortex model. *Physical Review E* **77**, 056301 (2008).

Wilson, J.D., and Sawford, B.L., Review of Lagrangian stochastic models for trajectories in the turbulent atmosphere. *Boundary-Layer Meteorology* **78**, 191-210 (1996).

Xu, X.G., Li, S.Q., Liu, G.D., and Yao, Q., Effect of co-firing straw with two coals on the ash deposition behavior in a down-fired pulverized coal combustor. *Energy & Fuels* 24(1), 241–249 (2010).

Zaichik, L.I., Alipchenkov, V.M., and Avetissian, A.R., Modelling turbulent collision rates of inertial particles. *International Journal of Heat and Fluid Flow* **27**, 937-944 (2006).

Zhang, Y., Li, S., Deng, S., Yao, Q., and Tse, S.D., Direct synthesis of nanostructured TiO_2 films with controlled morphologies by stagnation swirl flames. *Journal of Aerosol Science* **44**, 71-82 (2012).

Chapter 4: A Stochastic Vortex Structure Method for Interacting Particles in Turbulent Shear Flows

Farzad F. Dizaji, Jeffrey S. Marshall and John R. Grant
Department of Mechanical Engineering, The University of Vermont
Burlington, VT 05405, U.S.A.

Corresponding Author: Jeffrey S. Marshall, Department of Mechanical Engineering, The University of Vermont, Burlington, VT 05405, U.S.A. PHONE: 1 (802) 656-3826, EMAIL: jmarsha1@uvm.edu.

Keywords: stochastic vortex structures; fast multipole method; particle collision; turbulent shear flow

Abstract

In recent work we have proposed a new synthetic turbulence method based on stochastic vortex structures, and we have demonstrated that this method can accurately predict particle transport, collision and agglomeration in homogeneous, isotropic turbulence in comparison to direct numerical simulation results. The current paper extends the stochastic vortex structure (SVS) method to non-homogeneous, anisotropic turbulence. The key element of this extension is a new inversion procedure, by which the vortex initial orientation can be set so as to generate a prescribed Reynolds stress field. After validating this inversion procedure for simple problems, we apply the SVS method to the problem of interacting particle transport by a turbulent planar jet. Measures of the turbulent flow and of particle dispersion, clustering and collision obtained by the new SVS simulations are shown to compare well with direct numerical simulation results. The influence of different numerical parameters, such as number of vortices and vortex lifetime, on the accuracy of the SVS predictions is also examined.

4.1. Introduction

Computational modeling of the motion of interacting particles, droplets or bubbles subject to subgrid-scale fluctuations in turbulent flows is a long-standing challenge in multiphase flow simulations. The Reynolds-averaged Navier-Stokes (RANS) approach remains the most common method for engineering solution of practical turbulent flows, providing both manageable computation times and reasonably accurate prediction of key flow features, such as boundary layer separation. However, when used in conjunction with Lagrangian simulation of particulate fluids, it is necessary to augment the RANS equations with some model to account for the effect of the turbulent fluctuations when computing the particle trajectories. This problem also arises when using the large eddy simulation (LES) approach with sufficiently small values of the Kolmogorov-scale particle Stokes number [1]. A number of effective methods exist for dealing with this problem for *non-interacting* particles (see [2] for a review), but subgrid-scale modeling for transport of *interacting* particles in turbulent flows remains an unresolved challenge. Particle interaction is essential in a wide range of turbulent flow problems occurring in nature, such as turbulence effects on collision of rain droplets or snow flakes, contact electrification of dust particles in sand storms, and agglomeration of particles in volcanic plumes or of pollution particulates in the atmosphere. Particle interaction also plays an important role in many industrial particulate flow problems, such as pharmaceutical manufacturing, paint production, wastewater treatment, additive manufacturing processes, 3D printing, flame synthesis of nanoparticles, and fly ash capture from combustion furnaces.

The challenges associated with subgrid-scale modeling for turbulent transport of interacting particles arise from three considerations. First, it is critical for simulation of particle interaction to accurately model small values of the particle separation distance. However, small separation distances imply that the nearby particles are experiencing forcing from the same set of nearby turbulent eddies, so that the fluid fluctuation velocity at the particle positions is highly correlated. As a consequence, any model in which each particle experiences uncorrelated forcing will not be appropriate for simulation of interacting particles. Second, particle collision and adhesion processes occur over time scales that are very small, typically much smaller than those associated with the fluid flow. The numerical calculation consequently becomes numerically stiff when particle interactions are included, particularly when using methods such as the soft-sphere discrete-element method (DEM). Synthetic turbulence models commonly used to approximate the subgrid-scale turbulent fluctuations must therefore be highly efficient in order to be manageable with small time steps. Third, turbulent eddy structures are known to expel particles with higher density than the surrounding fluid, leading to formation of particle clusters in the region in-between the eddies that can have local particle concentrations an order of magnitude or more above the average concentration [3-7]. This phenomenon leads to the so-called *preferential concentration effect*, which can dramatically increase particle collision rate, agglomeration and other interactions in these high-concentration regions [8-9].

Since particle clustering in turbulent flows occurs due to interaction of particles with coherent eddies, it is natural to utilize a vortex structural approach in modeling the effect of turbulent fluctuations on interacting particles. Vortex structural models have

long been used in turbulence flow modeling, dating back to Townsend's [10] model of homogeneous turbulence as a collection of Burger's vortices and Lundgren's [11] spiral vortex model, as well as extensions of these models by Pullin and Saffman [12] and Saffman [13]. The scaling and structure of coherent vortices was studied numerically for homogeneous turbulence by Jiménez et al. [14] and experimentally for turbulent shear flows by Belin et al. [15], among others. Both studies found that the turbulent vorticity field is dominated by a set of strong, coherent vortex structures of finite length and with tubular shape, surrounded by a sea of weak random (non-coherent) vorticity. The length and core radius of the coherent vortices were found to scale with the Lagrangian integral length scale and the Kolmogorov length scale, respectively, and the vortex strength was found to scale with the square root of the microscale Reynolds number. Theoretical proof of these scaling observations was provided by Kambe and Hatakeyama [16]. Kivotides and Leonard [17] report a computational study in which homogeneous turbulence is represented by a set of finite-length vortex structures, and show that this system generates an energy spectrum that satisfies the Kolmogorov $k^{-5/3}$ scaling in the turbulence inertial range. The effectiveness of vortex structural models for prediction of turbulence structure functions and various velocity and vorticity probability density functions was discussed by Refs. [18-22]. Extensions of the vortex filament method were successfully utilized for simulation of a number of turbulent shear flows, including mixing layers [23], co-flowing jets [24], and boundary layers [25].

Ayyalasomayajula et al. [26] proposed a vortex structural model for transport of particles in homogeneous isotropic turbulence using a two-dimensional array of uniformly spaced vortices, where a stochastic algorithm is used to determine the vortex

strength. Somewhat surprisingly, given the highly simplified nature of this model, the predicted particle acceleration statistics and clustering was similar to direct numerical simulation (DNS) results. Sala and Marshall [27] proposed a three-dimensional stochastic vortex structure (SVS) model, again for homogeneous isotropic turbulence, where the turbulent eddies are represented by a set of finite-length vortex structures which are randomly positioned and oriented in the flow field. The vortex length and core radius were assumed to be proportional to the turbulence integral and Kolmogorov length scales, respectively. Unlike the vortex filament method, the SVS method does not use the vortex structures to evolve the turbulent flow field; instead, the vortex structures are used only to approximate a subgrid-scale synthetic turbulence to use for particle evolution in a flow with a given Reynolds stress distribution. An accelerated version of the SVS method was developed by Dizaji and Marshall [28] using both the fast multipole method and a local Taylor series expansion which speeds up the computations by up to two orders of magnitude with negligible difference in flow field or particle interaction statistics. The SVS model was shown to yield predictions for turbulence energy spectrum, velocity and acceleration PDF, and particle collision rate that are in close agreement with DNS predictions. Dizaji and Marshall [28] also verified that the SVS model is highly effective at accurately predicting various measures characterizing agglomerate formation for adhesive particles in turbulent flows.

One criticism of the SVS model is that, to date, all applications of this model have been for isotropic, homogeneous turbulence. The objective of the current paper is to extend the SVS model to non-homogeneous, anisotropic turbulent flows and to validate this extended model by comparison to direct numerical simulation (DNS) results.

Extension of the SVS model for anisotropic turbulence is described in Section 4.2.1, with particular focus on a proposed inversion algorithm by which the orientation of the SVS vortex structures can be adjusted to yield a prescribed Reynolds stress field. This vortex structure initialization method is examined and validated in Section 4.2.2 for both homogeneous and inhomogeneous anisotropic flow fields. Computational methods used for particle transport and for direct numerical simulation (DNS) for validation of the SVS model are described in Section 4.3. Validation of the SVS model with comparison to DNS results for particulate turbulent planar jet flow are reported in Section 4.4. Conclusions are given in Section 4.5.

4.2. Stochastic Vortex Structure Method for Anisotropic Turbulence

4.2.1. Anisotropic SVS Method

The stochastic vortex structure (SVS) model approximates the turbulent vorticity field by a collection of vortex structures placed in the flow field. In its simplest version, the vortex structures in the SVS model all have the same finite length *L*, core radius δ, and strength Γ. The vortex length *L* is of the order of magnitude of the turbulence Lagrangian integral length scale $\ell_0 = 0.5\, u_0^{\,3} / \varepsilon$, where u_0 is the turbulence root-mean-square velocity and ε is the turbulence dissipation rate per unit mass. The core radius δ of the coherent vortices was estimated numerically by Jimenez et al. [14], experimentally by Belin et al. [15], and theoretically by Kambe and Hatakeyama [16] to be 3-4 times the Kolmogorov length scale, $\eta = (\nu^3 / \varepsilon)^{1/4}$, where *v* is the fluid kinematic viscosity. In the current work we use somewhat larger vortex structures with core radius of 8η so as to

ensure sufficient number of grid points to resolve the velocity variation across the vortex cores; however, SVS computations were repeated with core radius $\delta = 4\eta$ and the results were found to be almost identical to those with larger core radius. Each vortex structure has a lifetime T_V which is proportional to the integral time scale, $T_\ell = q/3\varepsilon$, where $q = 1.5u_0^2$ is the turbulent kinetic energy per unit mass, although we note that the model results are not sensitive to choice of vortex lifetime.

4.2.1.1. Vortex structure initialization

The Reynolds stress tensor **R** has components in the global Cartesian coordinate system given by $R_{ij} = \overline{u_i' u_j'}$, where a prime denotes the fluctuating velocity component and an overbar denotes a time average. In the SVS simulation, the anisotropy of the turbulent fluctuations is produced via preferential orientation of the vortex structures. It is necessary to develop a method for specifying the probability distribution of the vortex structure orientation so as to be consistent with the given Reynolds stress tensor, which is a type of inverse problem. Turbulence anisotropy is related both to differences in value of the three normal components of Reynolds stress and to the off-diagonal Reynolds stress components. We employ a four-step approach for setting the vortex orientation in accordance with a given Reynolds stress tensor, as described below. Prior to implementing this procedure, we compute a set of $M = 642$ evenly-spaced *test points* on the surface of a unit sphere by dividing the faces of an icosahedron a prescribed number of times and projecting the vertices to the unit sphere.

In the *first* step, the Reynolds stress tensor is interpolated from the grid covering the flow field onto the centroid position of a vortex structure. In the *second* step, we

rotate the coordinate system to a frame in which the Reynolds stress tensor at the vortex centroid is diagonal. This is achieved by computing the set of three eigenvalues $\lambda^{(k)}$ and associated normalized eigenvectors $\mathbf{x}^{(k)}$ of the Reynolds stress tensor. We define a principal direction coordinate system as a coordinate frame whose base vectors are the three eigenvectors of **R**. The components of the Reynolds tensor in the principal direction coordinate system, denoted by R_{ij}^{*}, are given by

$$R_{ij}^{*} = \begin{pmatrix} \lambda^{(1)} & 0 & 0 \\ 0 & \lambda^{(2)} & 0 \\ 0 & 0 & \lambda^{(3)} \end{pmatrix}. \tag{4-1}$$

In the *third* step, the vortex structure orientation is set in this principal direction coordinate system. The inverse procedure by which this is achieved is based on the observation that a vortex structure oriented in the *x*-direction, say, would induce a velocity field in which $R_{11} = 0$ and $R_{22} = R_{33}$. We define vortex orientation weighting coefficients c_1, c_2 and c_3, normalized by $c_1 + c_2 + c_3 = 1$, such that

$$c_2 + c_3 = \lambda^{(1)}, \qquad c_1 + c_3 = \lambda^{(2)}, \qquad c_1 + c_2 = \lambda^{(3)}. \tag{4-2}$$

Solving the system (2) for the three orientation weighting coefficients gives

$$c_1 = \frac{1}{2}(\lambda^{(2)} + \lambda^{(3)} - \lambda^{(1)}), \tag{4-3a}$$

$$c_2 = \frac{1}{2}(\lambda^{(1)} + \lambda^{(3)} - \lambda^{(2)}), \tag{4-3b}$$

$$c_3 = \frac{1}{2}(\lambda^{(1)} + \lambda^{(2)} - \lambda^{(3)}). \tag{4-3c}$$

The orientation of a vortex structure is specified at the initial time step by randomly selecting one of the M test points on the unit sphere, obtained using the procedure described at the beginning of this section. The coordinates of the selected test point in principal direction coordinates is denoted by $(\xi_1^*, \xi_2^*, \xi_3^*)$. Using the weighting coefficients obtained in (4.3), the vortex structure orientation $\boldsymbol{\zeta}$ is set in principal direction coordinates as

$$\zeta_1^* = \frac{c_1 \xi_1^*}{\Delta}, \qquad \zeta_2^* = \frac{c_2 \xi_2^*}{\Delta}, \qquad \zeta_3^* = \frac{c_3 \xi_3^*}{\Delta}, \tag{4-4}$$

where $\Delta \equiv [(c_1\xi_1^*)^2 + (c_2\xi_2^*)^2 + (c_3\xi_3^*)^2]^{1/2}$. In isotropic turbulence the three orientation weighting coefficients are equal, so that (4.4) results in random vortex orientation with uniform distribution.

The *fourth* step of the vortex structure initialization process is to rotate the structure back into the global coordinate system used for the computation. We recall that the components of the rotation tensor $\mathbf{A}$ from the global Cartesian coordinates to a principal direction coordinate system form an orthonormal 3×3 matrix whose three columns are the components of the three eigenvectors $\mathbf{x}^{(k)}$. The components of the vortex structure orientation vector $\boldsymbol{\zeta}$ in the global coordinate frame can therefore be written in terms of the components in (4) as

$$\zeta_i = \zeta_j^* A_{ji}. \tag{4-5}$$

4.2.1.2. Velocity calculation

The vortex structures induce a velocity field $\mathbf{u}$, which is computed on the flow grid using the fast multipole acceleration method described by Dizaji and Marshall [28].

The accelerated velocity computation method first partitions the computational domain into a tree-structure composed of uniform-size boxes, where at every level of the tree structure each box from the previous level is divided into eight 'offspring' boxes by dividing the side lengths in half in each direction. For each of the smallest 'target' boxes in the tree structure, a list of other 'source' boxes with which it interacts 'directly' and 'indirectly' is developed based on the analytical error estimate for the multipole expansion by Salmon and Warren [29]. For source boxes on the direct interaction list, we compute the induced velocity from each vortex structure in the source box on each grid cell node in the target box by interpolation from a planar section, where the induced velocity from a unit strength vortex structure on the plane is pre-computed at the start of the simulation. For source boxes on the indirect interaction list, the induced velocity from all sources in the box is computed at the centroid of the target box using multipole expansion [30-31]. The contribution of this induced velocity at the individual grid cell nodes within the target box is then determined using a local Taylor series expansion. Induced velocity from vortex structures from one period of the computational domain in each direction are also induced in the computation. This accelerated method was shown by Dizaji and Marshall [28] to produce very accurate results with computation times that are nearly two orders of magnitude less than the direct computation method using only four levels of the box structure.

4.2.1.3. Vortex time evolution

Each of the N_V vortex structures are advected in time by moving the two endpoints of the vortex structure by solving

$$\frac{d\mathbf{x}_{n,i}}{dt} = \mathbf{u}(\mathbf{x}_{n,i}, t), \tag{4-6}$$

where the index n identifies the vortex structure and i (=1,2) identifies the endpoint of the structure under consideration. After moving the end points, the vortex length is reset to L. The centroid position $\mathbf{x}_n$ and unit tangent vector $\boldsymbol{\lambda}_n$ for each structure are then recomputed from the positions of the new endpoint locations.

The initial age of the n^{th} vortex structure, τ_{0n}, is specified as a random variable, where the ratio τ_{0n}/T_V has a uniform distribution between 0 and 1. If t_{0n} denotes the time at which the vortex structure is initiated, then the current age of the vortex structure $\tau_n(t)$ is given by

$$\tau_n = \tau_{0n} + t - t_{0n}. \tag{4-7}$$

When $\tau_n(t)$ exceeds the specified lifespan T_V, the vortex structure is removed and a new vortex structure is introduced with random position $\mathbf{x}_n$ and orientation given by the same four-part procedure as used to initialize the vortex structure orientation.

4.2.2. Reynolds Stress Consistency Test

4.2.2.1. Limitations of inversion method

The inverse method for initialization of the SVS vortex structures described in Section 4.2.1 is validated in this section for different test computations in which the vortex structures are initialized using a prescribed Reynolds stress field, and then the Reynolds stress is evaluated from the computed SVS velocity field and compared to the prescribed field. In conducting this validation, it is important to bear in mind that the

inversion procedure described in Section 4.2.1 is subject to limitations, which can be ultimately associated with the fact that we are attempting to generate a turbulence field using only the induced velocity from tubular vortex structures. Mathematically, these restrictions require that the three coefficients c_1, c_2 and c_3 defined in (4.3a-c) must all be positive. This in turn introduces the following three restrictions on the values of the eigenvalues $\lambda^{(k)}$:

$$\lambda^{(2)} + \lambda^{(3)} - \lambda^{(1)} > 0, \tag{4-8a}$$

$$\lambda^{(1)} + \lambda^{(3)} - \lambda^{(2)} > 0, \tag{4-8b}$$

$$\lambda^{(1)} + \lambda^{(2)} - \lambda^{(3)} > 0. \tag{4-8c}$$

If we now consider the special case of a two-dimensional turbulent mean flow, such as a plane jet or channel flow, the Reynolds stress tensor R_{ij} has the form

$$R_{ij} = \begin{pmatrix} R_{11} & R_{12} & 0 \\ R_{12} & R_{22} & 0 \\ 0 & 0 & R_{33} \end{pmatrix}. \tag{4-9}$$

Solving for the eigenvalues of the Reynolds stress tensor gives

$$\lambda^{(1)} = \frac{1}{2}(R_{11} + R_{22}) + \frac{1}{2}\left[(R_{11} - R_{22})^2 + 4R_{12}^2\right]^{1/2}, \tag{4-10a}$$

$$\lambda^{(2)} = \frac{1}{2}(R_{11} + R_{22}) - \frac{1}{2}\left[(R_{11} - R_{22})^2 + 4R_{12}^2\right]^{1/2}, \tag{4-10b}$$

$$\lambda^{(3)} = R_{33}. \tag{4-10c}$$

Using R_{33} for normalization, Reynolds stress ratios can be defined as

$$r_{11} = \frac{R_{11}}{R_{33}}, \qquad r_{22} = \frac{R_{22}}{R_{33}}, \qquad r_{12} = \frac{|R_{12}|}{R_{33}}, \tag{4-11}$$

which are all positive by definition. From the solutions (4.10), we find that the limitation (4.8b) is always satisfied and the limitations (4.8a) and (4.8c) become, respectively,

$$r_{11} + r_{22} - 1 > 0\,, \tag{4-12a}$$

$$1 - \left[(r_{11} - r_{22})^2 + 4r_{12}^2\right]^{1/2} > 0\,. \tag{4-12b}$$

Specific limitations for several special cases, as computed from (4.12), are listed in Table 4.1.

Table 4.1. Special cases for limiting values of the Reynolds stress ratios for two-dimensional turbulent mean flow.

Special Case	Prescribed Values		Limitation
A	$r_{22} = 1$	$r_{12} = 0$	$r_{11} < 2$
B	$r_{22} = r_{11}$	$r_{12} = 0$	$r_{11} > 1/2$
C	$r_{11} = 1$	$r_{22} = 1$	$r_{12} < 1/2$

4.2.2.2. Validation for homogeneous turbulence

The inversion method described in Section 4.2.1 was validated first for the case of homogeneous turbulence, in which the Reynolds stress is uniform in space. The Reynolds stress tensor is assumed to be anisotropic, so that the diagonal components are not equal to each other and the diagonal component R_{12} in (4.9) does not vanish. While it is unlikely that an anisotropic Reynolds stress would actually develop in a homogeneous turbulent flow, this is still a useful special case in which to examine performance of the inverse procedure before going to fully inhomogeneous, anisotropic turbulence in the next sub-section. The tests were performed using a rectangular domain with side lengths $L_x = 4$ and $L_y = L_z = 2$ on a computational grid with 128, 64 and 64 points in the *x*-, *y*-

and z- directions, respectively. The computations assumed triply periodic boundary conditions, which were enforced by including one period of the SVS vortex structures in each direction, including the diagonal directions, in the velocity computation as vorticity sources. The computed Reynolds stresses were averaged over all computational points and over 10 different runs with different random vortex positions.

A listing of different prescribed Reynolds stress values used for the validation tests for homogeneous turbulence are given in Table 4.2. Results are plotted in Figure 4.1 both for cases with $R_{12} = 0$ (Figure 4.1a, for cases H.1-H.3) and for cases with $R_{12} \neq 0$ (Figure 4.1b, for cases H.4-H.6). In each case, we plot the ratio R_{ij}/q for each non-zero Reynolds stress component, with the predicted components on the y-axis and the prescribed components on the x-axis. The turbulent kinetic energy q was computed separately from the prescribed and predicted diagonal components of the Reynolds stress as

$$q = \frac{1}{2}\left(R_{11} + R_{22} + R_{33}\right). \tag{4-13}$$

The predicted Reynolds stresses shown in Figure 4.1 are in good agreement with the prescribed values for all cases examined, demonstrating success of the inversion procedure described in Section 4.2.1 for homogeneous turbulence.

Table 4.2. Listing of specified Reynolds stress values used in for validation of the inversion method for homogeneous turbulence, shown in Figure 4.1.

Case	R_{11}	R_{22}	R_{33}	R_{12}	q	Symbol in Fig. 4.1
H.1	0.0603	0.0403	0.0353	0	0.06795	Open
H.2	0.0553	0.0453	0.0353	0	0.06795	Gray
H.3	0.0653	0.0403	0.0303	0	0.06795	Black
H.4	0.0603	0.0403	0.0353	0.010	0.06795	Open
H.5	0.0553	0.0453	0.0353	0.015	0.06795	Gray
H.6	0.0653	0.0403	0.0303	0.005	0.06795	Black

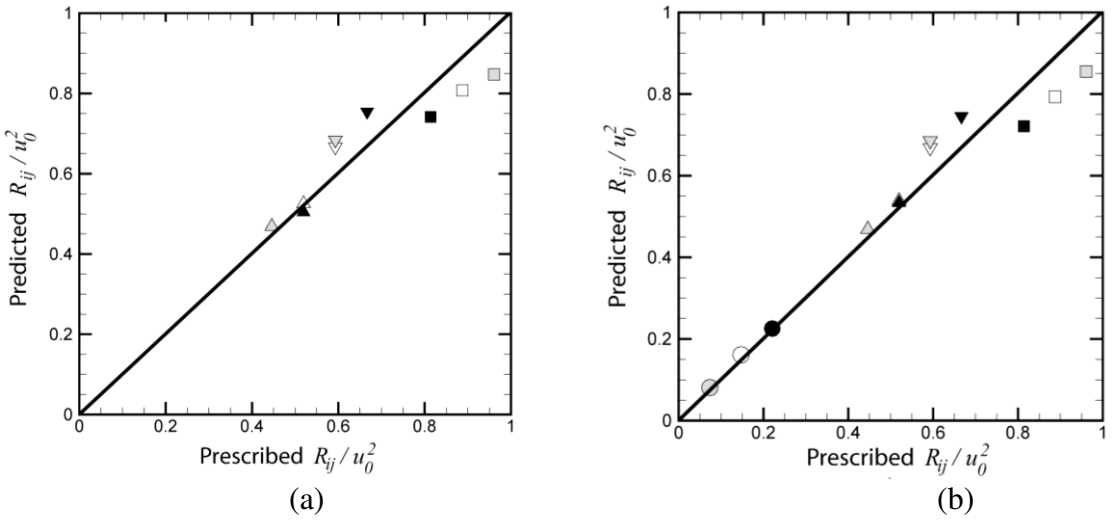

Figure 4.1. Plots showing the prescribed Reynolds stresses (*x*-axis) and the predicted Reynolds stresses (*y*-axis) for SVS simulation of homogeneous turbulence, with $R_{ij} = \overline{u_i u_j}$ normalized by the square of the root-mean-square velocity u_0. Plots are for cases (a) with $R_{12} = 0$ (cases H.1-H.3) and (b) with $R_{12} \neq 0$ (cases H.4-H.6), where the prescribed Reynolds stress values are listed in Table 4.2. Values of dimensionless Reynolds stress are plotted with R_{11}/u_0^2 denoted by squares □, R_{22}/u_0^2 denoted by gradients ∇, R_{33}/u_0^2 denoted by deltas Δ, and R_{12}/u_0^2 denoted by circles O. The open, gray (shaded) and black-filled symbols correspond to the cases indicated in Table 4.2.

4.2.2.3. Validation for inhomogeneous turbulence

In actuality, anisotropic turbulence tends to form under non-homogeneous turbulent flow conditions. In this section, we examine the performance of the SVS

concept and of the inversion procedure described in Section 4.2.1 for two examples of inhomogeneous turbulent flows. In both cases the mean flow is two-dimensional, so that the Reynolds stress has the form (4.9), and the flow is assumed to be periodic only in the *x*- and *y*-directions. The tests were performed using a rectangular domain with side lengths $L_x = 4$ and $L_y = L_z = 2$ on a computational grid with 128, 64 and 64 points in the *x*-, *y*- and *z*- directions, respectively. The predicted Reynolds stress values were averaged over the *x*-*y* plane for each *z* value, as well as over 20 repeated runs with different vortex positions.

The first test was for a case with isotropic prescribed Reynolds stress ($R_{11} = R_{22} = R_{33},\ R_{12} = 0$) which varies as a top-hat distribution in *y*, as shown by the solid black line in Figure 4.2a. Comparison of the predicted Reynolds stresses with the prescribed distribution illustrate the nonlocal characteristics of the SVS method. The normal components of the predicted Reynolds stresses, plotted using the three color lines in Figure 4.2a, appear similar to a diffused (or filtered) form of the original profile. All three normal components are close to equal for the predicted Reynolds stress, and the predicted off-normal (shear) component (R_{12}) is close to zero.

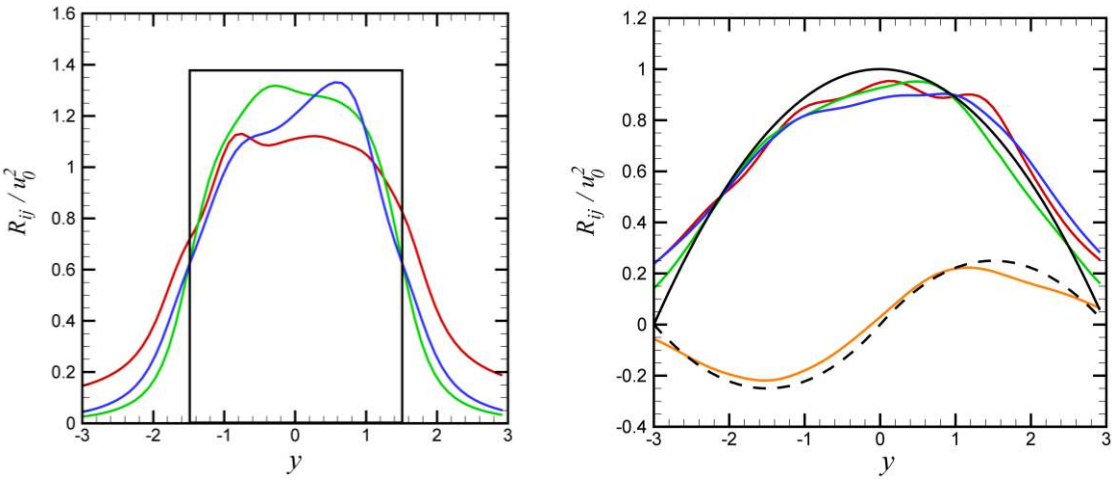

Figure 4.2. Plots showing the distributions of prescribed Reynolds stresses (black lines) and the predicted Reynolds stresses (colored lines), normalized by the square of the root-mean-square velocity u_0, for (a) a top-hat Reynolds stress distribution with prescribed Reynolds stress components $R_{11} = R_{22} = R_{33}$ and $R_{12} = 0$, and (b) a Reynolds stress field typical of an idealized planar jet with prescribed Reynolds stresses $R_{11} = R_{22} = R_{33}$ and $R_{12} \neq 0$. The predicted Reynolds stress is plotted for R_{11} (red line), R_{22} (green line), R_{33} (blue line) and R_{12} (orange line), and the prescribed Reynolds stresses are denoted using a solid black line for the diagonal components and a dashed black line for R_{12}.

The second test was for a case similar to an idealized turbulent planar jet, with $R_{11} = R_{22} = R_{33}$ and $R_{12} \neq 0$, as shown by the solid and dashed black curves in Figure 4.2b for the normal and shear Reynolds stresses, respectively. For simplicity, the normal stresses were prescribed as a quadratic function of y and the R_{12} component was prescribed as one period of a sine wave. The predicted Reynolds stresses are in very good agreement to the prescribed values, although there is observed to be a slight flattening of the peak normal Reynolds stresses in the predicted values as compared to the prescribed values.

4.3. Computational Methods for Used for Validation Test

Validation tests of the SVS method for transport of interacting particles in anisotropic, inhomogeneous turbulence are reported in Section 4.4 for turbulent planar jet flow. The current section briefly describes the computational methods used for direct numerical simulation of the fluid flow and for simulating interacting particle transport in the validation computations.

4.3.1. Computational Method for Direct Numerical Simulations

Direct numerical simulations (DNS) of turbulent planar jet flow were used to validate the SVS predictions. The DNS computations were performed using a fractional-step method [32-34], with time advancement performed using a third-order Runga-Kutta method for convective terms and the 2nd order Crank-Nicholson method for viscous terms. Algorithms for all spatial derivatives except the convective terms are approximated using second-order centered finite differences (three point stencil) on a non-staggered grid. The discretized equations for the *k*th Runge-Kutta step are given by

$$\tilde{\mathbf{u}} = \mathbf{u}^{k-1} + \Delta t\left(2\alpha_k \nu \nabla^2 \mathbf{u}^{k-1} - 2\alpha_k \nabla p^{k-1} - \gamma_k [(\mathbf{u}\cdot\nabla)\mathbf{u}]^{k-1} - \zeta_k [(\mathbf{u}\cdot\nabla)\mathbf{u}]^{k-2}\right), \quad (4\text{-}14a)$$

$$\nabla^2 \mathbf{u}^* - \frac{\mathbf{u}^*}{\alpha_k \nu \Delta t} = -\frac{\tilde{\mathbf{u}}}{\alpha_k \nu \Delta t} + \nabla^2 \mathbf{u}^{k-1}, \quad (4\text{-}14b)$$

$$\nabla \cdot \left(\nabla \phi^k\right) = \frac{\nabla \cdot \mathbf{u}^*}{2\alpha_k \Delta t}, \quad (4\text{-}14c)$$

$$\mathbf{u}^k = \mathbf{u}^* - 2\alpha_k \Delta t \nabla \phi^k, \quad (4\text{-}14d)$$

$$p^k = p^{k-1} + \phi^k - \alpha_k \nu \Delta t \nabla^2 \phi^k, \quad (4\text{-}14e)$$

where **u** and p are the fluid velocity and pressure and the coefficients α_k, γ_k, and ζ_k are given by Rai and Moin [32]. Continuity is enforced by a projection method leading to equation (4.14c) for the pseudo-pressure, denoted by ϕ. In the multigrid solution of this equation, the five-point stencil produced by successive application of the gradient operation followed by the divergence operation was employed, rather than a numerical approximation to the Laplacian. The Crank-Nicholson method was used to solve the Helmholtz problem, given in (4.14b). A tenth-order approximation was used for the convective terms, requiring an 11-point stencil. To control non-linear instabilities, at the end of each time step the velocity components were filtered using a tenth-order filter (again using an 11-point stencil) [35-36]. After filtering to obtain $\mathbf{u}^{filtered}$, the velocity **u** was replaced by $(1-q)\mathbf{u} + q\mathbf{u}^{filtered}$, with q = 0.05. The mean flow was initialized in the x-direction with cross-directional variation in the z-direction. A very weak initial turbulence was introduced using a synthetic turbulence generator, similar to Smirnov et al. [37], with initial turbulent kinetic energy of 10^{-5}. The turbulent flow was assumed to be periodic in the x- and y-directions, and a symmetry boundary condition was imposed in the z-direction. A layer of five ghost points in each direction surrounded the computational domain, so that no adjustment of the differentiation schemes was needed near the domain boundaries.

4.3.2. Discrete Element Method for Particle Transport

Particle transport and collisions were computed in both the DNS and SVS computations using a soft-sphere discrete-element method (DEM) for a set of N_p colliding non-adhesive particles of finite diameter d and mass m. The computations

evolve the particle velocity **v** and rotation rate **Ω** by solution of the momentum and angular momentum equations for individual particles, given by

$$m\frac{d\mathbf{v}}{dt} = \mathbf{F}_F + \mathbf{F}_A, \qquad I\frac{d\mathbf{\Omega}}{dt} = \mathbf{M}_F + \mathbf{M}_A, \tag{4-15}$$

where $m = \pi\rho_p d^3/6$ and $I = (1/10)md^2$ are the particle mass and moment of inertia. The momentum and angular momentum equations include fluid-induced forces and torques on the particle ($\mathbf{F}_F$ and $\mathbf{M}_F$) and forces and torques resulting from particle collision ($\mathbf{F}_A$ and $\mathbf{M}_A$). The computations employ a multiple-time-step algorithm to accurately resolve numerical stiffness problems introduced by the different time scales associated with the fluid flow, particle transport, and particle collisions. The time steps, including the fluid time step $\Delta t = O(L/U)$, the particle time step $\Delta t_p = O(d/U)$, and the collision time step $\Delta t_c = O(d(\rho_p^2/E_p^2U)^{1/5})$, satisfy $\Delta t > \Delta t_p > \Delta t_c$, where L and U are characteristic length and velocity scales of the fluid flow. Here, ρ_p and E_p are the particle density and elastic modulus.

The fluid velocity **u** was interpolated from the Cartesian grid onto the particle locations with cubic accuracy using the M4′ method of Monaghan [38]. The dominant fluid-induced force is the drag force, given by the Stokes drag law for low particle Reynolds numbers as

$$\mathbf{F}_d = -3\pi d\mu(\mathbf{v} - \mathbf{u}). \tag{4-16}$$

Particle rotation relative to the fluid gives rise to a torque acting on the particles

$$\mathbf{M}_F = -\pi\mu d^3(\mathbf{\Omega} - \frac{1}{2}\boldsymbol{\omega}) \tag{4-17}$$

where $\boldsymbol{\omega}$ is the local fluid vorticity vector. Additional fluid-induced forces included in the computation include both the Saffman and Magnus lift forces [39-40], added mass force, and pressure gradient force, as discussed by Maxey and Riley [41].

The collision forces and torques include the normal Hertzian elastic force $F_{ne}\mathbf{n}$, the normal dissipative force $F_{nd}\mathbf{n}$, the force and torque resulting from resistance to sliding ($F_s\mathbf{t}_S$ and $aF_s(\mathbf{n}\times\mathbf{t}_S)$, respectively), and a torque $M_t\mathbf{n}$ associated with resistance to twisting, where a denotes the particle radius. The unit normal vector $\mathbf{n}$ is defined by $\mathbf{n}=(\mathbf{x}_j-\mathbf{x}_i)/\left|\mathbf{x}_j-\mathbf{x}_i\right|$, where $\mathbf{x}_i$ and $\mathbf{x}_j$ are the centroids of particles i and j, and the unit vector $\mathbf{t}_S$ indicates the direction of relative motion of the particle surfaces at the contact point projected onto the contact plane. The Hertzian expression [42] for elastic normal force of two colliding particles is

$$F_{ne}=-K\delta_N^{3/2}, \tag{4-18}$$

where the particle overlap $\delta_N=a_i+a_j-\left|\mathbf{x}_i-\mathbf{x}_j\right|$ is written in terms of the radii a_i and a_j of particles i and j. The nonlinear spring coefficient K can be expressed as $K=(4/3)E\sqrt{R}$, where the equivalent radius R and elastic modulus E are defined by

$$\frac{1}{R}\equiv\frac{1}{a_i}+\frac{1}{a_j}, \qquad \frac{1}{E}\equiv\frac{1-\sigma_i^2}{E_i}+\frac{1-\sigma_j^2}{E_j}. \tag{4-19}$$

Here, E_i and E_j are the Young's moduli and σ_i and σ_j are the Poisson's moduli of the two particles. The normal damping force F_{nd} is approximated by

$$F_{nd}=-\eta_N\,\mathbf{v}_R\cdot\mathbf{n}, \tag{4-20}$$

where $\mathbf{v}_R = \mathbf{v}_i - \mathbf{v}_j$ is the relative particle velocity, $\mathbf{v}_i$ and $\mathbf{v}_j$ are the particle centroid velocities, and the normal damping coefficient η_N can be related to the restitution coefficient *e* using an expression due to Tsuji et al. [43]. The current computations are performed with a fixed, small value of restitution coefficient ($e = 0.10$), which is consistent with the observation that particle collisions occur in this problem with small values of the Stokes number, $St = \rho_p d^2 U / 18 \mu L$.

A spring-dashpot-slider model is used to approximate the sliding resistance [44]. In this model, the sliding force F_s is first absorbed by the spring and dashpot until its magnitude reaches a critical value $F_{crit} = \mu_f |F_n|$. The friction coefficient μ_f is selected to have a value of 0.3, which is in approximately the middle of the range of typical values for dry surfaces discussed by Johnson [45]. If $|F_s| > F_{crit}$, then the colliding particle surfaces slip relative to each other and the friction coefficient is given by the Amonton expression

$$F_s = -F_{crit}. \tag{4-21}$$

For the subcritical case $|F_s| < F_{crit}$, the sliding resistance due to the spring and dashpot for particle *i* is given by

$$F_s = -k_T \left(\int_{t_0}^{t} \mathbf{v}_S(\xi)\, d\xi \right) \cdot \mathbf{t}_S - \eta_T \mathbf{v}_S \cdot \mathbf{t}_S, \tag{4-22}$$

where the slip velocity $\mathbf{v}_S(t)$ is defined by

$$\mathbf{v}_S = \mathbf{v}_R - (\mathbf{v}_R \cdot \mathbf{n})\mathbf{n} + a_i \boldsymbol{\Omega}_i \times \mathbf{n} + a_j \boldsymbol{\Omega}_j \times \mathbf{n} \tag{4-23}$$

and the slip direction is $\mathbf{t}_S = \mathbf{v}_S / |\mathbf{v}_S|$. The time integral in the first term in (4.22) gives the tangential elastic displacement of the material before slipping occurs, where t_0 is the time of initial particle impact. The expression for the tangential stiffness coefficient k_T derived by Mindlin [46] can be expressed as

$$k_T = 8G\sqrt{R\delta_N}\ , \tag{4-24}$$

where $G^{-1} \equiv \frac{2-\sigma_i}{G_i} + \frac{2-\sigma_j}{G_j}$ is the equivalent shear modulus and $G_i = E_i / 2(1+\sigma_i)$ and $G_j = E_j / 2(1+\sigma_j)$ are the shear moduli of the two particles. We follow Tsuji et al. [43] in assuming that the tangential dissipation coefficient is of the same order as the normal viscous damping coefficient, and thus set $\eta_T = \eta_N$.

Twisting occurs when the two colliding particles have different rotation rate in the direction **n**. The relative twisting rate Ω_T is defined by

$$\Omega_T = (\mathbf{\Omega}_i - \mathbf{\Omega}_j)\cdot\mathbf{n}, \tag{4-25}$$

The twisting resistance force is given by

$$M_t = -k_Q \int_{t_0}^{t} \Omega_T(\xi)\, d\xi - \eta_Q \Omega_T\ , \tag{4-26}$$

where the time integral represents the angular displacement prior to torsional sliding. Expressions for the torsional stiffness and viscous friction coefficient are similarly given by [47] $k_Q = k_T \delta_N R/2$ and $\eta_Q = \eta_T \delta_N R/2$. The particles begin to spin relative to each other when the torque exceeds a critical value, given by

$$M_{t,crit} = \frac{2}{3} F_{crit} \sqrt{\delta_N R}\ . \tag{4-27}$$

When $|M_t| > M_{t,crit}$, the torsional resistance is given by

$$M_t = -M_{t,crit}\Omega_T / |\Omega_T| . \tag{4-28}$$

4.4. Validation Test of SVS for Turbulent Planar Jet Flow

4.4.1. Direct Numerical Simulation

Direct numerical simulations were conducted for a particulate turbulent planar jet flow with one-way coupling between the fluid and particles, and the results were compared to SVS simulations of the same problem. The computational domain was discretized using a Cartesian grid over the intervals $-2 \le x/H \le 2$, $-3 \le y/H \le 3$ and $-2 \le z/H \le 2$, where H is the plane jet inlet slot width. Use of a uniform grid with (N_x, N_y, N_z) = (129, 193, 129) points for DNS led to grid increments that were nearly the same in all directions. The initial jet Reynolds number is given by $\mathrm{Re}_H = U_0 H/\nu = 3200$, where U_0 is the nominal jet velocity and ν is the kinematic viscosity. The initial mean velocity profile $U(z)$ was chosen to be of the hyperbolic tangent form

$$U(z) = \frac{U_0}{2} + \frac{U_0}{2}\tanh\left[\frac{H}{4\theta_0}\left(1 - \frac{2|y|}{H}\right)\right], \tag{4-29}$$

where θ_0 is the initial momentum thickness and the centerline of the jet corresponds to $y = 0$. For the current computations, we select $H/\theta_0 = 35$, for which value da Silva and Pereira [48] show that the most unstable Kelvin-Helmholtz instability wavelength is $\lambda_{KH} = 0.87H$, which is less than one-quarter the grid domain length in the streamwise direction. The DNS simulations were performed using a fixed time step of $\Delta t = 0.005 H/U_0$, which was selected to yield a CFL number less than 0.1. In the

following, length, velocity and time are nondimensionalized by H, U_0 and H/U_0, respectively.

Results for time variation of the turbulent kinetic energy q, the dissipation rate per unit mass ε, and enstrophy per unit volume Ω for the jet flow are shown in Figure 4.3, defined by

$$E = \frac{1}{2V_{ave}} \int_V \mathbf{u} \cdot \mathbf{u} \, dv, \qquad \varepsilon = \frac{2\nu}{V_{ave}} \int_V D_{ij} D_{ij} \, dv, \qquad \Omega = \frac{1}{2V_{ave}} \int_V \boldsymbol{\omega} \cdot \boldsymbol{\omega} \, dv, \quad (4\text{-}30)$$

where D_{ij} are the components of the rate of deformation tensor, $\mathbf{u}$ and $\boldsymbol{\omega}$ are the velocity and vorticity vectors, respectively, and V_{ave} is the averaging volume. Since we want these measures to be independent of the size of the computational domain, we performed the averaging only over the region $-1 \le y \le 1$ initially occupied by the jet. The turbulent kinetic energy initially increases as the turbulence develops in the jet, up to about a time of $t \cong 10.5$, at which the peak value of q is observed. It then gradually decreases for times greater than about 10 as the turbulence within the jet decays. The time variation of dissipation rate and enstrophy also exhibit an increase at the beginning of the computation, a peak and then a gradual decrease, although the peak value for enstrophy and dissipation rate occurs a little later than for kinetic energy (close to $t \approx 12$).

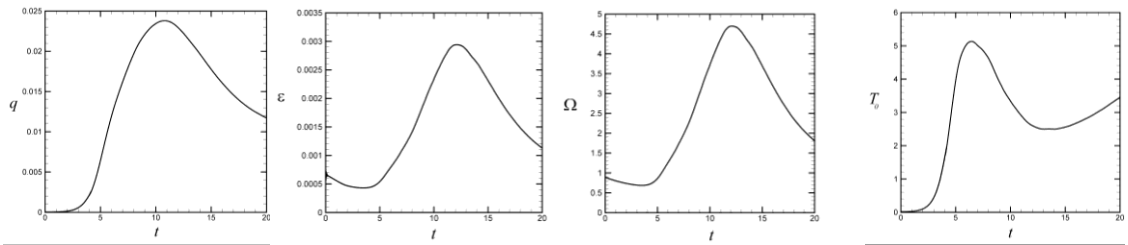

(a) (b) (c) (d)

Figure 4.3. Plots showing time variation of the (a) turbulent kinetic energy q, (b) dissipation rate ε, (c) enstrophy Ω, and (d) integral time scale T_0 from the DNS computation.

Contours of velocity magnitude at a series of times during the jet development are shown for both the DNS computation and the comparison SVS computation over a series of times in Figure 4.4. These contours illustrate the development of instability and turbulence at the beginning of the run ($t \leq 10$), followed by decay of both the mean jet velocity and the turbulence within the jet at later times ($t \geq 15$). The turbulence decay is accompanied by outward spreading of the turbulent velocity field and decrease in velocity magnitude values within the central region of the jet. The jet decay is often characterized in the similarity theory by two time-varying parameters – the centerline velocity U_C and the distance $\delta_{1/2}$ from the centerline at which the mean velocity equals one-half the centerline value. The former of these parameters characterizes the jet strength and the latter characterizes the jet width. It is recalled that in their experiments with a spatially-varying planar jet, Gutmark and Wygnanski [49] observed that $\delta_{1/2}$ and $1/U_C^2$ both vary approximately linearly with distance. This observation suggests that by replacing the downstream coordinate of the spatially-varying jet in Gutmark and Wygnanski's experiments with the product $U_0 t$, where U_0 is the initial centerline velocity, a linear variation for $\delta_{1/2}$ and $1/U_C^2$ with time might be observed for the current problem of a temporally-varying jet. Figure 4.5 plots time variation of both $\delta_{1/2}$ and $1/U_C^2$, exhibiting nearly linear variation in time in both cases.

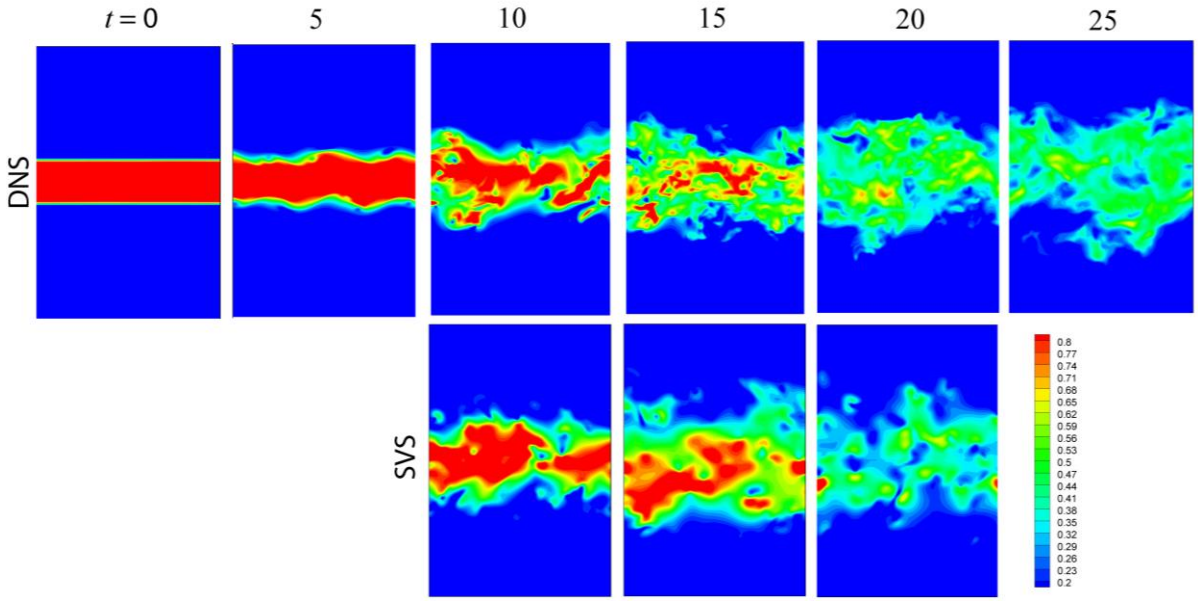

Figure 4.4. Time series of contour plots of the velocity magnitude illustrate the flow field for DNS (top row) at t = 0, 5, 10, 15, 20, and 25 and SVS Case S (bottom row) at t = 10, 15 and 20.

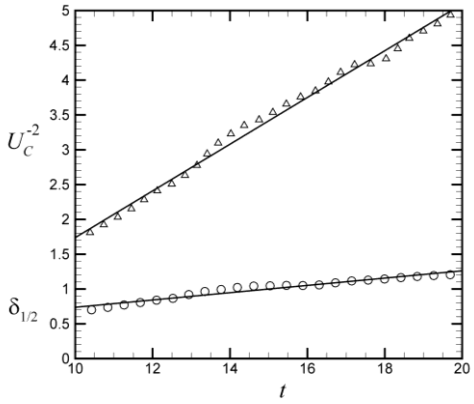

Figure 4.5. Plot of the DNS predictions for the inverse square of the centerline velocity U_C^{-2} (deltas) and jet width measure $\delta_{1/2}$ (circles) as functions of time. The solid lines are best-fit lines. The observation of linear variation of these parameters agrees with experimental observations of Gutmark and Wygnanski [49].

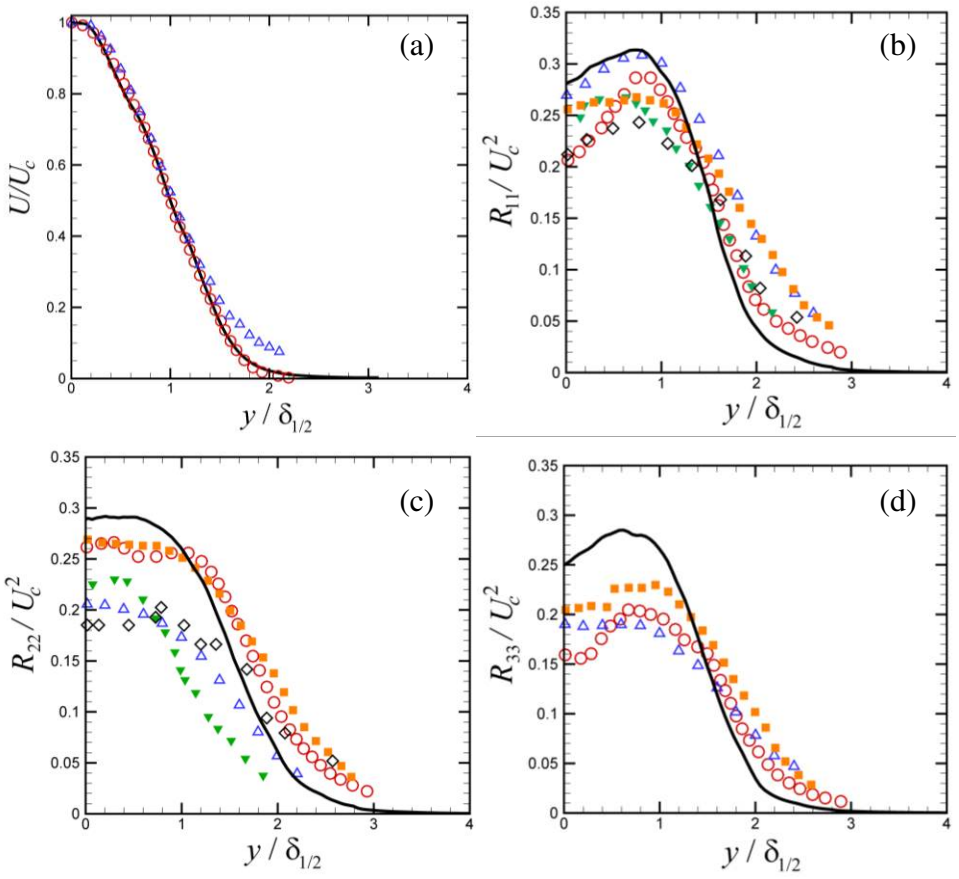

Figure 4.6. Comparison of our DNS results for the planar jet flow (black line) with results of other investigators for (a) mean velocity, (b) Reynolds stress R_{11}, (c) Reynolds stress R_{22}, and (d) Reynolds stress R_{33}. The comparison data includes experimental results from Gutmark and Wygnanski [49] (blue deltas) and Ramaprian and Chandrasekhara [50] (solid diamonds) and computational results from da Silva and Pereira [48] (red circles), Stanley et al. [51] (orange squares), and Thomas and Prakash [52] (green gradients).

A comparison of the mean velocity and normal Reynolds stresses from our DNS computations with results from previous experimental and numerical studies is given in Figure 4.6. The values are non-dimensionalized using $U_C(t)$ and $\delta_{1/2}(t)$ to write them be in similarity form, and we have confirmed that the results are nearly independent of time during the similarity regime of the computation ($10 \le t \le 20$). The mean velocity curve from our DNS results is very close to the mean velocity in the comparison studies. The

normal Reynolds stress results are also reasonably close to the values in the comparison studies, although the Reynolds stresses exhibit more scatter among the different studies than do the mean flow results.

4.4.2. Comparison of DNS Flow Field to SVS Results

The grid used for the SVS computations had (N_x, N_y, N_z) = (128, 128, 128) points. It is a requirement of the accelerated method used for the SVS method that the number of points on each side be a multiple of two. The SVS simulations were conducted using the DNS Reynolds stress results over the interval $10 \le t \le 20$ for which the similarity solution was found to be valid in the DNS results. Before this time period the DNS results show that the turbulence is still developing, and after this time period the turbulence exhibits rapid dissipation. The Reynolds stress predictions from DNS were written in dimensionless similarity form (as shown in Figure 4.6) and averaged over the computational time period $10 \le t \le 20$, in order to smooth out temporal fluctuations. These averaged Reynolds stresses in similarity form were then read into the SVS simulations, along with the DNS predictions for $U_C(t)$ and $\delta_{1/2}(t)$ shown in Figure 4.5, and used to generate time-varying prescribed Reynolds stress profiles for use during the SVS computation. The SVS computation was initialized with a prescribed number N_V vortices positioned randomly in the SVS domain. The vortex strength and orientation was set using the prescribed Reynolds stress field at $t = 10$, obtained from the DNS results as described above, using the inversion method described in Section 4.2.1. A plot showing the initial strength distribution and initial orientation of the SVS vortices is given in Figure 4.7. While the vortices were located throughout the computational domain, the

vortices with significant strength were located primarily within the interval $-1 \le y \le 1$. All initial vortices were randomly assigned an initial 'age', which advanced with time during the computation. When a vortex age exceeded the prescribed vortex lifespan T_V, the vortex was removed and a new vortex was introduced at a random location within the computational domain. The strength and orientation of the new vortex were again set using the procedure described in Section 4.2.1 using the prescribed Reynolds stress field for the time that the vortex is introduced. Consequently, as the turbulence decays in time during the SVS computation, the strength of the newly initiated SVS vortices generally decreases at a given position in the flow field. A series of SVS computations with different values of N_V and T_V were performed, as listed in Table 4.3. The 'standard' SVS computation (Case S) was selected as one with $N_V = 1024$ and T_V equal to the integral time scale T_0 at $t = 10$.

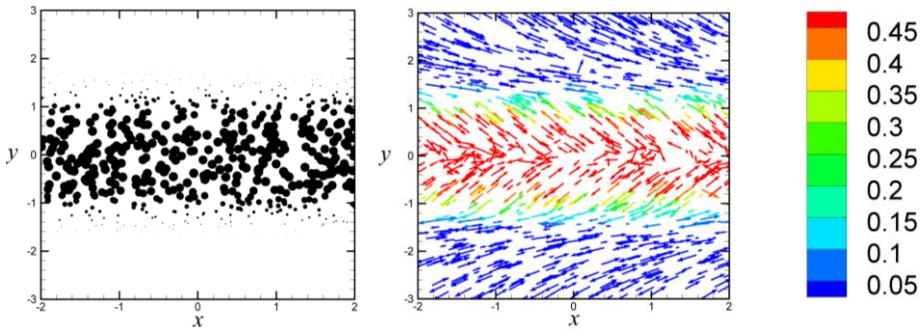

Figure. 4.7. (a) Scatter plot showing SVS vortex locations, with size of the scatter symbol proportional to the vortex strength. (b) Vector plot showing vortex orientation vector in the *x*-*y* plane, colored to identify vortex strength.

Table 4.3. Computational parameters used for the SVS simulations.

Case	Number of vortices, N_V	Vortex life time, T_V / T_0
S	1024	1
NV.1	256	1
NV.2	512	1
NV.3	2048	1
NV.4	4096	1
T.1	1024	0.25
T.2	1024	0.5
T.3	1024	1.5
T.4	1024	2

A comparison of the time variation of the velocity magnitude contours for the SVS generated flow field at t = 10, 15 and 20 is given in Figure 4.4 immediately below the DNS plot at the same time (and using the same color scale). We do not expect exact agreement since the SVS vortex structures are randomly distributed in space, but it is noted that the velocity magnitudes and general tendencies of the SVS generated flow field is similar to the DNS flow. In both cases the simulated jet turbulence gradually spreads in the y-direction and decays over this time interval. As would be expected from the uniform vortex size used in the SVS formulation, we observe that the DNS flow field results in Figure 4.4 exhibit more small-scale structures than do the SVS flow fields.

A plot showing the time variation of the jet centerline velocity U_c and the jet width measure $\delta_{1/2}$ is given in Figure 4.8. The value of U_c decreases during the time interval and the value of $\delta_{1/2}$ increases, as expected for decaying turbulence. The SVS predictions for U_c and $\delta_{1/2}$ are observed to be significantly noisier than the DNS predictions. This noise in the SVS predictions is associated with the 'death' of some

vortices and the 'birth' of new vortices at random positions in the flow field. The SVS predictions for U_c fluctuate closely about the DNS results. The SVS predictions for $\delta_{1/2}$ are also close to the DNS predictions in the beginning part of the computation ($t \le 14$), but by the end of the computation the predicted jet width measure for SVS is about 10% lower than that for DNS. Similar fluctuations in the SVS predictions are shown in Figure 4.9a, in which we compare the time variation of the turbulent kinetic energy for the DNS and SVS computations. The SVS result is again observed to fluctuate around the smoother DNS prediction, with a root-mean-square value that decreases when the value of the vortex lifetime T_V is reduced. The power spectrum is plotted in Figure 4.9b at time $t = 15$ for both the DNS and SVS computations. Both computations exhibit a $k^{-5/3}$ Kolmogorov spectrum in the inertial range, with DNS and SVS spectra in close agreement. At high wavenumber, the SVS spectrum reduces much faster than the DNS spectrum as a consequence that SVS contains only vortices with length and velocity scaled to the integral scale eddies.

A comparison of the time-averaged Reynolds stresses, nondimensionalized using the similarity variables, is given for DNS and SVS in Figure 4.10. The DNS values of U_c and $\delta_{1/2}$ are used to write the Reynolds stresses and lateral distance in similarity form for both computations. The three normal Reynolds stress values are very close for the DNS and SVS predictions. The SVS prediction for the dimensionless Reynolds shear stress R_{12}/U_c^2 exhibits lower peak values than for the DNS predictions, but otherwise has the same form.

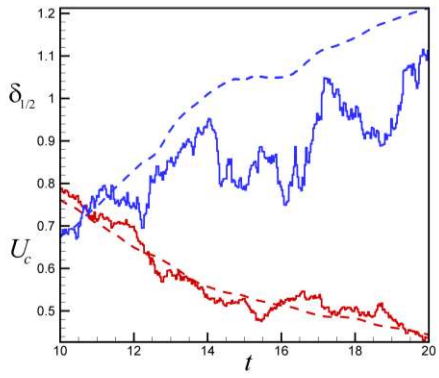

Figure. 4.8. Predicted values of centerline velocity $U_c(t)$ (red, lower curves) and jet width measure $\delta_{1/2}(t)$ (blue, upper curves) as functions of time for DNS (dashed lines) and SVS case S (solid lines).

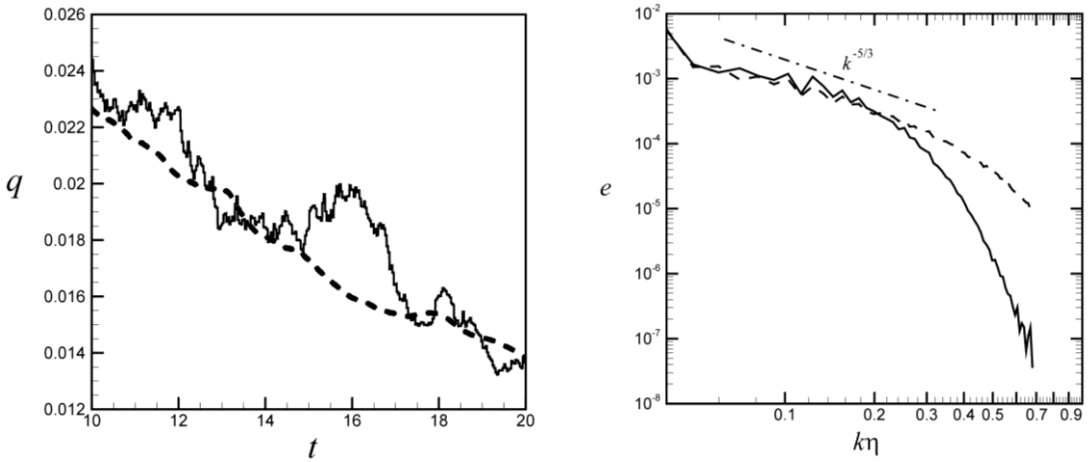

Figure. 4.9. Comparison of (a) the prescribed turbulent kinetic energy q and (b) the power spectrum from direct numerical simulation (dashed line) and the predicted value using the SVS method (solid line) for case S in Table 4.3.

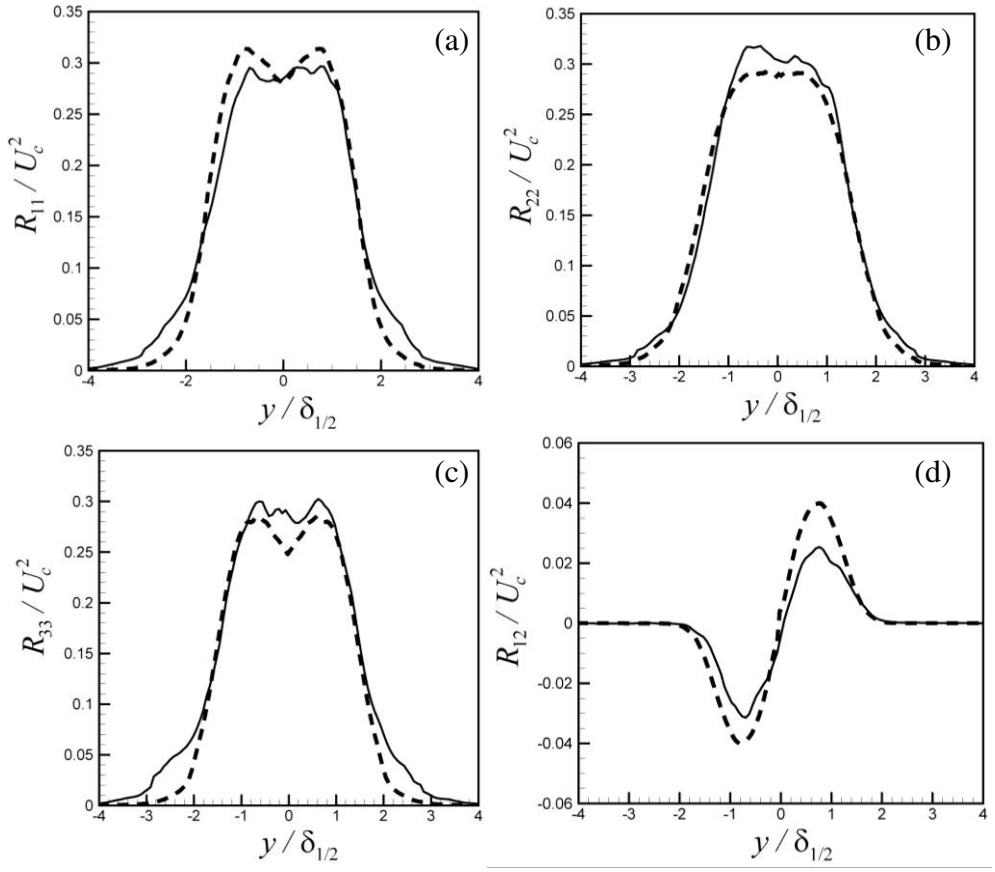

Figure. 4.10. Comparison of the DNS results (dashed line) and the similarity solution with case S (solid line) for dimensionless Reynolds stresses R_{ij}, plotted using similarity scaling and averaged over the time period (10,20). Plots are for (*i,j*) values of (a) (1,1), (b) (2,2), (c) (3,3) and (d) (1,2).

4.4.3. Comparison of DNS Particle Transport to SVS Results

An initial DNS flow computation was conducted out to a time of $t = 10$ with no particles in order to allow the turbulence to develop and to achieve a self-similar state. The DNS computation was then restarted with particles present and continued out to a time $t = 20$. A total of $N_p = 32{,}000$ particles of diameter $d = 0.04$ and density ratio $\chi = \rho_f / \rho_p = 1$ were used. The particles were initially placed randomly within the region

$-1 \le y \le 1$ covering the jet. The particle Stokes number based on the jet width scaling, St_H, is given by

$$\mathrm{St}_H = \frac{\rho_p d^2 U_0}{18 \mu H} = \frac{1}{18\chi} \mathrm{Re}_H (d/H)^2 = 0.28 . \tag{4-31}$$

Particle initial positions were identical for both the DNS and SVS simulations.

The particle concentration profile in y was computed by dividing the flow field into bins, and then adding the volume of particles contained in each bin. For particles that straddle the boundary between bins, the particle volume is divided along the bin boundary and only that portion of the volume lying in each bin is included in the sum. The concentration field for SVS and DNS is identical at the initial time $t = 10$, and has a top-hat form as shown in Figure 4.11a. During the time period of the flow computation $10 \le t \le 20$ the concentration field spreads outward into the lateral regions around the jet due to forcing by the jet turbulence. The resulting concentration field for both DNS and SVS computations at time $t = 20$ is plotted in Figure 4.10b, exhibiting excellent agreement between the two methods. This comparison demonstrates that the SVS method accurately simulates dispersion of the particle field.

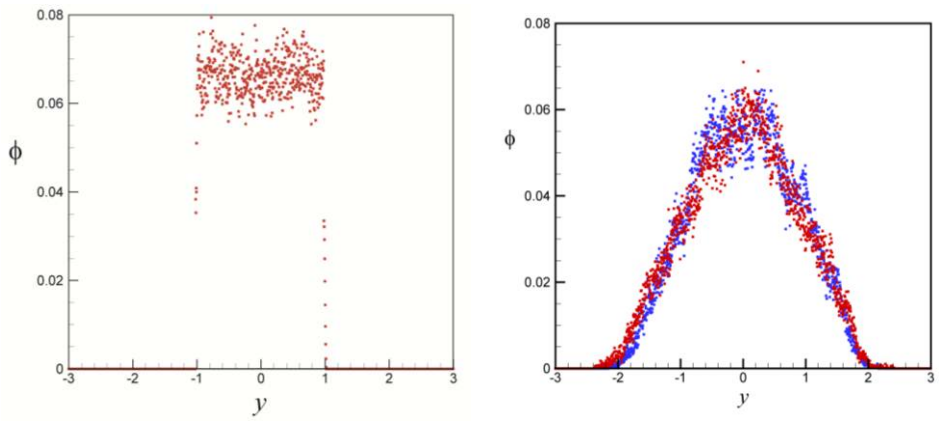

Figure. 4.11. Particle positions (a) at the start of the particle runs at $t = 10$ and (b) at the end of the run at $t = 20$ for DNS (red) and SVS case S (blue). (The particle positions at $t = 10$ are the same for DNS and SVS.)

Another way to examine particle dispersion is to calculate the root-mean-square particle position y_{rms}, defined by

$$y_{rms} = \sqrt{\frac{1}{N_p}\sum_{n=1}^{N_p} y_{n,par}^2}\,, \tag{4-32}$$

where $y_{n,par}$ denotes the *y*-position of particle *n*. A comparison of y_{rms} as a function of time for DNS and for a variety of SVS computations with different parameter values is plotted in Figure 4.12. Figure 4.12a shows the effect of number of vortices N_V on the lateral particle dispersion in cases with $T_V = T_0$. As the number of vortices decreases the strength of each vortex is increased so as to hold the turbulent kinetic energy fixed. As can be seen, cases with smaller number of vortices (e.g., N_V =256) exhibit slower lateral dispersion, resulting in lower values of y_{rms} at the given time than the DNS predictions. At higher number of vortices, the predictions of the various SVS computations appear to

converge to a value of y_{rms} that is close to the DNS prediction up to a time of about $t = 17$, after which the SVS predictions are somewhat less than that for DNS. Figure 4.12b shows the effect of vortex lifetime on lateral particle dispersion. Increase in vortex lifetime is found to increase the rate of particle dispersion from the center of the jet, up to a lifetime value of about $T_V = 1.5T_0$, above which the particle dispersion rate remains close to the DNS prediction. This increase in dispersion rate occurs because longer residence of strong vortices near the jet center allows them longer time to repel particles via centrifugal force. We also note that the turbulent kinetic energy in the SVS computation increases (above the DNS prediction) as the vortex lifetime is increased significantly above the integral time scale T_0, which also increases the lateral dispersion rate.

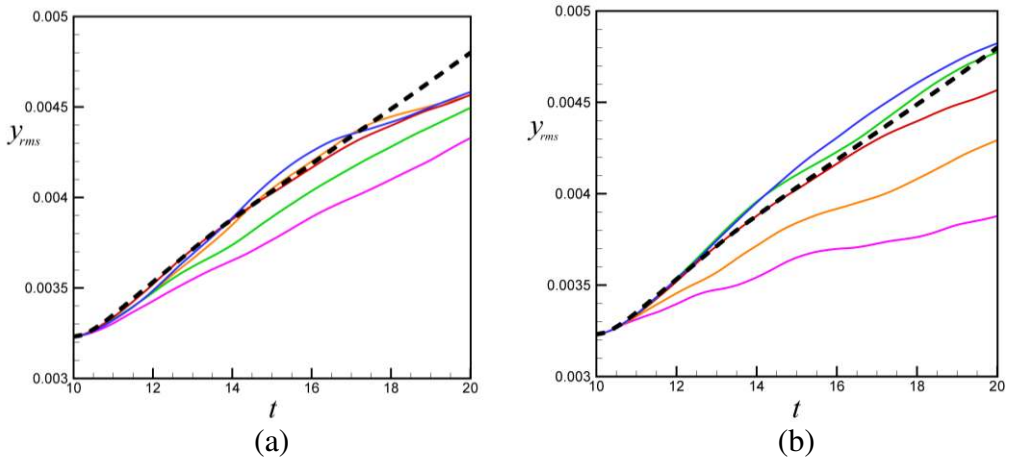

Figure 4.12. Time variation of the root-mean-square particle position in the lateral *y*-direction for DNS (dashed line) and for SVS with (a) different number of vortices and (b) different vortex lifetime. Plot (a) is for Cases NV.1 (pink), NV.2 (orange), S (red), NV.3 (green) and NV.4 (blue). Plot (b) is for Cases T.1 (pink), T.2 (orange), S (red), T.3 (green), and T.4 (blue).

The total number of particle collisions is plotted as a function of time in Figure 4.13 for DNS and for a variety of SVS computations with different values of N_V and T_V. Figure 4.13a shows that the number of collisions in SVS computations is lower than for DNS for small numbers of vortices, but that the collision number increases to close to the DNS results as the number of vortices increases. Variation of vortex lifetime is seen in Figure 4.13b to have little effect on the number of particle collisions, which we believe to be a consequence of two opposing influences. As discussed previously, increasing the vortex lifetime tends to disperse the particles more rapidly in *y*-direction, consequently decreasing particle concentration and leading to lower numbers of collisions. On the other hand, increasing the vortex lifetime also introduces a lag that increases the turbulent kinetic energy slightly in a decaying turbulent flow, resulting in an increase in number of particle collisions. These two phenomena counteract each other, so that little change in collision number with vortex lifetime is observed in Figure 4.13b.

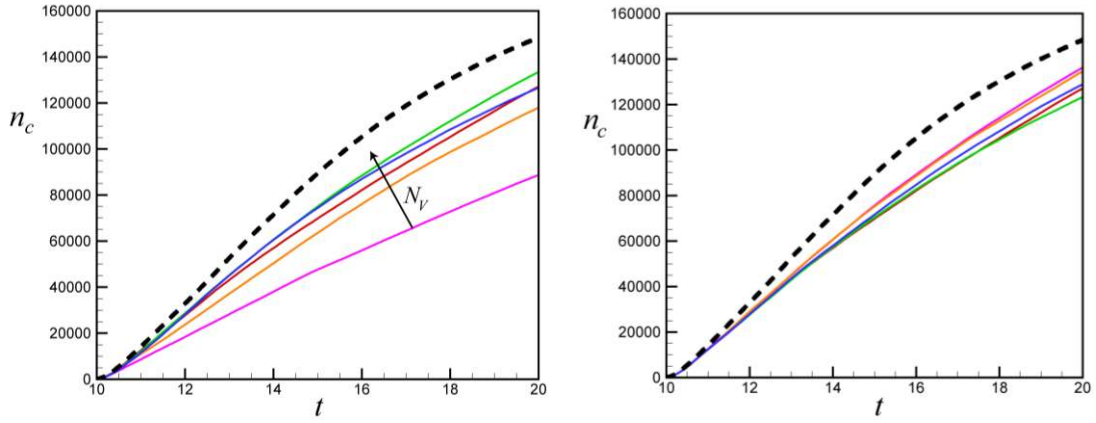

Fig 4.13. Time variation of the number of collision for DNS (dashed line) and for SVS with (a) different number of vortices and (b) different vortex lifetime. Plot (a) is for Cases NV.1 (pink), NV.2 (orange), S (red), NV.3 (green) and NV.4 (blue). Plot (b) is for Cases T.1 (pink), T.2 (orange), S (red), T.3 (green), and T.4 (blue).

The tendency of particles to cluster can be characterized by the radial distribution function (RDF), $g(r)$, which is defined by

$$g(r) = \frac{1}{4\pi\rho_0 r^2}\frac{dN}{dr}, \tag{4-33}$$

where the average number of particles per unit volume ρ_0 is related to the particle volume fraction C_p by $\rho_0 = 6C_p/\pi$, and $N(r)$ is obtained by computing the average number of neighboring particles whose centroids are located within a radial distance *r* from a given particle centroid. In order to smooth the RDF values, we have averaged the predicted RDF for both DNS and SVS over the time interval $14 \le t \le 16$, which was selected because this time interval is in the middle of the computational interval ($10 \le t \le 20$). It is sufficiently small that the turbulence kinetic energy does not change by a large amount, and yet it is also sufficiently large that noticeable smoothing of the data is observed. The radial distribution function is plotted in Figure 4.14 for both DNS and SVS computations, and found to compare well. The RDF peak in the SVS computations is a little higher than the DNS result, which might be a consequence of the observation that DNS was observed to disperse particles a little more rapidly in the lateral *y*-direction, and so the resulting concentration is slightly lower, but the effect is small.

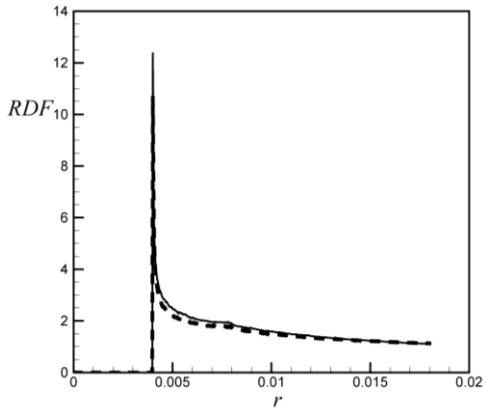

Figure 4.14. Comparison between our DNS results (dashed line) and SVS case S (solid line) for the radial distribution function (RDF) a function of distance r. The data are averaged over the time interval from t = 14 to 16.

4.5. Conclusions

The paper presents a novel inverse method by which the orientation and strength of a set of finite-length vortices can be set to reproduce a prescribed anisotropic Reynolds stress field. This inverse method was incorporated into the stochastic vortex structure (SVS) algorithm to generate a time-varying synthetic turbulence field for transport of interacting particles in anisotropic, non-homogeneous turbulent flows. The proposed SVS method is well suited for simulation of interacting particles, since the statistics of the generated synthetic turbulence are both structurally and temporally consistent with the original turbulence and it can be computed rapidly with use of the fast multipole accelerated method [28]. It has been previously demonstrated [27, 28] for homogeneous, isotropic turbulence that the SVS method accurately reproduces the turbulence energy spectrum, the probability density function of the acceleration, velocity and vorticity fields, the collision rate of advected particles, and a variety of agglomeration measures (fractal dimension, size distribution, etc.) for adhesive particles. The current paper

extends the SVS approach to make it a viable method for arbitrary turbulent flows, and not only for homogeneous turbulence.

The effectiveness of the proposed inverse method was demonstrated in a series of computational experiments. We first examined the accuracy of the inverse method for an anisotropic, but homogenous, turbulent field with different prescribed values of the Reynolds stresses. Next, we examined the performance of the inversion procedure for setting the initial vortex orientation and strength in two different nonhomogeneous turbulent shear flows. Prescribed and predicted Reynolds stresses were compared for the above cases and show good agreement. Finally, the SVS predictions for flow and particle transport in a planar turbulent jet flow were compared with direct numerical simulation (DNS) results. The SVS computations used the Reynolds stress profiles computed from DNS together with our inverse procedure to specify the initial orientation and strength of the stochastic vortices, both at the start of the computation and when new vortices were introduced during the computation. The Reynolds stress profiles of both DNS and SVS computations were normalized in similarity form and averaged over the duration of the SVS computation, and found to compare well. Measures of particle dispersion, clustering and collision during the SVS and DNS computations were also found to be in good agreement. The effect on the SVS predictions of variation of the number and lifetime of vortices was also investigated, as these are two important numerical parameters that must be specified in the SVS computations. Computations with small numbers of vortices yield too low collision rate and weak dispersion, but the results approach the DNS predictions as the number of vortices is increased. The particle dispersion predictions were poor when the vortex lifetime was significantly below the turbulence integral time

scale, but values near the integral time scale up to about twice the integral scale yielded acceptable results. The number of particle collisions was not sensitive to the vortex lifetime.

With the extension to anisotropic, nonhomogeneous turbulence described in the current paper, the stochastic vortex structure method offers an accurate, viable method for simulation of the subgrid fluctuation effects on interacting particles in a large range of turbulent flows. However, we should note that the method in its current form does have a number of restrictions which arise from the fact that all turbulence fluctuations are generated by a set of tubular vortices in the SVS formulation. Consequently, the method is not well suited for simulating the near-wall region of wall bounded turbulent flows and would not be able to satisfy the no-slip condition on the wall, although the method might be expected to perform well in the boundary layer wake region. Secondly, the SVS method has to date only been used for problems with one-way coupling between the fluid and the particles. It is possible that Stokesian dynamics methods, or related methods based on Oseenlet solutions [53-56], could be used to account for two-way coupling (e.g., within agglomerates) within the framework of the SVS method, but this has not yet been attempted. As mentioned in Section 4.2.2.1, the method also has some limitations for the inversion procedure used to set the initial vortex orientation, which stem from restrictions on the amount of anisotropy that one can achieve using only vortex tubes to generate the fluctuating turbulence field. In the current formulations the SVS method is designed to be used together with a RANS simulation, for which only the mean flow and averaged measures of turbulent kinetic energy, etc., are known. A similar problem of accounting for effect of sub-grid scales on particle transport exists for large-eddy simulations, but in

this case it is not clear whether injection of stochastic subgrid-scale vortices or other methods, such as the approximate deconvolution method of Shotorban and Mashajek [57], would be the most suitable approach.

Acknowledgements

The authors are grateful for the assistance of Mr. Xing Jin and Mr. Ran Tao during the early stages of the paper. This research was supported by the U.S. National Science Foundation under grant CBET-1332472.

References

[1] Jin, G., He, G.W., and Wang, L.P., Large-eddy simulation of turbulent collision of heavy particles in isotropic turbulence. *Physics of Fluids* **22**, 055106 (2010).

[2] Loth, E., Numerical approaches for motion of dispersed particles, droplets and bubbles. *Progress in Energy and Combustion Science* **26**, 161-223 (2000).

[3] Bec, J., Biferale, L., Cencini, M., Lanotte, A., Musacchio, S., and Toschi, F., Heavy particle concentration in turbulence at dissipative and inertial scales. *Physical Review Letters* **98**, 084502 (2007).

[4] Collins, L.R. and Keswani, A., Reynolds number scaling of particle clustering in turbulent aerosols. *New Journal of Physics* **6**, 119 (2004).

[5] Falkovich, G., and Pumir, A., Intermittent distribution of heavy particles in a turbulent flow. *Physics of Fluids* **16**(7), L47-L50 (2004).

[6] Grits, B., Pinsky, M., and Khain, A., Investigation of small-scale droplet concentration inhomogeneities in a turbulent flow. *Meteorol Atmos Phys* **92**, 91-204 (2006).

[7] Squires, K.D., and Eaton, J.K., Preferential concentration of particles by turbulence. *Physics of Fluids A* **3**, 1169-1178 (1991).

[8] Reade, W.C. and Collins, L.R., A numerical study of the particle size distribution of an aerosol undergoing turbulent coagulation. *Journal of Fluid Mechanics* **415**, 45-64 (2000).

[9] Sundaram, S. and Collins, L.R., Collision statistics in an isotropic particle-laden turbulent suspension. I. Direct numerical simulations. *Journal of Fluid Mechanics* **335**, 75-109 (1997).

[10] Townsend, A.A., On the fine scale of turbulence. *Proceedings of the Royal Society of London A* **208**, 534-542 (1951).

[11] Lundgren, T.S., Strained spiral vortex model for turbulent fine structure. *Physics of Fluids* **25**(12), 2193-2203 (1982)

[12] Pullin, D.I., and Saffman, P.G., On the Lundgren-Townsend model of turbulent fine scales. *Physics of Fluids* **5**(1), 126-145 (1993).

[13] Saffman, P.G., Vortex models of isotropic turbulence. *Philosophical Transactions of the Royal Society of London A* **355**, 1949-1956 (1997).

[14] Jiménez, J., Wray, A.A., Saffman, P.G., and Rogallo, R.S., The structure of intense vorticity in isotropic turbulence. *Journal of Fluid Mechanics* **255**, 65-90 (1993).

[16] Kambe, T., and Hatakeyama, N., Statistical laws and vortex structures in fully developed turbulence. *Fluid Dynamics Research* **27**, 247-267 (2000).

[17] Kivotides, D., and Leonard, A., Quantized turbulence physics. *Physical Review Letters* **90**(23), 234503 (2003).

[18] Hatakeyama, N., and Kambe, T., Statistical laws of random strained vortices in turbulence. *Physical Review Letters* **79**(7), 1257-1260 (1997).

[19] Malik, N.A., and Vassilicos, J.C., Eulerian and Lagrangian scaling properties of randomly advected vortex tubes. *Journal of Fluid Mechanics* **326**, 417-436 (1996).

[20] Min, I.A., Mezić, I., and Leonard, A., Lévy stable distributions for velocity and vorticity difference in systems of vortex elements. *Physics of Fluids* **8**, 1169-1180 (1996).

[21] Wilczek, M., and Friedrich, R., Dynamical origins for non-Gaussian vorticity distributions in turbulent flows. *Physical Review E* **80**, 016316 (2009).

[22] Wilczek, M., Jenko, F., and Friedrich, R., Lagrangian particle statistics in turbulent flows from a simple vortex model. *Physical Review E* **77**, 056301 (2008).

[23] Bernard, P.S., Grid-free simulation of the spatially growing turbulent mixing layer. *AIAA Journal* **46**(7), 1725-1737 (2008).

[24] Bernard, P.S., Vortex filament simulation of the turbulent coflowing jet. *Physics of Fluids* **21**, 025107 (2009).

[25] Bernard, P.S., Collins, P., and Potts, M., Vortex filament simulation of the turbulent boundary layer. *AIAA Journal* **48**(8), 1757-1771 (2010).

[26] Ayyalasomayajula, S., Warhaft, Z., and Collins, L.R., Modeling inertial particle acceleration statistics in isotropic turbulence. *Physics of Fluids* **20**, 095104 (2008).

[27] Sala, K., and Marshall, J.S., Stochastic vortex structure method for modeling particle clustering and collisions in homogeneous turbulence. *Physics of Fluids* **25**(10), 103301 (2013).

[28] Dizaji, F.F., and Marshall, J.S., An accelerated stochastic vortex structure method for particle collision and agglomeration in homogeneous turbulence. *Physics of Fluids* **28**, 113301 (2016).

[29] Salmon, J.K., and Warren, M.S., Skeletons from the treecode closet. *Journal of Computational Physics* **111**, 136-155 (1994).

[30] Greengard, L., and Rokhlin, V., A fast algorithm for particle simulations. *Journal of Computational Physics* **73**, 325-348 (1987).

[31] Marshall, J.S., Grant, J.R., Gossler, A.A. and Huyer, S.A., Vorticity transport on a Lagrangian tetrahedral mesh. *Journal of Computational Physics* **161**, 85-113 (2000).

[32] Rai, M., and Moin, P., Direct simulation of turbulent flow using finite-difference schemes. *Journal of Computational Physics* **96**, 15–53 (1991).

[33] Verzicco, R., and Orlandi, P., A finite-difference scheme for three-dimensional incompressible flows in cylindrical coordinates. *Journal of Computational Physics* **123**, 402-414 (1996).

[34] Uhlmann, M., An immersed boundary method with direct forcing for the simulation of particulate flows. *Journal of Computational Physics* **209**, 448-476 (2005).

[35] Lele, S.K., Compact finite difference schemes with spectral-like resolution. ***Journal of Computational Physics*** 103**(1), 16-42 (1992).**

[36] Steijl, R., Computational Study of Vortex Pair Dynamics. Ph.D. Dissertation, University of Twente, Enschede, The Netherlands, p. 64 (2001).

[37] Smirnov, A., Shi, S., and Celik, I., Random flow generation technique for large eddy simulations and particle-dynamics modeling. *Journal of Fluids Engineering* **123**, 359-371 (2001).

[38] Monaghan, J.J., Extrapolating B splines for interpolation. *Journal of Computational Physics* **60**, 253-262 (1985).

[39] Saffman, P.G., The lift on a small sphere in a slow shear flow. *Journal of Fluid Mechanics* **22**, 385-400 (1965).

[40] Rubinow, S.I., and Keller, J.B., The transverse force on a spinning sphere moving in a viscous fluid. *Journal of Fluid Mechanics* **11**, 447-459 (1961).

[41] Maxey, M.R., and Riley, J.J., Equation of motion for a small rigid sphere in a non-uniform flow. *Physics of Fluids* **26**, 883-889 (1983).

[42] Hertz, H., Über die Berührung fester elastischer Körper. *J. reine und angewandte Mathematik* **92**, 156-171 (1882).

[43] Tsuji, Y., Tanaka, T., and Ishida, T., Lagrangian numerical simulation of plug flow of cohesionless particles in a horizontal pipe. *Powder Technology* **71**, 239-250 (1992).

[44] Cundall, P.A., and Strack, O.D.L., A discrete numerical model for granular assembles. *Geotechnique* **29**(1), 47-65 (1979).

[45] Johnson, K.L., 1985. *Contact Mechanics*. Cambridge University Press, New York, 204-210.

[46] Mindlin, R.D., 1949. Compliance of elastic bodies in contact. *Journal of Applied Mechanics* 16, 259-268.

[47] Marshall, J.S., Discrete-element modeling of particulate aerosol flows. *Journal of Computational Physics* **228**, 1541-1561 (2009).

[48] da Silva, C.B. and Pereira, J.C.F., Invariants of the velocity-gradient, rate-of-strain, and rate-of-rotation tensors across the turbulent/nonturbulent interface in jets. *Physics of Fluids* **20**, 055101 (2008).

[49] Gutmark, E. and Wygnansky, I., The planar turbulent jet. *Journal of Fluid Mechanics* **73**, 465-495 (1976).

[50] Ramaprian, B.R. and Chandrasekhara, M.S., LDA measurements in plane turbulent jets. *ASME Journal of Fluids Engineering* **107**, 264-271 (1985).

[51] Stanley, S., Sarkar, S., and Mellado, J.P., A study of the flowfield evolution and mixing in a planar turbulent jet using direct numerical simulation. *Journal of Fluid Mechanics* **450**, 377-407 (2002).

[52] Thomas, F.O. and Prakash, K.M.K., An investigation of the natural transition of an untuned planar jet. *Physics of Fluids* A **3**, 90-105 (1991).

[53] Subramanian, G. and Koch, D.L., Evolution of clusters of sedimenting low-Reynolds-number particles with Oseen interactions. *Journal of Fluid Mechanics* **603**, 63-100 (2008).

[54] Pignatel, F., Nicolas, M., and Guazzelli, É., A falling cloud of particles at a small but finite Reynolds number. *Journal of Fluid Mechanics* **671**, 34-51 (2011).

[55] Yang, M., Li, S., and Marshall, J.S., Effects of long-range particle-particle hydrodynamic interaction on the settling of aerosol particle clouds. *Journal of Aerosol Science* **90**, 154-160 (2015).

[56] Faletra, M., Marshall, J.S., Yang, M., and Li, S., Particle segregation in falling polydisperse suspension droplets. *Journal of Fluid Mechanics* **769**, 79-102 (2015).

[57] Shotorban, B., and Mashayek, F., Modeling subgrid-scale effects on particles by approximate deconvolution. *Physics of Fluids* **17**, 081701 (2005).

Chapter 5: On the Significance of Two-Way Coupling in Simulation of Turbulent Particle Agglomeration

Farzad F. Dizaji and Jeffrey S. Marshall

Department of Mechanical Engineering, The University of Vermont,
Burlington, VT 05405, U.S.A.

Corresponding Author: Jeffrey S. Marshall, Department of Mechanical Engineering, The University of Vermont, Burlington, VT 05405, U.S.A. PHONE: 1 (802) 656-3826, EMAIL: jmarsha1@uvm.edu.

Abstract

A study is reported that examines computations of turbulent particle agglomeration with one-way and two-way phase coupling for cases with small overall particle concentration. The fluid flow was computed using a direct numerical computation using the point-force approximation for particle-induced body force, and a soft-sphere, adhesive discrete-element method was used to simulate the particulate transport and agglomerate formation. Computations were performed with different values of the Stokes number and the adhesion parameter. A variety of measures were used to examine both the effect of particle agglomeration on the fluid turbulence and the structure and flow field within the particle agglomerates. It was found that agglomeration has little influence on the attenuation of turbulence by the particles, at least in the range of Stokes numbers examined in the paper. Computations with two-way coupling generated agglomerates that were larger and contained more particles than those for one-way coupling. The agglomerate structure for both one-way and two-way coupling cases had a fractal structure with a similar value of the fractal dimension. As the agglomerate size increased, the fluid motion inside the agglomerates was found to become increasingly correlated to the agglomerate velocity, acting to decrease the relative velocity and shear stress of the inner particles within the agglomerate.

Keywords: particle agglomeration; collisions; turbulence modulation; fractal structure; turbulent agglomeration

5.1. Introduction

Particle agglomeration by fluid turbulence occurs in a large range of natural flow problems and industrial processes. Examples of natural processes include dispersion of atmospheric particulates, sediment transport and deposition in estuaries, removal of pollutants by sediment deposition in aquatic systems, particle transport from volcanic plumes, and agglomeration of ice crystals in the atmosphere during formation of snowflakes. The number of industrial processes involving turbulent agglomeration is immense, a few examples being fine particle separation in gas cyclones, wastewater treatment, additive manufacturing processes, flame synthesis of nanoparticles, and ash capture from combustion furnaces. Many industrial products are produced from powders or by precipitation from reactive solutions, examples including 3D printing, ceramic materials, catalysts, and many pharmaceutical products.

Numerous experimental studies have shown that the number of particles in an agglomerate tends to vary as a power-law function of the agglomerate size (e.g., as represented by the gyration radius), where the exponent of this power law (known as the fractal dimensional of the agglomerate group) is typically less than the dimension of the three-dimensional space in which the agglomerate is contained [1-3]. As a consequence, the average void fraction of the agglomerate increases as the number of particles within the agglomerate increases [4]. The value of the fractal dimension depends on the process by which the agglomerate was formed as well as the stage of the formation process. Typical values range from about 1.5 - 3.0 [5]. The effective mechanical properties of the agglomerate, such as the shear and elastic moduli, depend on the fractal dimension [6-8].

The fractal structure of the agglomerate also influences the density of force chains, which affects the shear stress necessary to induce agglomerate breakup and erosion [9-13].

Much of the theoretical and computational literature on turbulent agglomeration deals with the beginning stage of agglomeration, in which agglomerates are growing in size by collision of particles and of smaller agglomerates [14-19]. This literature uses several important approximations, including the approximation that two colliding particles will stick together, the approximation that an agglomerate can be represented by an equivalent spherical particle, and the approximation that the fluid turbulence is unaffected by the particle agglomeration process (one-way coupling). The particle collisions are typically assumed to be controlled by shear stress at the Kolmogorov scale, and various stochastic theories are used to model the particle collision rate, some of which (but not all) additionally assume small Stokes numbers. An experimental test of some of these stochastic collision rate theories was presented by Duru et al. [20] for aerosol droplets in oscillating grid turbulence. The experimental values were observed to be between 50-100% larger than the theoretical predictions of Chun and Koch [17], and in typical experiments the mean droplet size increased by about 3% during the experiment. A direct numerical simulation of the early stages of particle agglomeration was given by Reade and Collins [21], which again uses the equivalent sphere approximation and examines how the size distribution of the equivalent spheres varies with Stokes number.

There is an extensive literature examining the effect of particles on fluid turbulence. Reviews were given by Crowe [22], Eaton [23], Saber et al. [24], Poelma and Ooms [25], Rao et al. [26] and Balachandar and Eaton [27]. While most work has

focused on turbulence modulation by relatively dilute particulate suspensions, Nasr and Ahmadi [28] demonstrated the importance of including particle collisions in modeling particle effects on fluid turbulence. However, there is almost no research to date on the effect of particle agglomeration on turbulent flows. While one might proceed by employing the equivalent sphere approximation for the particle agglomerates and using existing literature for turbulence modulation from suspensions of individual particles, such an approach would neglect a number of fundamental physical aspects of particle agglomeration. Due to the fractal structure of turbulent agglomeration, the particle volume fraction within agglomerates varies strongly as a function of agglomerate size, which in turn has a strong influence on the effective particle mass and the properties controlling agglomerate deformation and breakup [6, 7, 8, 10, 11, 29] which would not be accurately represented by a set of equivalent spheres with uniform properties. Particle agglomerates are porous to various degrees, and depending on the agglomerate size and structure the flow through an agglomerate can have a significant effect on agglomerate response to turbulent fluctuations and to collisions with other agglomerates [30, 31]. Particle agglomerates are typically not spherical, but can be elongated or even have a convoluted structure with various branches. Finally, the bonds holding particles into an agglomerate can break, either due to fluid forces and due to collisions with other agglomerates, which might cause a gradual erosion of particles from the agglomerate or a sudden rupture of the agglomerate into some number of offspring agglomerates [12, 13, 32].

The current paper presents a computational study of turbulent agglomeration that resolves the individual agglomerate particles and their interactions with surrounding

particles. Since we do not invoke the approximation of treating the agglomerates as equivalent spheres, as used in previous research, important phenomena such as agglomerate permeability [30] and breakup [13] were included in the simulations without the need to introduce additional phenomenological models. A particular objective of the current paper is to examine the significance of two-way coupling on the turbulent agglomeration process, which was done by comparing results of computations performed with two-way coupling to those of computations conducted with one-way coupling, and by examining the flow field around the agglomerate structures that give rise to differences between the one-way and two-way coupling results. The computations were performed using a soft-sphere discrete element method (DEM) for adhesive particles subject to van der Waals adhesion [33], and the fluid flow computations were performed using a pseudo-spectral method to simulate forced turbulence in a triply-periodic domain. The two-way coupling effect of particle forces on the fluid flow was accounted for using an effective body force in the fluid flow simulations, similar to the approach used for simulation of sedimenting particle agglomerates by Bosse et al. [34]. The various computational methods used to simulate particle and fluid transport are summarized in Section 5.2, followed by results and discussion in Section 5.3. Section 5.3.1 examines the effect of turbulent agglomeration on modulation of the turbulence by the particulate phase. Section 5.3.2 examines various measures of agglomerate structure for cases with and without two-way coupling. Conclusions are given in Section 5.4.

5.2. Computational Methods

The computations of particle agglomeration were performed using an adhesive discrete element method (DEM) to model particle transport and collisions. Homogeneous

turbulence was simulated using a forced pseudo-spectral direct numerical simulation (DNS) method on a triply-periodic domain. Each of these methods has been described in detail elsewhere, but the key points and appropriate references are summarized below.

5.2.1. Discrete Element Method (DEM) for Particle Transport

The discrete-element method (DEM) of Marshall [33] was used to transport adhesive particles in the turbulent flow. The computational method uses a multiple time step algorithm, in which the fluid time step $\Delta t = O(\ell / u_0)$, the particle time step $\Delta t_p = O(d / u_0)$, and the collision time step $\Delta t_c = O(d(\rho_p^2 / E_p^2 u_0)^{1/5})$ satisfy $\Delta t > \Delta t_p > \Delta t_c$. Here d is the particle diameter, ρ_p is the particle density, and E_p is the particle elastic modulus. The method follows the motion of individual particles in the three-dimensional fluid flow by solution of the particle momentum and angular momentum equations

$$m\frac{d\mathbf{v}}{dt} = \mathbf{F}_F + \mathbf{F}_A, \qquad I\frac{d\mathbf{\Omega}}{dt} = \mathbf{M}_F + \mathbf{M}_A, \tag{5-5}$$

subject to forces and torques induced by the fluid flow ($\mathbf{F}_F$ and $\mathbf{M}_F$) and by the particle collision and adhesion ($\mathbf{F}_A$ and $\mathbf{M}_A$). Here, m is the particle mass, I is the moment of inertia, and $\mathbf{v}$ and $\mathbf{\Omega}$ are the particle velocity and rotation rate, respectively. The dominant fluid force is the drag force, which is given by the Stokes drag law modified to account for the effect of local particle crowding as

$$F_d = 3\pi\mu d(\mathbf{u} - \mathbf{v})f, \tag{5-6}$$

where **u** is the fluid velocity evaluated at the particle centroid. The friction factor f was given empirically by Di Felice [35] for particle Reynolds numbers $\mathrm{Re}_p \equiv |\mathbf{u}-\mathbf{v}|d/\nu$ in the range 0.01 to 10^4 as a function of the local particle volume fraction ϕ as

$$f = (1-\phi)^{1-\zeta}, \qquad \zeta = 3.7 - 0.65\exp\left(-\frac{1}{2}[1.5 - \ln(\mathrm{Re}_p)]^2\right). \tag{5-7}$$

This expression approaches the Wen and Yu [36] expression for low particle Reynolds number. The associated viscous fluid torque arises from a difference in rotation rate of the particle and the local fluid element, and was given by [37] as

$$\mathbf{M}_F = -\pi\mu d^3(\boldsymbol{\Omega} - \frac{1}{2}\boldsymbol{\omega}), \tag{5-8}$$

where $\boldsymbol{\omega}$ is the fluid vorticity vector at the particle centroid. Other fluid forces of lesser importance accounted for in the computation include the Saffman and Magnus lift terms [38-39], which together with drag make up the fluid force $\mathbf{F}_F$.

The total collision and adhesion force and torque fields on particle i with radius r_i are given by

$$\mathbf{F}_A = -F_n\mathbf{n} + F_s\mathbf{t}_S, \qquad \mathbf{M}_A = rF_s(\mathbf{n}\times\mathbf{t}_S) + M_r(\mathbf{t}_R\times\mathbf{n}) + M_t\mathbf{n}, \tag{5-9}$$

where $\mathbf{n} = (\mathbf{x}_j - \mathbf{x}_i)/|\mathbf{x}_j - \mathbf{x}_i|$ is the unit normal vector oriented along the line connecting the centers of the two colliding particles, i and j. The normal component of the collision and adhesion force F_n is further divided into an elastic-adhesion part F_{ne} and a dissipative part F_{nd}. The sliding resistance is composed of a force with magnitude F_s acting in a direction $\mathbf{t}_S$, corresponding to the direction of relative motion of the particle surfaces at the contact point projected onto the contact plane (the plane orthogonal to **n**),

as well as a related torque in the $\mathbf{n}\times\mathbf{t}_S$ direction. The rolling resistance, which arises due to the effects of particle adhesion, exerts a torque of magnitude M_r on the particle in the $\mathbf{t}_R\times\mathbf{n}$ direction, where $\mathbf{t}_R$ is the direction of the "rolling" velocity. The twisting resistance torque M_t is oriented along the unit normal direction **n**. While all of these various collision-adhesion forces and torques were included in the current computations, the dynamics of small adhesive particles are dominated by the normal elastic-adhesive force and the rolling resistance torque.

The adhesive force between the two particles depends on the surface energy potential γ, where the work required to separate two spheres colliding over a contact region of radius $a(t)$ is given by $2\pi\gamma a^2$ in the absence of further elastic deformation. Particle normal elastic rebound force and adhesion force were simulated by employing the soft-sphere collision model of Johnson et al. [40], hereinafter referred to as the JKR model, which can be written in terms of the contact region radius $a(t)$ and the normal particle overlap $\delta_N = r_i + r_j - \left|\mathbf{x}_i - \mathbf{x}_j\right|$ as [41]

$$\frac{\delta_N}{\delta_c} = 6^{1/3}\left[2\left(\frac{a}{a_o}\right)^2 - \frac{4}{3}\left(\frac{a}{a_o}\right)^{1/2}\right], \qquad \frac{F_{ne}}{F_c} = 4\left(\frac{a}{a_o}\right)^3 - 4\left(\frac{a}{a_o}\right)^{3/2}, \tag{5-10}$$

The critical overlap δ_c, the critical normal force F_c, and the equilibrium contact region radius a_o are given by [40]

$$F_c = 3\pi\gamma R, \qquad \delta_c = \frac{a_o^2}{2(6)^{1/3}R}, \qquad a_o = \left(\frac{9\pi\gamma R^2}{E}\right)^{1/3}. \tag{5-11}$$

As two particles move away from each other following collision, they remain in contact until the point where $F_n = -F_c$ and $\delta_N = -\delta_c$ due to the necking of the material in the contact region. Beyond this state any further separation leads the two particles to break apart.

The effect of the fluid squeeze-film within the contact region is to limit the minimum approach distance between the particles (i.e., the contact region gap size) and to reduce the particle restitution coefficient. Experimental studies of particle collisions at different Stokes numbers [42] indicate that the coefficient of restitution is essentially zero when the Stokes number is less than about 10 due to dissipation in the squeeze-film. Since our Stokes numbers are well below this value, we set the dissipative part of the normal collision force F_{nd} such that the restitution coefficient vanishes using the model of Tsuji et al. [43].

The second major effect of particle adhesion is to introduce a torque that resists particle rolling. For uniform-size spherical particles, the "rolling velocity" $\mathbf{v}_L$ of particle *i* is given by [44]

$$\mathbf{v}_L = -R(\boldsymbol{\Omega}_i - \boldsymbol{\Omega}_j) \times \mathbf{n} \ . \tag{5-12}$$

A linear expression for the rolling resistance torque M_r was postulated as

$$M_r = -k_R \, \xi \, , \tag{5-13}$$

where $\xi = (\int_{t_0}^{t} \mathbf{v}_L(\tau)\, d\tau) \cdot \mathbf{t}_R$ is the rolling displacement in the direction $\mathbf{t}_R = \mathbf{v}_L / |\mathbf{v}_L|$. Rolling involves an upward motion of the particle surfaces within one part of the contact region and a downward motion in the other part of the contact region. The presence of an

adhesion force between the two contacting surfaces introduces a torque resisting rolling of the particles. An expression for the rolling resistance due to van der Waals adhesion was derived by Dominik and Tielens [45], which yields the coefficient k_R as

$$k_R = 4F_C(a/a_0)^{3/2}. \tag{5-14}$$

Dominik and Tielens [45] further argue that the critical resistance occurs when the rolling displacement ξ achieves a critical value, corresponding to a critical rolling angle $\theta_{crit} = \xi_{crit}/R$. For $\xi > \xi_{crit}$, the rolling displacement ξ in (5-13) is replaced by ξ_{crit}. The expressions used for twisting and sliding resistances are given by Marshall [33].

5.2.2. Direct Numerical Simulation (DNS) of Homogeneous Turbulence

The DNS computations of isotropic, homogeneous turbulence used for validation were performed using a triply-periodic pseudo-spectral method with second-order Adams-Bashforth time stepping and exact integration of the viscous term [46]. In this approach, the spectral Navier-Stokes equations are evolved in time after having been projected onto a divergence-free space using the operator $P_{ij} = k_i k_j / k^2 - \delta_{ij}$ according to the expression

$$\overline{\mathbf{u}}^{n+1} = \overline{\mathbf{u}}^n \exp(-\nu k^2 \Delta t) + \Delta t\, \mathbf{P} \cdot \left[\frac{3}{2} \overline{\mathbf{F}}^n \exp(-\nu k^2 \Delta t) - \frac{1}{2} \overline{\mathbf{F}}^{n-1} \exp(-2\nu k^2 \Delta t) \right], \tag{5-15}$$

where an overbar denotes Fourier transform in three space dimensions, a superscript indicates the time step, ν is the kinematic viscosity, and **k** is the wavenumber vector with magnitude *k*. The force vector **F** on the right-hand side has Fourier transform given by

$$\bar{\mathbf{F}} = \overline{\mathbf{u} \times \boldsymbol{\omega}} + \bar{\mathbf{f}}_F + \bar{\mathbf{f}}_P \,, \tag{5-16}$$

where $\bar{\mathbf{f}}_F$ is the small wavenumber forcing term required to maintain the turbulence with approximately constant kinetic energy and $\bar{\mathbf{f}}_P$ is the particle-induced body force due to relative motion between the particles and the fluid. The velocity field was made divergence-free at each time step by taking its Fourier transform and using the spectral form of the continuity equation, given by

$$\mathbf{k} \cdot \bar{\mathbf{u}} = 0 \,. \tag{5-17}$$

The forcing vector was assumed to be proportional to the fluid velocity [47-48], such that

$$\bar{\mathbf{f}}_F = \begin{cases} C\bar{\mathbf{u}} & \text{for } k < k_{crit} \\ 0 & \text{for } k > k_{crit} \end{cases}, \tag{5-18}$$

where the coefficient C was set equal to $C = 0.0045 / E_{low}$ and $E_{low} = \frac{1}{2} \sum_{k<k_{crit}} \bar{\mathbf{u}} \cdot \bar{\mathbf{u}}$ is the kinetic energy in all modes with wavenumber amplitude $k < k_{crit}$. The current computations were performed with $k_{crit} = 5$, so that the forcing acts only on the large-scale eddies.

The particle body force $\mathbf{f}_P$ was computed by associating a regularized delta function $\delta_h(\mathbf{x} - \mathbf{X}_n)$ with each Lagrangian particle, where $\mathbf{X}_n$ denotes the particle centroid location of particle *n*. The value of the body force $\mathbf{f}_P$ was evaluated at each grid node *i* of the Cartesian grid using

$$\mathbf{f}_p(\mathbf{x}_i) = -\sum_{n=1}^{N} \mathbf{F}_{F,n}\, \delta_h(\mathbf{x}_i - \mathbf{X}_n), \tag{5-19}$$

where $\mathbf{F}_{F,n}$ denotes the fluid force on the n^{th} particle. The regularized delta function used for the current problem distributes the particle force uniformly over a stencil consisting of the grid cell containing the particle and one grid cell on each side. This choice of delta function is conservative in both the force and torque for any value of $\mathbf{X}_n$.

The turbulence kinetic energy q and dissipation rate ε were obtained from the power spectrum, $e(k)$, as

$$q = \int_0^{k_{\max}} e(k)dk, \qquad \varepsilon = 2\nu \int_0^{k_{\max}} k^2 e(k)dk. \tag{5-20}$$

Various dimensionless measures describing the turbulence in the validation computations are listed in Table 5.1, including the root-mean-square velocity magnitude u_0, the average turbulence kinetic energy q, the integral length scale $\ell_0 = 0.5\, u_0^{\,3} / \varepsilon$, the Taylor microscale $\lambda = (15\nu/\varepsilon)^{1/2} u_0$, and the Kolmogorov length scale $\eta = (\nu^3/\varepsilon)^{1/4}$. The corresponding microscale Reynolds number is $\mathrm{Re}_\lambda = u_0\lambda/\nu = 99$.

Table 5.1. Dimensionless simulation parameters and physical parameters of the fluid turbulence.

Simulation Parameters		**Turbulence Parameters**	
Time step	0.002	Turbulent kinetic energy, q	0.122
Cycles	15000	Mean dissipation rate, ε	0.015
Grid	128^3	Kinematic viscosity, ν	0.001
		Integral length, ℓ_0	0.771
		Taylor microscale, λ	0.285
		Kolmogorov length, η	0.016
		Integral velocity, u_0	0.285
		Integral time, T_ℓ	2.71

5.2.3. Dimensionless Parameters

One of the most important dimensionless parameters is the Stokes number, which is defined as the ratio of the particle time scale $\tau_p = m/3\pi\mu d$ to a characteristic fluid time scale, where *m* is the particle mass. For turbulent flow, different Stokes numbers can be defined using different fluid time scales. Two common choices are the Kolmogorov-scale Stokes number St_K and the integral-scale Stokes number St_0, defined by

$$\mathrm{St}_K = \tau_p / \tau_\eta, \qquad \mathrm{St}_0 = \tau_p / \tau_\ell. \tag{5-21}$$

The Kolmogorov time scale τ_η is defined in terms of the kinematic viscosity and turbulence dissipation rate as $\tau_\eta = (\nu/\varepsilon)^{1/2}$ and the integral time scale is given by $\tau_\ell = \ell_0 / u_0$. The Stokes number determines the particle response to changes in the fluid flow, such that in cases with small Stokes numbers particles nearly follow fluid streamlines and in cases with large Stokes numbers the fluid has only a small influence on the particle motion.

The tendency for colliding particles to adhere to each other can be characterized by the adhesion parameter Ad, defined in terms of the adhesive surface energy density γ as [49]

$$\mathrm{Ad} = \frac{2\gamma}{\rho_p U^2 d}. \tag{5-22}$$

In this equation, *U* is a characteristic velocity scale of the fluid, which might be set equal to the root-mean-square turbulent fluctuation velocity u_0 to obtain the integral-scale adhesion parameter Ad_0 or to the Kolmogorov velocity $u_\eta = (\nu\varepsilon)^{1/4}$ to obtain the Kolmogorov-scale adhesion parameter Ad_K. The adhesive energy density γ can be

related to the Hamaker coefficient A for the particle material operating in the given fluid medium by

$$\gamma = \frac{A}{24\pi\delta^2}, \tag{5-23}$$

where δ is the gap thickness within the contact area.

The elastic rebound force on the particle is characterized using an elasticity parameter El, defined by

$$\mathrm{El} = \frac{E}{\rho_p U^2}, \tag{5-24}$$

where E is the effective elastic modulus, which together with the effective particle radius R is defined by

$$\frac{1}{E} \equiv \frac{1-\sigma_i^2}{E_i} + \frac{1-\sigma_j^2}{E_j}, \qquad \frac{1}{R} \equiv \frac{1}{r_i} + \frac{1}{r_j}, \tag{5-25}$$

where E_i, σ_i, and r_i are the elastic modulus, Poisson ratio, and radius of particle i, respectively. Both the elasticity parameter El and the adhesion parameter Ad are important in determining the radius of the contact region upon particle collision. In (5-23), the fluid velocity scale U may again be modeled using either the integral scale (root-mean-square) velocity u_0 or the Kolmogorov-scale velocity u_η.

5.3. Results and Discussion

The computations were initialized by positioning 46,656 particles on a uniform array across the computational domain. A preliminary computation was conducted with no particles to allow the turbulence to develop a range of length scales characteristic of statistically stationary homogeneous isotropic turbulence. The computation was then

restarted with particles using the three-level multiple time-step DEM algorithm of Marshall [33], with a fluid time step of $dt_f = 0.005$, 10 particle time steps per fluid time step, and 40 collision time steps per particle time step. A listing of the parameter values for the different runs with particles is given in Table 5.2, where the different runs are referred to in the following as case 1-12.

Table 5.2. List of computational cases examined. For each case computations were performed with and without two-way coupling. Variables listed include ratio of particle radius to integral length scale, average particle volume concentration $\bar{\phi}$, mass loading Z, Kolmogorov and integral scale Stokes number, and Kolmogorov and integral scale adhesion parameter.

Case	r_p / ℓ_0	$\bar{\phi}$	Z	St_K	St_0	Ad_K	Ad_0
1	0.0129	0.000788	0.00789	0.860	0.082	260	12.3
2	0.0259	0.0063	0.0634	3.44	0.328	260	12.3
3	0.0389	0.0213	0.218	7.74	0.738	260	12.3
4	0.0516	0.0504	0.531	13.8	1.31	260	12.3
5	0.0129	0.000788	0.00789	0.860	0.082	0	0
6	0.0259	0.0063	0.0634	3.44	0.328	0	0
7	0.0389	0.0213	0.218	7.74	0.738	0	0
8	0.0516	0.0504	0.531	13.8	1.31	0	0
9	0.0259	0.0063	0.0634	3.44	0.328	130	6.16
10	0.0259	0.0063	0.0634	3.44	0.328	520	24.6
11	0.0259	0.0063	0.0634	3.44	0.328	1041	49.3
12	0.0259	0.0063	0.0634	3.44	0.328	2081	98.5

5.3.1. Effect of Particle Agglomeration on Turbulence

The turbulent kinetic energy q and turbulent dissipation rate ε are plotted as functions of time for cases with both one-way and two-way coupling in Figure 5.1 for case 2. For the one-way coupling computations, both q and ε fluctuate in time with root-

mean-square values of 4.6% and 7.5% of their mean values, respectively. The computations with two-way coupling result in values of turbulent kinetic energy that exhibit fluctuations with a similar root-mean-square value up to about $t \approx 87$, after which the kinetic energy decreases sharply. The turbulent dissipation for the two-way coupling computation is observed to decrease to about 20% below the average value for the one-way coupling simulation up to a time of about $t \approx 60$, after which the dissipation rate in the two-way coupling computation decreases steadily. We note that the dissipation rate measure ε reported here is due to fluid gradients, and it does not include the dissipation caused by the particle drag force on the fluid.

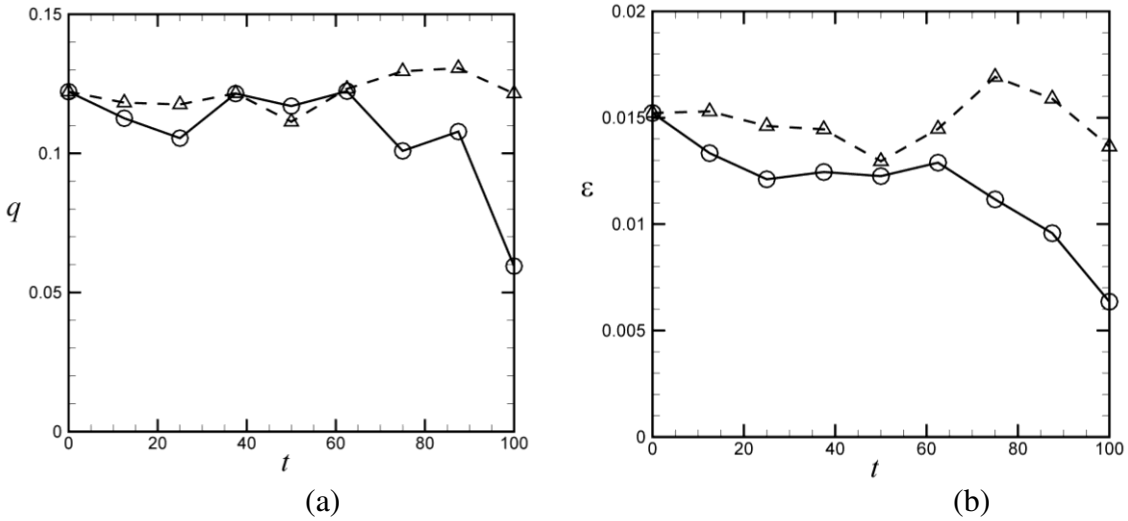

Figure 5.1. Time variation of (a) turbulent kinetic energy q and (b) turbulence dissipation rate ε, with results from computations with one-way coupling (dashed line, deltas) and two-way coupling (solid line, circles).

A plot of the power spectrum at three different times is presented in Figure 5.2a, showing a gradual decrease in the spectrum with time for the case with two-way coupling. The power spectrum is nearly constant in time for the one-way coupling case. The $k^{-5/3}$ scaling of the power spectrum in the inertial range is indicated by a dashed

line. A comparison of the power spectra for cases with different Stokes numbers is given in Figure 5.2b. The change in Stokes number in this figure was produced by changing the particle radius, with all other parameters held fixed. Two computations were conducted with each value of particle radius, one with adhesive particles ($Ad_0 = 12.3$, cases 1-4) and one with no adhesion ($Ad_0 = 0$, cases 5-8). The power spectra were plotted in Figure 5.2b at time $t = 87.5$, near the end of the runs and just before the turbulent kinetic energy decreases sharply. The power spectra curves for the case with lowest Stokes number ($St_K = 0.86$) are almost identical to the initial power spectrum, showing almost no change with the addition of the particles.

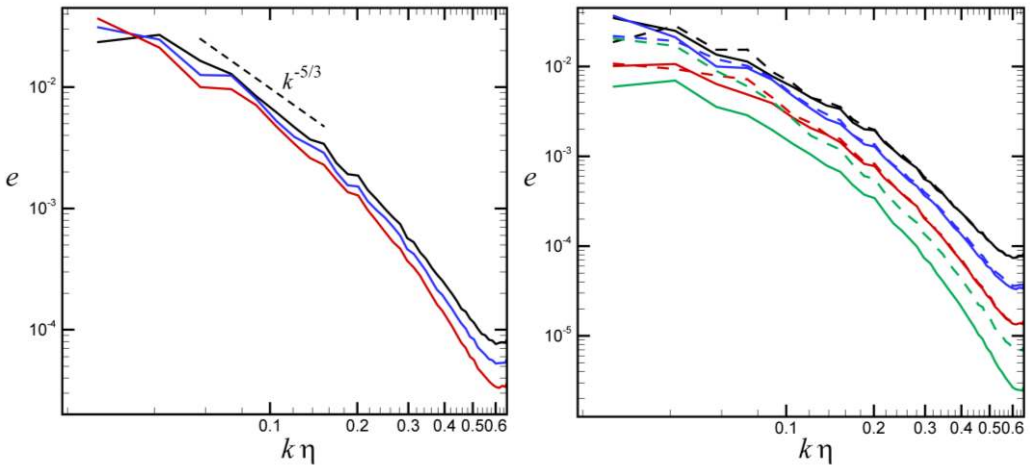

Figure 5.2. (a) Power spectrum for computation with two-way coupling for case 2 at three different times: t = 0 (black line), 50 (blue line) and 87.5 (red line). (b) Power spectrum for computations with Kolmogorov-scale Stokes numbers $\mathbf{St}_K = 0.86$ (black), 3.44 (blue), 7.74 (red), and 13.8 (green) at $t = 87.5$ both with adhesion (Ad0 = 12.3, cases 1-4)(solid lines) and without adhesion (Ad0 = 0, cases 5-8)(dashed lines).

The cases with higher Stokes number exhibit progressively lower power spectra curves as the particle size is increased. It is noted that several different regimes characterizing turbulence modulation by particles have been noted in the literature. For

very small particles with Kolmogorov-scale Stokes number St_K <<1, the particles are found to enhance the fluid inertia and hence increase the turbulent kinetic energy [50, 51]. For particles with larger Stokes number (St_K >>1) but with diameter d less than about 10% of the integral length scale ℓ_0, the particles reduce the turbulent kinetic energy. This reduction is generally associated with the preferential concentration of particles in regions of low fluid vorticity [52-55]. Druzhinin [51] reported the transition between these two regimes to occur at $St_K \cong 0.8$. Finally, sufficiently large particles are again observed to enhance turbulent kinetic energy due to shedding of vortex structures in the particle wakes. Gore and Crowe [56] and Crowe [22] propose that this third regime corresponds to particles with diameter d satisfying $d/\ell_0 > 0.1$, but various other criteria have been suggested by other researchers. As seen from Tables 5.1 and 5.2, the current computations are clearly in this middle regime of turbulence modulation, and the observed enhanced attenuation of turbulent kinetic energy with increase in particle size and mass loading is consistent with the previous literature cited above for this regime.

The cases with the three smallest values of Stokes number in Figure 5.2b exhibit almost no difference in the power spectra between computations with and without adhesion. The case with largest Stokes number exhibits a reduction in the power spectrum for the case with adhesion compared to that with no adhesion. The fact that the power spectra shown in Figure 5.2b are so similar for the cases with and without adhesion, even though the curves exhibit significant decrease due to the presence of particles compared to the power spectrum for the one-way coupling computation, provides strong evidence that particle agglomeration has little influence on turbulence attenuation, at least for sufficiently small particles. This observation is consistent with the

conclusion of Druzhinin [51] that the attenuation of turbulence by particles in this regime is primarily a consequence of the particle inertia, which depends only on net particle mass and is independent of agglomeration of the particles.

The size of the agglomerates that develop during the turbulent flow simulation depends upon the value of the adhesion parameter. As indicated in Table 5.2, the value of the adhesion parameter was varied in our computations over a factor of about 16. For significantly smaller values of adhesion parameter than those examined, there is only a small amount of particle adhesion during the computational run time and the agglomerates are relatively small, with only 2-5 or so particles. For much larger values of adhesion parameter than those examined, the agglomerates grow to very large sizes during the computations, in some cases with all particles forming a single agglomerate. Our desire in this paper was to examine agglomerates that were sufficiently large (i.e., several hundred particles) so that measures such as fractal dimension are sensible, but also agglomerates whose maximum size was of the order of magnitude of the integral length scale of the turbulence. Figure 5.3a shows the average number of particles per agglomerate, N_{pagg}, at time t = 87.5 as a function of adhesion parameter. The agglomerate size can be estimated by the radius of gyration, R_{gyr}, defined for an agglomerate i by

$$R_{gyr,i} = \left[\frac{1}{N_i} \sum_{j=1}^{N_j} \left| \mathbf{x}_j - \bar{\mathbf{x}}_i \right|^2 \right]^{1/2}, \qquad (5\text{-}26)$$

where $\bar{\mathbf{x}}_i$ denotes the centroid position of agglomerate i and $\mathbf{x}_j$ is the centroid position of the j^{th} particle within the agglomerate. The average value of the radius of gyration

tends to be dominated by the smallest, but more numerous, agglomerates. Instead, we define a particle-weighted radius of gyration, $\overline{R}_{gry}$, by

$$\overline{R}_{gyr} = \frac{1}{N_{agg}} \sum_{i=1}^{N_{agg}} N_i R_{gry,i}, \tag{5-27}$$

where N_i is the number of particles in agglomerate *i* and N_{agg} is the total number of agglomerates. A plot of $\overline{R}_{gry} / r_p$, where r_p is the radius of a single particle, at time *t* = 87.5 is presented in Figure 5.3b as a function of adhesion parameter for both computations with one-way and two-way coupling.

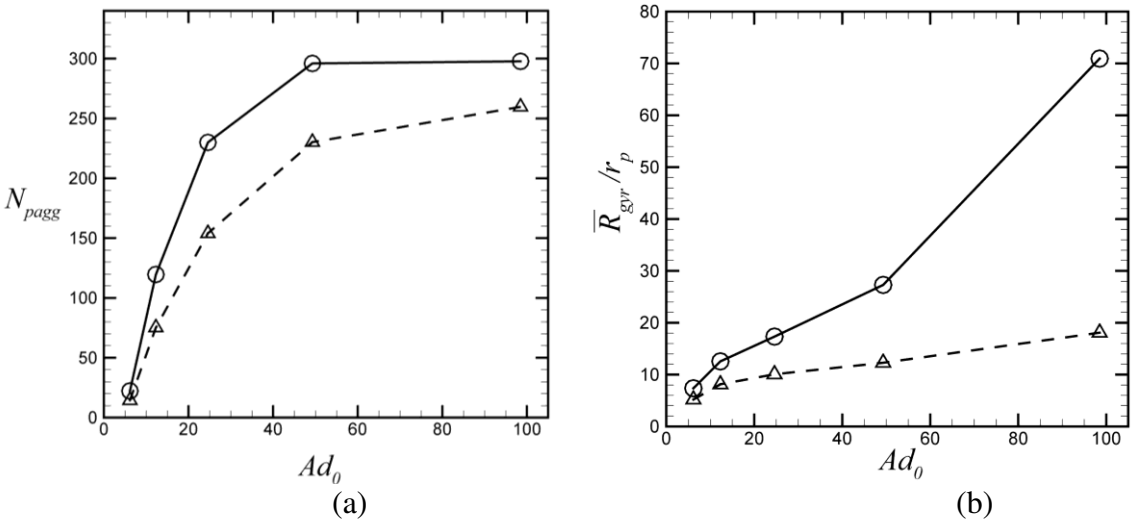

Figure 5.3. Plots showing (a) the number of particles per agglomerate N_{pagg} and (b) the dimensionless particle-weighted average radius of gyration, $\overline{R}_{gyr} / r_p$, as a function of integral-scale adhesion parameter, Ad0, for computations with two-way coupling (solid lines, circles) and one-way coupling (dashed lines, deltas) at time $t = 87.5$. Computations are for cases 2 and 9-12.

5.3.2. Structure of Particle Agglomerates

This section examines the detailed structure of the particle agglomerates, as predicted using both one-way and two-way coupling simulations. This study was

performed starting from a state in which no particles were touching, and hence there were no agglomerates, and ending at a time of $t = 87.5$. By this end time the agglomerates had developed into large structures, but they had not yet achieved an equilibrium condition where agglomerate breakup balances agglomerate formation by collision. This end time was selected because shortly after this time in the two-way coupling simulations, the turbulent kinetic energy decreases sharply, leading eventually to a state where the small-scale turbulence completely vanishes. On the other hand, at $t = 87.5$ the turbulent kinetic energy is still reasonably close to its initial value, as shown in Figure 5.1a.

Agglomerates are defined as groups of particles that are in contact with each other, either directly or via contacts with other particles. The agglomerates were identified at each time step of the computation and a variety of measures were employed to examine their characteristics. The total number of agglomerates N_{agg} is plotted as a function of time for case 2 in Figure 5.4a for computations with both one-way and two-way coupling of the particle and fluid phases. Shortly after the start of the computation, individual particles collide and attach to each other to form small agglomerates. A maximum in the number of agglomerates is reached at $t \cong 15$, equal to approximately 7400 agglomerates. The number of agglomerates then decreases as these small agglomerates collide and adhere to each other to form larger agglomerates. The number of particles N_i in each agglomerate was counted and averaged over all agglomerates to obtain the average number of particles per agglomerate, which is plotted as a function of time in Figure 5.4b. The dimensionless particle-weighted radius of gyration, $\overline{R}_{gyr} / r_p$, is plotted as a function time in Figure 5.4c.

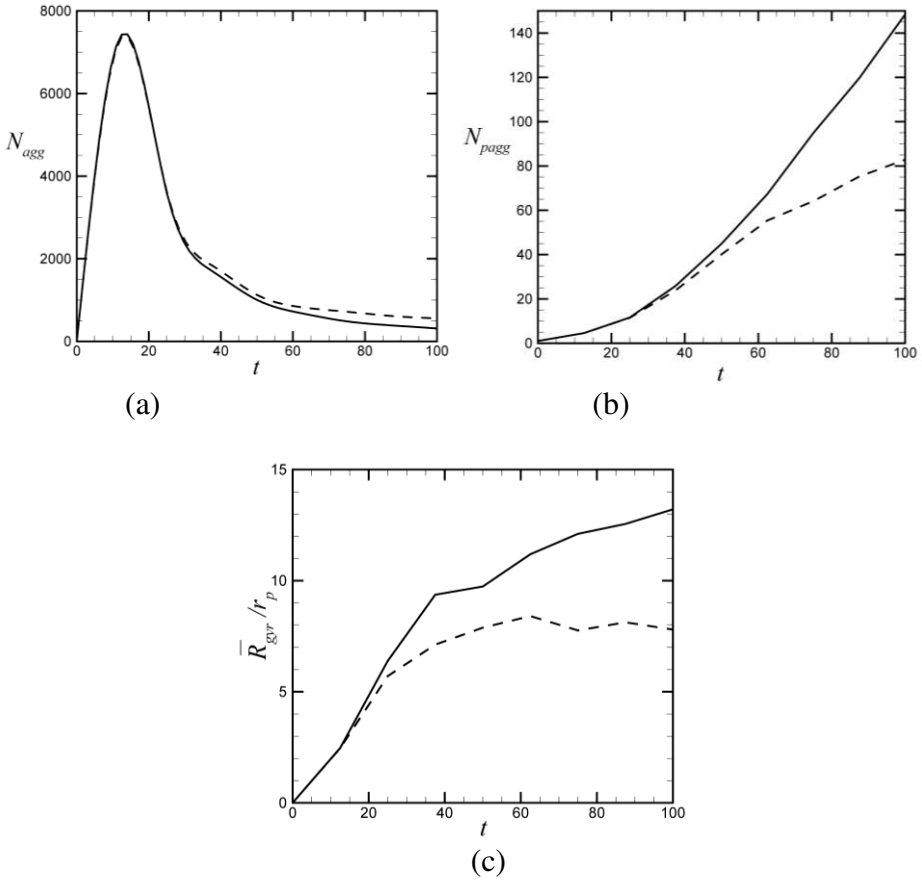

Figure 5.4. Time variation of (a) the total number of agglomerates (N_{agg}) and (b) the average number of particles per agglomerate (N_{pagg}) and (c) the dimensionless particle-weighted radius of gyration of agglomerates ($\overline{R}_{gyr} / r_p$) with results from computations with one-way coupling (dashed lines) and two-way coupling (solid lines) for case 2.

In all three of the plots in Figure 5.4, the one-way and two-way coupling results are quite close to each other for times near the beginning of the calculation. At $t \approx 20$ we notice that the radius of gyration in Figure 5.4c for the two-way coupling run increases above that for the one-way coupling run. The number of particles per agglomerate in Figure 5.4b similarly is greater for the two-way coupling run than it is for the case with one-way coupling; however, the differences between the one-way and two-way coupling runs appear later than for the radius of gyration. Since the agglomerates for two-way

coupling are both larger and have more particles than for one-way coupling, it follows that the number of agglomerates shown in Figure 5.4a for the two-way coupling computation is less than that for one-way coupling, although again we see that this difference appears significantly later than in the plot of the radius of gyration.

As noted by a number of previous authors [1-3], the number of particles N_i in agglomerate *i* can be expressed as a power-law function of the agglomerate size, such that

$$N_i = K(R_{gyr,i} / r_p)^{d_f}, \tag{5-28}$$

where *K* is a coefficient (called the fractal pre-factor) and the exponent d_f is called the fractal dimension of the set of agglomerates. The value of d_f varies over the interval $1 \le d_f \le 3$ depending on the agglomeration formation mechanism [5]. For instance, Eggersdorfer et al. [57] cited typical values of $d_f = 2.5$ for diffusion-limited agglomeration, $d_f = 3.0$ for ballistic particle-cluster agglomeration, and $d_f = 1.8$ for diffusion-limited cluster-cluster agglomeration. For turbulent agglomeration of latex particles in stirred tanks, Selomulya et al. [58] reported values of d_f between 1.7 and 2.1 and Waldner et al. [59] reported values of d_f between 1.8 and 2.6. A log-log plot of *N* versus R_{gyr} / r_p is shown in Figure 5.5a at time $t = 87.5$ for both one-way and two-way coupling computations. It was found that for both methods fractal dimension values are close, with $d_f = 2.064$ for one-way coupling and $d_f = 2.118$ for two-way coupling. This value of fractal dimension for the particle agglomerates is in good agreement with values noted above obtained in previous experimental literature for turbulent agglomeration.

The fractal dimension was calculated at different time intervals during the computations. The calculated fractal dimension is plotted as a function of time and is shown in Figure 5.5b. The fractal dimension for one-way and two-way coupling computations is quite close; however, the result for two-way coupling is a little higher near the end of the computation (for $t > 70$). A larger value of fractal dimension for two-way coupling implies that the agglomerates were more densely packed in comparison to the one-way coupling results.

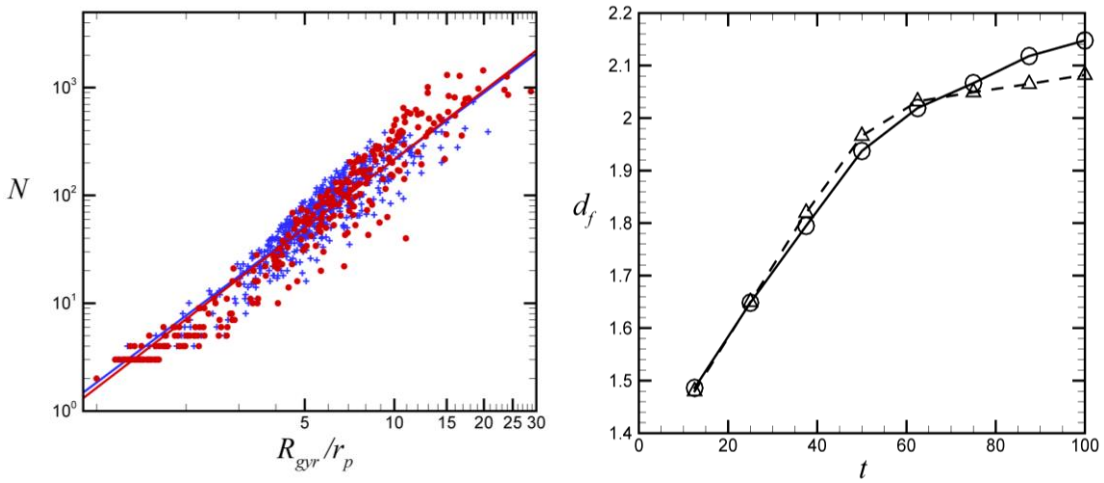

Figure 5.5. (a) Plot showing power-law fit given in Eq. (28) between the number of particles in an agglomerate N, versus the ratio of the gyration radius to the primitive particle radius, R_{gyr}/r_p. Slope of lines on the log-log plot are equal to the fractal dimension d_f at $t = 87.5$, and results are given for both one-way coupling (blue crosses) and two-way coupling (red circles). (b) Plot showing time variation of the fractal dimension, comparing results with one-way coupling (dashed line, deltas) and two-way coupling (solid line, circles) for case 2.

Figure 5.6a shows the distribution of agglomerate sizes at $t = 87.5$. The number of particles in the agglomerate is divided into a set of logarithmic bins of base 2, such that the width of each bin is twice the width of the previous bin. The *x*-axis plots the median number of particles in the bin and the *y*-axis plots the number of agglomerates falling into

that bin, where both axes are logarithmic. A similar plot is shown in Figure 5.6b, with the difference that the agglomerate size is characterized by bins of the ratio R_{gyr}/r_p of agglomerate gyration radius to individual particle radius. Because the values of this ratio have a narrower size variation than the number of particles in the agglomerate, the bins used in Figure 5.6b are linear, with a constant width. The plots in Figure 5.6 demonstrate that the two-way coupling computation generates larger agglomerates with more particles than does the one-way coupling computation.

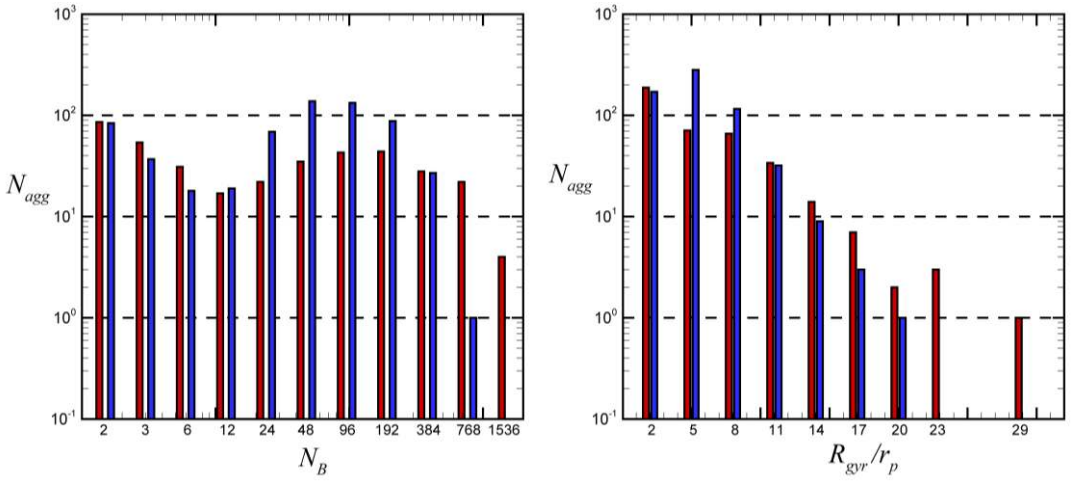

Figure 5.6. Distribution plots showing number of agglomerates N_{agg} as a function of (a) number of particles in the agglomerate averaged over a set of logarithmic bins, N_B, and (b) dimensionless radius of gyration, R_{gyr}/r_p, averaged over a set of linear bins. Results are from computations with one-way coupling (A, blue bars) and two-way coupling (B, red bars) at t = 87.5 for case 2.

The particle volume fraction ϕ_i is computed for each agglomerate by dividing the volume of all particles associated with the agglomerate, $V_p = (4\pi/3)N_i r_p^3$, by the effective volume V_{eff} occupied by the agglomerate. The agglomerate effective volume is estimated by $V_{eff} = (4\pi/3)R_{eff,i}^3$, where the effective radius of the agglomerate R_{eff} is

related to the radius of gyration as $R_{gyr} = \sqrt{2/5}\, R_{eff}$. This latter expression is based on the expression for radius of gyration of a solid sphere of uniform density. The particle volume fraction of the agglomerate can be related to the fractal dimension by [2, 30]

$$\phi_i = \phi_0 (R_{gyr,i} / r_p)^{d_f - 3}, \tag{5-29}$$

where ϕ_0 is a constant. If $d_f < 3$, an increase in agglomerate size results in a decrease in average particle volume fraction [4]. A log-log plot of the averaged agglomerate volume fraction versus the dimensionless radius of gyration (R_{gyr} / r_p) is given in Figure 5.7a at time $t = 87.5$. The observed decrease in volume fraction as the agglomerate size increases is substantial. The two-way and one-way coupling results for volume fraction are fairly close for the smaller agglomerates, but for the larger agglomerates the two-way coupling simulations yield somewhat larger particle volume fraction than do the simulations with one-way coupling. This result is consistent with our previous observation that the fractal dimension for two-way coupling simulations is slightly larger than for one-way coupling. Figure 5.7b shows a log-log plot of volume fraction ϕ versus R_{gyr} / r_p at time $t = 87.5$ for both one-way and two-way coupling computations. The slopes of the best-fit lines to the data were obtained as -0.9351 and -0.8818 for one-way and two-way coupling, respectively. These values almost exactly agree with the exponent $d_f - 3$ given in (5.29) using the previously cited values of fractal dimension d_f.

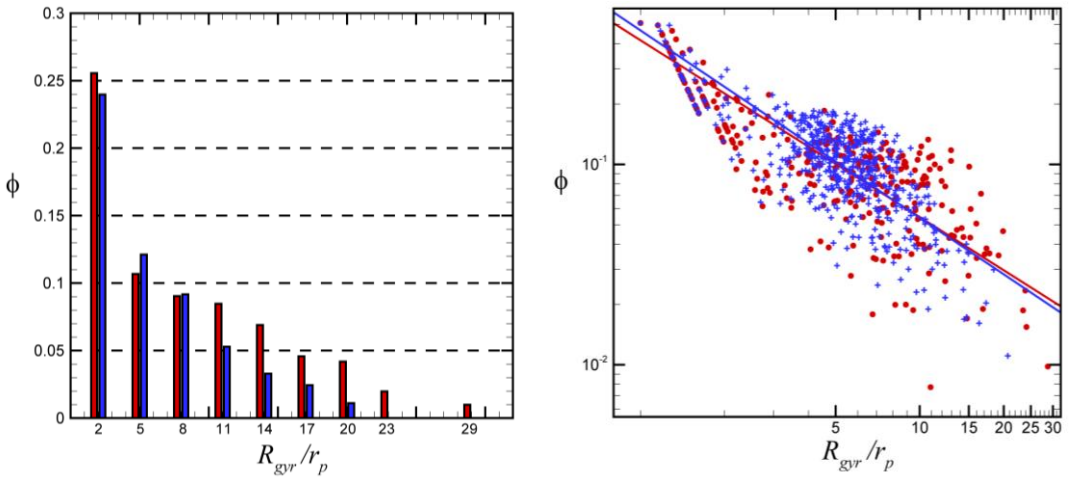

Figure 5.7. (a) Distribution plot showing the particle volume fraction as a function of the dimensionless radius of gyration, R_{gyr}/r_p, on a log-linear plot for both one-way coupling (blue bars) and two-way coupling (red bars). (b) Plot showing the power-law fit given in Eq. (29), where the slope of lines on the log-log plot are equal to the fractal dimension $d_f - 3$. The data is for case 2 at $t = 87.5$, for one-way coupling (blue crosses) and two-way coupling (red circles).

In order to better clarify the physical differences between the one-way and two-way coupling computational results, we define V_{par} and V_{rel} as the average magnitudes of the particle velocity $\mathbf{v}$ and the particle slip velocity $\mathbf{v}_{slip} = \mathbf{v} - \mathbf{u}$, respectively. The magnitudes of the particle velocity and the particle slip velocity were computed for all particles, and then averaged over all particles contained within agglomerates (omitting values for single particles that are not in an agglomerate). Time variation of both V_{par} and V_{rel} is plotted in Figure 5.8a for case 2. The average particle velocity magnitude V_{par} fluctuates for both the one-way and two-way coupling computations within the interval 0.35-0.45, which is slightly greater than the root-mean-square turbulence fluctuation velocity $u_0 \cong 0.285$ listed in Table 5.1. The average particle slip velocity V_{rel} similarly remains approximately constant in time for the one-way coupling run. For the two-way

coupling case, by contrast, the value of V_{rel} is observed to gradually decrease in time, with a value at the end of the run that is nearly half of the initial value. The decrease in particle slip velocity with time for the two-way coupling computation is an indication that the fluid velocity within the agglomerate is becoming correlated with the particle velocity, resulting in a reduction of the relative velocity between the two phases within the larger agglomerates. Another measure of this phenomenon is represented by the agglomerate penetration parameter *P*, which is defined as

$$P = \frac{V_{rel}}{V_p}. \tag{5-30}$$

The time variation of *P* is plotted in Figure 5.8b, showing approximately constant value for one-way coupling and a steady reduction in time for the two-way coupling computation. Both the higher volume fraction of agglomerates with two-way coupling and the correlation between the fluid and particle velocity fields makes it increasingly difficult for the fluid to penetrate into the agglomerates of the two-way coupling run as the agglomerate size increases.

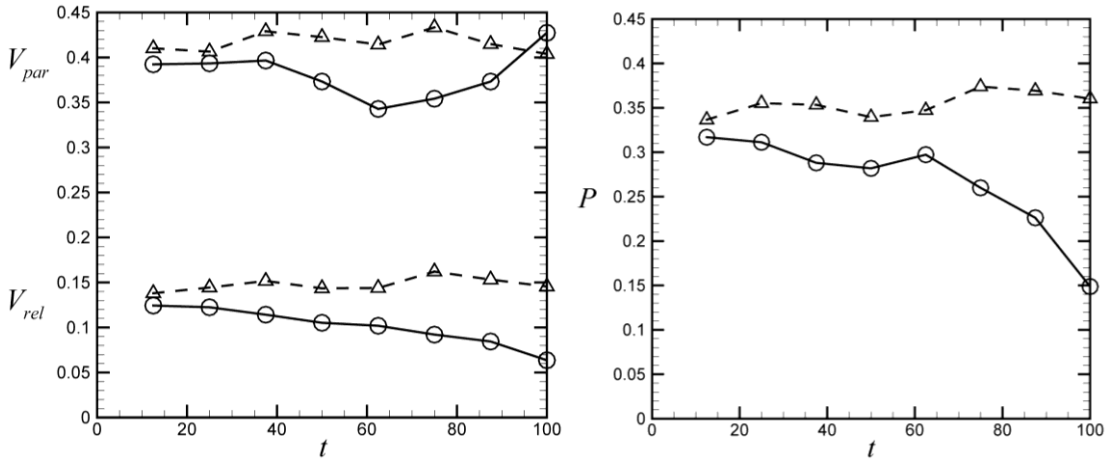

(a) (b)

Figure 5.8. Time variation of (a) the average particle velocity magnitude V_{par} (upper curves) and the average particle slip velocity magnitude V_{rel} (lower curves) and (b) the agglomerate flow penetration parameter P for computations with one-way (dashed lines, deltas) and two-way (solid lines, circles) coupling for case 2.

To further examine the spatial variation of various fields within the agglomerate, we introduce a second-moment measure $\mu_i(F)$ of a given field $F(\mathbf{x})$ for each agglomerate *i* as

$$\mu_i(F) = \frac{N_i \left(\sum_{j=1}^{N_j} \left| \mathbf{x}_j - \bar{\mathbf{x}}_i \right|^2 F_j \right)}{\left(\sum_{j=1}^{N_i} \left| \mathbf{x}_j - \bar{\mathbf{x}}_i \right|^2 \right) \left(\sum_{j=1}^{N_i} F_j \right)}, \tag{5-31}$$

where $\bar{\mathbf{x}}_i$ is the centroid of agglomerate *i* and F_j is the value of the function $F(\mathbf{x})$ evaluated at the centroid $\mathbf{x}_j$ of the j^{th} particle within the agglomerate. The second-moment measure is shown in Figures 5.9a and 5.9b for two different fields – the relative velocity magnitude $\left|\mathbf{v}_{slip}\right|$ and a strain rate measure $S = \sqrt{2\mathbf{D}:\mathbf{D}}$, where $\mathbf{D}$ is the fluid rate of deformation tensor. For each of these two fields, the average value of the moment

$\mu_i(F)$ is plotted as a function of number of particles in the agglomerate using the same logarithmic bins as used in Figure 5.6a, where the averaging is performed for all agglomerates in each bin. A value of the second moment $\mu(F)$ equal to unity indicates that the function $F(\mathbf{x})$ is uniform (or statistically randomly varying) across the agglomerate, whereas a value of $\mu_i(F)$ that is less (greater) than unity implies that particles with higher (lower) values of $F(\mathbf{x})$ are found near the center of the agglomerate compared to particles on the outer parts of the agglomerate. Obviously, for the smallest bin representing agglomerates with only two particles, all second moments are equal to unity by definition.

The second moment of the relative velocity magnitude is shown in Figure 5.9a. The second moment is observed to be larger than unity for both one-way and two-way coupling computations, particularly within the middle range of agglomerate size spanning from 6 to 1500 particles. The second moment for the one-way coupling computation tends to be higher in the lower end of this range, for agglomerates with between about 6 to 40 particles, and the values for the two-way coupling computation tend to be higher for the upper part of this range, for agglomerates with between 700 to 1500 particles. Several mechanisms play a role in increasing the second moment of the relative velocity above unity. A mechanism that is present for both one-way and two-way coupling computations is the rotational inertia of the particles, which leads to a particle velocity magnitude that increases linearly with distance from the agglomerate centroid. Consequently, the value of V_{rel} is higher for the outermost particles, which are a farther distance away from the agglomerate center than the innermost particles, hence causing the second moment to

increase above unity. A similar linear velocity variation with distance from the centroid exists for shearing or elongational deformation of the agglomerates. For the computation with two-way coupling, the fluid within the inner region of the agglomerate is influenced by the particle-induced body force and becomes correlated to the particle velocity, such that the fluid within the agglomerate moves with the inner particles. This effect will tend to decrease V_{rel} for the inner particles (and increase the second moment) in the two-way coupling computation, but it occurs primarily for larger agglomerates.

The second moment of the straining rate measure $S = \sqrt{2\mathbf{D}:\mathbf{D}}$ is shown in Figure 5.9b. The value of this measure is nearly equal to unity for the one-way coupling computation since the straining measure depends only on the fluid flow, and hence can be treated as a random variable. The second moment of the straining measure is also close to unity for small agglomerates with two-way coupling. As the number of particles per agglomerate increases (to a value greater than about 100), the straining rate measure gradually increases above unity, indicating that the straining rate experienced by the particles is higher for particles near the outer edges of the agglomerate than for particles near the center. The outermost particles can act almost like a screen for the larger agglomerates with two-way coupling, preventing the inner particles from being exposed to high strain rate. This observation is consistent with the results of studies, such as Binder et al. [60] or Fellay et al. [61], that use direct simulation techniques such as lattice-Boltzmann or Stokesian dynamics to compute simple flow fields or rotational motion for single agglomerate structures. For larger-size agglomerates that are nearly spherical in shape, our findings are also approximately consistent with the shell-core model for agglomerate structure proposed by Kusters et al. [30], in which each

agglomerate is idealized as a two-layer sphere, where the outer ‘shell’ layer is porous and the inner ‘core’ layer is impermeable.

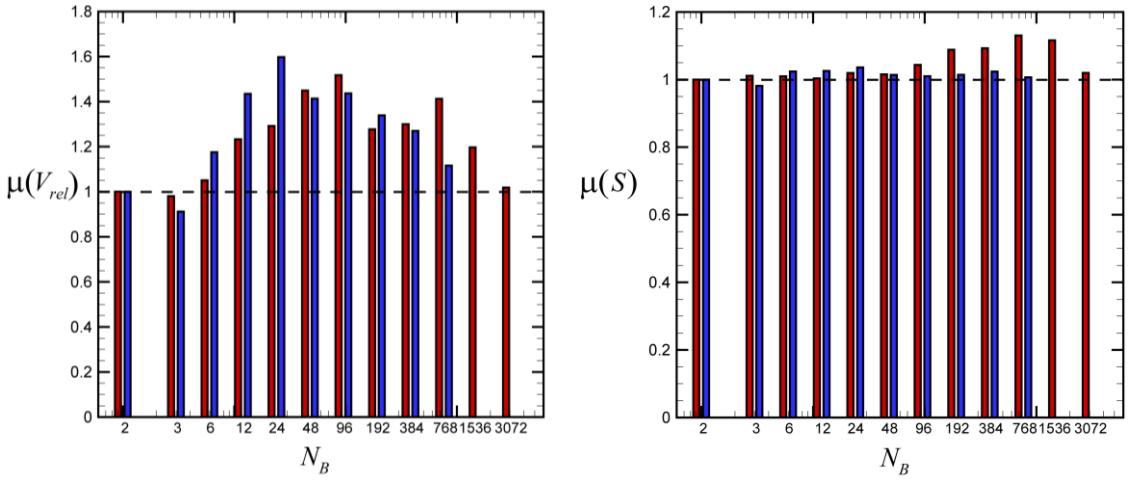

Figure 5.9. Second-order moment plots for (a) relative velocity magnitude V_{rel}, and (b) shear measure $S = \sqrt{2\mathbf{D}:\mathbf{D}}$, shown for results of computations with one-way coupling (blue bars) and two-way coupling (red bars) for case 2 at $t = 87.5$. The number of particles in the agglomerate are grouped logarithmically into bins, with average number of particles for the given bin indicated by N_B.

There is, of course, some inaccuracy in the second moment measure discussed above, since the agglomerates are not particularly spherical in shape, but instead appear to have a wide variety of jagged and/or elongated shapes. To make the relative velocity and strain rate measures more understandable, we have visualized the relative velocity and strain rate measures for some sample agglomerates from the two-way coupling computation in Figures 5.10a and 5.10b. These figures visually confirm that outer regions of the agglomerates experience higher values of the relative velocity and shear measures compared to points in the inner region of the agglomerates, even for non-spherical agglomerates.

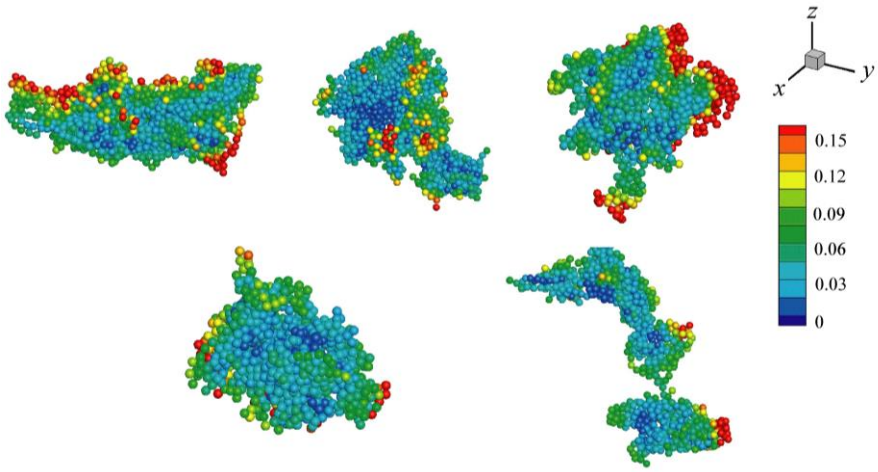

(a)

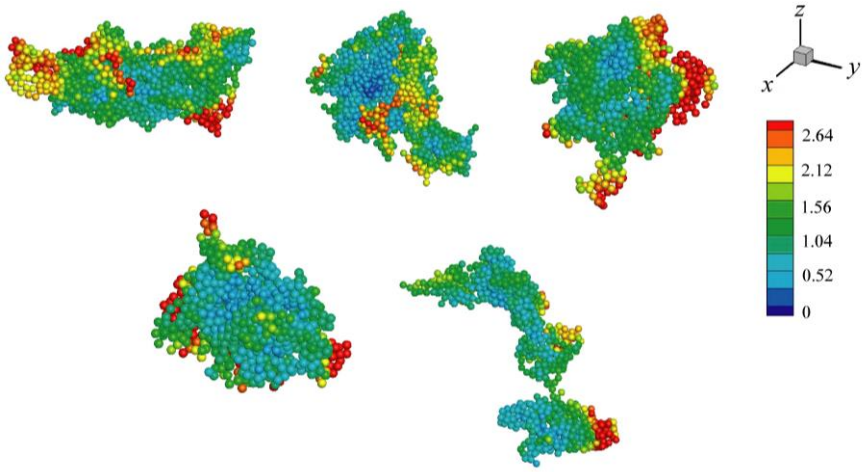

(b)

Figure 5.10. Scatter plots of the five largest agglomerates with colors indicating (a) the relative velocity magnitude and (b) the shear stress measure S for the two-way coupling run for case 2 at $t = 100$.

5.4. Conclusions

A series of computations were performed to examine the differences between computations of turbulent particle agglomeration with one-way and with two-way phase coupling. The computations examined cases with Kolmogorov-scale Stokes numbers varying from about 0.8 to about 14. In agreement with previous literature examining turbulence modulation by particles in this range of Stokes numbers, we observe that the

particles cause enhanced attenuation of the turbulent kinetic energy compared to computations with no particles. The rate of attenuation increased with increase in the particle size and mass loading. In a series of computations repeated both with adhesion and without adhesion, we observe little difference in the rate of particle attenuation, except for the largest size particles. Examination of the agglomeration process indicates that significant agglomeration occurred during the computations, but without any significant influence on the turbulence modulation. This observation reinforces the notion expressed in previous literature [51] that the turbulence attenuation in this Stokes number regime is dominated by particle inertia.

Examination of agglomerate structure during the turbulent agglomeration process indicated that agglomerates formed with two-way coupling were larger and contained more particles than those generated under one-way coupling computations, even though at the time of comparison the turbulent kinetic energy for the two cases was about the same. Agglomerates formed with both one-way and two-way coupling computations had about the same fractal dimension d_f, which compared well with values cited in previous experimental literature for turbulent agglomeration. The volume concentration of particles in each agglomerate was computed and found to vary as a power function with exponent equal to $3-d_f$, in agreement with previous literature on agglomerate fractal structure [2]. While the magnitude of the particle velocity is similar for agglomerates computed with one-way and two-way coupling, the relative velocity between the particle and the fluid is much lower for the two-way coupling computations, particularly once larger-size agglomerates start to form. Several different measures indicated that the fluid flow generated in agglomerates acts to shield the inner-most

particles, so that the highest shear stresses and relative velocity occurs for the outer particles in agglomerate. The motion of fluid inside the large agglomerates was found to be highly correlated to the agglomerate motion.

Acknowledgement

This research was supported by the U.S. National Science Foundation under grant CBET-1332472.

References

[1] J. Liu, W.Y. Shih, M. Sarikaya, I.A. Aksay, Fractal colloidal aggregates with finite interparticle interactions: energy dependence of the fractal dimension, Physical Review A 41(6) (1990) 3206-3213.

[2] Q. Jiang, B.E. Logan, Fractal dimensions of aggregates determined from steady-state size distributions, Environmental Science and Technology 25 (1991) 2031-2038.

[3] Y. Adachi and S. Ooi, Geometrical structure of a floc, Journal of Colloid and Interface Science 135(2) (1990) 374-384.

[4] J.S. Olfert, J.P.R. Symonds, N. Collings, The effective density and fractal dimension of particles emitted from a light-duty vehicle with a diesel oxidation catalyst, Journal of Aerosol Science 38 (2007) 69-82.

[5] A.M. Brasil, T.L. Farias, M.G. Carvalho, U.O. Koylu, Numerical characterization of the morphology of aggregated particles, Journal of Aerosol Science 32 (2001) 489-508.

[6] W.H. Shih, W.Y. Shih, S.I. Kim, J. Liu, I.A. Aksay, Scaling behavior of the elastic properties of colloidal gels, Physical Review A 42(8) (1990) 4772-4780.

[7] S.S. Narine, A.G. Marangoni, A.G., Fractal nature of fat crystal networks, Physical Review E 59(2) (1999) 1908-1920.

[8] S.S. Narine, A.G. Marangoni, Mechanical and structural model of fractal networks of fat crystals at low deformations, Physical Review E 60(6) (1999) 6991-7000.

[9] D.H. Bache, Floc rupture and turbulence: a framework for analysis, Chemical Engineering Science 59 (2004) 2521-2532.

[10] M. Kobayashi, Y. Adachi, S. Ooi, Breakup of fractal flocs in a turbulent flow, Langmuir 15 (1999) 4351-4356.

[11] K. Higashitani, K. Iimura, H. Sanda, Simulation of deformation and breakup of large aggregates in flows of viscous fluids, Chemical Engineering Science 56 (2001) 2927-2938.

[12] A. Scurati, D.L. Feke, I. Manas-Zloczower, Analysis of the kinetics of agglomerate erosion in simple shear flows, Chemical Engineering Science 60 (2005) 6564-6573.

[13] R. Wengeler, H. Nirschl, Turbulent hydrodynamic stress induced dispersion and fragmentation of nanoscale agglomerates, Journal of Colloid and Interface Science 306, (2007) 262-273.

[14] B.K. Brunk, D.L. Koch, L.W. Lion, Hydrodynamic pair diffusion in isotropic random velocity fields with application to turbulent coagulation, Physics of Fluids 9 (1997) 2670-2691.

[15] B.K. Brunk, D.L. Koch, L.W. Lion, Turbulent coagulation of colloidal particles, Journal of Fluid Mechanics 364 (1998) 81-113.

[16] B.K. Brunk, D.L. Koch, L.W. Lion, Observations of coagulation in isotropic turbulence. Journal of Fluid Mechanics 371 (1998) 81-107.

[17] J. Chun, D.L. Koch, Coagulation of monodisperse aerosol particles by isotropic turbulence, Physics of Fluids 17 (2005) 027102.

[18] D.L. Koch, S.B. Pope, Coagulation-induced particle-concentration fluctuations in homogeneous, isotropic turbulence, Physics of Fluids 14 (2002) 2447-2455.

[19] L.P. Wang, A.S. Wexler, Y. Zhou, Statistical mechanical descriptions of turbulent coagulation, Physics of Fluids 10 (1998) 2647-2651.

[20] P. Duru, D.L. Koch, C. Cohen, Experimental study of turbulent-induced coalescence in aerosols, International Journal of Multiphase Flow 33 (2007) 987-1005.

[21] W.C. Reade, L.R. Collins, L.R., A numerical study of the particle size distribution of an aerosol undergoing turbulent coagulation, Journal of Fluid Mechanics 415 (2000) 45-64.

[22] C.T. Crowe, On models for turbulence modulation in fluid-particulate flows, International Journal of Multiphase Flows 26 (2000) 719-727.

[23] J.K. Eaton, Two-way coupled turbulence simulations of gas-particle flows using point-particle tracking, International Journal of Multiphase Flow 35 (2009) 792-800.

[24] A. Saber, T.S. Lundström, J.G. Hellström, Turbulent modulation in particulate flow: a review of critical variables, Engineering 7 (2015) 597-609.

[25] C. Poelma, G. Ooms, Particle-turbulence interaction in a homogeneous, isotropic turbulent suspension, Applied Mechanics Reviews 59 (2006) 78-90.

[26] A. Rao, J.S. Curtis, B.C. Hancock, C. Wassgren, Simulation of dilute turbulent gas-particle flow with turbulence modulation, AIChE Journal 58 (2012) 1381-1396.

[27] S. Balachandar, J.K. Eaton, Turbulent dispersed multiphase flow, Annual Review of Fluid Mechanics 42 (2010) 111-133.

[28] H. Nasr, G. Ahmadi, The effect of two-way coupling and inter-particle collisions on turbulence modulation in a vertical channel flow, International Journal of Heat and Fluid Flow 28 (2007) 1507-1517.

[29] H. Rumpf, The strength of granules and agglomerates, in: W.A. Knepper (Ed.) Agglomeration, John Wiley, New York, 1962, pp. 379-418.

[30] K.A. Kusters, J.G. Wijers, D. Thoenes, Aggregated kinetics of small particles in agitates vessels, Chemical Engineering Science 52(1) (1997) 107-121.

[31] P. Vainshtein, M. Shapiro, Porous agglomerates in the general linear flow field, Journal of Colloid and Interface Science 298 (2006) 183-191.

[32] S. Hansen, D.V. Khakhar, J.M. Ottino, Dispersion of solids in nonhomogeneous viscous flows, Chemical Engineering Science 53(10) (1998) 1803-1817.

[33] J.S. Marshall, Discrete-element modeling of particulate aerosol flows, Journal of Computational Physics 228 (2009) 1541-1561.

[34] T. Bosse, L. Kleiser, C. Härtel, E. Meiburg, Numerical simulation of finite Reynolds number suspension drops settling under gravity, Physics of Fluids 17 (2005) 037101.

[35] R. Di Felice, The voidage function for fluid-particle interaction systems, International Journal of Multiphase Flow 20 (1994) 153-159.

[36] C.Y. Wen, Y.H. Yu, Mechanics of fluidization, Chemical Engineering Progress Symposium Series 62(62) (1966) 100-111.

[37] C.T. Crowe, J.D. Schwarzkopf, M. Sommerfeld, Y. Tsuji, Multiphase Flows with Droplets and Particles, second ed., CRC Press, Boca Raton, Florida, 2012.

[38] P.G. Saffman, The lift on a small sphere in a slow shear flow, Journal of Fluid Mechanics 22 (1965) 385-400.

[39] S.I. Rubinow, J.B. Keller, The transverse force on a spinning sphere moving in a viscous fluid, Journal of Fluid Mechanics 11 (1961) 447-459.

[40] K.L. Johnson, K. Kendall, A.D. Roberts, Surface energy and the contact of elastic solids, Proceedings of the Royal Society of London A 324 (1971) 301-313.

[41] A. Chokshi, A.G.G.M. Tielens, D. Hollenbach, Dust coagulation, The Astrophysical Journal 407 (1993) 806-819.

[42] G.G. Joseph, R. Zenit, M.L. Hunt, A.M. Rosenwinkel, Particle-wall collisions in a viscous fluid, Journal of Fluid Mechanics 433 (2001) 329-346.

[43] Y. Tsuji, T. Tanaka, T. Ishida, Lagrangian numerical simulation of plug flow of cohesionless particles in a horizontal pipe, Powder Technology 71 (1992) 239-250.

[44] K. Bagi, M.R. Kuhn, A definition of particle rolling in a granular assembly in terms of particle translations and rotations, Journal of Applied Mechanics 71 (2004) 493-501.

[45] C. Dominik, A.G.G.M. Tielens, Resistance to rolling in the adhesive contact of two elastic spheres, Philosophical Magazine A 92(3) (1995) 783-803.

[46] A. Vincent, M. Meneguzzi, The spatial structure and statistical properties of homogeneous turbulence, Journal of Fluid Mechanics 225 (1991) 1-20.

[47] T.S. Lundgren, Linearly forced isotropic turbulence, Annual Research Briefs, CTR, Stanford, 2003, pp. 461-473.

[48] C. Rosales, C. Meneveau, Linear forcing in numerical simulations of isotropic turbulence: physical space implementations and convergence properties, Physics of Fluids 17(9) (2005) 095106.

[49] J.S. Marshall, S. Li, Adhesive Particle Flow: A Discrete Element Approach, Cambridge University Press, New York, 2014.

[50] O.A. Druzhinin, S.E. Elghobashi, On the decay rate of isotropic turbulence laden with microparticles, Physics of Fluids 11 (1999) 602-610.

[51] O.A. Druzhinin, The influence of particle inertia on the two-way coupling and modification of isotropic turbulence by microparticles, Physics of Fluids 13(12) (2001) 3738-3755.

[52] K.D. Squires, J.K. Eaton, Particle response and turbulence modification in isotropic turbulence, Physics of Fluids A 2 (1990) 1191-1203.

[53] M. Boivin, O. Simonin, K.D. Squires, Direct numerical simulation of turbulence modulation by particles in isotropic turbulence, Journal of Fluid Mechanics 375 (1998) 235-263.

[54] S.E. Elghobashi, G.C. Truesdell, On the two-way interaction between homogeneous turbulence and dispersed solid particles. I. Turbulence modification, Physics of Fluids A 5 (1993) 1790-1801.

[55] S. Sundaram, L.R. Collins, A numerical study of the modulation of isotropic turbulence by suspended particles, Journal of Fluid Mechanics 379 (1999) 105-143.

[56] R.A. Gore, C.T. Crowe, The effect of particle size on modulating turbulent intensity, International Journal of Multiphase Flow 15 (1989) 279-285.

[57] M.L. Eggersdorfer, D. Kadau, H.J. Hermann, S.E. Pratsinis, Multiparticle sintering dynamics: From fractal-like aggregates to compact structures, Langmuir 27 (2011) 6358-6367.

[58] C. Selomulya, R. Amal, G. Bushell, T.D. Waite, Evidence of shear rate dependence on restructuring and breakup of latex aggregates, Journal of Colloid and Interface Science 236 (2001) 67-77.

[59] M.H. Waldner, J. Sefcik, M. Soos, M. Morbidelli, Initial growth kinetics of aggregates in turbulent coagulator, Powder Technology 156 (2005) 226-234.

[60] C. Binder, C. Feichtinger, H.-J. Schmid, N. Thürey, W. Peukert, U. Rüde, Simulation of the hydrodynamic drag of aggregated particles, Journal of Colloid and Interface Science 301 (2006) 155-167.

[61] L.S. Fellay, C. Twist, M. Vanni, Motion of rigid aggregates under different flow conditions, Acta Mechanica 224 (2013) 2225-2248.

Chapter 6: Collision and Breakup of Fractal Particle Agglomerates in a Shear Flow

Farzad Dizaji, Jeffrey S. Marshall and John R. Grant
Department of Mechanical Engineering
The University of Vermont

Corresponding Author: Jeffrey S. Marshall, Department of Mechanical Engineering, The University of Vermont, Burlington, VT 05405, U.S.A. PHONE: 1 (802) 656-3826, EMAIL: jmarsha1@uvm.edu.

Keywords: particle agglomeration; agglomerate collisions; turbulent agglomeration

Abstract

A computational study was performed of both a single agglomerate and the collision of two agglomerates in a simple shear flow. The agglomerates were extracted from a direct numerical computation of a turbulent agglomeration process, and had the loosely-packed fractal structure typical of agglomerate structures formed in turbulent agglomeration processes. The computation was performed using a discrete-element method for adhesive particles with two-way coupling between the particles and the surrounding fluid flow. In addition to understanding and characterizing the particle dynamics, the study focused on illuminating the fluid flow field induced by the agglomerate in the presence of a background shear and the effect of collisions on this particle-induced flow. Perhaps the most interesting result of the current work was the observation that the flow field induced by a particle agglomeration rotating in a simple shear background flow has the form of two tilted vortex rings with opposite sign circulation. These rings are surrounded by a sea of stretched vorticity from the background shear flow. The agglomerate rotates in the shear flow, but at a slower rate than the ambient fluid elements. In the computations with two colliding agglomerates, we observed cases resulting in agglomerate merger, bouncing and fragmentation. However, the bouncing cases were all observed to also result in an exchange of particles between the two colliding agglomerates, so that they were influenced both by elastic rebound of the agglomerate structures as well as by tearing away of particulate matter between the agglomerates. Overall, the problems of agglomerate-flow interaction and of the collision of two agglomerates in a shear flow are considerably richer in physical phenomena and more complex than can be described by

the common, but simplistic, approximation that represents each agglomerate by an 'equivalent sphere'.

6.1. Introduction

Collision of particle agglomerates with each other and with container walls or other obstacles in turbulent flow fields is important during both the agglomerate formation and breakup processes. The significance of agglomerate collisions has been studied for important industrial processes such as drug particle dispersion in dry particle inhalers (Tong et al., 2013, 2016; Yang et al., 2014), cyclone operation (Tong et al., 2010), and particle filtration (Iimura et al., 2009a,b). Similar agglomerate-agglomerate collision processes occur in astrophysics during formation of protoplanatary disks (Ormel et al, 2007, 2009) and in the dynamics of planetary rings (Schäfer et al., 2007).

The development of particle agglomerates in turbulent flows occurs through a series of processes in which individual particles collide and adhere to form small agglomerates, and these small agglomerates then collide and adhere to each other to form larger agglomerates, and so forth (Dizaji and Marshall, 2016). As the agglomerates increase in size, the agglomerates begin to lose particles by processes such as erosion of small groups of particles from an agglomerate surface or rupture of the agglomerate into smaller pieces in response to the fluctuating turbulent shear flow (Serra et al., 1997; Higashitani et al., 2001), eventually balancing the agglomerate formation processes to achieve a quasi-equilibrium state (provided that the turbulence itself is in an equilibrium state). As discussed by Sayvet and Navard (2000), a dominant agglomerate breakup process for turbulent flows at lower shear stress values is simply fragmentation of agglomerates during collisions with other agglomerates. The question of whether two

colliding agglomerates will merge together, bounce off of each other, or split apart into a large number of fragments is thus one of central importance for a wide range of processes. All three of these outcomes were observed under different conditions in a microgravity experiment of particle agglomerates in a vibrated box by Brisset et al. (2016) for different values of the collision velocity and in a normal gravity experiment by Ihalainen et al. (2012) in which agglomerates were impacted onto a flat surface.

An important simplification that is often made in modeling turbulent agglomeration is to replace a particle agglomerate by single 'effective particle', often selected as a sphere with the same mass as the agglomerate. This assumption is integral to the traditional population balance models for agglomerate formation (Smoluchowski. 1917; Lu and Wang, 2006; Reinhold and Briesen, 2012), and it plays an important part in many analytical statistical models for the early stages of agglomerate formation in turbulence (Brunk et al., 1998; Chun and Koch, 2005; Koch and Pope, 2002; Wang et al., 1998). This equivalent sphere assumption is also used in the 'extended hard-sphere' DEM method, which seeks to use the hard-sphere approach for binary collisions to study formation of particle agglomerates (Kosinski and Hoffmann, 2010; Balakin et al., 2011). All such applications of this equivalent sphere approximation must impose some external criterion for whether or not an agglomerate will stick or bounce upon collision. While an equivalent sphere might have the same particle mass as an actual agglomerate, its mechanical properties and behavior would be dramatically different. As we note above, and will discuss in more detail later in the paper, agglomerate collisions are often much more complicated than a simple stick or bounce decision, with agglomerates exchanging

particles with each other or ejecting multiple fragments as a result of the collision. Such behavior generally is not captured with the equivalent sphere approximation.

There is a fairly large literature on use of the discrete element method (DEM) for examining collision of tightly-packed agglomerates with a wall (Kafui and Thornton, 2000; Lian et al., 1998; Moreno et al., 2003; Moreno-Atanasio et al., 2006; Thornton et al., 1999; Ning et al., 1997; Thornton and Liu, 2004), with each other (Kun and Herrmann, 1999; Schäfer et al., 2007; Seizinger and Kley, 2013; Tong et al., 2009), or with some other obstacle, such as a cylinder or sphere in the flow field (Iimura et al., 2009a,b; Yang et al., 2014). Experimental studies of compressed particle aggregates with each other (Beitz et al., 2011) and with a wall (Samimi et al., 2004) have also been reported. Much of this work is motivated by the problem of deagglomeration of particles in dry powder inhalers (Tong et al., 2013, 2016; Yang et al., 2014), used to break-up agglomerates and deliver small drug particles to the lungs, where they are absorbed. In this application, the particles are initially compressed into tightly-packed aggregates at the time of manufacture, which then need to be broken up to release the small drug particles at time of use. Alternatively, ice particles can form tightly-packed aggregates in planetary rings (Schäfer et al., 2007), and the dynamics of their collision plays a central role in understanding the ring dynamics.

A useful definition of agglomerate strength is given by given by Moreno-Atanasio and Ghadiri (2006), based on the work of Rumph (1962), as “the force that is required to break all contacts simultaneously on a prescribed failure plane”. This force depends both on the strength of the individual contacts and the number of contacts in the failure plane. The number of contacts in any given cross-sectional plane increases with the agglomerate

fractal dimension, with higher values for tightly-packed agglomerates with fractal dimension close to $d_f \cong 3$ and lower values for the loosely-connected agglomerates more typically formed in turbulent flocculation processes, with fractal dimension closer to $d_f \sim 2$. For instance, in experiments with turbulent agglomeration of latex particles in stirred tanks, Selomulya et al. (2001) reported d_f between 1.7 - 2.1 and Waldner et al. (2005) reported d_f between 1.8 - 2.6. The above definition of agglomerate strength is based on the idea of pulling an agglomerate apart in tension, whereas the agglomerate response to collision is more dependent on its behavior under compression. In compressive deformation, agglomerates with lower values of particle concentration are more susceptible to buckling of force chains due to having fewer surrounding particles (Marangoni and Narine, 2001). The sensitivity of agglomerate collisions to particle concentration c (or void fraction $\varepsilon = 1 - c$) was noted in DEM simulations by Gunkelmann et al. (2016), who in a study of head-on collision of two agglomerates in a vacuum and found that agglomerates with higher porosities are more fragile during collision and have higher tendency to fragment. These conclusions are also supported by the simulations of Nguyen et al. (2014) of the collision of a loose agglomerate of fine particles with a larger spherical particle, who found a higher tendency of the loose agglomerate to fragment compared to simulations with highly packed agglomerates.

The current paper examines the collision of two particle agglomerates in a shear flow under conditions typical of agglomerate collision in turbulent flows. The agglomerate collision is computed using a CFD-DEM approach based on the soft-sphere method with two-way coupling. Loosely-structured agglomerates are first generated from

a direct numerical simulation of turbulent agglomeration (Dijazi and Marshall, 2016), and from which agglomerates are extracted and placed in a shear flow. We first examine agglomerate evolution and breakup in shear with no collision, and then examine the effect of two-agglomerate collision on agglomerate merger, bouncing, and fragmentation. The paper differs from previous work in its focus on agglomerate collision in shear flows, in its use of loosely-structured agglomerates typical of turbulent flocculation processes, and in its focus on fluid effects on the agglomerate collision.

6.2. Computational Method

The computational method used in the paper proceeds in two parts. The first part is concerned with the initial formation of agglomerates in a turbulent flow, and the approach used for these computations have been described in detail in a previous paper (Dizaji and Marshall, 2016). The second part conducts a detailed examination of the collision process which occurs when two of the agglomerates are extracted and placed in a plane shear flow, which is intended to represent a very small section of the overall turbulent flow. The agglomerate collision is computed using a soft-sphere DEM method for the particles and a high-order finite-difference method for the fluid. A summary of each of these methods is given below.

6.2.1. Discrete element method

The computations of particle agglomerate collision are performed using a soft-sphere adhesive discrete element method (DEM) to model particle transport and collisions (Marshall, 2009). The computational method uses a multiple time step algorithm, in which the fluid time step $\Delta t = O(\ell / u_0)$, the particle time step $\Delta t_p = O(d / u_0)$, and the collision time step $\Delta t_c = O(d(\rho_p^2 / E_p^2 u_0)^{1/5})$ satisfy

$\Delta t > \Delta t_p > \Delta t_c$. Here d is the particle diameter, ρ_p is the particle density, and E_p is the particle elastic modulus. The method follows the motion of individual particles in the three-dimensional fluid flow by solution of the particle momentum and angular momentum equations

$$m\frac{d\mathbf{v}}{dt} = \mathbf{F}_F + \mathbf{F}_A, \qquad I\frac{d\boldsymbol{\Omega}}{dt} = \mathbf{M}_F + \mathbf{M}_A, \tag{6-1}$$

subject to forces and torques induced by the fluid flow ($\mathbf{F}_F$, $\mathbf{M}_F$) and by the particle collision and adhesion ($\mathbf{F}_A$, $\mathbf{M}_A$). In this equation, m is the particle mass, I is the moment of inertia, and $\mathbf{v}$ and $\boldsymbol{\Omega}$ are the particle velocity and rotation rate, respectively. The dominant fluid force is the drag force, which is given by the Stokes drag law modified to account for the effect of local particle crowding

$$F_d = 3\pi\mu d(\mathbf{u} - \mathbf{v})f, \tag{6-2}$$

where the friction factor $f = C_I C_C$ is written as the product of an inertial correction term C_I and a particle crowding correction term C_C. An expression for the inertial correction was given by Schiller and Naumann (1933) as

$$C_I = 1 + 0.15\,\mathrm{Re}_p^{0.687}, \tag{6-3}$$

where $\mathrm{Re}_p = \rho_f d v_s / \mu$ is the particle Reynolds number and $v_s = |\mathbf{v} - \mathbf{u}|$ is the magnitude of the particle slip velocity relative to the fluid. This expression is valid to within 5% of comparison experimental data for particle Reynolds number up to about 800. An expression for the crowding correction factor was determined empirically by Di Felice (1994) for particle Reynolds numbers in the range 0.01 to 10^4 as a function of the void fraction ε as

$$C_C = \varepsilon^{1-\zeta}, \qquad \zeta = 3.7 - 0.65\exp\left(-\frac{1}{2}[1.5 - \ln(\mathrm{Re}_p)]^2\right). \tag{6-4}$$

This expression approaches the Wen and Yu (1966) expression for low particle Reynolds number. A viscous fluid torque arises from a difference in rotation rate of the particle and the local fluid element (Crowe et al., 2012), and is given by

$$\mathbf{M}_F = -\pi\mu d^3(\boldsymbol{\Omega} - \frac{1}{2}\boldsymbol{\omega}), \tag{6-5}$$

where $\boldsymbol{\omega}$ is the fluid vorticity vector. While the drag is the primary fluid force acting on the particle, we also include in the computations several secondary forces such as the added mass force and the Saffman and Magnus lift forces (Saffman, 1965; Rubinow and Keller, 1961).

The collision and adhesion force and torque fields on particle *i* with radius r_i are given by

$$\mathbf{F}_A = F_n\mathbf{n} + F_s\mathbf{t}_S, \qquad \mathbf{M}_A = rF_s(\mathbf{n}\times\mathbf{t}_S) + M_r(\mathbf{t}_R\times\mathbf{n}), \tag{6-6}$$

where $\mathbf{n} = (\mathbf{x}_j - \mathbf{x}_i)/|\mathbf{x}_j - \mathbf{x}_i|$ is the unit normal vector oriented along the line connecting the centers of the two colliding particles, *i* and *j*. The normal component of the collision and adhesion force F_n is further divided into an elastic-adhesion part F_{ne} and a dissipative part F_{nd}. The sliding resistance is composed of a force with magnitude F_s acting in a direction $\mathbf{t}_S$, corresponding to the direction of relative motion of the particle surfaces at the contact point projected onto the contact plane (the plane orthogonal to **n**), as well as a related torque in the $\mathbf{n}\times\mathbf{t}_S$ direction. The rolling resistance, which arises due to the effects of particle adhesion, exerts a torque of magnitude M_r on the particle in the

$\mathbf{t}_R \times \mathbf{n}$ direction, where $\mathbf{t}_R$ is the direction of the "rolling" velocity. While all of these various collision-adhesion forces and torques are included in the current computations, the dynamics of small adhesive particles are dominated by the normal elastic-adhesive force and the rolling resistance torque.

The effective elastic modulus *E* and the effective radius *R* are defined by

$$\frac{1}{E} \equiv \frac{1-\sigma_i^2}{E_i} + \frac{1-\sigma_j^2}{E_j}, \qquad \frac{1}{R} \equiv \frac{1}{r_i} + \frac{1}{r_j}, \tag{6-7}$$

where E_i, σ_i, and r_i are the elastic modulus, Poisson ratio, and radius of particle *i*, respectively. The adhesive force between the two particles depends on the surface energy potential γ, where the work required to separate two spheres colliding over a contact region of radius $a(t)$ is given by $2\pi\gamma a^2$ in the absence of further elastic deformation. Particle normal elastic rebound force and adhesion force are simulated by employing the soft-sphere collision model of Johnson, Kendell and Roberts (1971), hereinafter referred to as the JKR model, which can be written in terms of the contact region radius $a(t)$ and the normal particle overlap $\delta_N = r_i + r_j - \left|\mathbf{x}_i - \mathbf{x}_j\right|$ as (Chokshi et al. 1993)

$$\frac{\delta_N}{\delta_c} = 6^{1/3}\left[2\left(\frac{a}{a_o}\right)^2 - \frac{4}{3}\left(\frac{a}{a_o}\right)^{1/2}\right], \qquad \frac{F_{ne}}{F_c} = 4\left(\frac{a}{a_o}\right)^3 - 4\left(\frac{a}{a_o}\right)^{3/2}, \tag{6-8}$$

The critical overlap δ_c, the critical normal force F_c, and the equilibrium contact region radius a_o are given by (Johnson et al. 1971)

$$F_c = 3\pi\gamma R, \qquad \delta_c = \frac{a_o^2}{2(6)^{1/3}R}, \qquad a_o = \left(\frac{9\pi\gamma R^2}{E}\right)^{1/3}. \tag{6-9}$$

As two particles move away from each other following collision, they remain in contact until the point where $F_n = -F_c$ and $\delta_N = -\delta_c$ due to the necking of the material in the contact region. Beyond this state any further separation leads the two particles to break apart.

The effect of the fluid squeeze-film within the contact region is to limit the minimum approach distance between the particles (i.e., the contact region gap size) and to reduce the particle restitution coefficient. Experimental studies of particle collisions at different Stokes numbers (e.g., Joseph et al., 2001) indicate that the coefficient of restitution is essentially zero when the Stokes number is less than about 10 due to dissipation in the squeeze-film. We use the model of Tsuji et al. (1992) for the dissipative part of the normal collision force F_{nd} and set the damping parameter such that the restitution coefficient vanishes.

The second major effect of particle adhesion is to introduce a torque that resists particle rolling. For uniform-size spherical particles, the "rolling velocity" $\mathbf{v}_L$ of particle *i* is given by (Bagi and Kuhn 2004)

$$\mathbf{v}_L = -R(\boldsymbol{\Omega}_i - \boldsymbol{\Omega}_j) \times \mathbf{n} \ . \tag{6-10}$$

A linear expression for the rolling resistance torque M_r is postulated as

$$M_r = -k_R \, \xi \, , \tag{6-11}$$

where $\xi = (\int_{t_0}^{t} \mathbf{v}_L(\tau) \, d\tau) \cdot \mathbf{t}_R$ is the rolling displacement in the direction $\mathbf{t}_R = \mathbf{v}_L / |\mathbf{v}_L|$.

Rolling involves an upward motion of the particle surfaces within one part of the contact region and a downward motion in the other part of the contact region. The presence of an

adhesion force between the two contacting surfaces introduces a torque resisting rolling of the particles. An expression for the rolling resistance due to van der Waals adhesion was derived by Dominik and Tielens (1995), which yields the coefficient k_R as

$$k_R = 4F_c(a/a_0)^{3/2}. \tag{6-12}$$

Dominik and Tielens (1995) further argue that the critical resistance occurs when the rolling displacement ξ achieves a critical value, corresponding to a critical rolling angle $\theta_{crit} = \xi_{crit}/R$. For $\theta > \theta_{crit}$, the rolling displacement ξ in (6-11) is replaced by ξ_{crit}. Data for critical rolling angle with particles having diameter of approximately 10 μm were reported by Ding et al. (2008), who found critical rolling angles θ_{crit} of between 0.02 and 0.06 radians.

A simplified expression for the effect of van der Waals adhesion on tangential sliding resistance was proposed by Thornton (1991). In this model, the sliding resistance force F_s is given by a spring-like expression of the form (Cleary et al., 1998)

$$F_s = -k_T \left(\int_{t_0}^{t} \mathbf{v}_S(\xi)\, d\xi \right) \cdot \mathbf{t}_S \tag{6-13}$$

when F_s is less than a critical value F_{crit}. In (6-13), the sliding velocity $\mathbf{v}_S(t)$ is the relative tangential surface velocity of the particles at the contact point projection. The tangential stiffness coefficient k_T is derived by Mindlin (1949) and can be written in terms of the contact region radius $a(t)$ as

$$k_T = 8G\, a(t). \tag{6-14}$$

The critical sliding force is approximated using the expression

$$F_{crit} = \mu_f \left| F_{ne} + 2F_c \right|, \tag{6-15}$$

where F_c is the critical force for pull-off given in given in (6-9) and μ_f is the friction coefficient. The expression (6-15) was shown Thornton (1991) to provide results in reasonable agreement to experiments. For $\left|F_s\right| \geq F_{crit}$, the sliding resistance is given by the Amonton expression $F_s = -F_{crit}$.

6.2.2. Agglomerate formation

The agglomerates are formed using a turbulent agglomeration process with two-way coupling, similar to that described by Dizaji and Marshall (2016). The computations employed a pseudo-spectral method for forced turbulence on a triply-periodic domain measuring $(2\pi)^3$, with 128 grid points in each direction. The turbulence is initiated with random perturbations and allowed to develop with no particles until it approached a quasi-steady state corresponding to microscale Reynolds number $\mathrm{Re}_\lambda = u_0 \lambda / \nu = 99$. Particles are then added to the computation, with 46,656 particles spread randomly over the flow field with diameter $d = 0.04$ and particle-to-fluid density ratio $\rho_p / \rho_f = 10$. Over time as the particles are advected by the flow, small agglomerates first form and then collide with each other to form progressively larger agglomerates.

The computation was stopped once the agglomerates achieved a broad range of sizes. One common way to measure the size of an agglomerate is the radius of gyration R_g, which for an agglomerate with N particles is defined by

$$R_g = \left[\sum_{i=1}^{N} \left| \mathbf{x}_i - \bar{\mathbf{x}} \right|^2 \right]^{1/2}. \tag{6-16}$$

In this equation, $\bar{\mathbf{x}}$ denotes the position vector of the agglomerate centroid and $\mathbf{x}_i$ is the centroid of the i^{th} particle within the agglomerate. Particle agglomerates admit a power law relating N and R_g given by (Adachi and Ooi, 1990)

$$N = K\left(R_g / r_p\right)^{d_f}, \tag{6-17}$$

where K is a coefficient (called the fractal pre-factor), r_p is the individual particle radius, and the exponent d_f is the fractal dimension of the agglomerate. The value of d_f for particle agglomerates varies over the interval $1 \le d_f \le 3$ depending on the agglomeration formation mechanism (Brasil et al., 2001); however, typical values for turbulent particle agglomeration processes are between about 1.7 - 2.8 (Selomulya et al., 2001; Waldner et al.). A log-log plot of N versus R_g / r_p for the current turbulent flow simulation is given in Figure 6.1. The best-fit line to DNS data has slope $d_f = 2.12$, which is consistent with the range of fractal dimension observed in the experimental turbulent particle agglomeration studies listed above.

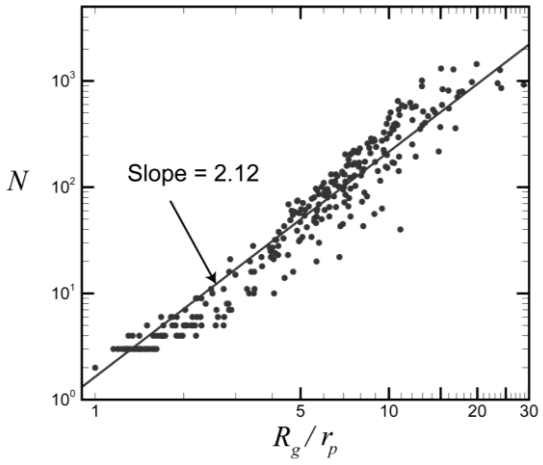

Figure 6.1. Plot of the number of particles in an agglomerate N versus the ratio of the radius and gyration of the agglomerate R_g and the individual particle radius r_p. The slope of the plot indicates the dimension $d_f = 2.12$ of the power law in Eq. (17).

6.2.3. Shear flow simulation

The agglomerates extracted from the turbulent agglomeration calculation described in Section 6.2.2 are immersed in a linear shear flow, where the initial configuration appears as shown in Figure 6.2a for cases with a single agglomerate in the shear flow and as shown in Figure 6.2b for cases with agglomerate collision.

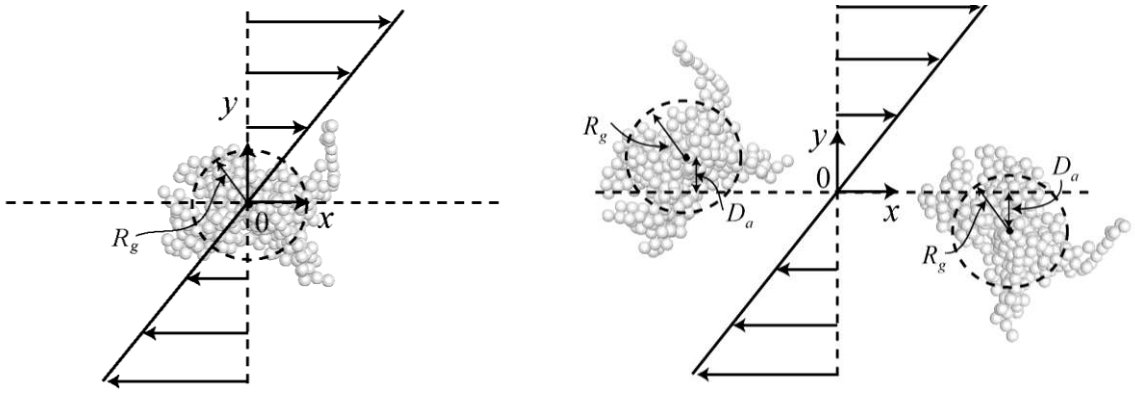

Figure 6.2. Schematic diagram of the initial conditions for the problems of (a) a single agglomerate in a shear flow and (b) two-agglomerate collision in a shear flow. Circles indicate the radius of gyration R_g, and the offset distance D_a is indicated in (b) in both positive and negative directions.

Over time, the shear flow is modified by the presence of the particles, as described below. The fluid flow is assumed to be incompressible and is governed by the continuity and momentum equations of the form

$$\nabla \cdot \mathbf{u} = 0\,, \tag{6-18a}$$

$$\frac{\partial \mathbf{u}}{\partial t} + (\mathbf{u} \cdot \nabla)\mathbf{u} = -\frac{1}{\rho_f}\nabla p + \nu \nabla^2 \mathbf{u} + \mathbf{F}_p\,. \tag{6-18b}$$

In this equation, $\mathbf{u}$, p and $\mathbf{F}_p$ are the fluid velocity, the pressure and the particle-induced body force per unit mass, respectively. The void fraction $\varepsilon = 1 - c$ was not included in (6-

17) since our computations indicate that local void fraction remains above 90% even within the agglomerates for current computations due to the loose structuring of agglomerates typical of turbulent flow.

Both the particle-induced body force and the particle concentration field (a post-processing variable) were computed using the conservative particle blob method described by Marshall and Sala (2013). In this method, the particle body force field $\mathbf{F}_p(\mathbf{x},t)$ is written as the sum of some number N particle 'blobs', centered at positions $\mathbf{x}_n$, as

$$\mathbf{F}_p(\mathbf{x},t) = \sum_{n=1}^{N} \mathbf{A}_n f_w(\mathbf{x}-\mathbf{x}_n, R_n)\,. \tag{6-19}$$

The Gaussian weighting function f_w is a function of position and the characteristic blob 'radius' R_n as

$$f_w(\mathbf{x}-\mathbf{x}_n, R_n) = \frac{2}{3\pi R_n^3}\exp[-|\mathbf{x}-\mathbf{x}_n|^2 / R_n^2]\,. \tag{6-20}$$

The blob amplitude, $\mathbf{A}_n$, is given by

$$\mathbf{A}_n = \frac{(-\mathbf{F}_{f,n})}{G_{cell}\sum_{j=1}^{Q} f_w(\mathbf{g}_j - \mathbf{x}_n, R_n)}, \tag{6-21}$$

where $\mathbf{g}_j$ is the location of the centroid of grid cell j, and $\mathbf{x}_n$ is the centroid of particle n, G_{cell} is the grid cell volume, and $\mathbf{F}_{f,n}$ is the fluid-induced force acting on particle n (which imposes an equal and opposite force $-\mathbf{F}_{f,n}$ back on the fluid). The force $\mathbf{F}_{f,n}$ is given by the sum of the drag force in (6-2) plus minor forces such as lift, added mass force, and pressure gradient force. Each particle distributes part of its force to a set Q of

surrounding grid cells, and the sum in the denominator of (6-21) is evaluated over all grid cells in this set Q. With the choice (6-21) for blob amplitude, the discrete-to-continuum conversion operation is discretely conservative. This method can be applied to other quantities, such as the particle concentration, simply by replacing the particle force with the particle volume.

The computations were performed using a fractional-step method (Rai and Moin, 1991; Verzicco and Orlandi, 1996; Uhlmann, 2005), with time advancement performed using a third-order Runga-Kutta method for convective terms and the 2nd order Crank-Nicholson method for viscous terms. Algorithms for all spatial derivatives except the convective terms are approximated using second-order centered finite differences (three point stencil) on a non-staggered grid. The discretized equations for the kth Runge-Kutta step are given by

$$\begin{aligned}\tilde{\mathbf{u}} = \mathbf{u}^{k-1} &+ \Delta t\left(2\alpha_k \nu \nabla^2 \mathbf{u}^{k-1} - 2\alpha_k \nabla p^{k-1}\right) \\ &- \Delta t\left\{\gamma_k[(\mathbf{u}\cdot\nabla)\mathbf{u} + \mathbf{F}_p]^{k-1} + \zeta_k[(\mathbf{u}\cdot\nabla)\mathbf{u} + \mathbf{F}_p]^{k-2}\right\},\end{aligned} \tag{6-22a}$$

$$\nabla^2 \mathbf{u}^* - \frac{\mathbf{u}^*}{\alpha_k \nu \Delta t} = -\frac{\tilde{\mathbf{u}}}{\alpha_k \nu \Delta t} + \nabla^2 \mathbf{u}^{k-1}, \tag{6-22b}$$

$$\nabla \cdot \left(\nabla \phi^k\right) = \frac{\nabla \cdot \mathbf{u}^*}{2\alpha_k \Delta t}, \tag{6-22c}$$

$$\mathbf{u}^k = \mathbf{u}^* - 2\alpha_k \Delta t \nabla \phi^k, \tag{6-22d}$$

$$p^k = p^{k-1} + \phi^k - \alpha_k \nu \Delta t \nabla^2 \phi^k, \tag{6-22e}$$

where α_k, γ_k, and ζ_k are coefficients given by Rai and Moin (1991). Continuity is enforced by a projection method leading to equation (6-22c) for the pseudo-pressure, denoted by ϕ. In the multigrid solution of this equation, the five-point stencil produced

by successive application of the gradient operation followed by the divergence operation was employed, rather than the finite-difference approximation to the Laplacian. The Crank-Nicholson method was used to solve the Helmholtz problem, given in (6-22b). A tenth-order approximation was used for the convective terms, requiring an 11-point stencil. To control non-linear instabilities, at the end of each time step the velocity components were filtered using a tenth-order filter (again using an 11-point stencil)(Lele, 1992; Steijl, 2001). After filtering to obtain $\mathbf{u}^{filtered}$, the velocity $\mathbf{u}$ was replaced by $(1-q)\mathbf{u} + q\mathbf{u}^{filtered}$, with $q = 0.05$.

The flow was initialized in the x-direction with linear variation in the y-direction. The upper wall at $y = 2$ was maintained at a velocity $u = 1$ and the lower wall at $y = -2$ was maintained at a velocity of $u = -1$, giving a dimensionless shear rate of $S = 0.5$. The no-slip boundary condition was applied at both the top and bottom wall in the y-direction, and the flow was assumed to be periodic in the x- and z-directions. A layer of five ghost points in each direction surrounded the computational domain, so that no adjustment of the differentiation schemes was needed near the domain boundaries. The velocity on the ghost points was set at the upper and lower edges of the grid by linearly extrapolating the velocity from the point on the wall and the first point off of the wall. The velocity on the ghost points at the horizontal edges of the grid were set so as to enforce periodicity. The fluid flow calculations were carried out on a Cartesian grid with equal spacing in each direction. The computations were performed on a 128^3 grid covering the interval (-2,2) in each coordinate direction. The time step was held fixed at $\Delta t = 0.005$. The dimensionless fluid kinematic viscosity was set to $\nu = 0.0003$ for all computations.

6.3. Agglomerate Motion and Breakup in Shear Flow

In this section we examine the dynamics of a single particle agglomerate exposed to shear flow, with particular focus on examination of the particle-induced flow field associated with rotation of the agglomerate in the shear flow and on the conditions for agglomerate breakup. This section helps to set the stage for the study of agglomerate collision in shear flow in the next section. The problem of agglomerate dynamics in a shear flow has been previously examined by a number of authors. A series of experiments on this problem were reported by Sonntag and Russel (1986), who found that the average radius of gyration of the agglomerates could be expressed as a power law function of the shear rate as $R_g^3 \propto S^{-1.06}$. Since the average number of particles in the agglomerate N was related to radius of gyration by a power law expression of the form (6-16), with $d_f \cong 2.48$ in their experiments, their expression for agglomerate size in the shear flow could alternatively be expressed as $N \propto S^{-0.878}$.

A number of DEM simulations of agglomerate dynamics in a shear flow have been reported (Potanin, 1993; Higashitani et al., 2001; Fanelli et al., 2006; Becker et al., 2009) based on the so-called free-draining approximation, which assumes that the particles do not influence the fluid flow (one-way coupling). Potanin (1993) and Becker et al. (2009) further assumed that particles did not influence fluid forces on each other (even under close packing in the agglomerate), whereas Higashitani et al. (2001) and Fanelli et al. (2006) assumed that fluid drag forces act only on particle surfaces on the outside of the agglomerate (i.e., that fluid does not penetrate into the agglomerate). Higashitani et al. (2001) observed that the average number of particles in broken

agglomerate fragments, N, varies with the adhesion parameter as $N \propto \mathrm{Ad}^{0.872}$, where Ad represents a ratio of adhesive to hydrodynamic force. Since Ad is inversely proportional to shear rate, this observation is consistent with the scaling found experimentally by Sonntag and Russel (1986). Becker et al. (2009) compared the DEM simulations using the free-draining approximation to a full finite-element simulation of the flow field and found that the free-draining approximation breaks down as the agglomerate size increases. This observation is consistent with that made in a recent DEM/CFD study of turbulent agglomeration by Dizaji and Marshall (2016), who compared results with one-way and two-way coupling and found significant deviance between the two as the agglomerate size increased. Becker et al. (2009) observed that small agglomerates rotate in an almost rigid-body fashion in the shear flow, large agglomerates break up into pieces, and agglomerates of an intermediate size undergo a restructuring, in which they deform and change form as they rotate but do not break up.

A full CFD-DEM study of agglomerate dynamics in a shear flow was reported by Zeidan et al. (2007), but the computations are restricted to two-dimensions and the models used for particle collision and adhesion forces were highly simplified. For instance, no tangential forces on the particles were included to resist rolling and sliding motions, which as noted by Becker et al. (2009) are important in modeling agglomerate deformation under the shear flow.

In the current section, we report on a three-dimensional CFD-DEM study of agglomerate dynamics in a shear flow using a complete and well-validated DEM approach, with a focus on resolving and understanding the flow field induced by the particles. In order to work with agglomerate structures typical of those found in turbulent

agglomeration processes, the computations were initiated by extracting an agglomerate from the turbulent flow computation described in Section 6.2.3 and inserting it into an initially linear shear flow. The flow evolution is then computed using the CFD method described in Section 6.2.2 and the DEM model described in Section 6.2.1.

The shear flow acts to rotate and stretch the agglomerate, whereas the adhesion force acts to hold the agglomerate together as a rigid body. The competition between these two effects determines the agglomerate behavior in the shear flow. We let R_{g0} denote the initial radius of gyration of the agglomerate and S denote the ambient shear rate. The characteristic length, time and velocity scales of the flow were selected as R_{g0}, $1/S$, and SR_{g0}, respectively. The primary dimensionless parameter governing the agglomerate behavior in the shear flow is the adhesion parameter, which for current purposes is defined as the ratio of the adhesion force between individual particles ($O(\gamma d)$) to the viscous force ($O(\mu dU)$) imposed on a particle by the fluid flow. Using $U \sim SR_{g0}$ as the typical velocity scale, the adhesion parameter for this problem takes the form

$$\mathrm{Ad} = \frac{\gamma}{\mu S R_{g0}}. \tag{6-23}$$

This measure is essentially the same as the inverse of the fragmentation number proposed by Hansen et al. (1998). A secondary parameter characterizing the particle motion is the Stokes number St, which is interpreted as the ratio of particle characteristic time scale $\tau_p = m/3\pi\mu d$ to the fluid time scale $\tau_f = 1/S$, giving

$$\mathrm{St} = \frac{\rho_p d^2 S}{18\mu}. \tag{6-24}$$

The values of the adhesion parameter Ad, the initial number of particles N_0, and the ratio R_{g0}/d of initial agglomerate gyration radius to particle diameter are given for all single-agglomerate runs in Table 6.1. All computations reported in the paper have Stokes number of St = 1.4 and density ratio of $\rho_p/\rho_f = 10$. The shear Reynolds number can be defined in terms of shear rate and radius of gyration as $\mathrm{Re}_S = SR_{g0}^2/\nu$, which is found to have a value ranging from 52-102 in the current computations, depending on which of the three extracted agglomerates are under consideration. In a turbulent flow, the parameters used in these computations would therefore be larger than the Kolmogorov scale and smaller than the integral scale, perhaps typical of the Taylor microscale of the turbulent motion.

Table 6.1. Listing of parameter values for cases examined with a single agglomerate in a shear flow, including adhesion parameter, initial number of particles, and ratio of initial gyration radius to particle diameter. For all cases examined St = 1.4 and $\rho_p/\rho_f = 10$.

Case Number	Ad	N_0	R_{g0}/d
A.1	133	328	4.81
A.2	333	328	4.81
A.3	666	328	4.81
A.4	999	328	4.81
A.5	146	269	4.40
A.6	364	269	4.40
A.7	728	269	4.40
A.8	1092	269	4.40
A.9	104	577	6.17
A.10	259	577	6.17
A.11	518	577	6.17
A.12	778	577	6.17

Computations in this section were performed using three different agglomerates selected from the turbulent agglomeration simulation, and for four different adhesion parameter values for each agglomerate. A time series of the particle positions during a typical run (Case A.4) for a case where the agglomerate rotates without breakup, but exhibits some restructuring during the rotation, is shown in Figure 6.3. The particles in Figure 6.3 are colored by the magnitude of the *relative particle velocity*, defined by $\mathbf{w} \equiv \mathbf{v} - \mathbf{u}$, where $\mathbf{v}$ is the particle velocity and $\mathbf{u}$ is the fluid velocity. We will also later refer to the *relative fluid velocity* $\mathbf{u}_{rel} = \mathbf{u} - Sy\mathbf{e}_x$, which is simply the fluid velocity field minus the velocity of the ambient shear flow. The initial velocity of the agglomerate particles is set equal to a rigid body rotation at the rotation rate $S/2$ of the shear flow, for which there exists a vertical y-component of velocity in addition to the x-component of velocity characteristic of the ambient shear. This initial rotation rate of the agglomerate gives rise to a linear variation of the relative particle velocity extending outward from the agglomerate center, as shown in Figure 6.3a. At later times, the size of the region of low relative particle velocity near the agglomerate center appears to grow and the particles with higher values of relative particle velocity are restricted to the outer parts of the agglomerate. This development is due to the effects of the particle-induced velocity field in shielding the inner regions of the agglomerate.

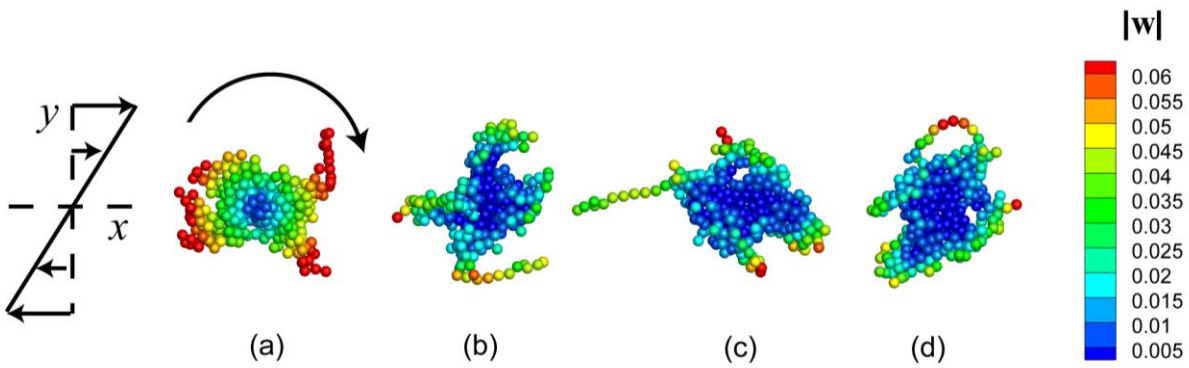

Figure 6.3. Particle positions at times (a) $t = 0$, (b) 10, (c) 20, and (d) 30 for Case A.4. The particles are colored by the magnitude of the relative velocity vector. The agglomerate is rotating clockwise in the shear flow and completes approximately one rotation in the time interval shown.

In the following, we shall examine the results for Case A.4 in detail, which is typical of a case where the agglomerate does not break up in the shear flow. The particle coordination number for this computation remains nearly constant with time at a value of 3.9. The radius of gyration R_g and the particle concentration c_{agg} within the agglomerate oscillate in time, as shown in Figure 6.4b. The value of c_{agg} is computed by dividing the volume of all particles associated with the agglomerate, $V_p = (\pi/6)Nd^3$, by the effective volume V_{eff} occupied by the agglomerate. The agglomerate effective volume is estimated by $V_{eff} = (4\pi/3)R_{eff,i}^3$, where the effective radius of the agglomerate R_{eff} is related to the radius of gyration by $R_{eff} = \sqrt{5/2}\,R_g$. This expression is based on the expression for radius of gyration of a solid sphere of uniform density. The particle volume fraction of the agglomerate can be related to the fractal dimension by (Jiang et al., 1991; Kusters et al., 1997)

$$c_{agg,i} = c_0 (R_{g,i}/d)^{d_f - 3}, \tag{6-25}$$

where c_0 is a constant. If the fractal dimension $d_f < 3$, an increase in agglomerate size results in a decrease in average particle volume fraction (Olfert et al., 2007). Both the radius of gyration and the particle concentration c_{agg} within the agglomerate oscillate during the computation as agglomerate restructuring occurs, with oscillation amplitude of about 3% of the mean radius of gyration and 9% of the mean particle concentration.

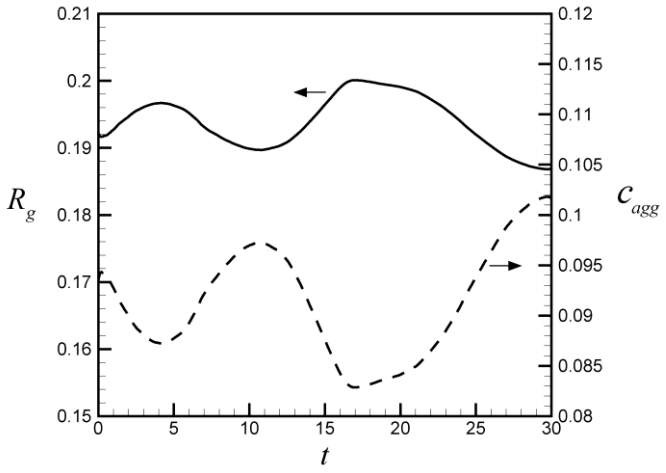

Figure 6.4. Plot showing the time-variation of the gyration radius R_g (solid line, left-hand axis) and the particle concentration within the agglomerate c_{agg} (dashed line, right-hand axis) for Case A.4.

The time variation of the magnitude of the particle velocity **v** and the relative particle velocity **w** are plotted in Figure 6.5a. The particle velocity magnitude oscillates during the computation and the relative particle velocity exhibits a rapid initial decrease and then oscillates during the remainder of the computation. The latter result indicates that the fluid flow within the agglomerate responds quickly to changes in the particle velocity. The fact that the relative particle velocity magnitude is lower than the particle velocity magnitude for most of the computation is a result of the particles dragging the

fluid flow around with them as they rotate in the flow field, thereby decreasing their relative velocity.

The distribution of different measures within the agglomerate is examined by computing the second-moment measure $\mu_i(F)$ of a given field $F(\mathbf{x})$ for each agglomerate *i* as

$$\mu_i(F) = \frac{N_i \left(\sum_{j=1}^{N_j} \left| \mathbf{x}_j - \bar{\mathbf{x}}_i \right|^2 F_j \right)}{\left(\sum_{j=1}^{N_i} \left| \mathbf{x}_j - \bar{\mathbf{x}}_i \right|^2 \right) \left(\sum_{j=1}^{N_i} F_j \right)}, \tag{6-26}$$

where $\bar{\mathbf{x}}_i$ is the centroid of agglomerate i and F_j is the value of the function $F(\mathbf{x})$ evaluated at the centroid $\mathbf{x}_j$ of the j^{th} particle within the agglomerate (Dizaji and Marshall, 2017). The second-moment measure is shown in Figure 6.5b for three different fields – the particle coordination number n_c, the magnitude of the relative particle velocity magnitude **w**, and the magnitude of the relative particle rotation rate about the agglomerate center

$$\mathbf{\Omega}_{agg,rel} = (\mathbf{x} - \mathbf{x}_{c,agg}) \times \mathbf{w} \ / \ \left| \mathbf{x} - \mathbf{x}_{c,agg} \right|^2. \tag{6-27}$$

A value of the second moment $\mu(F)$ equal to unity indicates that the function $F(\mathbf{x})$ is uniform (or statistically randomly varying) across the agglomerate, whereas a value of $\mu_i(F)$ that is less (greater) than unity implies that particles with higher (lower) values of $F(\mathbf{x})$ are found near the center of the agglomerate compared to particles on the outer parts of the agglomerate. Figure 6.5b shows that the second moment measure for the coordination number is consistently less than unity (close to 0.9), indicating that the

agglomerate is more compact near its center than in its outer parts, as would be expected of a fractal agglomerate structure. The second moment of the relative velocity magnitude oscillates as the agglomerate restructures during rotation in the shear flow, but its value remains well above unity, varying from about 1.35 to 1.95. This observation supports the statement made earlier that small values of relative particle velocity are found near the center of the agglomerate and larger values are found only on the outermost particles. While this difference is related, in part, simply to the rotation of the agglomerate about its centroid, it is evident by comparison of Figure 6.3a and 6.3d that this effect becomes more pronounced with time, indicating that the particle-induced flow also plays a role. The relative particle rotation rate about the agglomerate centroid, also oscillates in time, increasing from near unity at the start of the computation to an average value of about 1.2 in the second half of the computation. This quantity can be viewed as a measure of the effect of the particle-induced fluid flow - if there were no particle-induced flow the value of this quantity would remain at unity. The fact that this measure increases above unity is an indication that the particle-induced flow shields the inner parts of the agglomerate, resulting in a lower ratio of the relative velocity to radial distance in this region than in the outer part of the agglomerate. A somewhat similar observation of shielding of the center parts of agglomerates falling in a fluid was noted by Kusters et al. (1997).

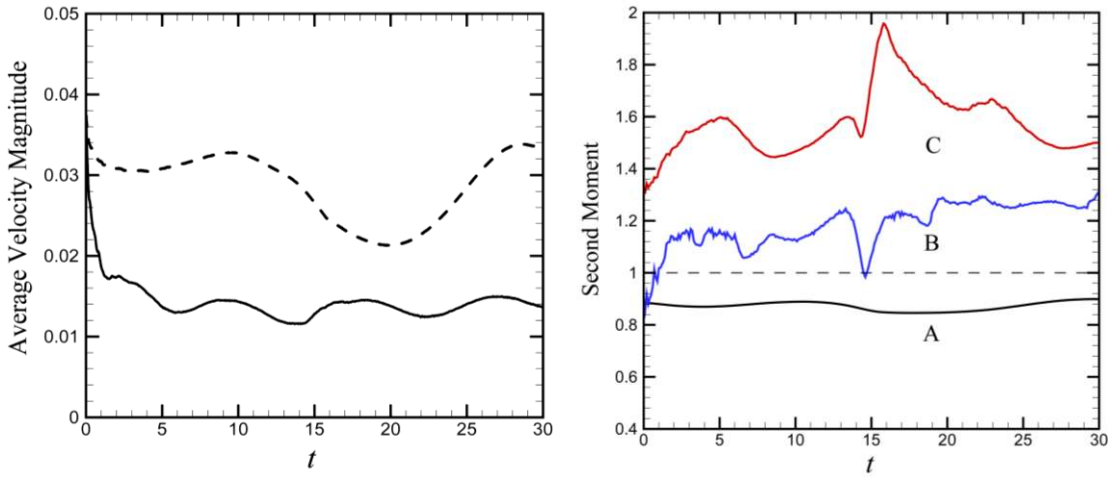

Figure 6.5. Plot showing the time-variation of (a) the average value of the magnitude of the particle velocity **v** (dashed line) and the relative particle velocity vector $\mathbf{w} \equiv \mathbf{v} - \mathbf{u}$ (solid line) and (b) the second-moment measure for particle coordination number (black line), relative rotation rate about the agglomerate centroid (blue line), and relative velocity magnitude (red line) for Case A.4.

The rotation frequency of a fluid element in the shear flow is equal to $f_{fluid} = (S/2)/2\pi \cong 0.0398$. The rotation period of the agglomerate was estimated by labeling each point and observing the time required for one rotation. This measurement is necessarily somewhat imprecise since there is some restructuring of the agglomerate during the rotation, but we took care to also estimate the uncertainty in the estimate. Taking the inverse of the rotation period, our estimate of agglomerate rotation frequency for this computation is $f_{agg} \cong 1/37.3 = 0.027 \pm 0.002$. Consequently, we observe that the particle agglomerate is rotating about 30% more slowly than would a fluid element in the shear flow. This observation is consistent with the findings of Li et al. (2016), who found that a porous circular particle in a two-dimensional shear flow rotates in the flow more slowly than a fluid element. In Figure 6.6a, we plot contours of the relative fluid velocity in the streamwise (x) direction, u_{rel}, at time t = 20, which is typical of the results

observed throughout the computation. The relative fluid velocity is found to be oriented in a direction opposite to the ambient shear velocity, with negative value for $y > 0$ and positive value for $y < 0$. A profile of the relative fluid velocity along the y-axis ($x = z = 0$) is shown in Figure 6.6b as dots, with the ambient shear flow drawn as a solid line. We again see that the computed velocity in the region near the agglomerate ($|y| < 0.4$) lags behind the ambient shear velocity, which is due to the fact that the particle agglomerate is rotating more slowly than the fluid element so that the forces induced by the particles retard the fluid flow.

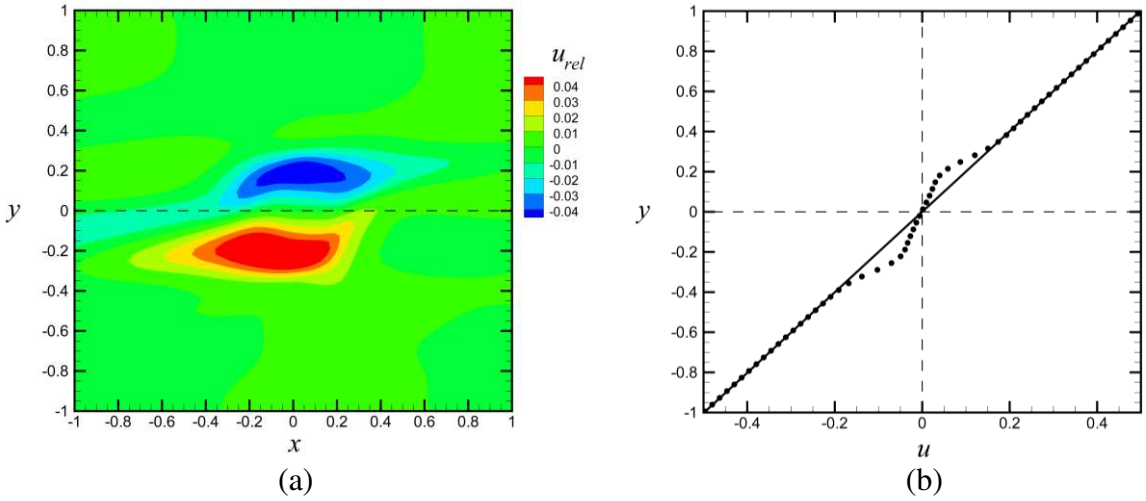

Figure 6.6. (a) Contour plot of the x-component u_{rel} of the relative velocity in the x-y plane, for Case A.4 at $t = 26$. (b) Profile of the x-component of velocity u along the y-axis. The solid line denotes the ambient shear flow and the dots denote the computed velocity profile.

A series of plots in the three cross-sectional planes (x-y, x-z, and y-z) are shown in Figure 6.7, where for each plane we plot the in-plane streamlines (obtained by setting the normal velocity component to zero) and the contours of both the normal vorticity and velocity components. The plots do not include the entire computational domain, but instead focus on the central part of the domain near the agglomerate.

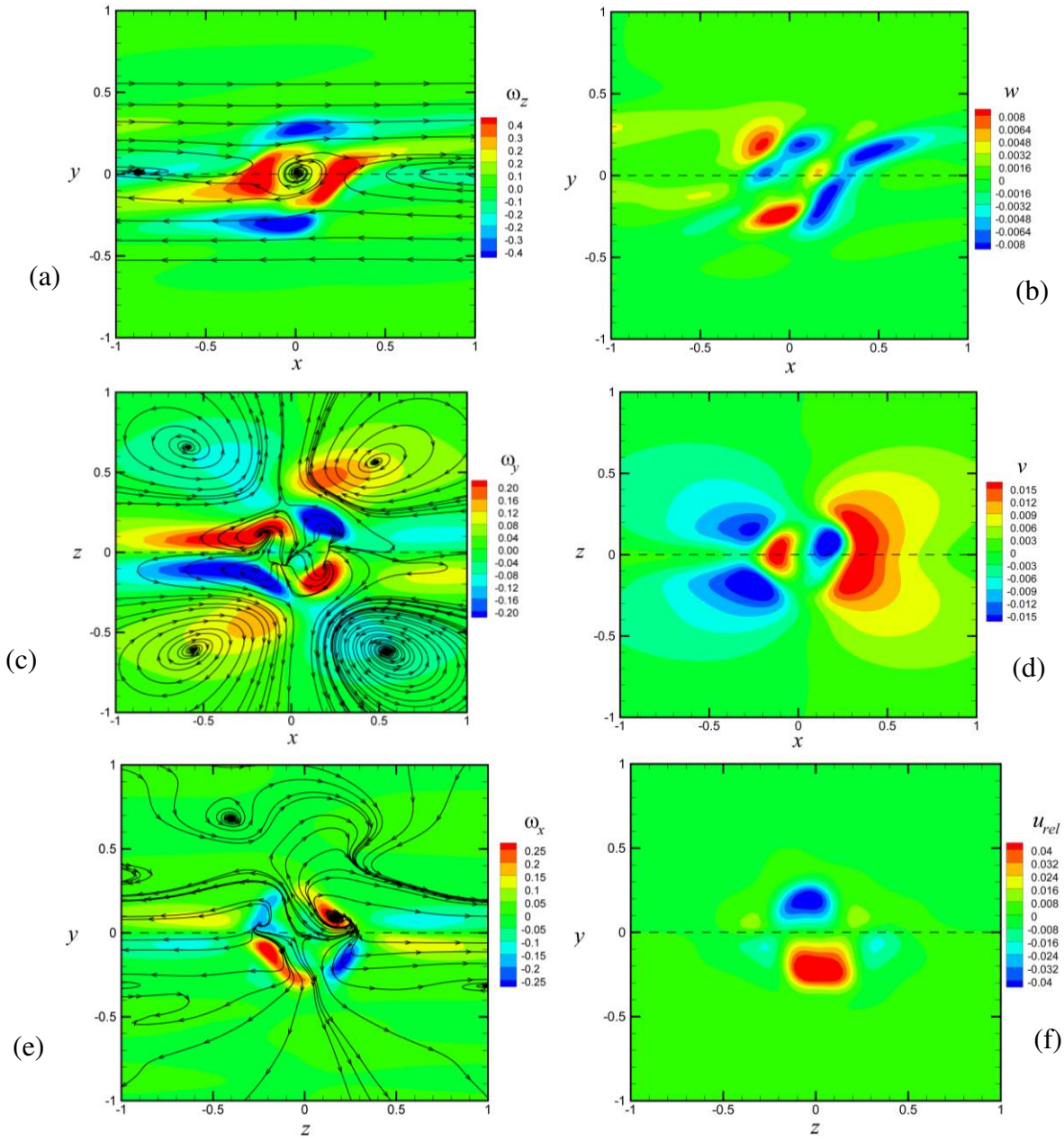

Figure 6.7. (Left) contours of normal vorticity and streamlines of the in-plane velocity field and (right) contours of normal component of the relative velocity $\mathbf{u}_{rel}$ in three orthogonal planes passing through the agglomerate, for Case A.4 at t = 26.

In Fig. 6.7a, the streamlines in the x-y plane are seen to exhibit a vortex at the origin (i.e., at the center of the agglomerate); however, we note that the fluid velocity near the vortex center is very weak, and hence the normal vorticity magnitude at the

vortex center is small. In all three cross-sectional planes, the normal vorticity component has a quadrapole structure, with four vorticity patches of alternating sign. From these cross-sectional plots, the velocity and vorticity fields associated with the rotating particle agglomerate appear to have the form of two tilted vortex rings with opposite circulation immersed in the shear flow.

To better illustrate this flow field, we compute the velocity fluid vorticity $\boldsymbol{\omega}_{rel} = \boldsymbol{\omega} + S\mathbf{e}_z$, where we recall that the vorticity of the ambient shear flow is $-S\mathbf{e}_z$. The iso-surface $\omega_{rel} = 0.46$ of the magnitude of $\boldsymbol{\omega}_{rel}$ is plotted in Figure 6.8 in both the *x*-*y* plane (looking from the side) and the *x*-*z* plane (looking from the top). The same two views of this iso-surface are also shown in Figure 6.8 showing contours of ω_{rel} on a slice of the flow field in the normal plane. The ω_{rel} iso-surfaces clearly show that the particle-induced flow field for a single rotating agglomerate in a shear flow has the form of a pair of tilted vortex rings of opposite sign, with tilt angle of approximately $45°$ relative to the ambient shear flow (*x*-direction). As seen in the slices of the flow field in Figures 6.8c and 6.8d, each vortex ring is surrounded by stretched and reoriented vorticity from the ambient shear flow which trails behind the vortex rings in each direction. The dynamics of a single vortex ring in a linear shear flow was studied by Cheng et al. (2009), who found that the vortex ring becomes tilted relative to the shear and maintains a ring-like form while it drifts upward in the shear field (in the *y*-direction). This upward drift is negated in the current situation by the mutually-induced flow field when two rings of opposite sign exist, leading to a quasi-stationary flow with a quadrapole far-field structure (as is evident in the streamlines in Figure 6.7c). For computations where the

shear flow does not trigger breakup of the agglomerate, such as for Case A.4, this flow structure is observed to remain nearly constant with time as the agglomerate rotates in the shear flow.

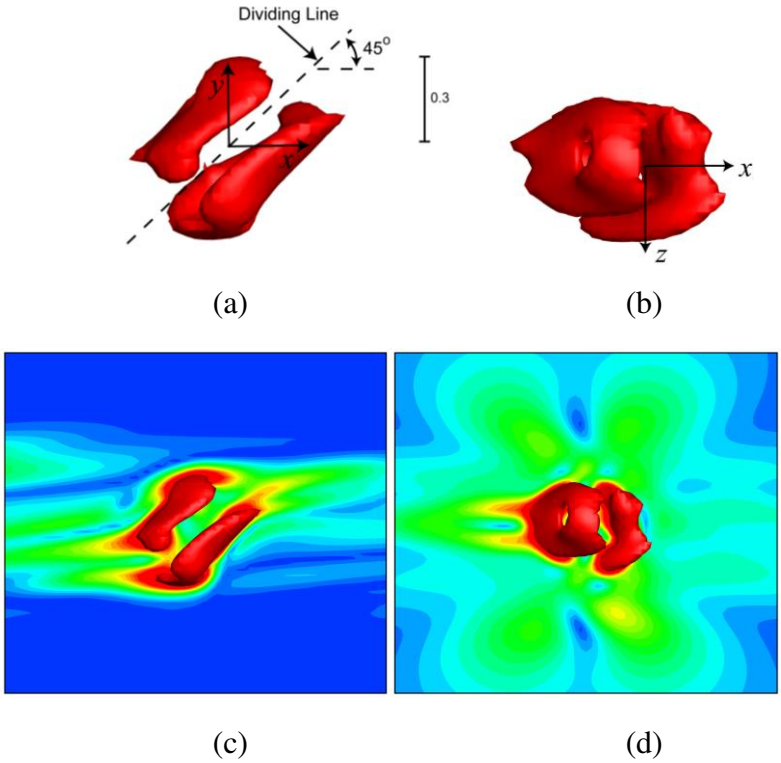

Figure 6.8. Iso-surface of the relative vorticity magnitude $\omega_{rel} = 0.46$ obtained from the velocity field for Case A.4 at $t = 26$, showing two tilted vortex rings generated by the particle-induced velocity field near the rotating agglomerate. The top two plots show iso-surfaces in the (a) x-y plane and (b) x-z plane. The bottom two plots, (c) and (d), show the same iso-surface views together with a slice showing ω_{rel} contours in the normal plane.

As the adhesion parameter is varied in different computations, different behavior of the particle agglomerates in the shear flow is observed. For sufficiently low adhesion parameter values, some agglomerates are observed to break up into multiple fragments in the presence of the shear flow. A time series illustrating agglomerate breakup in the shear flow is shown in Figure 6.9 for Case A.1. We note from this example that while the

fragments that shed from the agglomerate are limited by the maximum size that the agglomerate can attain without breakup in the shear flow, there are also many agglomerates that are formed of a much smaller size. The set of fragments this has a wide size distribution.

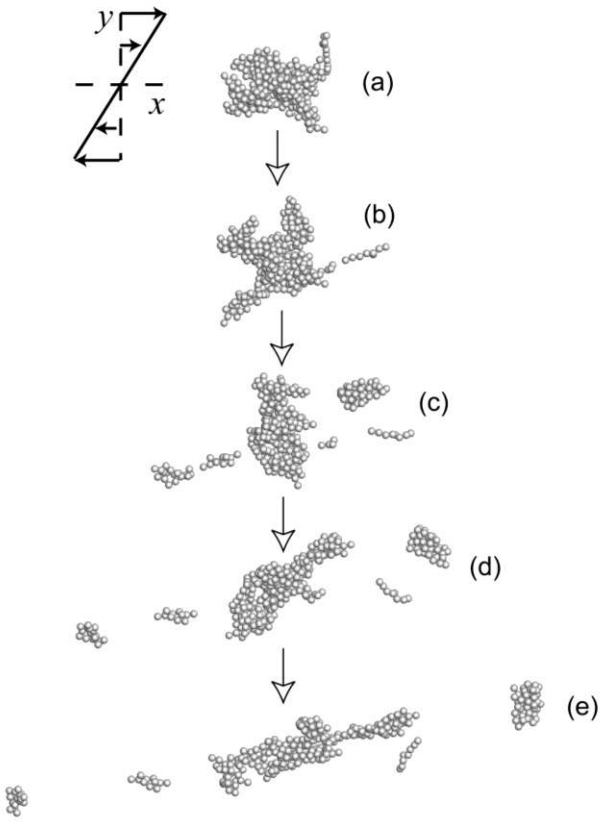

Figure 6.9. Time series showing breakup of single agglomerate in a shear flow, for Case A.1 at times (a) $t = 0$, (b) 5, (c) 10, (d) 15 and (e) 20.

A set of plots summarizing the computed agglomerate evolution for all of the single-agglomerate computations (Cases A.1 - A.12) is given in Figure 6.10. In Figure 6.10a, we plot the number of fragments N_{frag} into which the agglomerate breaks up as a function of the adhesion parameter Ad, defined in (6-22). The data are from three agglomerates extracted from the turbulent agglomeration computation, and different

symbols are used in Figure 6.10 to denote the data from each agglomerate. For sufficiently high values of adhesion parameter, the agglomerate doesn't break up and the value of $N_{frag} = 1$ in Figure 6.10a. The number of particles N in each fragment at the end of the computation ($t = 30$) is plotted versus adhesion parameter in Figure 6.10b on a log-log plot. The power law expression $N \propto S^{-0.878}$ of Sonntag and Russel (1986) can be written in terms of the adhesion parameter as $N \propto \mathrm{Ad}^{0.878}$. This expression is plotted as a dashed line in Figure 6.10b, where the coefficient of proportionality is fit to the data. The expression is found to be a reasonable fit for the maximum values of N, thus setting the largest size agglomerates that can survive without breakup in the shear flow.

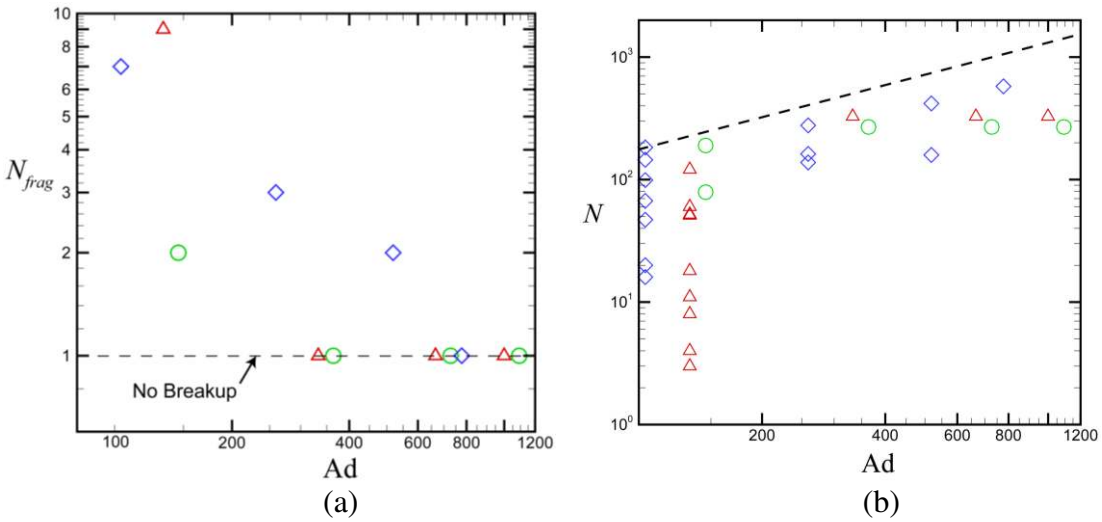

Figure 6.10. Plots showing measures characterizing breakup of a single agglomerate in a shear flow. (a) Number of fragments that an agglomerate breaks up into versus adhesion parameter. When the agglomerate does not break up, $N_{frag} = 1$. (b) Number of particles N in agglomerates following breakup versus adhesion parameter. The dashed line is the experimental power-law fit $N \propto \mathrm{Ad}^{0.879}$ from Sonntag and Russel (1986) for maximum number of particles, where the proportionality coefficient is fit to the data. The data is plotted for Cases A.1-A.4 (red deltas), A.5-A.8 (green circles), and A.9-A.12 (blue diamonds) from Table 6.1.

6.4. Agglomerate Pair Collision in Shear Flow

In this section, we examine the collision of two agglomerates in a shear flow. Three different agglomerates were extracted from the turbulent agglomeration computation described in Section 6.2.2, which were used to conduct 30 computations of agglomerate collision, the parameters for which are listed in Table 6.2. For each computation, the agglomerates are initialized as shown in Figure 6.2b, with orientations of $\pm 45°$ and displacement of the agglomerate centroid by an amount $\pm D_a$ in the *y*-direction. Each computation examines collision of an agglomerate with an exact copy, and we did not consider collisions of different size agglomerates.

Table 6.2. Listing of parameter values for cases examined for collision of two agglomerates, including adhesion parameter, initial numbers of particles in each agglomerate (N), ratio of initial gyration radius (R_{g0}) of each agglomerate to particle diameter *d*, and ratio of initial offset distance to R_{g0}. For each case examined St = 1.4 and $\rho_p / \rho_f = 10$. Also listed was the observed type of collision - merger (M), bouncing (B) or fragmentation (F) – and the number of particles in each remaining agglomerate (Aggl 1-5) after the collision.

Case Number	Ad	N_0	R_{g0}/d	D_a/R_{g0}	Collision Type	Aggl 1	Aggl 2	Aggl 3	Aggl 4	Aggl 5
B.1	333	328	4.81	0.52	F	213	392	51	-	-
B.2	666	328	4.81	0.52	M	656	-	-	-	-
B.3	999	328	4.81	0.52	M	656	-	-	-	-
B.4	1998	328	4.81	0.52	M	656	-	-	-	-
B.5	333	328	4.81	0.78	F	338	168	8	5	3
B.6	666	328	4.81	0.78	F	331	317	8	-	-
B.7	999	328	4.81	0.78	F	276	380	-	-	-
B.8	1998	328	4.81	0.78	M	656	-	-	-	-
B.9	333	328	4.81	1.04	F	262	315	69	8	-
B.10	666	328	4.81	1.04	B	350	305	-	-	-
B.11	999	328	4.81	1.04	B	358	298	-	-	-
B.12	1998	328	4.81	1.04	B	326	330	-	-	-
B.13	364	269	4.40	0.57	F	326	161	51	-	-
B.14	728	269	4.40	0.57	M	538	-	-	-	-
B.15	1092	269	4.40	0.57	M	538	-	-	-	-
B.16	2184	269	4.40	0.57	M	538	-	-	-	-
B.17	364	269	4.40	0.85	B	291	247	-	-	-
B.18	728	269	4.40	0.85	B	286	252	-	-	-

B.19	1092	269	4.40	0.85	B	296	242	-	-	-
B.20	2184	269	4.40	0.85	M	538	-	-	-	-
B.21	364	269	4.40	1.14	B	268	270	-	-	-
B.22	728	269	4.40	1.14	B	268	270	-	-	-
B.23	1092	269	4.40	1.14	B	268	270	-	-	-
B.24	2184	269	4.40	1.14	B	268	270	-	-	-
B.25	778	577	6.17	0.41	B	749	405	-	-	-
B.26	1556	577	6.17	0.41	M	1154	-	-	-	-
B.27	778	577	6.17	0.61	F	171	619	364	-	-
B.28	1556	577	6.17	0.61	M	1154	-	-	-	-
B.29	778	577	6.17	0.81	B	579	575	-	-	-
B.30	1556	577	6.17	0.81	B	607	547	-	-	-

Consideration of the computational results indicates three different types of behaviors, which are illustrated in scatter plots in Figure 6.11. In these plots, each particle is colored either red or blue to indicate the agglomerate from which the particle originated. The first type of collision outcome is *merger* of the agglomerates into a single agglomerate, which then rotates in the shear flow. The second type of behavior, referred to as a *bouncing* collision, results in two separate agglomerates following the collision. As seen in Figure 6.11, it is common for some particles to be exchanged between the two colliding agglomerates during bouncing collisions. The third type of behavior is referred to as fragmentation, which describes collisions that result in three or more agglomerates. In the case shown in Figure 6.11, the collision results in three agglomerates - one composed entirely of red particles, one composed entirely of blue particles, and one composed of a combination of red and blue particles. In other cases, more than three agglomerates will form in a fragmentation collision, often yielding a wide variation in agglomerate sizes. Sometimes it is not clear whether a collision should be classified as a bouncing case or a fragmentation case; for instance, cases where two colliding agglomerates break away from each other but leave behind a very small third 'satellite' agglomerate composed of just a few particles can be regarded as somewhat in-between

these two classifications. For purposes of this paper, collisions are classified as bouncing cases if only a single 'satellite' particle is separated from the two main agglomerates, and they are classified as fragmentation cases if the satellite agglomerate consists of two or more particles. More typical fragmentation cases are similar to that shown in Figure 6.11, however, producing at least three large agglomerates and sometimes also several smaller agglomerates.

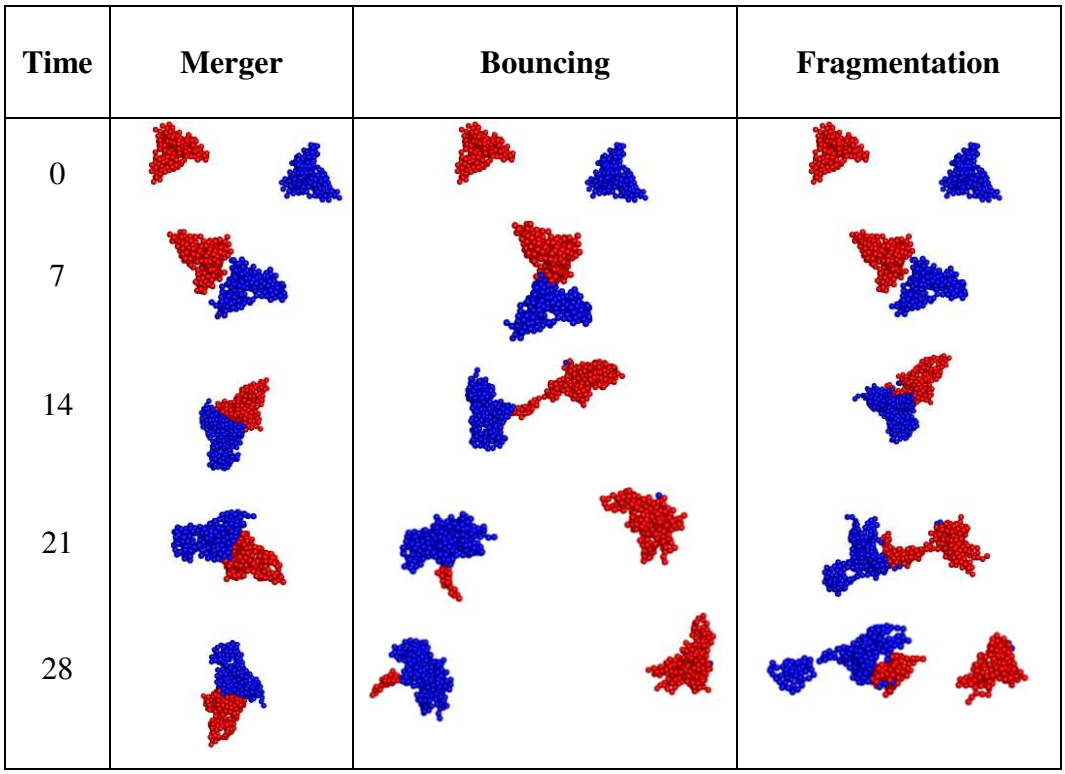

Figure 6.11. Scatter plots illustrating three types of agglomerate interactions: merger (Case B.15), bouncing (Case B.19) and fragmentation (Case B.13).

The question of whether a given collision will be of the merger, bouncing or fragmentation type depends primarily on the values of the adhesion parameter Ad and the ratio of the *y*-direction offset distance D_a to the initial radius of gyration R_{go} of the two

agglomerates. A plot identifying the type of collision for all computations conducted is shown in a mapping of Ad versus D_a / R_{g0} in Figure 6.12, and details of the number of particles in each agglomerate following collision are listed in Table 6.2. Regions of the map in Figure 6.12 are marked to provide a rough identification of values of Ad and D_a / R_{g0} for which the agglomerates individually break up in the shear flow (to the far left of the plot) and values resulting in merger, bouncing and fragmentation type collisions. The numbers indicate the number of agglomerates present at the conclusion of the computation, where an agglomerate is defined as a group of two or more touching particles. In general, collisions resulting in mergers occurred for smaller values of dimensionless offset distance D_a / R_{g0} and values of Ad well above the critical value for breakup of the individual agglomerate in shear flow. Bouncing collisions occur for larger values of D_a / R_{g0}, resulting in glancing collisions of the agglomerates. Fragmentation occurs for moderate values of D_a / R_{g0} with adhesion parameter values just slightly larger than the critical value for breakup of a single agglomerate in the shear flow. Two cases in Figure 6.12 requiring special discussion are indicated with asterisks. One of these cases, indicated by 2^*, was identified as a bouncing collision because it resulted in two agglomerates, but a much larger number of particles were exchanged between the two agglomerates compared to other bouncing cases. Indeed, 172 particles originating in the red agglomerate, out of an initial 577 particles, were torn off and captured by the blue agglomerate during the collision. The case indicated by 4^* in Figure 6.12 was, on the other hand, a fairly typical fragmentation case, resulting in three fairly large agglomerates with 263, 315 and 69 particles and one smaller 'satellite' agglomerate with 8 particles.

The presence of this fragmentation case in a region where we otherwise see a lot of bouncing cases is a reminder that each agglomerate has its own unique structure and each collision involves different parts of these unique agglomerates, so one must expect substantial variation from case to case. The plot in Figure 6.12 should therefore be regarded as providing only a rough indication of the conditions under which different types of collisions occur and not as a strict regime map.

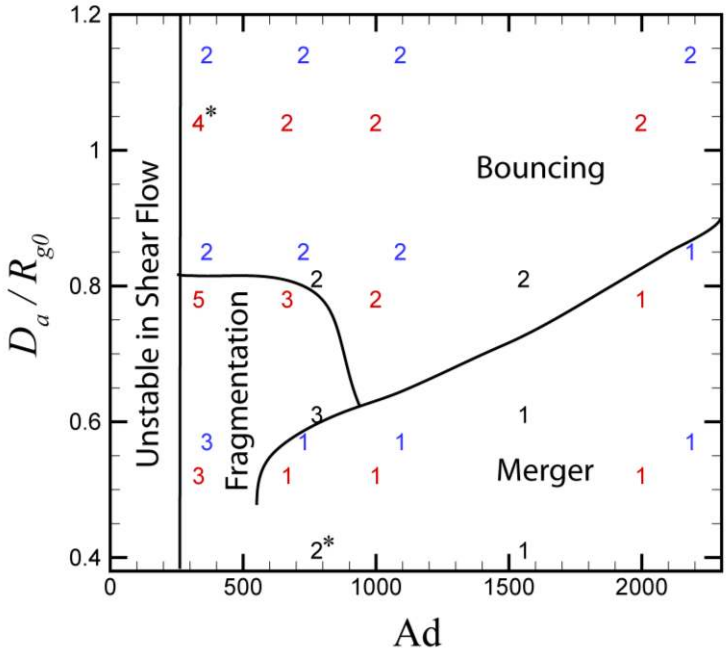

Figure 6.12. Summary of results for all agglomerate collision runs, showing the number of agglomerates (N_{agg}) remaining after collision as a function of adhesion parameter and the ratio D_a / R_{go} of offset distance to initial radius of gyration. Colors indicate results from different agglomerates. Numbers indicate cases with agglomerate merger ($N_{agg} = 1$), bounce ($N_{agg} = 2$), and fragmentation ($N_{agg} > 2$).

While we have used the term *bouncing collision* to be in conformity with terminology used in previous literature (e.g., Brisset et al., 2016), it is clear that the bouncing agglomerate collisions for the loosely-packed agglomerates described here differ substantially from the tradition bouncing collision of two elastic particles. In a

traditional bouncing process, two colliding elastic bodies deform locally near the collision point, resulting in an elastic (or sometimes plastic) repulsion force pushing the two bodies away from each other. In a bouncing case, this repulsion force is sufficiently strong to overcome the adhesive force between the bodies, so that the two bodies will detach and continue to move away from each other. The bouncing collisions of two loosely-packed agglomerates observed in the current paper are characterized more by tearing away and eventual capture of particles from the opposing agglomerate by the particle adhesion force. It is not that the elastic force between the agglomerates overcomes the adhesive force between the bodies, but rather that the adhesion force imposed on the captured particles by one agglomerate overcomes the adhesion force from the agglomerate to which the captured particles were originally attached. A plot showing number of captured particles from both agglomerates during the different bouncing collisions computed is given in Figure 6.13. As we see from this plot, all bouncing collisions included captured particles. In some cases only one agglomerate captures particles, and in other cases both colliding agglomerates capture particles from the other agglomerate.

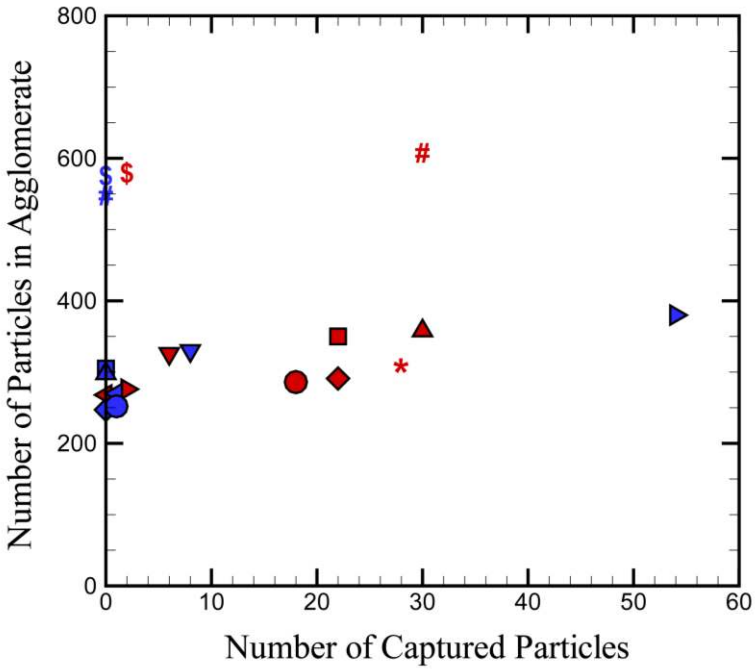

Figure 6.13. Plot indicating the number of captured particles in bouncing collisions versus the total number of particles in an agglomerate. The number of red particles captured by blue agglomerates is plotted in red, and the number of blue particles captured by red agglomerates is plotted in blue. Different symbols are used to indicate different computations, with one red and one blue symbol for each computation.

While exchange of particles was a characteristic feature of all bouncing collisions, this is not to say that there was no rebound force between the agglomerates. An examination of the rebound force is reported below for the bouncing collision in Case B.19, in which 28 particles originating in the red agglomerate are captured by the blue agglomerate and one blue particle is captured by the red agglomerate. The number of touching red-blue particles (i.e., touching particles originating from opposite agglomerates) is plotted as a function of time in Figure 6.14a. This number is zero until t = 5, at which time the collision occurs, and then suddenly spikes up to a peak value of 18 at a time of about t = 6.5. After this point the number of touching red-blue particles decreases to 14 and remains there, with the exception of a small blip at t = 10 due to

restructuring. The fact that the number of red-blue touching particles does not reduce to zero following the collision is due to the presence of captured particles. The total compressive force between the two agglomerates (which is characteristic of the elastic rebound force) is plotted as a function of time in Figure 6.14b. We again observe a sudden increase at collision onset at t = 5 and a peak value at t = 6.5, followed by a gradual decrease of the compression force as the two agglomerates tear away from each other.

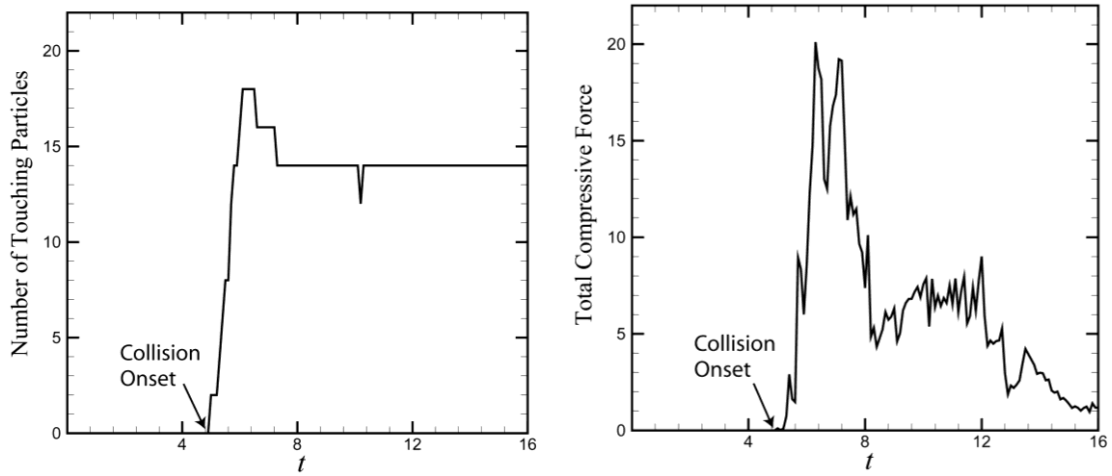

Figure 6.14. Time variation of (a) number of touching particles originating in different agglomerates and (b) total dimensionless compressive force between the agglomerates for a typical bouncing case (Case B.19). Collision occurs at approximately t = 5.

The position of particles carrying the compressive load between the two colliding agglomerates is illustrated in Figure 6.15 at a time of t = 7, close to the peak time of the collision. In Figure 6.15a, we color the particle scatter plot with red or blue to identify the originating agglomerate for each particle. In Figure 6.15b, each particle is colored by the magnitude of the total compressive force acting on the particle. The highest compressive loads are borne by a core of particles on the inside of the agglomerate, shown in Figure

6.15c with the lower-compression particles removed, within a tube of force chains radiating outward from the collision point. The highest compressive load occurs on the particles just at the collision point, indicated by red or orange in Figure 6.15c. We have thus confirmed that a rebound force does occur in bouncing collisions, and it may be reasonable to characterize this aspect of the collision phenomenon by some type of effective elastic modulus assigned to an effective spherical body representing the agglomerate. However, this effective sphere representation does not include the important phenomenon of particle capture during bouncing collisions, which in most of the cases that we have examined is very important to the agglomerate behavior during collision.

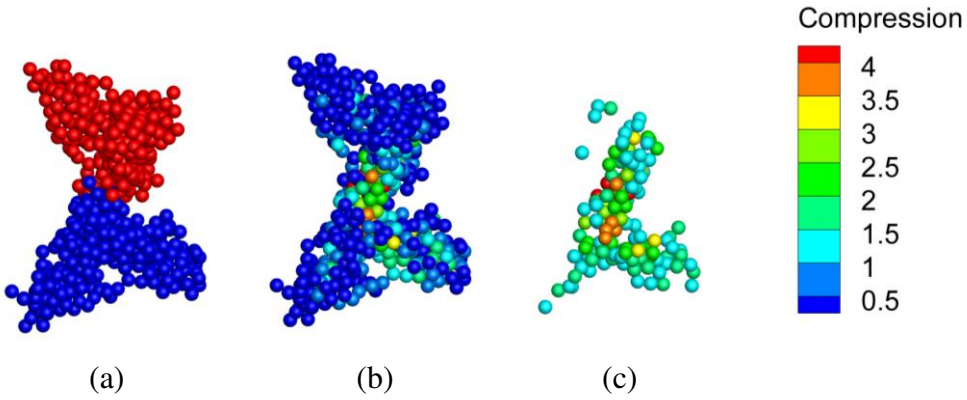

Figure 6.15. Scatter plots during a bouncing agglomerate collision (Case B.19) at $t = 7$, with colors indicating (a) agglomerate from which each particle originated, (b) total compressive force acting on each particle, and (c) same plot as in (b) with the low-compression particles (with compressive force < 1.5) blanked out. High compression force chains occur in a particle core region spreading outward from the collision point.

In Section 6.3, we discussed the observation that the particle-induced flow field from a single agglomerate in a shear flow has the form of two tilted vortex rings of opposite sign. In the event of a collision of two agglomerates, one naturally wonders what happens to the particle-induced flow during the collision. To examine this question, an iso-surface of the relative vorticity magnitude ω_{rel} is plotted at four different times

during a collision resulting in merger (Figure 6.16 for Case B.15) and during a collision resulting in bouncing (Figure 6.17 for Case B.19). The relative-vorticity iso-surface for fragmentation cases depends on the number of fragments produced, and so are highly variable.

In Figure 6.16, the particle-induced flow field at time t = 6 (just before the collision) has the form of two opposite-sign tilted vortex rings for each agglomerate, hence four tilted vortex rings in all. At time t = 8 the agglomerates are in the midst of colliding and the innermost vortex rings of each agglomerate collide with one another. At t = 10, the inner vortex rings have significantly decayed while the outer vortex rings have grown in strength. The inner rings continue to break up and be swept downstream by t = 12, leaving the two strong outer vortex rings, which have opposite sign from each other. With the exception of the small-scale remnants of the inner rings, the particle-induced flow for the merged agglomerates at t = 12 thus appears similar to that for a single agglomerate in a shear flow, as discussed in the previous section.

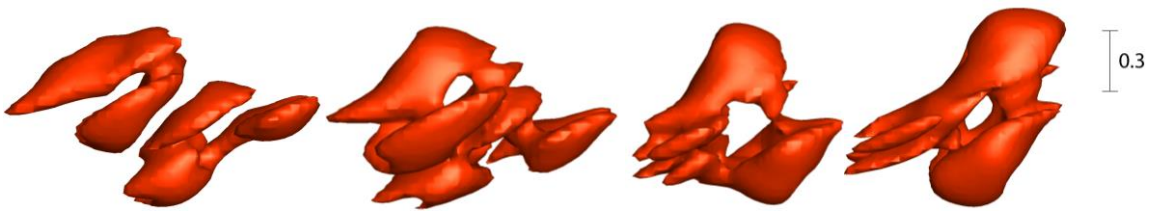

(a) (b) (c) (d)

Figure 6.16. Iso-surface of relative vorticity magnitude $\omega_{rel} = 0.3$ for a case where the particle agglomerates merge (Case B.15), at times (a) $t = 6$, (b) 8, (c) 10, and (d) 12 during which collision and merger of the agglomerates occurs.

In Figure 6.17, a time series of iso-relative vorticity magnitude surfaces are plotted for a case with bouncing agglomerate collision. The first two images in Figure

6.17 appear similar to those in Figure 6.16 for a merging collision. The two inner rings collide at time t = 6 and nearly extinguish each other by time t = 8 as the agglomerate collision occurs. However, as the agglomerates bounce and move away from each other, the inner rings reform, such that by t = 12 we see a pair of vortex rings for each agglomerate moving away from each other. A trail of vorticity connects these two vortex ring pairs, which is either left over from the collision or generated by stretching of the background shear vorticity.

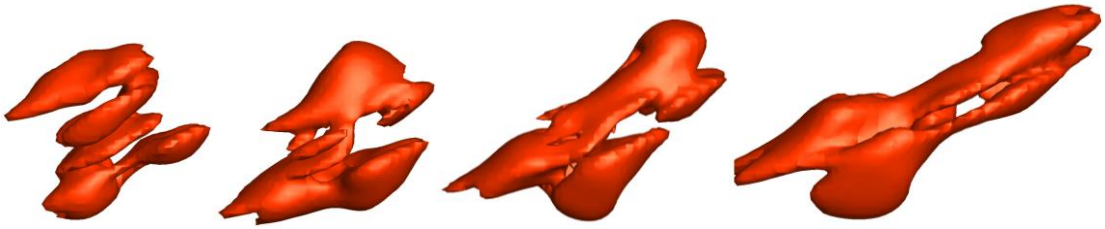

(a) (b) (c) (d)

Figure 6.17. Iso-surface of relative vorticity magnitude $\omega_{rel} = 0.3$ for a case where the particle agglomerates bounce (Case B.19), at times (a) $t = 6$, (b) 8, (c) 10, and (d) 12 during which collision of the agglomerates occurs.

6.5. Conclusions

A computational study was reported examining rotation and breakup of a single particle agglomerate and collision of two particle agglomerates in a shear flow. The agglomerates are extracted from a direct numerical simulation of turbulent agglomeration, and therefore have the characteristic loosely-packed fractal structure typical of turbulent agglomeration processes. Computations are performed with two-way coupling between the particles and the fluid and with sufficient resolution of the agglomerates to capture the details of the particle-induced flow field. Simulations of a

single agglomerate rotating in the shear flow with high values of the adhesion parameter indicate that the agglomerate rotates more slowly than would an ambient fluid element in the shear flow. The flow field induced by the particles of a rotating agglomerate in a shear flow are found to exhibit a very distinctive form, characterized by a pair of tilted vortex rings with opposite sign circulation, surrounded by a sea of stretched vorticity from the ambient shear flow. To our knowledge, this is the first time that the particle-induced flow of an agglomerate in shear flow has been examined in detail and the first time that the interesting vortex ring pair structure of this flow has been described. This vortex ring pair structure remains with constant orientation and strength as the particle agglomerate rotates. For sufficiently low values of the adhesion parameter, the agglomerate is observed to break up in the shear flow, where the exact value of adhesion parameter at breakup varies slightly with the specific choice of the agglomerate under examination.

The problem of collision of two agglomerates was found to result in either merger, bouncing or fragmentation, depending on the value of the adhesion parameter and the ratio of offset distance to agglomerate radius of gyration. In merger collisions, the inner vortex rings of the particle-induced flow from each agglomerate interact with each other and eventually break up into small scale structures, and the outer vortex rings grow stronger leading to development of the vortex ring pair structure typical of that observed for a single agglomerate. It was observed that bouncing collisions result both in repulsive force between the agglomerates due to elastic deformation as well as exchange of particles between agglomerates. The innermost vortex ring structures of the particle-induced flow for bouncing collisions similarly exhibit interaction of the two inner vortex

rings, but these inner rings are found to quickly reform as the agglomerates bounce and move away from each other. Fragmentation collisions may result in three or more agglomerates with widely different sizes, many of which are formed of a combination of particles originating in different agglomerate structures.

Many theoretical and computation models of turbulent agglomeration processes make use of the common approximation that an agglomerate can be replaced by an 'effective particle', in which some effective elastic modulus of the agglomerate is assigned. The current study clearly demonstrates that this effective particle approximation omits many of the important physical phenomena associated with agglomerate collision, including fragmentation collisions and exchange of particles between agglomerates in bouncing collisions. These physical omissions must also raise doubt regarding the predictions of bouncing versus merger behavior from the equivalent sphere model, particularly since this model does not include the critical processes of agglomerate restructuring during collision and capture of particles by the colliding agglomerates. The particle-induced flow field is also quite different for a loosely-packed agglomerate than it is for an equivalent sphere due to the fact that the fluid flow can penetrate into the outer parts of the agglomerate. This penetration affects the rotation rate of an agglomerate in a shear flow and gives rise to the tilted vortex ring structure of the particle-induced flow.

Acknowledgements

This research was supported by the U.S. National Science Foundation under grant CBET-1332472.

References

Adachi, Y. & Ooi, S. 1990 Geometrical structure of a floc. *Journal of Colloid and Interface Science* **135** (2), 374-384.

Bagi, K. & Kuhn, M.R. 2004 A definition of particle rolling in a granular assembly in terms of particle translations and rotations. *Journal of Applied Mechanics* **71**, 493-501.

Balakin, B., Hoffmann, A. C. & Kosinski, P. 2011 The collision efficiency in a shear flow. *Chemical Engineering Science* **68**, 305-312.

Becker, V., Schlauch, E., Behr, M. & Briesen, H. 2009 Restructuring of colloidal aggregates in shear flows and limitations of the free-draining approximation. *Journal of Colloid and Interface Science* **339**, 362-372.

Beitz, E., Güttler, C., Blum, J., Meisner, T., Teiser, J. & Wurm, G. 2011 Low-velocity collisions of centimeter-sized dust aggregates. *The Astrophysical Journal* **736** (1), 34.

Brasil, A. M., Farias, T. L., Carvalho, M. G. & Koylu, U. O. 2001 Numerical characterization of the morphology of aggregated particles. *Journal of Aerosol Science* **32**, 489-508.

Brisset, J., Heißelmann, D., Kothe, S., Weidling, R. & Blum, J. 2016 Submillimetre-sized dust aggregate collision and growth properties: Experimental study of a multi-particle system on a suborbital rocket. *Astronomy & Astrophysics* **593**, A3.

Brunk, B. K., Koch, D. L. & Lion, L. W. 1998 Turbulent coagulation of colloidal particles. *Journal of Fluid Mechanics* **364**, 81-113.

Chokshi, A., Tielens, A. G. G. M. & Hollenbach, D. 1993 Dust coagulation. *The Astrophysical Journal* **407**, 806-819.

Chun, J. & Koch, D. L. 2005 Coagulation of monodisperse aerosol particles by isotropic turbulence. *Physics of Fluids* **17**, 027102.

Cleary, P. W., Metcalfe, G. & Liffman, K. 1998 How well do discrete element granular flow models capture the essentials of mixing processes? *Applied Mathematical Modeling* **22**, 995-1008.

Crowe, C. T., Schwarzkopf, J. D., Sommerfeld, M. & Tsuji, Y. 2012 *Multiphase Flows with Droplets and Particles*, 2nd ed., CRC Press, Boca Raton, Florida.

Di Felice, R. 1994 The voidage function for fluid-particle interaction systems. *International Journal of Multiphase Flow* **20**, 153-159.

Ding, W., Zhang, H. & Cetinkaya, C. 2008 Rolling resistance moment-based adhesion characterization of microspheres. *Journal of Adhesion* **84**, 996-1006.

Dizaji, F. F. & Marshall, J. S. 2017 On the significance of two-way coupling in simulation of turbulent particle agglomeration. *Powder Technology* **318**, 83-94.

Dizaji. F. F. & Marshall, J. S. 2016 An accelerated stochastic vortex structure method for particle collision and agglomeration in homogeneous turbulence. *Physics of Fluids* **28**, 113301.

Dominik, C. & Tielens, A. G. G. M. 1995 Resistance to rolling in the adhesive contact of two elastic spheres. *Philosophical Magazine A* **92** (3), 783-803.

Eggersdorfer, M. L., Kadau, D., Hermann, H. J. & Pratsinis, S. E. 2011 Multiparticle sintering dynamics: From fractal-like aggregates to compact structures. *Langmuir* **27**, 6358-6367.

Fanelli, M., Feke, D. L. & Manas-Zloczower, I. 2006 Prediction of the dispersion of particle clusters in the nano-scale – Part I: Steady shearing responses. *Chemical Engineering Science* **61**, 473-488.

Gunkelmann, N., Ringl, C. & Urbassek, H. M. 2016 Influence of porosity on collisions between dust aggregates. *Astronomy & Astrophysics* **589**, A30.

Hansen, S., Khakhars, D. V. & Ottino, J.M. 1998 Dispersion of solids in nonhomogeneous viscous flows. *Chemical Engineering Science* **53**(10), 1803-1817.

Hatakeyama, N. & Kambe, T. 1997 Statistical laws of random strained vortices in turbulence. *Physical Review Letters* **79** (7), 1257-1260.

Higashitani, K., Iimura, K. & Sanda, H. 2001 Simulation of deformation and breakup of large aggregates in flows of viscous fluids. *Chemical Engineering Science* **56**, 2927-2938.

Ihalainen, M., Lind, T., Torvela, T., Lehtinen, K. E. J. & Jokiniemi, J. 2012 A method to study agglomerate breakup and bounce during impaction, *Aerosol Science and Technology* **46** (9), 990-1001.

Iimura, K., Suzuki, M., Hirota, M. & Higashitani, K. 2009a Simulation of dispersion of agglomerates in gas phase - acceleration field and impact on cylindrical obstacle. *Advanced Powder Technology* **20**, 210-215.

Iimura, K., Yanagiuchi, M., Suzuki, M., Hirota, M. & Higashitani, K. 2009b Simulation of dispersion and collection process of agglomerated particles in collision with fibers using discrete element method. *Advanced Powder Technology* **20**, 582-587.

Jiang, Q. & Logan, B. E. 1991 Fractal dimensions of aggregates determined from steady-state size distributions. *Environmental Science and Technology* **25**, 2031-2038.

Johnson, K. L., Kendall, K. & Roberts, A. D. 1971 Surface energy and the contact of elastic solids. *Proceedings of the Royal Society of London A* **324**, 301-313.

Joseph, G. G., Zenit, R., Hunt, M. L. & Rosenwinkel, A. M. 2001 Particle-wall collisions in a viscous fluid. *Journal of Fluid Mechanics* **433**, 329-346.

Kafui, K. D. & Thornton, C. 2000 Numerical simulations of impact breakage of a spherical crystalline agglomerate. *Powder Technology* **109**, 113-132.

Koch, D. L. & Pope, S. B. 2002 Coagulation-induced particle-concentration fluctuations in homogeneous, isotropic turbulence. *Physics of Fluids* **14**, 2447-2455.

Kosinski, P. & Hoffmann, A. C. 2010 An extension of the hard-sphere particle–particle collision model to study agglomeration. *Chemical Engineering Science* **65** (10), 3231-3239.

Kun, F. & Herrmann, H. J. 1999 Transition from damage to fragmentation in collision of solids. *Physical Review E* **59** (3), 2623-2632.

Kusters, K. A., Wijers, J. G. & Thoenes, D. 1997 Aggregated kinetics of small particles in agitates vessels. *Chemical Engineering Science* **52** (1), 107-121.

Lele, S. K. 1992 Compact finite difference schemes with spectral-like resolution. *Journal of Computational Physics* **103** (1), 16-42.

Li, C., Ye, M. & Liu, Z. 2016 On the rotation of a circular porous particle in 2D simple shear flow with fluid inertia. *Journal of Fluid Mechanics* **808**, R3.

Lian, G., Thornton, C. & Adams, M. J. 1998 Discrete particle simulation of agglomerate impact coalescence. *Chemical Engineering Science* **53** (19), 3381-3391.

Lu, J. & Wang, J. K. 2006 Agglomeration, breakage, population balance, and crystallization kinetics of reactive precipitation process. *Chemical Engineering Communications* **193**, 891-902.

Marangoni, A. G. & Narine, S. S. 2001 Elasticity of fractal aggregate networks: Mechanical arguments. In *Crystallization and Solidification Properties of Lipids*, Widlak,

N., Hartel, R.W., and Narine, S., eds., The American Oil Chemists Society, Champaign, IL.

Marshall, J. S. 2009 Discrete-element modeling of particulate aerosol flows. *Journal of Computational Physics* **228**, 1541-1561.

Marshall, J. S. & Li, S. 2014 *Adhesive Particle Flow: A Discrete Element Approach*, Cambridge University Press, New York.

Marshall, J. S. & Sala, K. 2013 Comparison of methods for computing the concentration field of a particulate flow. *International Journal of Multiphase Flow* **56**, 4-14.

Mindlin, R. D. 1949 Compliance of elastic bodies in contact. *Journal of Applied Mechanics* **16**, 259-268.

Moreno, R., Ghadiri, M. & Antony, S. J. 2003 Effect of the impact angle on the breakage of agglomerates: a numerical study using DEM. *Powder Technology* **130**, 132-137.

Moreno-Atanasio, R. & Ghadiri, M. 2006 Mechanistic analysis and computer simulation of impact breakage of agglomerates: Effect of surface energy. *Chemical Engineering Science* **61**, 2476-2481.

Nguyen, D., Rasmuson, A., Thalberg, K. & Björn, I. N. 2014 Numerical modelling of breakage and adhesion of loose fine-particle agglomerates. *Chemical Engineering Science* **116**, 91-98.

Ning, Z., Boerefijn, R., Ghadiri, M. & Thornton, C. 1997 Distinct element simulation of impact breakage of lactose agglomerates. *Advanced Powder Technology* **8** (1), 15-37.

Olfert, J. S., Symonds, J. P. R. & Collings, N. 2007 The effective density and fractal dimension of particles emitted from a light-duty vehicle with a diesel oxidation catalyst. *Journal of Aerosol Science* **38**, 69-82.

Ormel, C. W., Paszun, D., Dominik, C. & Tielens, A. G. G. M. 2009 Dust coagulation and fragmentation in molecular clouds: I. How collisions between dust aggregates alter the dust size distribution. *Astronomy & Astrophysics* **502**, 845–869.

Ormel, C. W., Spaans, M. & Tielens, A. G. G. M. 2007 Dust coagulation in protoplanetary disks: porosity matters. *Astronomy & Astrophysics* **461**, 215-232.

Potanin, A. A. 1993 On the computer simulation of the deformation and breakup of colloidal aggregates in shear flow. *Journal of Colloid and Interface Science* **157**, 399-410.

Rai, M. & Moin, P. 1991 Direct simulation of turbulent flow using finite-difference schemes. *Journal of Computational Physics* **96**, 15–53.

Reinhold, A. & Briesen, H. 2012 Numerical behavior of a multiscale aggregation model - coupling population balances and discrete element models. *Chemical Engineering Science* **70**, 165-175.

Rubinow, S. I. & Keller, J. B. 1961 The transverse force on a spinning sphere moving in a viscous fluid. *Journal of Fluid Mechanics* **11**, 447-459.

Rumpf, H. 1962 The strength of granules and agglomerates. In: W.A. Knepper (Ed.) *Agglomeration*, John Wiley, New York, pp. 379-418.

Saffman, P. G. 1965 The lift on a small sphere in a slow shear flow. *Journal of Fluid Mechanics* **22**, 385-400.

Saffman, P. G. & Turner, J. S. 1956 On the collision of drops in turbulent clouds. *Journal of Fluid Mechanics* **1** (1), 16-30.

Samimi, A., Moreno, R. & Ghadiri, M. 2004 Analysis of impact damage of agglomerates: effect of impact angle. *Powder Technology* **143-144**, 97-109.

Sayvet, O. & Navard, P. 2000 Collision-induced dispersion of agglomerate suspensions in a shear flow. *Journal of Applied Polymer Science* **78**, 1130–1133.

Schäfer, C., Speith, R. & Kley, W. 2007 Collisions between equal-sized ice grain agglomerates. *Astronomy and Astrophysics* **470**, 733-739.

Schiller, L. & Naumann, A. 1933 Über die gundlegenden Berechungen bei der Schwerkraftaufbereitung. *Zeitschrift des Vereines Deutscher Ingenieure* **77**, 318-320.

Selomulya, C., Amal, R., Bushell, G. & Waite, T. D. 2001 Evidence of shear rate dependence on restructuring and breakup of latex aggregates. *Journal of Colloid and Interface Science* **236**, 67-77.

Seizinger, A. & Kley, W. 2013 Bouncing behavior of microscopic dust aggregates. *Astronomy and Astrophysics* **551**, A65.

Serra, T., Colomer, J. & Casamitjana, X. 1997 Aggregation and breakup of particles in a shear flow. *Journal of Colloid and Interface Science* **187**, 466-473.

Smoluchowski, M. 1917 Versuch einer mathematischen Theorie der Koagulationskinetik kolloider Lösungen. *Zeitschrift für Physikalische Chemie* **92**, 129–168.

Sonntag, R. C. & Russel, W. B. 1986 Structure and breakup of flocs subjected to fluid stresses. I. Shear experiments. *Journal of Colloid and Interface Science* **113**(2), 399-413.

Steijl, R. 2001 Computational study of vortex pair dynamics. Ph.D. dissertation, University of Twente, Enschede, The Netherlands, p. 64.

Thornton, C. 1991 Interparticle sliding in the presence of adhesion. *Journal Physics D: Applied Physics* **24**, 1942-1946.

Thornton, C., Ciomocos, M. T. & Adams, M. J. 1999 Numerical simulations of agglomerate impact breakage. *Powder Technology* **105**, 74–82.

Thornton, C. & Liu, L. 2004 How do agglomerates break? *Powder Technology* **143–144**, 110–116.

Tong, Z. B., Yang, R. Y., Chu, K. W., Yu, A. B., Adi, S. & Chan, H. K. 2010 Numerical study of the effects of particle size and polydispersity on the agglomerate dispersion in a cyclonic flow. *Chemical Engineering Journal* **164**, 432–441.

Tong, Z. B., Yang, R. Y., Yu, A. B., Adi, S. & Chan, H. K. 2009 Numerical modelling of the breakage of loose agglomerates of fine particles. *Powder Technology* **196**, 213–221.

Tong, Z. B., Zheng, B., Yang, R. Y., Yu, A. B. & Chan, H. K. 2013 CFD-DEM investigation of the dispersion mechanisms in commercial dry powder inhalers. *Powder Technology* **240**, 19–24.

Tong, Z. B., Zhong, W., Yu, A. B., Chan, H. K. & Yang, R. Y. 2016 CFD–DEM investigation of the effect of agglomerate–agglomerate collision on dry powder aerosolisation. *Journal of Aerosol Science* **92**, 109–121.

Tsuji, Y., Tanaka, T. & Ishida, T. 1992 Lagrangian numerical simulation of plug flow of cohesionless particles in a horizontal pipe. *Powder Technology* **71**, 239-250.

Uhlmann, M. 2005 An immersed boundary method with direct forcing for the simulation of particulate flows. *Journal of Computational Physics* **209**, 448-476.

Verzicco, R. & Orlandi, P. 1996 A finite-difference scheme for three-dimensional incompressible flows in cylindrical coordinates. *Journal of Computational Physics* **123**, 402-414.

Waldner, M. H., Sefcik, J., Soos, M. & Morbidelli, M. 2005 Initial growth kinetics of aggregates in turbulent coagulator. *Powder Technology* **156**, 226-234.

Wang, L. P., Wexler, A. S. & Zhou, Y. 1998 Statistical mechanical descriptions of turbulent coagulation. *Physics of Fluids* **10**, 2647-2651.

Wen, C. Y. & Yu, Y. H. 1966 Mechanics of fluidization. *Chemical Engineering Progress Symposium Series* **62** (62), 100-111.

Yang, J., Wu, C. Y. & Adams, M. 2014 Three-dimensional DEM–CFD analysis of air-flow-induced detachment of API particles from carrier particles in dry powder inhalers. *Acta Pharmaceutica Sinica B* **4** (1), 52-59.

Zeidan, M., Xu, B. H., Jia, X. & Williams, R. A. 2007 Simulation of aggregate deformation and breakup in simple shear flows using a combined continuum and discrete model. *Chemical Engineering Research and Design* **85** (A12), 1645–1654.

COMPREHENSIVE BIBLIOGRAPHY

Abrahamson, J. (1975). Collision rates of small particles in a vigorously turbulent fluid. *Chemical Engineering Science*, *30*(11), 1371-1379.

Adachi, Y., & Ooi, S. (1990). Geometrical structure of a floc. *Journal of colloid and interface science*, *135*(2), 374-384.

Ayyalasomayajula, S., Warhaft, Z., & Collins, L. R. (2008). Modeling inertial particle acceleration statistics in isotropic turbulence. *Physics of Fluids*, *20*(9), 095104.

Babick, F. (2016). *Suspensions of colloidal particles and aggregates* (Vol. 20). Heidelberg: Springer.

Bache, D. H. (2004). Floc rupture and turbulence: a framework for analysis. *Chemical Engineering Science*, *59*(12), 2521-2534.

Bagi, K., & Kuhn, M. R. (2004). A definition of particle rolling in a granular assembly in terms of particle translations and rotations. *Journal of applied mechanics*, *71*(4), 493-501.

Balachandar, S., & Eaton, J. K. (2010). Turbulent dispersed multiphase flow. *Annual Review of Fluid Mechanics*, *42*, 111-133.

Balakin, B., Hoffmann, A. C., & Kosinski, P. (2012). The collision efficiency in a shear flow. *Chemical engineering science*, *68*(1), 305-312.

Bałdyga, J., Makowski, Ł., Orciuch, W., Sauter, C., & Schuchmann, H. P. (2008). Deagglomeration processes in high-shear devices. *Chemical Engineering Research and Design*, *86*(12), 1369-1381.

Bałdyga, J., Makowski, Ł., Orciuch, W., Sauter, C., & Schuchmann, H. P. (2009). Agglomerate dispersion in cavitating flows. *Chemical engineering research and design*, *87*(4), 474-484.

Bec, J., Biferale, L., Cencini, M., Lanotte, A., Musacchio, S., & Toschi, F. (2007). Heavy particle concentration in turbulence at dissipative and inertial scales. *Physical review letters*, *98*(8), 084502.

Beck, C. (2008). Superstatistics: Theoretical concepts and physical applications. *Anomalous Transport: Foundations and Applications*, 433-457.

Becker, V., Schlauch, E., Behr, M., & Briesen, H. (2009). Restructuring of colloidal aggregates in shear flows and limitations of the free-draining approximation. *Journal of colloid and interface science*, *339*(2), 362-372.

Beitz, E., Güttler, C., Blum, J., Meisner, T., Teiser, J., & Wurm, G. (2011). Low-velocity collisions of centimeter-sized dust aggregates. *The Astrophysical Journal*, *736*(1), 34.

Belin, F., Maurer, J., Tabeling, P., & Willaime, H. (1996). Observation of intense filaments in fully developed turbulence. *Journal de Physique II*, *6*(4), 573-583.

Bernard, P. S. (2008). Grid-free simulation of the spatially growing turbulent mixing layer. *AIAA journal*, *46*(7), 1725-1737.

Bernard, P. S. (2009). Vortex filament simulation of the turbulent coflowing jet. *Physics of Fluids*, *21*(2), 025107.

Bernard, P. S., Collins, P., & Potts, M. (2010). Vortex filament simulation of the turbulent boundary layer. *AIAA journal*, *48*(8), 1757-1771.

Binder, C., Feichtinger, C., Schmid, H. J., Thürey, N., Peukert, W., & Rüde, U. (2006). Simulation of the hydrodynamic drag of aggregated particles. *Journal of colloid and interface science*, *301*(1), 155-167.

Boivin, M., Simonin, O., & Squires, K. D. (1998). Direct numerical simulation of turbulence modulation by particles in isotropic turbulence. *Journal of Fluid Mechanics*, *375*, 235-263.

Bosse, T., Kleiser, L., Härtel, C., & Meiburg, E. (2005). Numerical simulation of finite Reynolds number suspension drops settling under gravity. *Physics of fluids*, *17*(3), 037101.

Brebbia, C. A., & Telles, J. C. F. Abramowitz, M. et Stegun, IA, Handbook of Mathematical Functions, Dover Publications, New York, 1965.

Brasil, A. M., Farias, T. L., & Carvalho, M. G. (1999). A recipe for image characterization of fractal-like aggregates. *Journal of Aerosol Science*, *30*(10), 1379-1389.

Brasil, A. M., Farias, T. L., Carvalho, M. D. G., & Koylu, U. O. (2001). Numerical characterization of the morphology of aggregated particles. *Journal of Aerosol Science*, *32*(4), 489-508.

Breuer, M., & Almohammed, N. (2015). Modeling and simulation of particle agglomeration in turbulent flows using a hard-sphere model with deterministic collision

detection and enhanced structure models. *International Journal of Multiphase Flow*, *73*, 171-206.

Brisset, J., Heißelmann, D., Kothe, S., Weidling, R., & Blum, J. (2016). Submillimetre-sized dust aggregate collision and growth properties-Experimental study of a multi-particle system on a suborbital rocket. *Astronomy & Astrophysics*, *593*, A3.

Brunk, B. K., Koch, D. L., & Lion, L. W. (1997). Hydrodynamic pair diffusion in isotropic random velocity fields with application to turbulent coagulation. *Physics of Fluids*, *9*(9), 2670-2691.

Brunk, B. K., Koch, D. L., & Lion, L. W. (1998). Turbulent coagulation of colloidal particles. *Journal of Fluid Mechanics*, *364*, 81-113.

Brunk, B. K., Koch, D. L., & Lion, L. W. (1998). Observations of coagulation in isotropic turbulence. *Journal of Fluid Mechanics*, *371*, 81-107.

Burgers, J. M. (1948). A mathematical model illustrating the theory of turbulence. In *Advances in applied mechanics* (Vol. 1, pp. 171-199). Elsevier.

Cates, M. E., Wittmer, J. P., Bouchaud, J. P., & Claudin, P. (1999). Jamming and static stress transmission in granular materials. *Chaos: An Interdisciplinary Journal of Nonlinear Science*, *9*(3), 511-522.

Choi, J. I., Kwon, O., & Lee, C. (2011). Inter-particle collision in particle-laden isotropic turbulence. In *Journal of Physics: Conference Series* (Vol. 318, No. 5, p. 052012). IOP Publishing.

Chokshi, A., Tielens, A. G. G. M., & Hollenbach, D. (1993). Dust coagulation. *The Astrophysical Journal*, *407*, 806-819.

Chun, J., & Koch, D. L. (2005). Coagulation of monodisperse aerosol particles by isotropic turbulence. *Physics of Fluids*, *17*(2), 027102.

Collins, L. R., & Keswani, A. (2004). Reynolds number scaling of particle clustering in turbulent aerosols. *New Journal of Physics*, *6*(1), 119.

Cottet, G. H., & Koumoutsakos, P. D. (2000). *Vortex methods: theory and practice*. Cambridge university press.

Cleary, P. W., Metcalfe, G., & Liffman, K. (1998). How well do discrete element granular flow models capture the essentials of mixing processes?. *Applied Mathematical Modelling*, *22*(12), 995-1008.

Crowe, C. T. (2000). On models for turbulence modulation in fluid–particle flows. *International Journal of Multiphase Flow*, *26*(5), 719-727.

Cundall, P. A., & Strack, O. D. (1979). A discrete numerical model for granular assemblies. *geotechnique*, *29*(1), 47-65.

Da Silva, C. B., & Pereira, J. C. (2008). Invariants of the velocity-gradient, rate-of-strain, and rate-of-rotation tensors across the turbulent/nonturbulent interface in jets. *Physics of fluids*, *20*(5), 055101.

Derksen, J. J. (2013). Direct simulations of aggregates in homogeneous isotropic turbulence. *Acta Mechanica*, *224*(10), 2415-2424.

Devenish, B. J., Bartello, P., Brenguier, J. L., Collins, L. R., Grabowski, W. W., IJzermans, R. H. A., ... & Warhaft, Z. (2012). Droplet growth in warm turbulent clouds. *Quarterly Journal of the Royal Meteorological Society*, *138*(667), 1401-1429.

Di Felice, R. (1994). The voidage function for fluid-particle interaction systems. *International Journal of Multiphase Flow*, *20*(1), 153-159.

Ding, W., Zhang, H., & Cetinkaya, C. (2008). Rolling resistance moment-based adhesion characterization of microspheres. *The Journal of Adhesion*, *84*(12), 996-1006.

Dizaji, F. F., & Marshall, J. S. (2016). An accelerated stochastic vortex structure method for particle collision and agglomeration in homogeneous turbulence. *Physics of Fluids*, *28*(11), 113301.

Dizaji, F. F., & Marshall, J. S. (2017). On the significance of two-way coupling in simulation of turbulent particle agglomeration. *Powder Technology*, *318*, 83-94.

Dominik, C., & Tielens, A. G. G. M. (1995). Resistance to rolling in the adhesive contact of two elastic spheres. *Philosophical Magazine A*, *72*(3), 783-803.

Dong, M., Zhou, F., Zhang, Y., Shang, Y., & Li, S. (2018). Numerical study on fine-particle charging and transport behaviour in electrostatic precipitators. *Powder Technology*, *330*, 210-218.

Druzhinin, O. A., & Elghobashi, S. (1999). On the decay rate of isotropic turbulence laden with microparticles. *Physics of Fluids*, *11*(3), 602-610.

Druzhinin, O. A. (2001). The influence of particle inertia on the two-way coupling and modification of isotropic turbulence by microparticles. *Physics of Fluids*, *13*(12), 3738-3755.

Duru, P., Koch, D. L., & Cohen, C. (2007). Experimental study of turbulence-induced coalescence in aerosols. *International Journal of Multiphase Flow*, *33*(9), 987-1005.

Eaton, J. K. (2009). Two-way coupled turbulence simulations of gas-particle flows using point-particle tracking. *International Journal of Multiphase Flow*, *35*(9), 792-800.

Eggersdorfer, M. L., Kadau, D., Herrmann, H. J., & Pratsinis, S. E. (2011). Multiparticle sintering dynamics: from fractal-like aggregates to compact structures. *Langmuir*, *27*(10), 6358-6367.

Elghobashi, S., & Truesdell, G. C. (1993). On the two-way interaction between homogeneous turbulence and dispersed solid particles. I: Turbulence modification. *Physics of Fluids A: Fluid Dynamics*, *5*(7), 1790-1801.

Elsinga, G. E., & Marusic, I. (2010). Universal aspects of small-scale motions in turbulence. *Journal of Fluid Mechanics*, *662*, 514-539.

Falkovich, G., & Pumir, A. (2004). Intermittent distribution of heavy particles in a turbulent flow. *Physics of Fluids*, *16*(7), L47-L50.

Faletra, M., Marshall, J. S., Yang, M., & Li, S. (2015). Particle segregation in falling polydisperse suspension droplets. *Journal of Fluid Mechanics*, *769*, 79-102.

Fanelli, M., Feke, D. L., & Manas-Zloczower, I. (2006). Prediction of the dispersion of particle clusters in the nano-scale—part I: steady shearing responses. *Chemical Engineering Science*, *61*(2), 473-488.

Farinella, P., Paolicchi, P., & Zappalà, V. (1982). The asteroids as outcomes of catastrophic collisions. *Icarus*, *52*(3), 409-433.

Fayed, H. E. H. H. (2014). *Particles and Bubbles Collisions Frequency in Homogeneous Turbulence and Applications to Minerals Flotation Machines* (Doctoral dissertation, Virginia Tech).

Fayed, H. E., & Ragab, S. A. (2013). Direct numerical simulation of particles-bubbles collisions kernel in homogeneous isotropic turbulence. *The Journal of Computational Multiphase Flows*, *5*(3), 167-188.

Fellay, L. S., Twist, C., & Vanni, M. (2013). Motion of rigid aggregates under different flow conditions. *Acta Mechanica*, *224*(10), 2225-2248.

Fiedler, H. E. (1988). Coherent structures in turbulent flows. *Progress in Aerospace Sciences*, *25*(3), 231-269.

Friedlander, S. K. (2000). Smoke, Dust, and Haze: Fundamentals of Aerosol Dynamics.

Frisch, U. (1995). *Turbulence: the legacy of AN Kolmogorov*. Cambridge university press.

Garcia, M. (2009). Développement et validation du formalisme euler-lagrange dans un solveur parallele et non-structuré pour la simulation aux grandes échelles. *France Thèse*.

Gastaldi, A., & Vanni, M. (2011). The distribution of stresses in rigid fractal-like aggregates in a uniform flow field. *Journal of colloid and interface science*, *357*(1), 18-30.

Goldstein, M. L., Roberts, D. A., & Matthaeus, W. H. (1995). Magnetohydrodynamic turbulence in the solar wind. *Annual review of astronomy and astrophysics*, *33*(1), 283-325.

Gore, R. A., & Crowe, C. T. (1989). Effect of particle size on modulating turbulent intensity. *International Journal of Multiphase Flow*, *15*(2), 279-285.

Greengard, L., & Rokhlin, V. (1987). A fast algorithm for particle simulations. *Journal of computational physics*, *73*(2), 325-348.

Grits, B., Pinsky, M., & Khain, A. (2006). Investigation of small-scale droplet concentration inhomogeneities in a turbulent flow. *Meteorology and Atmospheric Physics*, *92*(3-4), 191-204.

Gunkelmann, N., Ringl, C., & Urbassek, H. M. (2016). Influence of porosity on collisions between dust aggregates. *Astronomy & Astrophysics*, *589*, A30.

Gutmark, E., & Wygnanski, I. (1976). The planar turbulent jet. *Journal of Fluid Mechanics*, *73*(3), 465-495.

Hansen, S., Khakhar, D. V., & Ottino, J. M. (1998). Dispersion of solids in nonhomogeneous viscous flows. *Chemical engineering science*, *53*(10), 1803-1817.

Happel, J. (1958). Viscous flow in multiparticle systems: slow motion of fluids relative to beds of spherical particles. *AIChE Journal*, *4*(2), 197-201.

Hatakeyama, N., & Kambe, T. (1997). Statistical laws of random strained vortices in turbulence. *Physical Review Letters*, *79*(7), 1257.

Helsdon, J. H., Wojcik, W. A., & Farley, R. D. (2001). An examination of thunderstorm-charging mechanisms using a two-dimensional storm electrification model. *Journal of Geophysical Research: Atmospheres*, *106*(D1), 1165-1192.

Hertz, H. (1882). Über die Berührung fester elastischer Körper und über die Härte-Verhandlungen des Vereins zur Beförderung des Gewerbefleißes.

Higashitani, K., Iimura, K., & Sanda, H. (2001). Simulation of deformation and breakup of large aggregates in flows of viscous fluids. *Chemical Engineering Science*, *56*(9), 2927-2938.

Ihalainen, M., Lind, T., Torvela, T., Lehtinen, K. E. J., & Jokiniemi, J. (2012). A method to study agglomerate breakup and bounce during impaction. *Aerosol Science and Technology*, *46*(9), 990-1001.

Iimura, K., Suzuki, M., Hirota, M., & Higashitani, K. (2009a). Simulation of dispersion of agglomerates in gas phase–acceleration field and impact on cylindrical obstacle. *Advanced Powder Technology*, *20*(2), 210-215.

Iimura, K., Yanagiuchi, M., Suzuki, M., Hirota, M., & Higashitani, K. (2009b). Simulation of dispersion and collection process of agglomerated particles in collision with fibers using discrete element method. *Advanced Powder Technology*, *20*(6), 582-587.

Ishihara, T., Gotoh, T., & Kaneda, Y. (2009). Study of high–Reynolds number isotropic turbulence by direct numerical simulation. *Annual Review of Fluid Mechanics*, *41*, 165-180.

Jiang, Q., & Logan, B. E. (1991). Fractal dimensions of aggregates determined from steady-state size distributions. *Environmental Science & Technology*, *25*(12), 2031-2038.

Jin, G., He, G. W., & Wang, L. P. (2010). Large-eddy simulation of turbulent collision of heavy particles in isotropic turbulence. *Physics of Fluids*, *22*(5), 055106.

Jiménez, J., Wray, A. A., Saffman, P. G., & Rogallo, R. S. (1993). The structure of intense vorticity in isotropic turbulence. *Journal of Fluid Mechanics*, *255*, 65-90.

Johnson, K. L. (1985). Contact Mechanics, Cambridge University Press, Cambridge.".

Johnson, K. L., Kendall, K., & Roberts, A. D. (1971). Surface energy and the contact of elastic solids. *Proc. R. Soc. Lond. A*, *324*(1558), 301-313.

Jones, R. B. (1978). Hydrodynamic interaction of two permeable spheres III: Mobility tensors. *Physica A: Statistical Mechanics and its Applications*, *92*(3-4), 571-583.

Joseph, G. G., Zenit, R., Hunt, M. L., & Rosenwinkel, A. M. (2001). Particle–wall collisions in a viscous fluid. *Journal of Fluid Mechanics*, *433*, 329-346.

Kajikawa, M., Kikuchi, K., Asuma, Y., Inoue, Y., & Sato, N. (2000). Aggregation of needle snow crystals. *Atmospheric research*, *55*(2), 131-138.

Kafui, K. D., & Thornton, C. (2000). Numerical simulations of impact breakage of a spherical crystalline agglomerate. *Powder Technology*, *109*(1-3), 113-132.

Kambe, T., & Hatakeyama, N. (2000). Statistical laws and vortex structures in fully developed turbulence. *Fluid Dynamics Research*, *27*(4), 247-267.

Keeley, N., Raabe, R., Alamanos, N., & Sida, J. L. (2007). Fusion and direct reactions of halo nuclei at energies around the Coulomb barrier. *Progress in Particle and Nuclear Physics*, *59*(2), 579-630.

Kivotides, D., & Leonard, A. (2003). Quantized turbulence physics. *Physical review letters*, *90*(23), 234503.

Koch, D. L., & Pope, S. B. (2002). Coagulation-induced particle-concentration fluctuations in homogeneous, isotropic turbulence. *Physics of Fluids*, *14*(7), 2447-2455.

Kolmogorov, A. N. (1941, February). The local structure of turbulence in incompressible viscous fluid for very large Reynolds numbers. In *Dokl. Akad. Nauk SSSR* (Vol. 30, No. 4, pp. 299-303).

Kondic, L., Goullet, A., O'Hern, C. S., Kramar, M., Mischaikow, K., & Behringer, R. P. (2012). Topology of force networks in compressed granular media. *EPL (Europhysics Letters)*, *97*(5), 54001.

Kobayashi, M., Adachi, Y., & Ooi, S. (1999). Breakup of fractal flocs in a turbulent flow. *Langmuir*, *15*(13), 4351-4356.

Kosinski, P., & Hoffmann, A. C. (2010). An extension of the hard-sphere particle–particle collision model to study agglomeration. *Chemical Engineering Science*, *65*(10), 3231-3239.

Kraichnan, R. H. (1970). Diffusion by a random velocity field. *The physics of fluids*, *13*(1), 22-31.

Kun, F., & Herrmann, H. J. (1999). Transition from damage to fragmentation in collision of solids. *Physical Review E*, *59*(3), 2623.

Kusters, K. A., Wijers, J. G., & Thoenes, D. (1997). Aggregation kinetics of small particles in agitated vessels. *Chemical Engineering Science*, *52*(1), 107-121.

La Porta, A., Voth, G. A., Crawford, A. M., Alexander, J., & Bodenschatz, E. (2001). Fluid particle accelerations in fully developed turbulence. *Nature*, *409*(6823), 1017.

Lele, S. K. (1992). Compact finite difference schemes with spectral-like resolution. *Journal of computational physics*, *103*(1), 16-42.

Li, C., Ye, M., & Liu, Z. (2016). On the rotation of a circular porous particle in 2D simple shear flow with fluid inertia. *Journal of Fluid Mechanics*, *808*.

Lian, G., Thornton, C., & Adams, M. J. (1998). Discrete particle simulation of agglomerate impact coalescence. *Chemical Engineering Science*, *53*(19), 3381-3391.

Liu, J., Shih, W. Y., Sarikaya, M., & Aksay, I. A. (1990). Fractal colloidal aggregates with finite interparticle interactions: Energy dependence of the fractal dimension. *Physical Review A*, *41*(6), 3206.

Loth, E. (2000). Numerical approaches for motion of dispersed particles, droplets and bubbles. *Progress in energy and combustion science*, *26*(3), 161-223.

Lu, J., & Wang, J. K. (2006). Agglomeration, breakage, population balance, and crystallization kinetics of reactive precipitation process. *Chemical Engineering Communications*, *193*(7), 891-902.

Lund, T. S., Wu, X., & Squires, K. D. (1998). Generation of turbulent inflow data for spatially-developing boundary layer simulations. *Journal of computational physics*, *140*(2), 233-258.

Lundgren, T. S. (1982). Strained spiral vortex model for turbulent fine structure. *The Physics of Fluids*, *25*(12), 2193-2203.

Lundgren, T. S. (2003). Annual Research Briefs. *Center for Turbulence Research, Stanford, CA*, 461-473.

Malik, N. A., & Vassilicos, J. C. (1996). Eulerian and Lagrangian scaling properties of randomly advected vortex tubes. *Journal of Fluid Mechanics*, *326*, 417-436.

Marangoni, A. G., & Narine, S. S. (2001). Elasticity of fractal aggregate networks: Mechanical arguments. *Crystallization and solidification properties of lipids*, 153-159.

Marshall, J. S. (2009). Discrete-element modeling of particulate aerosol flows. *Journal of Computational Physics*, *228*(5), 1541-1561.

Marshall, J. S., & Grant, J. R. (1996). Penetration of a blade into a vortex core: vorticity response and unsteady blade forces. *Journal of Fluid Mechanics*, *306*, 83-109.

Marshall, J. S., Grant, J. R., Gossler, A. A., & Huyer, S. A. (2000). Vorticity transport on a Lagrangian tetrahedral mesh. *Journal of Computational Physics*, *161*(1), 85-113.

Marshall, J. S., & Li, S. (2014). *Adhesive particle flow*. Cambridge University Press.

Marshall, J. S., & Sala, K. (2013). Comparison of methods for computing the concentration field of a particulate flow. *International Journal of Multiphase Flow*, *56*, 4-14.

Matsoukas, T., & Friedlander, S. K. (1991). Dynamics of aerosol agglomerate formation. *Journal of Colloid and Interface Science*, *146*(2), 495-506.

Maxey, M. R., & Riley, J. J. (1983). Equation of motion for a small rigid sphere in a nonuniform flow. *The Physics of Fluids*, *26*(4), 883-889.

Meyer, C. J., & Deglon, D. A. (2011). Particle collision modeling–a review. *Minerals Engineering*, *24*(8), 719-730.

Min, I. A., Mezić, I., & Leonard, A. (1996). Levy stable distributions for velocity and velocity difference in systems of vortex elements. *Physics of fluids*, *8*(5), 1169-1180.

Mindlin, R. D. (1949). Compliance of elastic bodies in contact. *J. Appl. Mech. Trans. ASME*, *16*, 259-268.

Minier, J. P., Chibbaro, S., & Pope, S. B. (2014). Guidelines for the formulation of Lagrangian stochastic models for particle simulations of single-phase and dispersed two-phase turbulent flows. *Physics of Fluids*, *26*(11), 113303.

Mito, Y., & Hanratty, T. J. (2002). Use of a modified Langevin equation to describe turbulent dispersion of fluid particles in a channel flow. *Flow, turbulence and combustion*, *68*(1), 1-26.

Monaghan, J. J. (1985a). Extrapolating B splines for interpolation. *Journal of Computational Physics*, *60*(2), 253-262.

Monaghan, J. J. (1985b). Particle methods for hydrodynamics. *Computer Physics Reports*, *3*(2), 71-124.

Mordant, N., Lévêque, E., & Pinton, J. F. (2004). Experimental and numerical study of the Lagrangian dynamics of high Reynolds turbulence. *New Journal of Physics*, *6*(1), 116.

Moreno, R., Ghadiri, M., & Antony, S. J. (2003). Effect of the impact angle on the breakage of agglomerates: a numerical study using DEM. *Powder Technology*, *130*(1-3), 132-137.

Moreno-Atanasio, R., & Ghadiri, M. (2006). Mechanistic analysis and computer simulation of impact breakage of agglomerates: Effect of surface energy. *Chemical engineering science*, *61*(8), 2476-2481.

Narine, S. S., & Marangoni, A. G. (1999). Fractal nature of fat crystal networks. *Physical Review E*, *59*(2), 1908.

Narine, S. S., & Marangoni, A. G. (1999). Mechanical and structural model of fractal networks of fat crystals at low deformations. *Physical Review E*, *60*(6), 6991.

Nasr, H., & Ahmadi, G. (2007). The effect of two-way coupling and inter-particle collisions on turbulence modulation in a vertical channel flow. *International Journal of Heat and Fluid Flow*, *28*(6), 1507-1517.

Nejadmalayeri, A., Vezolainen, A., & Vasilyev, O. V. (2013). Reynolds number scaling of coherent vortex simulation and stochastic coherent adaptive large eddy simulation. *Physics of Fluids*, *25*(11), 110823.

Nguyen, D., Rasmuson, A., Thalberg, K., & Bjo, I. N. (2014). Numerical modelling of breakage and adhesion of loose fine-particle agglomerates. *Chemical Engineering Science*, *116*, 91-98.

Ning, Z., Boerefijn, R., Ghadiri, M., & Thornton, C. (1997). Distinct element simulation of impact breakage of lactose agglomerates. *Advanced Powder Technology*, *8*(1), 15-37.

Olfert, J. S., Symonds, J. P. R., & Collings, N. (2007). The effective density and fractal dimension of particles emitted from a light-duty diesel vehicle with a diesel oxidation catalyst. *Journal of Aerosol Science*, *38*(1), 69-82.

Ormel, C. W., Paszun, D., Dominik, C., & Tielens, A. G. G. M. (2009). Dust coagulation and fragmentation in molecular clouds-I. How collisions between dust aggregates alter the dust size distribution. *Astronomy & Astrophysics*, *502*(3), 845-869.

Ormel, C. W., Spaans, M., & Tielens, A. G. G. M. (2007). Dust coagulation in protoplanetary disks: porosity matters. *Astronomy & Astrophysics*, *461*(1), 215-232.

Özcan-Taşkin, N. G., Padron, G., & Voelkel, A. (2009). Effect of particle type on the mechanisms of break up of nanoscale particle clusters. *Chemical Engineering Research and Design*, *87*(4), 468-473.

Paiva, J., Salcedo, R., & Araujo, P. (2010). Impact of particle agglomeration in cyclones. *Chemical Engineering Journal*, *162*(3), 861-876.

Peters, J. F., Muthuswamy, M., Wibowo, J., & Tordesillas, A. (2005). Characterization of force chains in granular material. *Physical review E*, *72*(4), 041307.

Pignatel, F., Nicolas, M., & Guazzelli, E. (2011). A falling cloud of particles at a small but finite Reynolds number. *Journal of Fluid Mechanics*, *671*, 34-51.

Poelma, C., & Ooms, G. (2006). Particle-turbulence interaction in a homogeneous, isotropic turbulent suspension. *Applied Mechanics Reviews*, *59*(2), 78-90.
Pope, S. B. (2011). Simple models of turbulent flows. *Physics of Fluids*, *23*(1), 011301.

Pope, S. B., & Chen, Y. L. (1990). The velocity-dissipation probability density function model for turbulent flows. *Physics of Fluids A: Fluid Dynamics*, *2*(8), 1437-1449.

Potanin, A. A. (1993). On the computer simulation of the deformation and breakup of colloidal aggregates in shear flow. *Journal of colloid and interface science*, *157*(2), 399-410.

Pullin, D. I., & Saffman, P. G. (1993). On the Lundgren–Townsend model of turbulent fine scales. *Physics of Fluids A: Fluid Dynamics*, *5*(1), 126-145.

Rai, M. M., & Moin, P. (1991). Direct simulations of turbulent flow using finite-difference schemes. *Journal of computational physics*, *96*(1), 15-53.

Ramaprian, B. R., & Chandrasekhara, M. S. (1985). LDA measurements in plane turbulent jets. *Journal of Fluids Engineering*, *107*(2), 264-271.

Rao, A., Curtis, J. S., Hancock, B. C., & Wassgren, C. (2012). Numerical simulation of dilute turbulent gas-particle flow with turbulence modulation. *AIChE Journal*, *58*(5), 1381-1396.

Reade, W. C., & Collins, L. R. (2000). A numerical study of the particle size distribution of an aerosol undergoing turbulent coagulation. *Journal of Fluid Mechanics*, *415*, 45-64.

Reeks, M. W. (2014). Transport, mixing and agglomeration of particles in turbulent flows. In *Journal of Physics: Conference Series* (Vol. 530, No. 1, p. 012003). IOP Publishing.

Reinhold, A., & Briesen, H. (2012). Numerical behavior of a multiscale aggregation model—coupling population balances and discrete element models. *Chemical engineering science*, *70*, 165-175.

Rosales, C., & Meneveau, C. (2005). Linear forcing in numerical simulations of isotropic turbulence: Physical space implementations and convergence properties. *Physics of Fluids*, *17*(9), 095106.

Rubinow, S. I., & Keller, J. B. (1961). The transverse force on a spinning sphere moving in a viscous fluid. *Journal of Fluid Mechanics*, *11*(3), 447-459.

Rumpf, H. (1962). The Strength of Granules and Agglomeration. *Agglomeration*, John Wiley, 379-418.

Rwei, S. P., Manas-Zloczower, I., & Feke, D. L. (1990). Observation of carbon black agglomerate dispersion in simple shear flows. *Polymer Engineering & Science*, *30*(12), 701-706.

Rwei, S. P., Manas-Zloczower, I., & Feke, D. L. (1991). Characterization of agglomerate dispersion by erosion in simple shear flows. *Polymer Engineering & Science*, *31*(8), 558-562.

Saber, A., Lundström, T. S., & Hellström, J. G. I. (2015). Turbulent modulation in particulate flow: A review of critical variables. *Engineering*, *7*(10), 597.

Saffman, P. G. T. (1965). The lift on a small sphere in a slow shear flow. *Journal of fluid mechanics*, *22*(2), 385-400.

Saffman, P. G. T. (1968). Corrigendum to 'The lift on a small sphere in a slow shear flow', *Journal of fluid mechanics*, 31(3), 624

Saffman, P. G. (1997). Vortex models of isotropic turbulence. *Philosophical Transactions of the Royal Society of London A: Mathematical, Physical and Engineering Sciences*, *355*(1731), 1949-1956.

Saffman, P., & Turner, J. S. (1956). On the collision of drops in turbulent clouds. *Journal of Fluid Mechanics*, *1*(1), 16-30.

Sala, K., & Marshall, J. S. (2013). Stochastic vortex structure method for modeling particle clustering and collisions in homogeneous turbulence. *Physics of Fluids*, *25*(10), 103301.

Salmon, J. K., & Warren, M. S. (1994). Skeletons from the treecode closet. *Journal of Computational Physics*, *111*(1), 136-155.

Samimi, A., Moreno, R., & Ghadiri, M. (2004). Analysis of impact damage of agglomerates: effect of impact angle. *Powder technology*, *143*, 97-109.

Saunders, C. P. R. (1994). Thunderstorm electrification laboratory experiments and charging mechanisms. *Journal of Geophysical Research: Atmospheres*, *99*(D5), 10773-10779.

Sawford, B. L. (1991). Reynolds number effects in Lagrangian stochastic models of turbulent dispersion. *Physics of Fluids A: Fluid Dynamics*, *3*(6), 1577-1586.

Schäfer, C., Speith, R., & Kley, W. (2007). Collisions between equal-sized ice grain agglomerates. *Astronomy & Astrophysics*, *470*(2), 733-739.

Scurati, A., Feke, D. L., & Manas-Zloczower, I. (2005). Analysis of the kinetics of agglomerate erosion in simple shear flows. *Chemical Engineering Science*, *60*(23), 6564-6573.

Selomulya, C., Amal, R., Bushell, G., & Waite, T. D. (2001). Evidence of shear rate dependence on restructuring and breakup of latex aggregates. *Journal of colloid and interface science*, *236*(1), 67-77.

Seizinger, A., & Kley, W. (2013). Bouncing behavior of microscopic dust aggregates. *Astronomy & Astrophysics*, *551*, A65.

Serra, T., Colomer, J., & Casamitjana, X. (1997). Aggregation and breakup of particles in a shear flow. *Journal of Colloid and Interface Science*, *187*(2), 466-473.

Seyvet, O., & Navard, P. (2000). Collision-induced dispersion of agglomerate suspensions in a shear flow. *Journal of applied polymer science*, *78*(5), 1130-1133.

Schwarzkopf, J. D., Sommerfeld, M., Crowe, C. T., & Tsuji, Y. (2011). *Multiphase flows with droplets and particles*. CRC press.

Shapiro, M., Vainshtein, P., Dutcher, D., Emery, M., Stolzenburg, M., Kittelson, D. B., & McMurry, P. H. (2012). Characterization of agglomerates by simultaneous measurement of mobility, vacuum aerodynamic diameter and mass. *Journal of Aerosol Science*, *44*, 24-45.

Shih, W. H., Shih, W. Y., Kim, S. I., Liu, J., & Aksay, I. A. (1990). Scaling behavior of the elastic properties of colloidal gels. *Physical review A*, *42*(8), 4772.

Shotorban, B., & Mashayek, F. (2005). Modeling subgrid-scale effects on particles by approximate deconvolution. *Physics of Fluids*, *17*(8), 081701.

Smirnov, A., Shi, S., & Celik, I. (2001). Random flow generation technique for large eddy simulations and particle-dynamics modeling. *Journal of Fluids Engineering*, *123*(2), 359-371.

Smith, O. K. (1961). Eigenvalues of a symmetric 3× 3 matrix. *Communications of the ACM*, *4*(4), 168.

Smoluchowski, M. V. (1918). Versuch einer mathematischen Theorie der Koagulationskinetik kolloider Lösungen. *Zeitschrift für physikalische Chemie*, *92*(1), 129-168.

Sonntag, R. C., & Russel, W. B. (1986). Structure and breakup of flocs subjected to fluid stresses: I. Shear experiments. *Journal of colloid and interface science*, *113*(2), 399-413.

Squires, K. D., & Eaton, J. K. (1990). Particle response and turbulence modification in isotropic turbulence. *Physics of Fluids A: Fluid Dynamics*, *2*(7), 1191-1203.

Squires, K. D., & Eaton, J. K. (1991). Preferential concentration of particles by turbulence. *Physics of Fluids A: Fluid Dynamics*, *3*(5), 1169-1178.

Stanley, S. A., Sarkar, S., & Mellado, J. P. (2002). A study of the flow-field evolution and mixing in a planar turbulent jet using direct numerical simulation. *Journal of Fluid Mechanics*, *450*, 377-407.

Subramanian, G., & Koch, D. L. (2008). Evolution of clusters of sedimenting low-Reynolds-number particles with Oseen interactions. *Journal of Fluid Mechanics*, *603*, 63-100.

Sundaram, S., & Collins, L. R. (1997). Collision statistics in an isotropic particle-laden turbulent suspension. Part 1. Direct numerical simulations. *Journal of Fluid Mechanics*, *335*, 75-109.

Sundaram, S., & Collins, L. R. (1999). A numerical study of the modulation of isotropic turbulence by suspended particles. *Journal of Fluid Mechanics*, *379*, 105-143.

Sutherland, D. N., & Tan, C. T. (1970). Sedimentation of a porous sphere. *Chemical Engineering Science*, *25*(12), 1948-1950.

Steijl, R. (2001). Computational study of vortex pair dynamics.

Tabor, G. R., & Baba-Ahmadi, M. H. (2010). Inlet conditions for large eddy simulation: a review. *Computers & Fluids*, *39*(4), 553-567.

Tang, L., Wen, F., Yang, Y., Crowe, C. T., Chung J. N., & Troutt, T. R. (1992). Self-organizing particle dispersion mechanism in a plane wake. *Physics of Fluids A: Fluid Dynamics*, *4*(10), 2244-2251.

Taylor, G. I. (1938). Production and dissipation of vorticity in a turbulent fluid. *Proceedings of the Royal Society of London. Series A, Mathematical and Physical Sciences*, 15-23.

Thomas, F. O., & Prakash, K. M. K. (1991). An experimental investigation of the natural transition of an untuned planar jet. *Physics of Fluids A: Fluid Dynamics*, *3*(1), 90-105.

Thomson, D. J. (1987). Criteria for the selection of stochastic models of particle trajectories in turbulent flows. *Journal of Fluid Mechanics*, *180*, 529-556.

Thornton, C. (1991). Interparticle sliding in the presence of adhesion. *Journal of Physics D: Applied Physics*, *24*(11), 1942.

Thornton, C., Ciomocos, M. T., & Adams, M. J. (1999). Numerical simulations of agglomerate impact breakage. *Powder Technology*, *105*(1-3), 74-82.

Thornton, C., & Liu, L. (2004). How do agglomerates break?. *Powder Technology*, *143*, 110-116.

Tong, Z. B., Yang, R. Y., Chu, K. W., Yu, A. B., Adi, S., & Chan, H. K. (2010). Numerical study of the effects of particle size and polydispersity on the agglomerate dispersion in a cyclonic flow. *Chemical Engineering Journal*, *164*(2-3), 432-441.

Tong, Z. B., Yang, R. Y., Yu, A. B., Adi, S., & Chan, H. K. (2009). Numerical modelling of the breakage of loose agglomerates of fine particles. *Powder Technology*, *196*(2), 213-221.

Tong, Z., Zhong, W., Yu, A., Chan, H. K., & Yang, R. (2016). CFD–DEM investigation of the effect of agglomerate–agglomerate collision on dry powder aerosolisation. *Journal of Aerosol Science*, *92*, 109-121.

Torres, F. E., Russel, W. B., & Schowalter, W. R. (1991). Floc structure and growth kinetics for rapid shear coagulation of polystyrene colloids. *Journal of colloid and interface science*, *142*(2), 554-574.

Townsend, A. A. (1951). On the fine-scale structure of turbulence. *Proc. R. Soc. Lond. A*, *208*(1095), 534-542.

Tsuji, Y., Tanaka, T., & Ishida, T. (1992). Lagrangian numerical simulation of plug flow of cohesionless particles in a horizontal pipe. *Powder technology*, *71*(3), 239-250.

Tryggeson, H. (2007). Analytical Vortex Solutions to the Navier-Stokes Equation (doktorsavhandling).

Uhlmann, M. (2005). An immersed boundary method with direct forcing for the simulation of particulate flows. *Journal of Computational Physics*, *209*(2), 448-476.

Vainshtein, P., & Shapiro, M. (2005). Mobility of permeable fractal agglomerates in slip regime. *Journal of colloid and interface science*, *284*(2), 501-509.

Vainshtein, P., & Shapiro, M. (2006). Porous agglomerates in the general linear flow field. *Journal of colloid and interface science*, *298*(1), 183-191.

Verzicco, R., & Orlandi, P. (1996). A finite-difference scheme for three-dimensional incompressible flows in cylindrical coordinates. *Journal of Computational Physics*, *123*(2), 402-414.

Vincent, A., & Meneguzzi, M. (1991). The spatial structure and statistical properties of homogeneous turbulence. *Journal of Fluid Mechanics*, *225*, 1-20.

Vincent, A., & Meneguzzi, M. (1994). The dynamics of vorticity tubes in homogeneous turbulence. *Journal of Fluid Mechanics*, *258*, 245-254.

Von Schiller, L., & Naumann, A. (1933). Über die grundlegenden Berechnungen bei der Schwerkraftaufbereitung, Z. *Vereines Deutscher Ingenieure*, *44*, 318-320.

Voth, G. A., Satyanarayan, K., & Bodenschatz, E. (1998). Lagrangian acceleration measurements at large Reynolds numbers. *Physics of Fluids*, *10*(9), 2268-2280.

Waldner, M. H., Sefcik, J., Soos, M., & Morbidelli, M. (2005). Initial growth kinetics and structure of colloidal aggregates in a turbulent coagulator. *Powder technology*, *156*(2-3), 226-234.

Wang, L. P., Wexler, A. S., & Zhou, Y. (1998). Statistical mechanical descriptions of turbulent coagulation. *Physics of Fluids*, *10*(10), 2647-2651.

Wang, L. P., Wexler, A. S., & Zhou, Y. (2000). Statistical mechanical description and modelling of turbulent collision of inertial particles. *Journal of Fluid Mechanics*, *415*, 117-153.

Wen, C. Y. (1966). Mechanics of fluidization. In *Chem. Eng. Prog. Symp. Ser.* (Vol. 62, pp. 100-111).

Wengeler, R., & Nirschl, H. (2007). Turbulent hydrodynamic stress induced dispersion and fragmentation of nanoscale agglomerates. *Journal of colloid and interface science*, *306*(2), 262-273.

Wilczek, M., & Friedrich, R. (2009). Dynamical origins for non-Gaussian vorticity distributions in turbulent flows. *Physical Review E*, *80*(1), 016316.

Wilczek, M., Jenko, F., & Friedrich, R. (2008). Lagrangian particle statistics in turbulent flows from a simple vortex model. *Physical Review E*, *77*(5), 056301.

Wilson, J. D., & Sawford, B. L. (1996). Review of Lagrangian stochastic models for trajectories in the turbulent atmosphere.

Xu, X. G., Li, S. Q., Li, G. D., & Yao, Q. (2009). Effect of co-firing straw with two coals on the ash deposition behavior in a down-fired pulverized coal combustor. *Energy & Fuels*, *24*(1), 241-249.

Yang, J., Wu, C. Y., & Adams, M. (2014). Three-dimensional DEM–CFD analysis of air-flow-induced detachment of API particles from carrier particles in dry powder inhalers. *Acta Pharmaceutica Sinica B*, *4*(1), 52-59.

Yang, M., Li, S., & Marshall, J. S. (2015). Effects of long-range particle–particle hydrodynamic interaction on the settling of aerosol particle clouds. *Journal of Aerosol Science*, *90*, 154-160.

Zaichik, L. I., Alipchenkov, V. M., & Avetissian, A. R. (2006). Modelling turbulent collision rates of inertial particles. *International journal of heat and fluid flow*, *27*(5), 937-944.

Zeidan, M., Xu, B. H., Jia, X., & Williams, R. A. (2007). Simulation of aggregate deformation and breakup in simple shear flows using a combined continuum and discrete model. *Chemical Engineering Research and Design*, *85*(12), 1645-1654.

Zhang, Y., Shuiqing, L., Deng, S., Yao, Q., & Stephen, D. T. (2012). Direct synthesis of nanostructured TiO2 films with controlled morphologies by stagnation swirl flames. *Journal of Aerosol Science*, *44*, 71-82.

Zhang, L., Wang, Y., & Zhang, J. (2014). Force-chain distributions in granular systems. *Physical Review E*, *89*(1), 012203.